Structural Diversity of Ternary and Quaternary Alkali-Metal Pnictides

by

Mansura Khatun

A thesis submitted in partial fulfillment of the requirements for the degree of

Doctor of Philosophy

Department of Chemistry
University of Alberta

Abstract

To evaluate the applicability and expand the limit of the Zintl-Klemm concept, many new alkali-metal pnictides were synthesized by high temperature solid reactions in *A*-*M*-*Pn* or *A*-*Tt*-*Pn* ternary systems and *A*-*M*-*Tt*-*Pn* quaternary systems (*A* = Na, K, Rb; *M* = Mn, Zn, Cd; *Tt* = Si, Ge, Sn; *Pn* = As, Sb). Their crystal structures were characterized by X-ray diffraction methods. Their electronic structures and bonding interactions were determined using TB-LMTO calculations. Ternary pnictides adopt their own-type structures, having unique structural patterns: corrugated chains ($Rb_4Zn_7As_7$- and $Rb_7Mn_{12}Sb_{12}$-type structure) and layers (KSn_3As_3-type structure), GeAs-type layers ($NaGe_6As_6$), and 3D-networks ($K_2Zn_5As_4$). The quaternary $AM_{1.5}Tt_{0.5}As_2$ pnictides prefer to crystallize either in the $CaAl_2Si_2$- or $ThCr_2Si_2$-type structure, depending on the relative sizes of atoms, as expressed through a structure map. The structure map also suggested that $ACd_{1.5}Ge_{0.5}As_2$ (*A* = K, Rb) phases would not form; indeed, attempts to prepare them gave new triclinic phases $ACdGeAs_2$ instead.

Band structure calculations revealed electronic structures in good agreement with expectations: $K_2Zn_5As_4$ (0.4 eV), KGe_3As_3 (0.71 eV), and $KCdGeAs_2$ (0.80 eV) are small band-gap semiconductors; $NaZn_{1.5}Si_{0.5}As_2$ (small overlap at Fermi level) is a semimetal; $Rb_4Zn_7As_7$ (small gap above Fermi level), $Rb_7Mn_{12}Sb_{12}$ (pseudogap above Fermi level), and $NaGe_6As_6$ (small gap below Fermi level) are metallic. Pnictides that have *A*-to-*Pn* ratio of 1:2 to 1:3 follow the Zintl concept. $Rb_4Zn_7As_7$ and $Rb_7Mn_{12}Sb_{12}$ are electron-deficient Zintl phases having an *A*-to-*Pn* ratio of <2 whereas $NaGe_6As_6$ is an electron-rich Zintl phase

having an *A*-to-*Pn* ratio of >3. This work opens a new window to study substitutional chemistry.

Preface

This thesis presents research work which I completed during my graduate studies in the laboratory of Dr. Mar at the University of Alberta. Most of the research work has additional co-authors and has been published in different peer-reviewed journals. Here I summarize my contributions. Dr. Mar is the supervisory author who prepared and submitted all manuscripts to the journals.

All chapters have been published: Stoyko, S. S.; Khatun, M.; Mar, A. "Ternary Arsenides $A_2Zn_5As_4$ (A = K, Rb): Zintl Phases Built from *Stellae Quadrangulae,*" *Inorg. Chem.* **2012**, *51*, 9517–9521 (Chapter 2); Khatun, M.; Stoyko, S. S.; Mar, A. "Electron-Deficient Ternary and Quaternary Pnictides $Rb_4Zn_7As_7$, $Rb_4Mn_{3.5}Zn_{3.5}Sb_7$, $Rb_7Mn_{12}Sb_{12}$, and $Rb_7Mn_4Cd_8Sb_{12}$ with Corrugated Anionic Layers," *Inorg. Chem.* **2013**, *52*, 12682–12690 (Chapter 3); Khatun, M.; Stoyko, S. S.; Mar, A. "Ternary Arsenides ATt_3As_3 (A = K, Rb; Tt = Ge, Sn) with Layered Structures," *J. Solid State Chem.* **2016**, *238*, 229–235 (Chapter 4); Khatun, M.; Mar, A. "$NaGe_6As_6$: Insertion of Sodium into the Layered Semiconductor Germanium Arsenide GeAs," *Z. Naturforsch., B* **2016**, *71*, 375–380 (Chapter 5); Khatun, M.; Stoyko, S. S.; Mar, A. "Quaternary Arsenides $AM_{1.5}Tt_{0.5}As_2$ (A = Na, K, Rb; M = Zn, Cd; Tt = Si, Ge, Sn): Size Effects in $CaAl_2Si_2$- and $ThCr_2Si_2$-Type Structures," *Inorg. Chem.* **2013**, *52*, 3148–3158 (Chapter 6); and Khatun, M.; Stoyko, S. S.; Mar, A. "Quaternary Arsenides ACdGeAs$_2$ (A = K, Rb) Built of Ethane-Like Ge_2As_6 Units," *Inorg. Chem.* **2014**, *53*, 7756–7762 (Chapter 7). I synthesized samples, characterized them through XRD, SEM, and EDX, solved crystal structures, performed band structure calculations, and prepared the drafts for

all manuscripts. Dr. Stoyko proposed the project for Chapter 2; he assisted in synthesis and characterization for Chapters 3, 4, 6, and 7.

Dedicated to my beloved husband Delwar

and

our son Fardeen-the heart of our life.

My life is empty without you both!

Acknowledgements

I would like to thank Dr. Arthur Mar, my graduate supervisor and mentor. He inspired me to learn crystallography and solid state chemistry. He has been there whenever we got into any problem, he provided suggestions so we could resolve the problem ourselves, therefore building our extraordinary problem-solving skills. He was very friendly and a great mentor, he allowed us to work in the wide field of solid state research. He always inspired, appreciated, and supported us with what we have done in the laboratory. I also express my gratitude to him for correcting my thesis so patiently.

I gratefully acknowledge the University of Alberta and all the facilities needed for achieving my Ph.D. degree. My sincere thanks go to Anita Weiler for her administrative support during my entire doctoral study. I would like to thank Dr. Norman Gee for his tremendous support and mentorship that helped me to develop my customer service and teaching skills through staffing the help room and conducting undergraduate labs. I am also thankful to Dr. Robert McDonald and Dr. Michael Ferguson for helping me to operate the diffractometer. I would like to express my gratitude to my colleagues Stan, Krishna, Abishek, Anton, Xinsong, Wenlong, Brent, Brianna, Peter, Danisa, Dong, and Alex for making my graduate student life more enjoyable. Special thanks go to Stan for mentoring the initial solid state syntheses and characterization in the lab.

I would like to thank the faculty and staff in the Department of Chemistry. I am grateful to Dr. Eric Rivard and Dr. Mariusz Klobukowski for serving on my supervisory committee. I am also thankful to Dr. Rylan Lundgren and Dr. Robert Luth for serving on my

candidacy committee. I express my gratitude for their valuable suggestions and constructive criticisms that helped me to learn and develop my skills.

I express my special thanks and love to my dearest parents for their constant support and prayers. I would like to thank my brother and his family for the care and love I have received from them.

I cannot express enough thanks to my caring, loving, and supportive husband Delwar Sikder. I would not have completed my Ph.D. studies without your continued support. I am grateful to my son Fardeen. I would like to take this opportunity to express how deeply Delwar and I are in love with the little one who filled the last drop of happiness in our life.

This research was funded by the University of Alberta, the Natural Sciences and Engineering Research Council of Canada, Queen Elizabeth II Graduate Scholarship, and NSERC CREATE-IRTG ATUMS. I am thankful to all of you who are missing in the list, especially the readers.

Finally, I am thankful to Almighty Allah for giving me persistence to complete my graduate studies and all the success in my life.

List of Contents

List of Tables

List of Figures

List of Symbols and Abbreviations

θ	Angle of reflection
k	Wavevector
λ	Wavelength
ρ	Density
χ	Electronegativity
μ	Absorption coefficient
l	Orbital angular momentum
1D, 2D, 3D	One-, two-, three-dimensional
a, b, c, α, β, γ	Unit cell parameters
A	Alkali metal
ASA	Atomic spheres approximation
COHP	Crystal orbital Hamilton population
COOP	Crystal orbital overlap population
DFT	Density functional theory
DOS	Density of states
DSC	Differential scanning calorimetry
d_{hkl}	d-spacing
EDX	Energy dispersive X-ray analysis
e^-	Electron
E_f	Fermi level
E_g	Band gap

FT	Fourier transform
F_{hkl}	Structure factor
f_j	Scattering factor of atom *j*
hkl	Miller indices
j	Angular momentum
LDA	Local density approximation
LMTO	Linear muffin-tin orbital
M	d-block elements
n	Number of valence electrons
Pn	Pnicogens (N, P, As, Sb, Bi)
R	Reliability factor
RE	Rare-earth
S	Goodness-of-fit
SEM	Scanning electron microscope
T_c	Critical temperature
T	Temperature
TB	Tight-binding
Tr	Triels (Group 13 elements)
Tt	Tetrels (Group 14 elements)
V	Cell volume
VEC	Valence electron concentration
XRD	X-ray diffraction

Z	Atomic number
ZT	Thermoelectric figure of merit

Chapter 1

Introduction

1.1. Zintl Phases

Zintl phases are a special class of intermetallic compounds. In the 1930s, Eduard Zintl first studied a collection of solids which were later named as Zintl phases by Fritz Laves.[1,2] Although the precise definition of Zintl phases has become more generalized, the basic concept remains the same.[1–9] Originally, Zintl phases were binary compounds formed between alkali, alkaline-earth, or even rare-earth metals (electropositive components) and metalloids from groups 13 to 16 (electronegative components). Here, a complete charge transfer takes place from the electropositive to the electronegative component, and normal valence rules are followed. They possess some properties which distinguish them from other intermetallic compounds: (1) higher melting points than the elemental components, (2) large negative heats of formation, and (3) poor conductivity (usually semiconducting behaviour). Zintl phases thus exhibit salt-like properties and structures despite being composed of metals. Oxides and halides are excluded as Zintl phases because they are highly ionic in bonding character and insulating in electrical properties. Later, Wilhelm Klemm elaborated on Zintl's ideas by introducing the pseudoatom concept, in which the anionic unit $X^{(a/x)-}$ in a simple binary compound A_aX_x often attains a structure similar to the neutral isoelectronic element; this modification is now called the Zintl-Klemm concept.

Beyond the fascination of their unique structures and bonding character, Zintl phases are important because they are promising for many applications, including thermoelectric materials,[10–15] superconductors,[16] and magnetocaloric materials.[17] Because the physical

properties needed for these potential applications depend on crystal and electronic structures, a good understanding of the relationship between the structures and properties is essential.

Bonding character can be broadly classified into three extremes: ionic, covalent, and metallic. As illustrated on a van Arkel–Ketelaar triangle, these idealized types of bonding are located at the vertices; in reality, most bonds have intermediate character, which depends on the electronegativity difference and the average electronegativity (**Figure 1-1**).[18–19] Zintl phases show a combination of metallic, ionic, and covalent bonding character. Because they are composed of metals, they generally lie near the metallic corner of the van Arkel-Ketelaar diagram but the difference in electronegativity leads to polar character. This thesis describes several novel arsenides and antimonides which can be considered to be Zintl phases that exhibit interesting bonding patterns and physical properties.

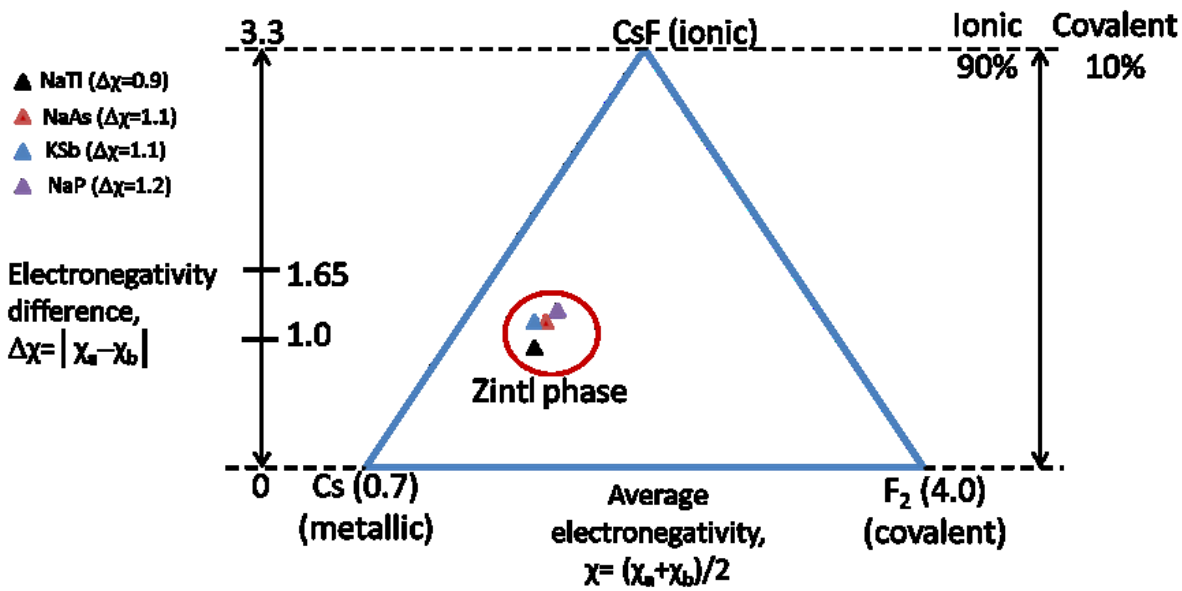

Figure 1-1. Schematic representation of the van Arkel-Ketelaar triangular diagram.

1.2. Electron Counting Schemes

Most molecular substances (such as organic and organometallic compounds) exhibit covalent bonding and obey simple $8e^-$ (octet) or $18e^-$ rules. In contrast, most intermetallic compounds do not follow simple electron-counting rules because they can exhibit a wide range of ionic, covalent, and metallic bonding interactions. Nevertheless, some categories of intermetallic compounds do appear to conform to such rules and have received special attention.[20] For this purpose, it is useful to define a valence electron concentration (*VEC*), which can be specified per atom (called the total *VEC*) or per anion (called the partial *VEC*). In general, for a binary compound A_aX_x containing e_A valence electrons for the electropositive component and e_X valence electrons for the electronegative component:

$$\text{Total } VEC = \frac{ae_a + xe_x}{a+x} \qquad \text{Equation 1-1a}$$

$$VEC(X) = \frac{ae_a + xe_x}{x} \qquad \text{Equation 1-1b}$$

1.2.1. Hume-Rothery Phases

Hume-Rothery phases are a class of alloys comprising binary solid solutions of Cu, Ag, or Au with a post-transition-metal (e.g., Zn, Sn) in which the components show only a small difference in electronegativity. Although they do not follow the normal valence rules because they are not covalent compounds, they do show a correlation between crystal structures with valence electron concentration ($VEC = \frac{valence\ electron}{atom\ ratio}$). Phases with the same *VEC* adopt the same crystal structure; e.g., CuZn ($VEC = \frac{1+2}{2}$) and Cu_5Sn ($VEC = \frac{5+4}{6}$) both have *VEC* of 1.50 and adopt the β-brass type structure.[21]

1.2.2. Valence Compounds

Introduced 100 years ago by Lewis and Kossel,[22,23] the octet (8–*N*) rule states that within a compound, electropositive components donate their valence electrons to the electronegative components so that they achieve a closed-shell (or noble-gas) configuration. Lewis applied this rule to covalent compounds (e.g., HCl, NH_3) and Kossel to ionic compounds (e.g., NaF, $MgCl_2$, Na_2O), but both assumed 2c–2e$^-$ bonds. The structures of many new crystalline inorganic solids were determined through the rapid development of X-ray crystallography. Many researchers provided theoretical and experimental concepts to understand bonding in intermetallic compounds.

The Zintl concept extends the octet rule to intermetallic compounds in which the electronegativity difference is much smaller than in ionic compounds. Initially, Zintl proposed a border separating the electropositive metals (mainly group 1 and 2 elements) to the left and the electronegative metals to the right which form binary Zintl phases (**Figure 1-2**). Later, Klemm adjusted the boundary between metametals and semimetals. Now, Zintl phases include not only binary phases (e.g., NaTl, Na_3As, K_8Ge_{44}) but also multinary ones (e.g., KSnAs, SrZnSb, $K_6Sn_3As_5$).[9,24]

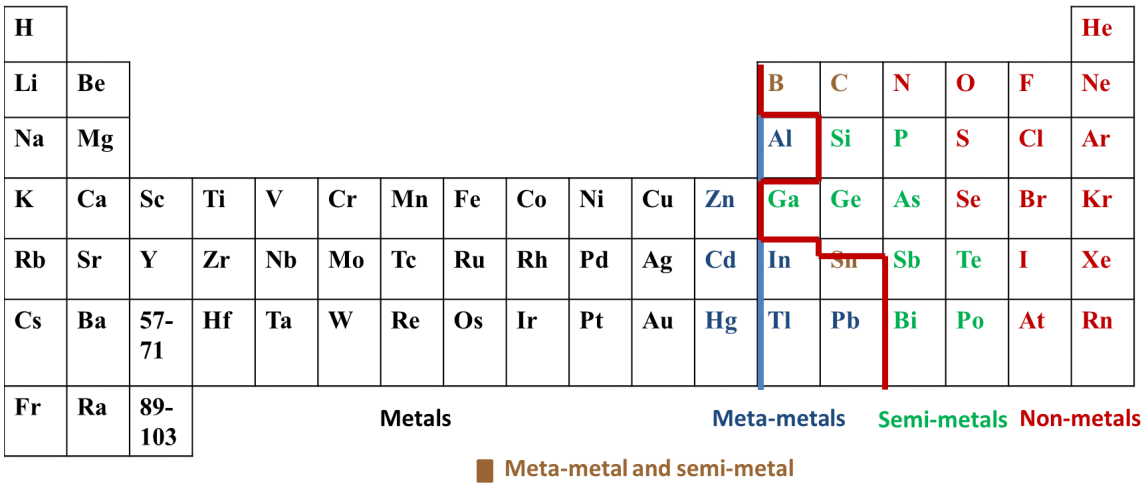

Figure 1-2. The periodic table: blue line suggested by Zintl and red line suggested by Klemm.

The compositions of some phases (e.g., NaTl) look like they appear to violate the octet rule. Zintl suggested that in these cases, additional homoatomic bonds form between the electronegative elements to satisfy the octet rule. In NaTl, for example, Na donates one valence electron to Tl; the resulting Tl^{-} species has four valence electrons but can attain an octet by forming four homoatomic Tl–Tl bonds, resulting in an anionic diamond-like sublattice structure, isoelectronic to Si.

Thus, if the electropositive components are unable to donate sufficient electrons to the electronegative components to achieve an octet, a polyanionic network must form to recover an octet. On the other hand, if the electropositive components have excess electrons remaining after valence electrons are transferred to the electronegative components, a polycationic network forms. The valence electron concentration per anion can be calculated using **Equation 1-1b**

If $VEC(X) = 8$, no homoatomic bonds form and only monoatomic cations and anions are present, as exemplified by Na_3As [$VEC(\text{As}) = (3+5)/1 = 8$].[25] If $VEC(X) < 8$, the number

of polyanionic X–X bonds formed is $b_X = 8 - VEC(X)$. Examples include the elemental forms of the pnicogens ($b_X = 3$, or three As–As bonds in arsenic),[26] NaAs ($b_X = 2$, or two As–As bonds),[27] and Ca_2As_2 ($b_X = 1$, or one As–As bond).[28] If $VEC(X) > 8$, the number of polycationic A–A bonds formed is $b_A = [(VEC(X) - 8)\cdot(x/a)]$, as exemplified in Ca_2As ($VEC(\text{As}) = 9$; $b_A = (9 - 8)\cdot(1/2) = ½$), suggesting fractional Ca–Ca bonds.[29] Polycationic compounds are typically less common than polyanionic or simple valence compounds. This thesis describes several new types of alkali-metal pnictides, mainly arsenides, some containing Ge–Ge or Sn–Sn bonds, and some containing As–As bonds, which can be considered to be polycationic or polyanionic compounds.

The bonding in ternary and quaternary Zintl phases contains a combination of ionic, metallic and covalent character (**Figure 1-3**). Covalent bonds are present in the polyanionic network, which interacts with the electropositive metal cations through ionic bonds. This hybrid bonding character leads to several interesting properties – like electrical and thermal conductivity.

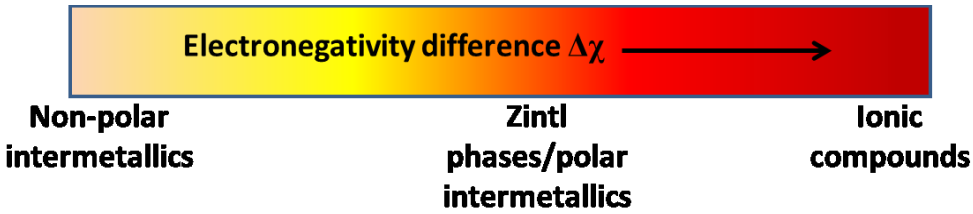

Figure 1-3. Graphical representation of the classification of intermetallic compounds depending on electronegativity difference.

1.2.3. Polyanionic Networks

The 8–*N* rule provides a simple way to predict the number of homoatomic bonds that are formed within a polyanionic network of pnicogens: isolated Pn^{3-} anions, one-bonded Pn^{2-} anions, two-bonded Pn^{1-} anions, and three-bonded Pn^{0} atoms (**Figure 1-4**). Therefore, pnictides exhibit structural diversity in the form of discrete units, 1D-chains, 2D-sheets, or 3D-networks.

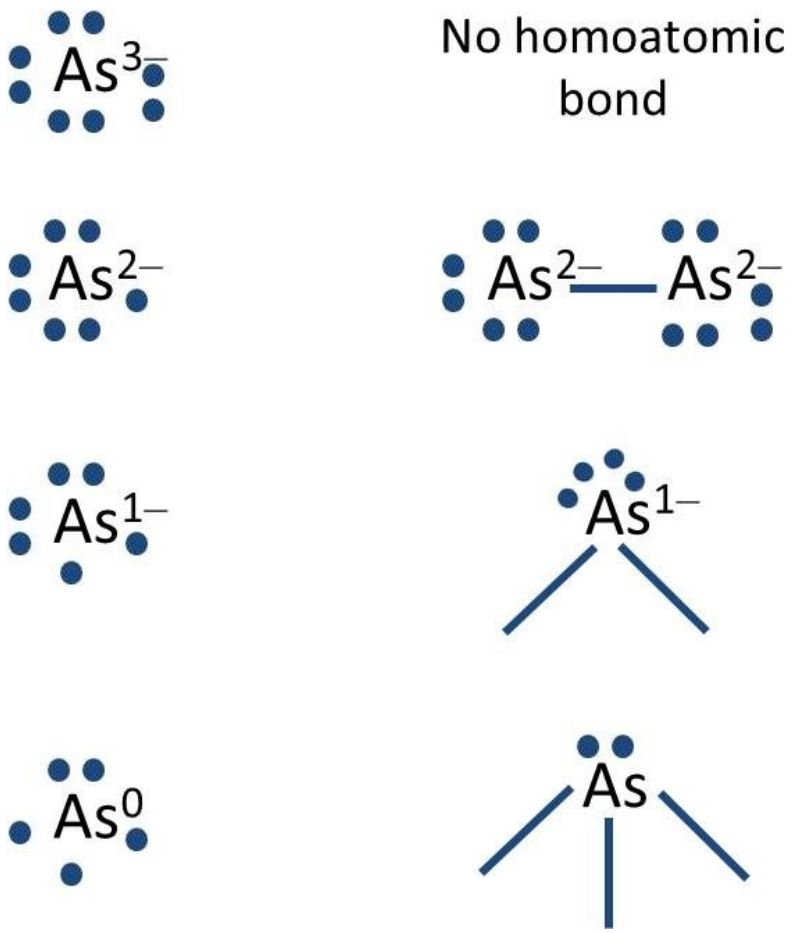

Figure 1-4. Possible bonding pictures are in homoatomic arsenide based on electron configuration [picture adapted from *Papoian et al.*][30]

Discrete units are found in A_3As_7 (A = Na, K, Rb, Cs), A_5Sb_4 (A = K, Rb), A_3As_{11} (A = K, Rb Cs), and A_2As_3 (A = Rb, Cs) (**Figure 1-5**). The compounds A_3As_7 adopt their own structure type,[31,32] consisting of As_7^{3-} cluster anions analogous to nortricyclene with formal charges of As^{1-} and As^0. K_5As_4 and other isostructural A_5Pn_4 compounds (A = K, Rb, Cs; Pn = Sb, Bi)[33] are formed at high temperature and contain isolated flat zigzag tetramers Pn^{4-} with terminal one-bonded Pn^{2-} and central two-bonded Pn^{1-} species. K_3As_{11} and Rb_3As_{11} crystallize with the orthorhombic Na_3P_{11}-type structure whereas Cs_3As_{11} crystallizes in a new monoclinic type; both structures contain isolated chiral As_{11}^{3-} anions with As–As bonds.[34] A_2As_3 adopts the K_2P_3-type structure[35] consisting of discrete cyclohexane-like six-membered rings As_6^{4-}. Infinite 1D Pn–Pn chains are found in different configurations in various pnictides (**Figure 1-5**). The structure APn (A = Na, K, Rb, Cs; Pn = P, As, Sb; CsP is not reported; and CsAs forms discrete triangle) and $ZnAs_2$ form helical infinite Pn–Pn chains resulting in Pn^{1-} species.[27,31,32,36,37] $GeAs_2$ contains infinite zigzag chains with As^{1-} species.[38] Several pnictides form 2D-sheets: KSb_2 contains graphite-like sheets (**Figure 1-5**),[39] Cs_5Sb_8 contains corrugated Sb–Sb chains connected through Sb–Sb bonds form complex-infinite network,[40] and $SrAs_3$ contains infinite network of As atoms (**Figure 1-6**)[41]

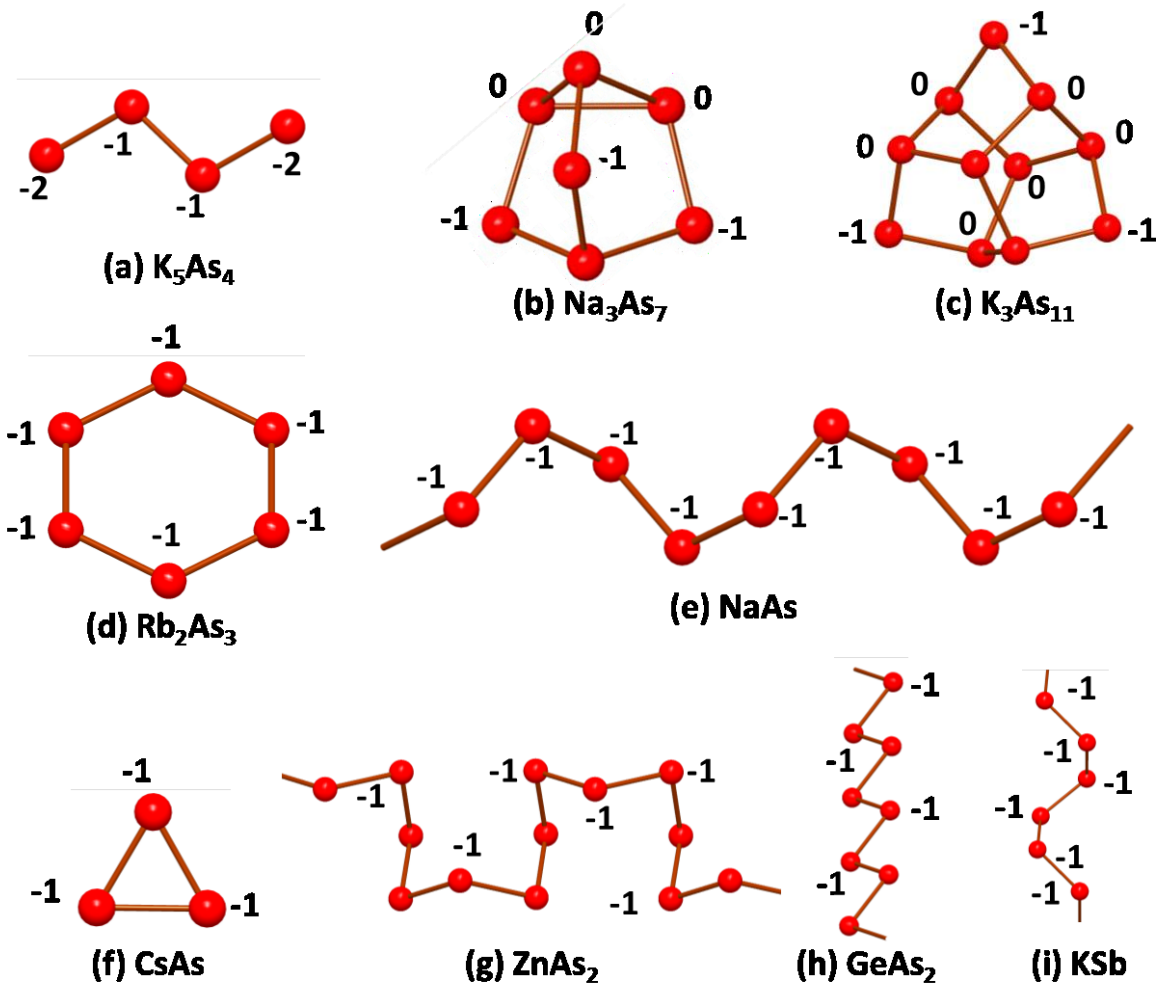

Figure 1-5. (a) Isolated zigzag tetramer As^{4-} in K_5As_4 (b) discrete nortricyclene-analogous cluster $\mathbf{As_7^{3-}}$ in Na_3As_7 (c) isolated cluster units $\mathbf{As_{11}^{3-}}$ in K_3As_{11} (d) discrete cyclohexane-type 6-membered ring in Rb_2As_3 (e) infinite 1D chain in NaAs (f) discrete 3-member ring in CsAs (g) Infinite 2D chain in $ZnAs_2$ (h) infinite zig-zag chain in $GeAs_2$ (i) infinite 1D chain in KSb.

Ternary and quaternary Zintl phases can have even more complex structures. Infinite square 2D-sheets of *Pn–Pn* are found in $LaCrSb_3$ and many $HfCuSi_2$-type compounds (e.g., *RE*$CuAs_2$, *RE*$AgAs_2$).[42–44] Corrugated networks are found in $Gd_6Ge_{5-x}Sb_{11+x}$, $Gd_6Zn_{1+x}Sb_{14}$, $La_{13}Ga_8Sb_{21}$, and $Pr_{12}Ga_4Sb_{23}$.[45–47] There are many more structures which contain one-bonded *Pn–Pn* bonds in complex anionic segments. In anionic segments, *Pn–Pn* bonds

connected either two subsequent layers or formed bond with other atoms to form 3D complex network. Such examples are found in $ThCr_2Si_2$-type structure (e.g., $BaFe_2As_2$),[48] $Ba_2Cd_2Sb_3$-type structure (e.g., $Sr_2Zn_2As_3$),[49] and $Yb_2Zn_3Ge_3$-type structure (e.g., $Sr_2Ag_2ZnAs_3$).[49]

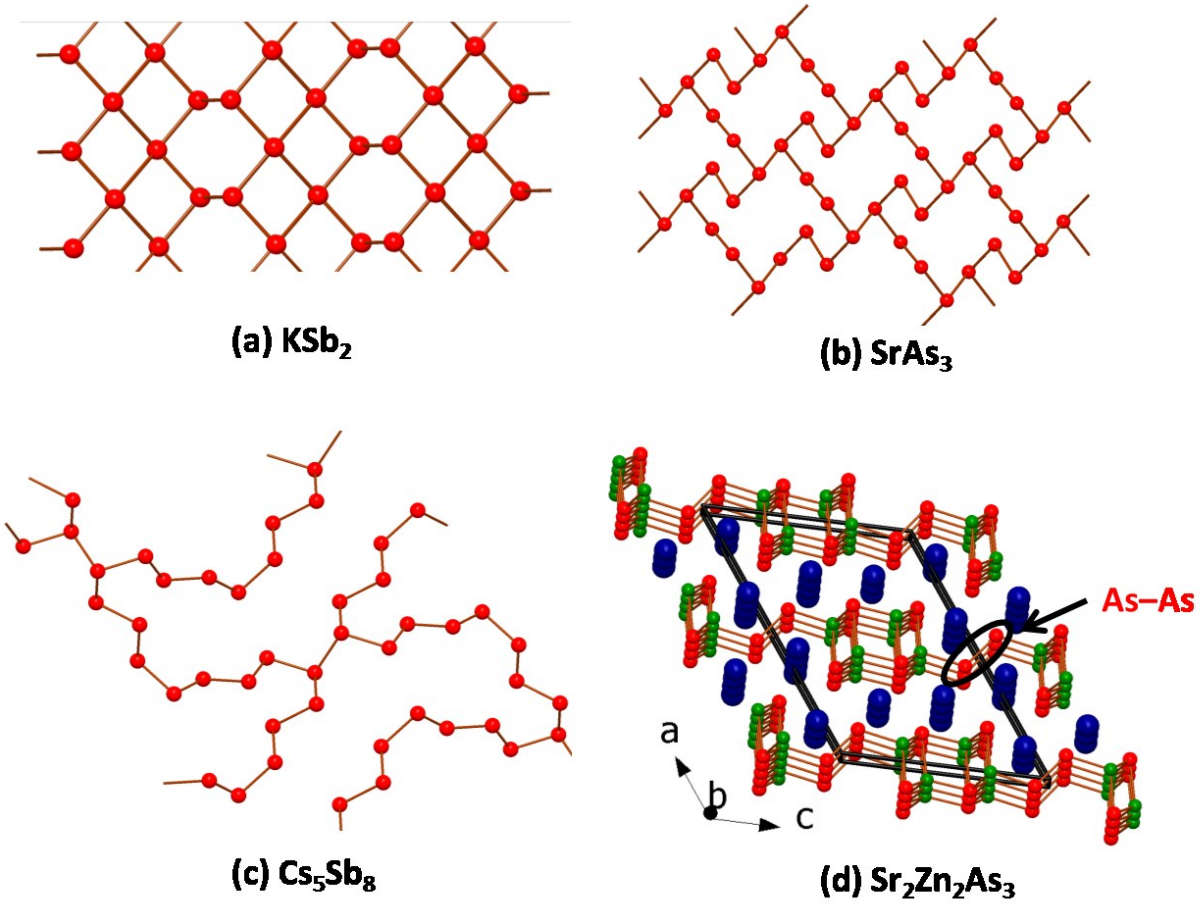

Figure 1-6. (a) Infinite 2D network in KSb_2 (b) zigzag infinite chains connected to form 3D network in $SrAs_3$ (c) corrugated chains connected formed 3D network in Cs_5Sb_8 (d) two anionic segments connected via As-As bond in $Sr_2Zn_2As_3$.

1.2.4. Polycationic Networks

Binary compounds containing polycationic networks can be classified into those in which the electronegativity difference is large (e.g., Ca_5As_3, Sr_2As) or small (e.g., GeP, GeAs, GaSe, InSe).[50] In Sr_2As, electron-counting rules give $VEC(As) = 2(2) + 5 = 9$ and

b(Sr–Sr) = (VEC(As) – 8) · (x/a) = (9 – 8) · (1/2) = 1/2; fractional Sr–Sr bonds are suggested in clusters (**Figure 1-7(a)**). In GeAs, only three out of the four valence electrons on Ge atom needs to be transferred to As so that the latter attains an octet; the remaining one electron on each Ge atom is then used to form a Ge–Ge bond (i.e., one-bonded Ge) in the form of dumbbells within ethane-like Ge_2As_6 units (**Figure 1-7(b)**).[51] The rules can be extended to ternary compounds. In $BaGe_2As_2$, both Ba and Ge atoms donate valence electrons to As atoms to give VEC(As) = (2 + 2(4) + 2(5))/2 = 10. The assumption is that the excess electrons are used to form homoatomic Ge–Ge bonds, with b(Ge–Ge) = (10 – 8) · (2/2) = 2, manifested as two-bonded Ge atoms within infinite zigzag chains.[52] In $K_6Sn_3As_5$ (b(Sn–Sn) = 1), a complex anionic framework $[Sn_3As_5]^{6-}$ is present which contain Sn–Sn homoatomic bond. (**Figure 1-7(c)**).[53] Many other ternary polycationic compounds are predicted to form fractional M–M bonds, such as KSi_3As_3 (VEC(As) = 28/3, b(Si–Si) = 4/3) and $NaGe_3P_3$ (VEC(P) = 28/3, b(Ge–Ge) = 4/3).[54,55] The structure of $NaGe_3P_3$ actually contains corrugated $[Ge_3As_3]$ layers in which Ge–Ge bonds are present within five-membered rings (Ge–As–Ge–Ge–As) connected via bridging As atoms (**Figure 1-7(d)**). The rules provide guidance about the existence of M–M bonds but may sometimes fail.

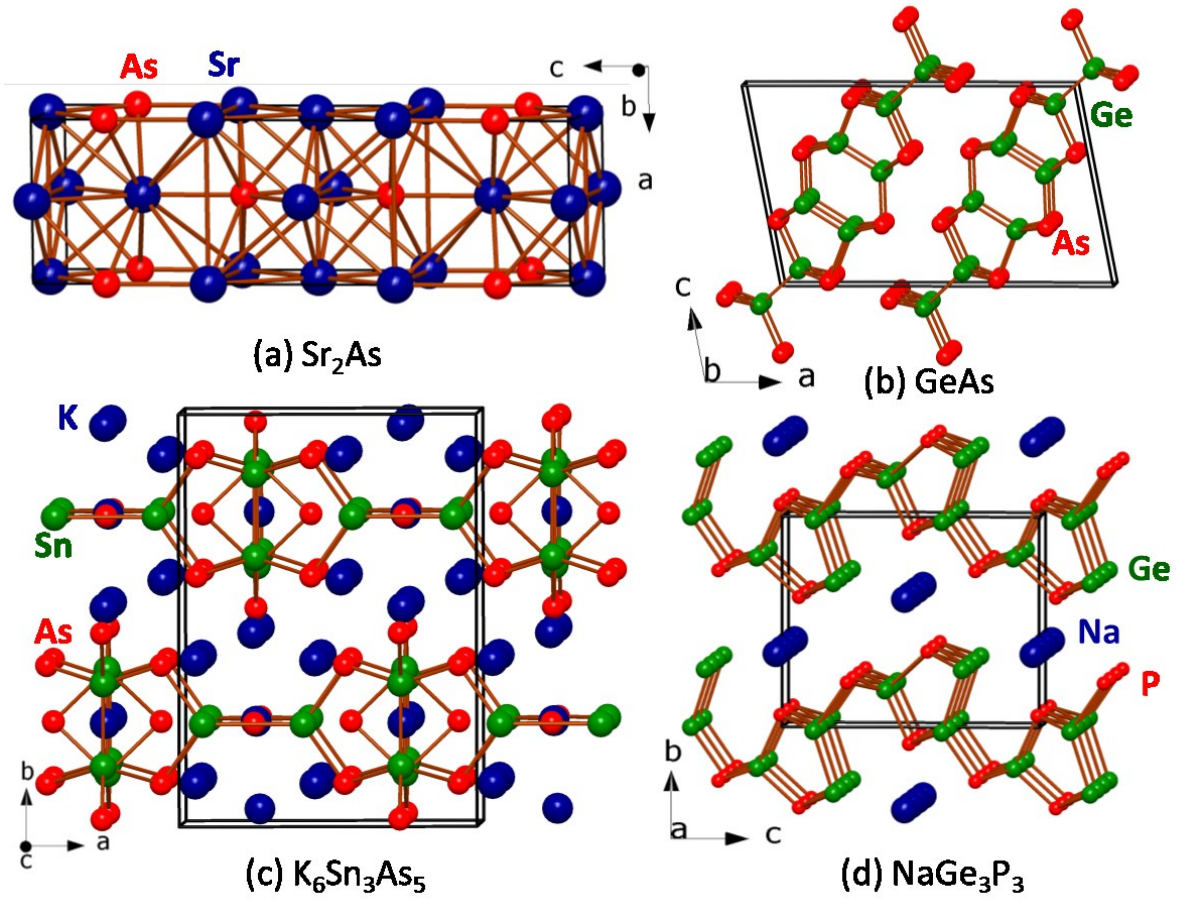

Figure 1-7. (a) Sr–Sr bond in Sr_2As (b) Ge–Ge homoatomic bond in GeAs (c) Sn–Sn homoatomic bonds in $K_6Sn_3As_5$ (d) Ge–Ge bond in $NaGe_3P_3$ corrugated layer.

Finally, there are unusual instances in which both *M–M* and *X–X* homoatomic bonding networks are present. The electron-counting rules can be expanded to include these cases but are more complicated. Some compounds adopting the $ThCr_2Si_2$-type structure exhibit these features. For example, in $CaNi_2P_2$, the Ca atoms donate their valence electrons to form anionic $[Ni_2P_2]^{2-}$ layers,[56] which contain not only heteroatomic Ni–P interactions, but also homoatomic Ni–Ni and P–P interactions, the latter serving to link layers together to form a complex 3D network (**Figure 1-8**).

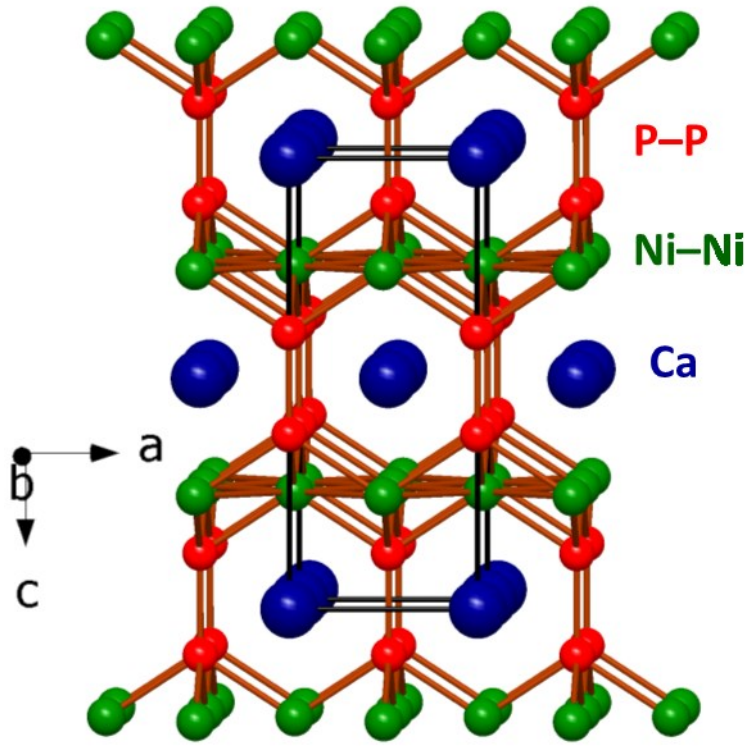

Figure 1-8. Ni-Ni bonds are present in $[Ni_2P_2]$ layers and P-P bonds are connected two layers to form 3D network in $CaNi_2P_2$ structure.

1.2.5. Electron-rich and Electron-deficient Zintl Phases

The Zintl-Klemm concept has been very successful in explaining the bonding for phases containing highly electropositive metals (alkali, alkaline-earth, and even rare-earth metals) as the electron donors. How far can this concept be pushed? The situation becomes complicated if one of the components is a transition metal, which can exhibit variable oxidation states and have electronegativities that are close to or even greater than those of the main-group components. Zintl phases containing transition metals often resemble isostructural ones containing main-group elements, but the degree of electron transfer may become ambiguous, resulting in apparently electron-excessive or electron-deficient phases relative to normal valence compounds. In electron-rich phases, one possible consequence

when the cations provide an excess of electrons is that clusters featuring hypervalent bonding are formed. For example, in compounds adopting the $Ca_{14}AlSb_{11}$-type structure (e.g., $Ca_{14}GaAs_{11}$, $Eu_{14}MnSb_{11}$),[57,58] the electropositive components transfer a total 31 valence electrons to the pnicogen atoms, eight of which form isolated Pn^{3-} anions (accounting for 24–), and the remaining three form a Pn_3 cluster carrying a 7– charge. Hypervalent $4e^{-}3c$ bonding is proposed to occur in the linear Pn_3^{7-} cluster. Other electron-rich phases described in the literature include A_8Tl_{11} (A = K, Rb, Cs), $K_{18}Tl_{20}Au_3$, and $Ba_7Ga_4Sb_9$.[59–61] In electron-deficient phases, electrons are removed from the top of the valence band so that the resulting partial occupancy gives rise to metallic conduction, as has been found in $Ba_5In_4Bi_5$ and La_3In_4Ge.[62, 63]

1.3. Limitations of Zintl Concept

Although the Zintl concept can rationalize the structures of many compounds, it has some limitations. First, the assumption is that the only types of bonding present are ionic interactions between the electropositive cations and the anionic network, and covalent interactions (if any) within the anionic network. The ionic interactions surely do influence the resulting anionic structure, but they are not considered in applying the Zintl concept to rationalize the structure. Second, although the presence (or absence) of homoatomic bonds can be predicted, the concept provides no guidance as to the detailed structure. In fact, diverse anionic networks can be formed from the same elements but we are unable to answer the question, "Why do they form different networks?" Third, structures containing two or more types of electropositive or electronegative components may show an ordered site distribution, but the concept offers no reasons for why this occurs. Thus, there remain many

unanswered questions about the applicability of the Zintl concept, and it is important to continue to probe its limits by experimentally preparing new phases.

1.4. Properties and Applications of Zintl Phases

Zintl phases can form by the combination of many different atoms and compositions. This thesis presents many new ternary and quaternary Zintl phases within the *A*-*M*-*Tt*-*Pn* (*A* = alkali metal, *M* = late d-block element, *Tt* = tetrel, *Pn* = pnicogen) systems. The properties of related previously known compounds are highlighted here.

Because Zintl phases contain atoms in closed-shell configurations, they should have a band gap in their electronic structures and thus be semiconductors. The gap depends on the electronegativity difference between cations and anions, and their relative radii. The small electronegativity differences in Zintl phases generally lead to narrow band gaps. Where measured, semiconducting behaviour in Zintl phases has been found in alkali-metal pnictides (KSb, KSb_2, $K_3Ga_3As_4$),[36,39,64] tetrelides (NaSi, $SrGe_2$, $K_4Zn_2Sn_{21}$),[65–67] and ternary compounds containing d-block elements (LiZnAs, $NaCd_4As_3$).[68,69] However, metallic behaviour has also been found in compounds containing pnicogen (e.g. *A*Bi, A_3Bi (*A* = Li, Na), A_5Pn_4 (*A* = K, Rb, Cs; *Pn* = As, Sb, Bi)),[33,50] which arises because weak bonding interactions cause the gap to vanish. A few examples are known of Zintl phases exhibiting semimetallic behaviour ($SrAg_4As_2$, $Sr_2Ag_2ZnAs_3$),[49,70] in which the valence and conduction bands just touch so that the band gap is zero or there is a pseudogap with a low density of states at the Fermi level.

Over the past 20 years, Zintl phases have attracted considerable interest in the search for new thermoelectric materials. The challenging task in finding a good thermoelectric

material is to optimize three contradictory properties: large thermopower, low electrical resistivity, and low thermal conductivity, all within a single material. The presence of different types of bonding and complex anionic networks in Zintl phases make them potential candidates for thermoelectric materials [e.g., $A_8M_{18}Pn_{28}$ (A = K, Rb, Cs; M = Zn, Cd; Pn = As, Sb), $CaZn_2Sb_2$, $Ca_{11}GaSb_9$].[71–73]. Another possible application for Zintl phases is to find new superconducting materials, especially with layered structures [e.g., LiFeAs (T_c = 18 K), $Ba_{1-x}K_xFe_2As_2$ (T_c = 38K)].[74] To expand on this search, it is necessary to investigate existing phases and discover new ones.

1.5. Pnictides

The pnicogens refer to the group 15 elements (N, P, As, Sb, Bi). Pnictides are compounds containing pnicogens. Depending on the number of constituent elements, pnictides can be binary, ternary, quaternary, or higher multinary compounds. Pnictides have diverse structures, properties, and applications, which are surveyed below, with a focus on alkali-metal, transition-metal, and p-block metal arsenides and antimonides.

Many binary alkali-metal arsenides and antimonides have been reported but their properties have not been well studied. Most are Zintl phases and follow conventional electron-counting rules. They acquire closed-shell configurations in the anionic clusters or networks, and are predicted to be semiconductors or insulators. Depending on the composition, the band gap varies between 0.1 and 2.5 eV.[75–79] Metallic behaviour has been found for some electron-rich or electron-poor phases. Reported alkali-metal arsenides and antimonides fall into several phase compositions: (1) APn (A = Na–Cs; Pn = As, Sb). Hönle and co-workers first synthesized NaAs and KAs, both with NaP-type structure. Later,

Emmerling and Röhr determined the single-crystal structures[27,32] of *A*As (*A* = Na, K, Rb, Cs). (2) A_3Pn (*A* = Na–Cs; *Pn* = As, Sb). The structures and some thermodynamic data ($\Delta H_f°$ and $\Delta S_f°$)[80,81] have been determined for Na_3As and K_3As. (3) A_3As_7 (*A* = Na–Cs). These have been prepared at high temperatures and their structures determined.[31] (4) A_5Pn_4 (*A* = K, Rb; *Pn* = As, Sb). Unusually, these exhibit metallic behavior because of the presence of extra delocalized electrons, and display temperature-independent (Pauli-like) paramagnetism.[33] (5) A_3As_{11} (*A* = K–Cs). These have been characterized using single-crystal X-ray diffraction.[82] (6) A_2As_3 (*A* = Rb, Cs). Blue reflecting black crystals were synthesized at 750-800 K.[35] (7) ASb_2 (*A* = K–Cs). KSb_2 is a semiconductor with a resistivity of 84.5 Ω·cm at room temperature.[39] (8) Cs_3Sb_7. Structure has been determined via single-crystal XRD.[83] (9) Cs_5Sb_8. Complete structure has been examined using XRD.[40]

Binary transition-metal or p-block-metal pnictides are numerous and their properties are well studied. Transition-metal pnictides show varied magnetic behavior: *M*As (*M* = Sc, Ta, Zr) are diamagnetic, *M*As (*M* = V, Ti, Ru, Co, Ni) are Pauli paramagnetic, *M*As (*M* = Fe, Cr) are order antiferromagnetically, and MnAs is ferromagnetic with a high Curie temperature of 317 K.[84] The Seebeck coefficients of *M*As are between +40 to –40 μV/K in the range of 2–300 K and the thermal conductivity is below 18 W/(m K).[84] TaAs (25%), NbAs (75%), and MnAs (90%) show large positive magnetoresistance at room temperature with the application of 8 T magnetic field.[84] Cd_3As_2 is semiconducting and has been identified as a thermoelectric material with a figure of merit (*ZT*) of 0.13–0.15 at room temperature.[85] The electron-deficient semiconductor CdSb is also a thermoelectric material with a high *ZT* value of 1.3 at 560 K (when doped with 0.5 at.% Ag) and is considered to be

a good candidate for multistage power generation.[86] Well-known p-block pnictides are III-V (GaP, GaAs, and derivatives), IV-V (SiP, GeP, SiAs, GeAs) and $Al_xGa_{1-x}As$ compounds, which are semiconductors with many applications in light-emitting diodes, solar cells, and optical devices.[87] GeAs is known as a semiconductor (0.65 eV band gap),[88] superconductor (at 3–3.5 K),[89] and thermoelectric material (ZT = 0.35 K at 660 K when Sn-doped),[90] and is used in optical and electronic applications.

Ternary pnictides containing alkali metals (or alkaline-earth metals) and transition metals (or p-block metals) are quite diverse. Those forming layered structures (alternating cationic and anionic layers) have captured a lot of attention. LiFeAs and $BaFe_2As_2$ (as well as oxypnictides such as $LaFeAsO_{0.89}F_{0.11}$)[74] are exciting examples of new unconventional Fe-based superconductors, all of which adopt structures containing conducting FeAs layers. LiFeAs has a critical temperature T_c of 18 K.[91] $BaFe_2As_2$ and its derivatives adopt the tetragonal $ThCr_2Si_2$-type structure and exhibit high-temperature superconductivity upon doping (T_c of 38 K for $Ba_{0.6}K_{0.4}Fe_2As_2$, 32 K for $Sr_{0.6}K_{0.4}Fe_2As_2$, 26 K for $Sr_{0.6}Na_{0.4}Fe_2As_2$, and 21 K for $Ca_{0.6}Na_{0.4}Fe_2As_2$).[92–94] Related ternary rare-earth pnictides that adopt the $ThCr_2Si_2$-type structure also show superconductivity (T_c of 35 K for Na-doped $EuFe_2As_2$, 4.1 K for $LaRu_2P_2$, and 7.8 K for $LaRu_2As_2$).[95–97] Ternary pnictides containing p-block metals exhibit rich variety of structures; examples are $Ba_2Sn_3Sb_6$ and $SrSn_3Sb_4$ both contain complex anionic networks and exhibit superconductivity at 3.9 K. [98,99]

Many ternary pnictides also adopt the trigonal $CaAl_2Si_2$-type structure and have received attention because of their structural flexibility and potential as thermoelectric materials, such as Ca-doped YbM_2Sb_2 (M = Mn, Zn, Cd).[100] These compounds are small

band gap semiconductors, and they contain rigid anionic layers that convey the electrical conduction while the cations between the layers reduce thermal vibrations. In contrast to $ThCr_2Si_2$-type pnictides, which are found for many transition metals, the $CaAl_2Si_2$-type pnictides are restricted to transition metals containing d^0, d^5, or d^{10} configurations.[101] Thermoelectric behavior has also been observed in LiZnSb,[102] KSn*Pn* (*Pn* = As, Sb),[103,104], $A_8M_{18}Pn_{28}$ (*A* = K, Rb, Cs; *M* = Zn, Cd; *Pn* = As, Sb),[71] A_8SnSb_4 (*A* = Na, K),[105] and $Ca_{14}AlSb_{11}$.[106]

Many ternary pnictides also exhibit other kinds of exciting properties. $Ca_{14}AlSb_{11}$-type compounds (e.g., $Yb_{14}MnSb_{11}$) have magnetoresistive properties,[107] Mn-doped LiZnAs is a dilute half-metallic ferromagnetic semiconductor that could be used in spintronics,[108] KHgSb is a weak topological insulator,[109] and KSnAs has varied optical properties (e.g., refractive index, extinction coefficient, optical reflectivity, absorption coefficient, and loss function which could be used in optoelectronic devices.)[110]

Quaternary alkali-metal pnictides in the *A–M–M′–Pn* and *A–M–Tt–Pn* systems have not yet been explored carefully. Very few quaternary pnictides are known in the *A–M–Pn–Ch, A–A′–Tr–Pn, A–A′–Tt–Pn, A–AE–M′–Pn, A–Tt–Pn–Ch* systems. **Tables 1-1 and 1-2** list previously reported ternary alkali-metal pnictides in the *A–M–Pn* (*M* = transition metal) and *A–Tt–Pn* (*Tt* = tetrel) systems.[50] To develop a greater understanding of the bonding, structure, reactivity, and properties of pnictides, this thesis aims to discover and investigate new ternary and quaternary arsenides and antimonides.

Table 1-1. Reported alkali-metal transition-metal pnictides (*Pn* = P, As, Sb)[50]

	Ti	V	Cr	Mn	Fe	Co	Ni	Cu	Zn
Na	Na_8TiAs_4			NaMn*Pn*	$NaFe_{1.62}As_2$ $NaFe_4Sb_{12}$		$Na_{2.3}Ni_{11.7}P_7$ $Na_{2.3}Ni_{11}As_7$	$NaCu_4Pn_2$ (P, Sb) Na_2CuPn(P, As)	NaZn*Pn* $NaZn_4As_3$
K				KMn*Pn*	KFe_2Pn_2 (P, As) KFe_4Sb_{12}	KCo_2Pn_2 (p, As)	K_2NiPn_2 (P, As) $K_2Ni_{12}As_7$	KCu_4Pn_2 $K_3Cu_3Pn_2$ (P, As) K_2CuPn K_5CuPn_2 (As, Sb)	KZn*Pn* K_4ZnPn_2 (P, As) KZn_4Pn_3 (P, As) $K_4Zn_9As_{14}$
Rb				RbMn*Pn*	$RbFe_2As_2$	$RbCo_2Pn_2$ (P, As)	Rb_2NiPn_2 (P, As)		$RbZn_4Pn_3$ (P, As) $Rb_4Zn_9As_{14}$ $Rb_2Zn_5Sb_4$
	Zr	**Nb**	**Mo**	**Tc**	**Ru**	**Rh**	**Pd**	**Ag**	**Cd**
Na								Na_2AgPn (As, Sb)	NaCdAs $NaCd_4As_3$
K					KRu_2Pn_2 (P, As)	KRh_2Pn_2 (P, As)	K_2PdPn_2 (P, As)	K_2AgPn $K_3Ag_3Pn_2$ (As, Sb)	KCd_4Pn_3 (P, As) K_4CdPn_2 (P, As) KCd*Pn* (As, Sb)
Rb					$RbRu_2Pn_2$ (P, As)	$RbRh_2Pn_2$ (P, As)	Rb_2PdPn_2 (P, As)		$RbCd_4As_3$ $Rb_2Cd_5As_4$ $Rb_4Cd_{6.35}Sb_9$

Table 1-2. Reported alkali-metal tetrel pnictides (*Pn* = P, As, Sb)[50]

	Si	Ge	Sn
Na	Na_5SiPn_3 (P, As)	$NaGe_3P_3$ Na_5GePn_3 (P, As)	NaSnP Na_5SnP_3 (P, As, Sb) $NaSn_2As_2$ Na_2SnAs_2 Na_8SnSb_4
K	KSi_2P_3 K_2SiPn_2(P, As) KSi_3As_3	K_2GeAs_2	KSnAs K_2SnAs_2 K_5SnAs_3 $K_6Sn_3As_5$ K_8SnSb_4
Rb	Rb_2SiAs_2 Rb_5SiAs_3	Rb_5GeP_3	Rb_2SnAs_2 Rb_4SnSb_6

1.6. Synthesis of Alkali-Metal Pnictides

Generally, solid state reactions require high temperatures and long times to overcome large activation barriers and slow diffusion rates. Several methods are commonly used to prepare intermetallic compounds, including direct reaction of the elements, use of fluxes, and chemical vapor transport.[111] The method and the conditions for preparation need to be optimized for a specific compound. Another problem is that detailed understanding of mechanisms for solid state reactions is lacking.

To prepare pnictides containing alkali metals, the constituent elements of high purity were freshly cleaned by scraping their surfaces and they were weighed out in appropriate stoichiometric ratios. The starting materials were cut into smaller pieces or ground to fine powder to increase surface area. They were placed in alumina crucibles, which were placed in turn within fused-silica tubes. The tubes were evacuated and sealed, and placed in a high-temperature furnace heated slowly to 600 °C (for Rb-containing samples) or 650 °C (for Na- and K-containing samples). A rule of thumb for selecting an appropriate heating temperature is that at least one of the constituent elements is molten.[111] The temperatures chosen above exceed the melting points of Na (98 °C), K (63 °C), or Rb (39 °C). The samples were heated for a week to ensure complete reaction, and then slowly cooled to room temperature to attain good quality single crystals (**Figure 1-9)**.

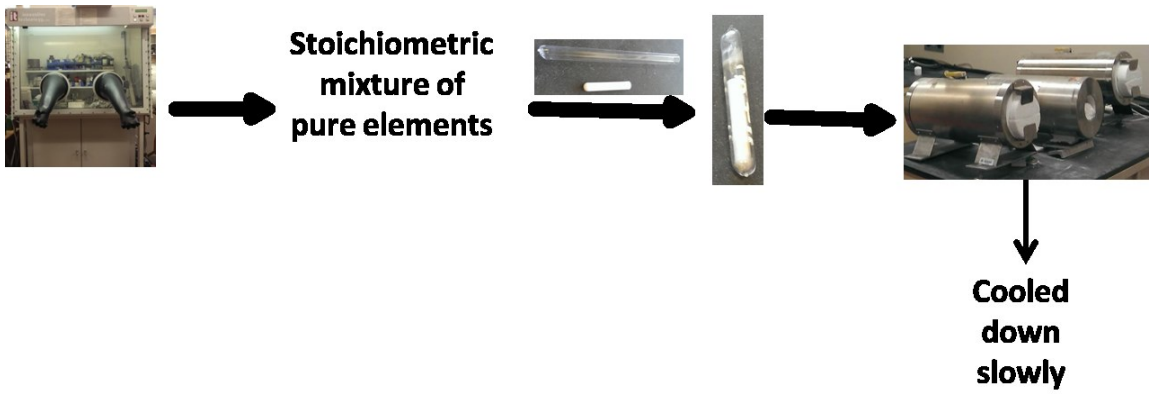

Figure 1-9. Synthesis of alkali-metal pnictides via the direct heating method.

Direct reaction of the elements was suitable for preparing ternary and quaternary pnictides in the *A–M–Pn*, *A–Tt–Pn*, *A–M–M′–Pn* and *A–M–Tt–Pn* systems. For the highly volatile elements, alkali-metals, Zn and As, slow heating is essential to avoid loss of these components.

Alkali metals are stored and handled under paraffin oil because they are highly reactive in air and water. Arsenic is toxic and slightly reactive in air (oxidized when exposed with air), so it is handled quickly and ground only when needed. Personal protection in the form of gloves, face masks, and safety glasses should be worn. All manipulations (sample preparation, examination of products) were performed within an argon-filled glove box. Although products differ in their air sensitivity, they were all examined the same way: ground samples for powder X-ray diffraction were covered with oil (even though this increases the background), and single crystals were mounted with oil and blanketed with a stream of nitrogen gas in the single-crystal X-ray diffractometer.

1.7. X-ray Diffraction Methods

X-ray diffraction is the most important method to characterize intermetallic compounds. In contrast, the typical spectroscopic methods (e.g., NMR or IR spectroscopy) used to characterize molecular substances (organic and organometallic compounds) are simply not applicable or useful.

X-rays are a form of highly energetic electromagnetic radiation with wavelengths on the order of 1 Å, comparable to the length scale of atoms. They are generated when electrons accelerated over a high potential (~30 kV) strike a metal target (e.g., Cr, Fe, Cu, Mo, Ag). The X-ray spectrum consists of a broad background of Bremsstrahlung or white radiation caused by inelastic collisions, and sharp intense peaks caused by elastic collisions that are characteristic of the target element (**Figure 1-10**). The *K*α and *K*β peaks arise when core electrons are ejected from the *K* shell (1s orbital) and the hole is filled by higher energy electrons from the *L* (2p orbitals) or *M* shell (3p orbitals), respectively. The specific wavelengths of these characteristic X-rays depends on the target element.

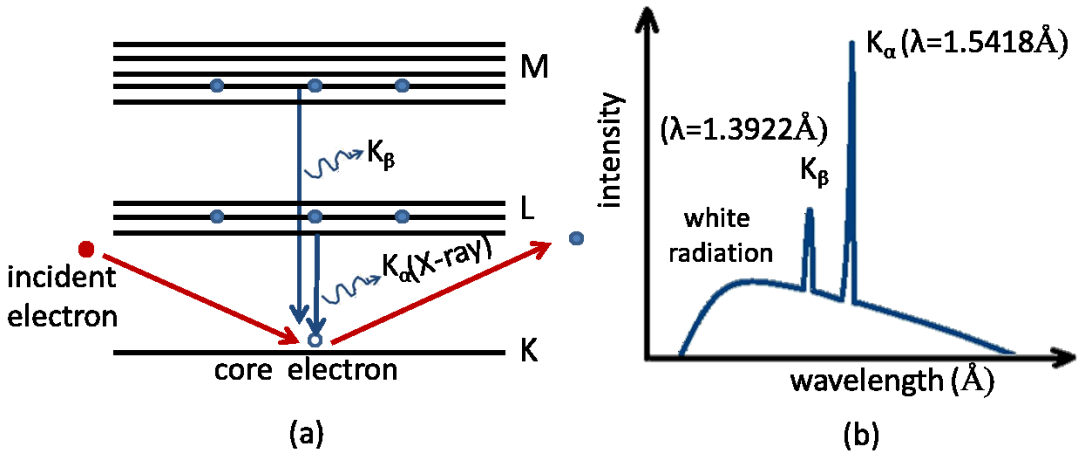

Figure 1-10. Schematic representation of (a) generation of X-ray and (b) the emission spectrum of copper.

The $K\alpha$ and $K\beta$ peaks are actually split into doublets as a result of spin-orbit coupling. A filter (e.g., Ni for Cu vs. Nb for Mo X-rays) is used to remove the weaker $K\beta$ peaks, and a crystal monochromator (e. g. graphite, quartz single crystal) is used to separate $K\alpha_2$ and an intense monochromatic $K\alpha_1$ X-rays are obtained. X-ray diffraction patterns can be obtained on single crystals or powder samples. Single-crystal X-ray diffraction is most useful to determine full crystal structures, whereas powder X-ray diffraction is mainly used for phase identification.

1.7.1. Single Crystal Diffraction

A crystal structure consists of a regular arrangement of atoms, which can be described in terms of a lattice (a set of points representing the symmetry of the repeat pattern) and basis (the set of atoms within a unit cell). The lattice points define sets of parallel planes, called lattice planes, each specified by a set of indices *hkl* and separated by a constant spacing d_{hkl}. Incident X-rays of a given wavelength striking a set of lattice planes undergo interference. According to the Laue's principle,[112] a crystal consists of a single row of atoms along an axis say *x*-axis. When an X-ray beam is irradiated the beam scatters with a scattering angle by an atom as shown in the **Figure 1-11**, producing a series of cones along the x-axis. Similar cones are created by atoms along the other axis as shown in the **Figure 1-11**. The intersection of the two series of cones (along x and y axes) will form a series of lines resulting in a diffraction pattern. Extending this to a three dimensional structure results in constructive interference, where the intersection of the cones satisfy a set of mathematical condition (**Equation 1-2**).

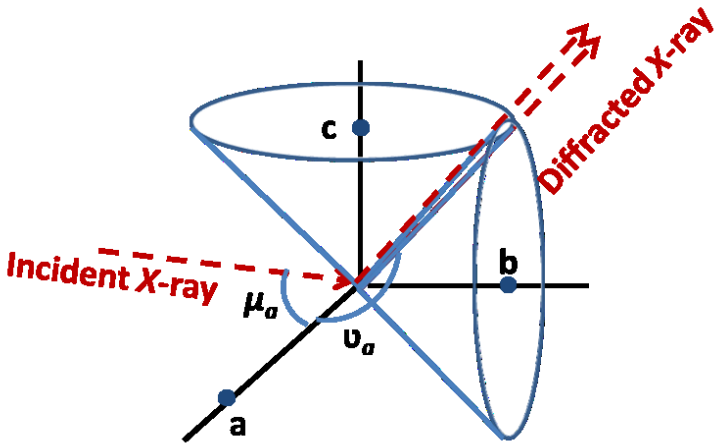

$$a(cos\mu_a + cos\upsilon_a) = n_a\lambda = h\lambda$$

$$b(cos\mu_b + cos\upsilon_b) = n_b\lambda = k\lambda$$

$$c(cos\mu_c + cos\upsilon_c) = n_c\lambda = l\lambda$$

. . . . .(Equation 1-2)

Figure 1-11. The principle of Laue law for X-ray diffraction. *a*, *b*, *c* are the distance between lattice points along *x*, *y*, *z* axis; μ and υ are the angles of incident and diffracted *X*-ray; λ is the wavelength, *h*,*k*,*l* are Miller indices.

The resulting diffraction pattern can be analyzed through these scattering equations called the Laue equations, but a simplified treatment regards each lattice plane as a mirror in which incident rays and reflected rays make equal angles (**Figure 1-11**). The condition for constructive interference, called Bragg's law,[113] is satisfied when the difference in path length of successive reflected X-rays is equal to an integer multiple of the wavelength λ:

$$2dsin\theta = n\lambda \qquad \text{Equation 1-3}$$

where *d* is the spacing between adjacent lattice planes, θ is the angle of reflection, and *n* is the reflection order. By measuring the angles of diffraction X-rays, the *d*-spacings of different lattice planes can be deduced and thus the unit cell geometry can be obtained.

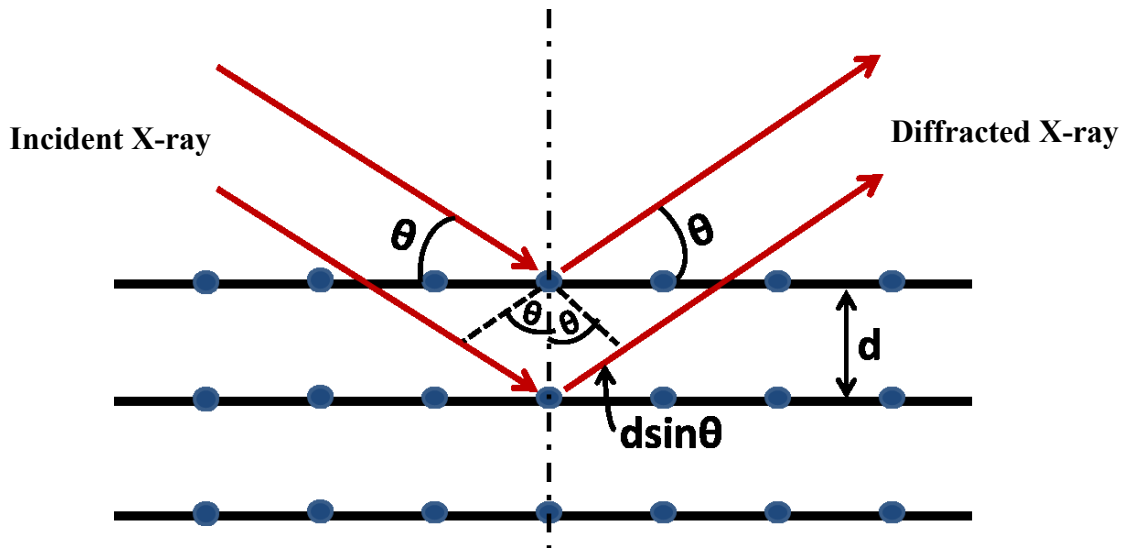

Figure 1-12. Principle of Bragg's law for X-ray diffraction.

A suitable single crystal for data collection is typically 0.01 to 0.5 mm in its longest dimension. It is examined and selected under a microscope. Air-sensitive crystals are handled under paraffin oil. Crystals that are too large may need to be cut to a desired size. The crystal is then mounted on a glass fiber using epoxy or oil, and in turn attached to a brass pin, which is placed on the goniometer of a Bruker PLATFORM diffractometer equipped with a SMART APEX II CCD area detector and a Mo $K\alpha$ radiation source. Full sets of data are typically collected using ω scans at different ϕ angles. The data set consists of many thousand reflections associated with specific crystal plane *hkl* and their intensities I_{hkl}. The intensity I_{hkl} is related to the square of the structure factor F_{hkl}, which reveals information about the electron density function of the crystal structure. Structure factor F_{hkl} is a complex number that can be expressed as both the amplitude and the phase of reflection shown in **Equation 1-4**. In the equation f_j is the scattering factor of atom j equals the number of electron at $(h.k.l) = (0\ 0\ 0)$. f_j depends on atom type, position of atoms and thermal

vibrations. The Fourier transform (*FT*) of F_{hkl} (an image of the reciprocal space) into the electron density (real space) can be used to interpret the position of atoms in the unit cell. Unfortunately the phases of the structure factors are not possible to determine through experiment; this is called the phase problem. Thus, the electron density cannot be directly evaluated because of the lack of phase information. Other techniques (e.g., direct methods, Patterson method) can be used to guess the phases of some structure factors to arrive at an initial model, which is then refined.

$$F_{hkl} = \sum_{j=1}^{atoms} f_j exp\left[2\pi \cdot i\left(hx_j + ky_j + lz_j\right)\right] \qquad \text{Equation 1-4}$$

A numerical face-indexed absorption correction was applied with the use of SADABS if the structure contains heavy atoms. Structural models are proposed by crystallographic SHELXTL programs package [114] and their feasibility is evaluated by their chemical reasonableness. The models are then refined through a least-square method to improve the agreement between calculated and experimental intensities. Various parameters, such as the atomic positions, site occupancies, and displacement parameters are adjusted. In the end, the structure should give reasonable bond distances, coordination environments, and displacement parameters. The quality of the refinement is monitored through agreement factor R ($= \frac{\sum_{hkl}||F_o|-|F_c||}{\sum_{hkl}|F_c|}$, F_o = observed structure factor and F_c = calculated structure factor), goodness of fit S ($= \sqrt{\frac{\sum_{hkl} w\left(F_o^2 - F_c^2\right)}{m-n}}$, $w = 1/\sigma^2$, m = number of reflections, n = number of parameters), and inspection of the residual electron density map ρ. In well refined structures, the agreement factors are small ($R < 0.05$ and $wR_2 < 0.15$) , the goodness of fit is close to

unity and for heavy atom compound the residual electron density is up to ±10 % of atomic number per $Å^{-3}$.

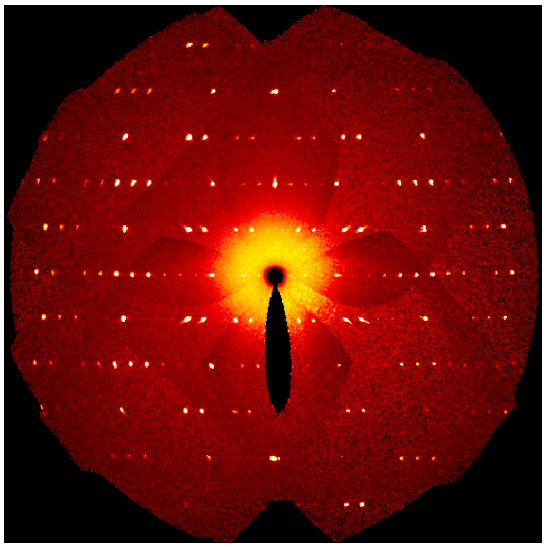

Figure 1-13. Reflections image of reciprocal crystal plane collected in single crystal diffractometer.

1.7.2. Powder X-ray Diffraction

A powder sample contains many crystallites in random orientations. Diffraction peaks from lattice planes with similar spacings will thus overlap at similar angles, and it becomes difficult to disentangle the individual intensities. Nevertheless, powder X-ray diffraction is useful as a fingerprinting method for identifying phases, since each phase has a unique pattern. Experimental patterns are compared with simulated ones from known phases. In a multiphase sample, the relative amounts of different phases can be estimated by comparing the peak intensities (**Figure 1-14**). If a new compound has a similar powder X-ray diffraction pattern as a previously known one, then it is possible to perform structure refinements, although this was not done in this thesis.

About 3 to 4 mg of finely ground powder samples are all that is required. The powder is placed on sample holder, while ensuring that the surface is plane and smooth. The diffraction patterns were collected on an Inel powder diffractometer equipped with a curved position-sensitive (CPS) detector, which allows peak intensities between 0 to 120º 2θ angle to be obtained simultaneously.

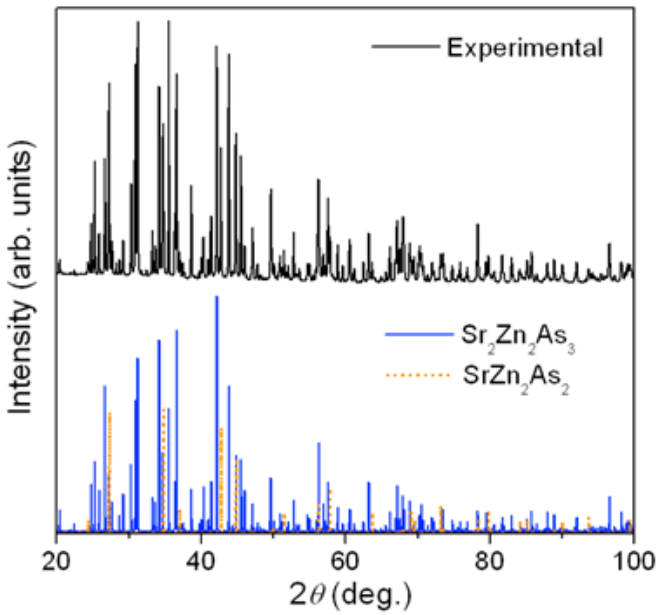

Figure 1-14. Powder diffraction pattern of $Sr_2Zn_2As_3$; experimental pattern compared with simulated pattern.

1.8 Bond Valence

X-ray diffraction is used to determine crystal structures, but it cannot easily locate lighter elements (like H) or distinguish between those having similar X-ray scattering factors (like Ge vs As). A useful way to check whether a structure is reasonable is to evaluate bond valence sums. The bond valence v_{ij} can be thought of as a measure of the bond strength between two atoms i and j:

$$v_{ij} = \exp[(R_{ij} - d_{ij})/b] \qquad \text{Equation 1-5}$$

where R_{ij} is the bond valence parameter (Å), d_{ij} is the experimentally observed distance (Å), and b is commonly taken as a constant value of 0.37.[115] The valence V_i of an atom i is equal to the sum of all the bond valences to it:

$$V_i = \Sigma v_{ij} \qquad \text{Equation 1-6}$$

If the valence matches with the expected value of the atom, then the assignment is likely correct. For example, the bond valence calculations on KZnAs provideed the valence as 0.9 for K, 1.8 for Zn, and 2.7 for As, which agrees well with the expected values.

Table 1-3. Bond valence sums (V_i) for KZnAs[50]

Bond types	R_{ij} **(Å)**	d_{ij} **(Å)**	v_{ij}	V_i
K–As (× 6)	2.83	3.532	0.15 (× 6)	0.9
Zn–As (× 3)	2.42	2.435	0.59 (× 3)	1.8
As–Zn (× 3)	2.42	2.435	0.59 (× 3)	
As–K (× 6)	2.83	3.532	0.15 (× 6)	2.7

1.9. Scanning Electron Microscopy

The main method for determining the chemical composition of the compounds prepared in this thesis is scanning electron microscopy, which also provides information about the surface topography and morphology of samples. A high-energy electron beam striking a surface of a solid can lead to many processes, including emission of Auger electrons, secondary electrons, backscattered electrons, transmitted electrons, and characteristic X-rays (**Figure 1-15**). A JEOL JSM-6010LA scanning electron microscope was used here with a typical accelerating voltage of 20 kV. Images of single crystals were

obtained from the secondary electrons, and chemical compositions were determined using energy-dispersive X-ray (EDX) spectroscopy.

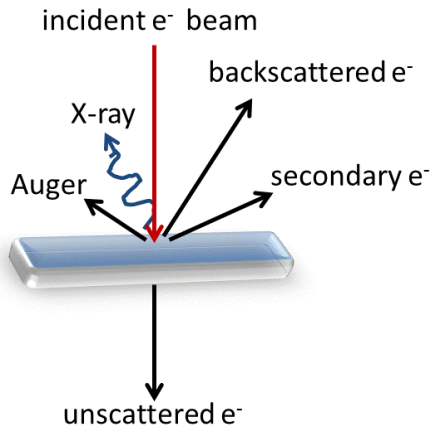

Figure 1-15. Schematic representation of the processes that occur on bombarding a sample with electrons.

Secondary electrons are formed when an incident electron transmits some of its energy to electrons (usually core) within the sample. The incident electron loses some of its energy, changes its path, and ionizes electrons within the sample. The ionized electron is ejected as a secondary electron with a small kinetic energy (~5 eV). These secondary electrons are detected and used to form an image of the surface of the solid (**Figure 1-16**)

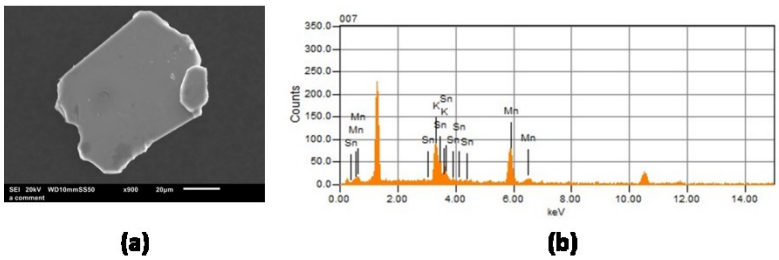

Figure 1-16. (a) Scanning electron microscopic image of $K_2Mn_3SnAs_4$ crystal (b) energy dispersive spectrum of composition analysis on the same crystal.

In EDX spectroscopy, characteristic X-rays are produced when the high-energy electron beam ejects core electrons (from the *K* shell) of atoms within the constituent

elements of the sample. The hole created is filled by higher energy electrons, and X-rays with a specific wavelength are emitted in the process. The emitted X-rays are characteristic of each element present in the sample. A typical EDX spectrum contains several peaks and their intensities give the relative amounts of each element (**Figure 1-16b**). The precision for the relative mole percents of each element is about 5%. There are some limitations. EDX cannot detect elements lighter than those with atomic number of 5 and may encounter difficulties in resolving elements with similar atomic number. For example, the EDX analysis of *A*–*M*–Ge–As (*A* = Na, K, Rb; *M* = Zn, Cd) samples is difficult because Na is a light element, and the atomic numbers are similar for Zn ($Z = 30$), Ge ($Z = 32$), and As ($Z = 33$).

1.10. Band Structure Calculation

The compounds presented in this thesis display a variety of bonding interactions, which can be examined in detail through calculations of electronic band structures. In contrast to molecules, which are composed of few atoms and have discrete energy levels, extended solids are composed of an extremely large number of atoms and have many energy levels so closely spaced that they constitute a continuum called a band. Just as for a molecule, the Schrödinger equation is used to evaluate the wavefunctions Ψ and energies E for an extended crystalline solid:

$$H\Psi = E\Psi \qquad \text{Equation 1-7}$$

The Hamiltonian operator H is composed of two terms, corresponding to the kinetic energy and the potential energy:

$$(k + V)\Psi = E\Psi \qquad \text{Equation 1-8}$$

A crystalline solid exhibits periodicity with lattice translations being one of the symmetry operations. The many electrons within a solid experience Coulombic attraction to the nuclei, and more complicated electron-electron interactions which are expressed via the exchange-correlation potential and the Hartree potential. Through the Kohn-Sham equation, this many electron problem can be reduced to a one-electron problem by combining the Coulomb, exchange correlation, and Hartree potentials.[116]

Just as atomic orbitals can be combined linearly to form molecular orbitals, they can also be combined in the same way in an extended solid. Consider a one-dimensional chain of atoms spaced apart by a regular distance a and containing an orbital χ_n on each atom (**Figure 1-17**).

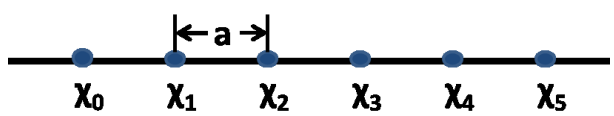

Figure 1-17. One-dimensional chain of crystal.

The linear combination of the basis functions χ_n, adapted to the translational symmetry, is called a Bloch function ψ:

$$\psi(k) = \sum_{n=1}^{N} e^{ikna}\chi_n \qquad \text{Equation 1-9}$$

Here, N is the total number of unit cells and k is a wavevector, which is quantized in reciprocal space. The unit cell in reciprocal space is called the first Brillouin zone and ranges over the values $-\frac{\pi}{a} \leq k \leq \frac{\pi}{a}$, although it is sufficient to plot over $0 \leq |k| \leq \frac{\pi}{a}$. A band dispersion diagram is a plot of E vs. k (**Figure 1-18**). For example, a linear chain of As atoms gives rise to Bloch functions constructed from linear combinations of each of the 4s

and 4p orbitals. At $k = 0$, the energy is lowest for the s, p_x, and p_y bands because the neighbouring interactions are bonding while the energy is highest for the p_z band because the interactions are antibonding. At $k = \pi/a$, the picture is reversed. The energy dispersion, or band width, depends on the type of orbitals and the strength of the orbital interactions.

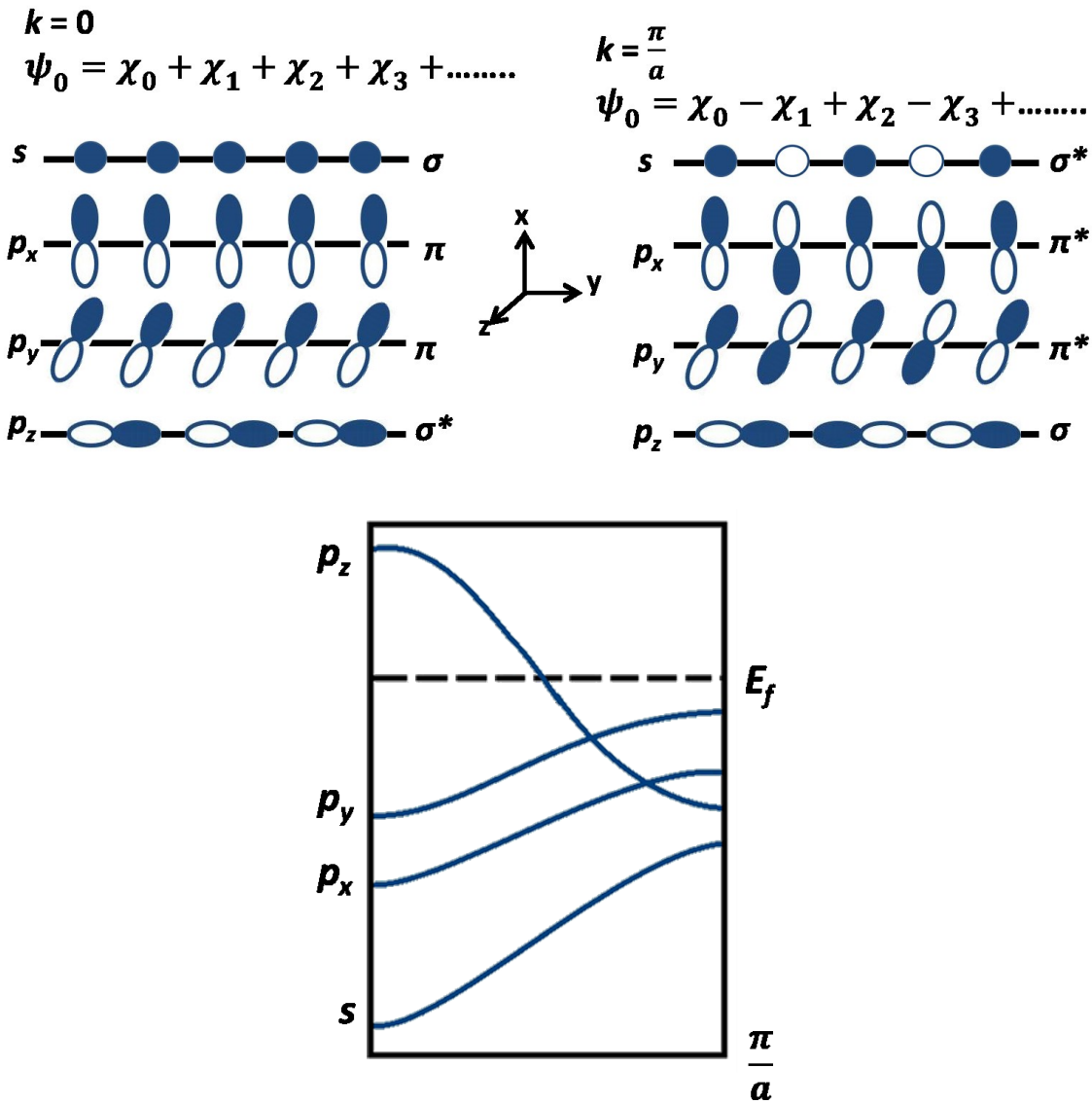

Figure 1-18. The band structure of 1D As^{2-} chain (adapted from *Papoian et al.*)[30]

The bands are drawn as continuous lines because the energy levels are very close together (or, put another way, the increment in k is very small). It is convenient to plot instead the density of states (DOS), which measures the number of states within small energy increments, as a function of energy. Basically, DOS is inversely proportional to the slope of the band dispersion curve. Electrons occupy states from the lowest energy upwards, up to the Fermi level, which can be arbitrarily set to 0 eV as a reference point. Where the Fermi level lies in the DOS curve gives information about the electrical property: metallic (no gap), semimetallic (zero or small pseudogap), semiconducting (small gap, 0.5 to 3.0 eV), or insulating (large gap, >3.0 eV). It is also useful to take atomic projections of the DOS curve to ascertain the contribution of each atom in the structure. The bonding character of different interactions can be evaluated by the crystal orbital overlap population (COOP) curves.[117]

In this thesis, band structure calculations were performed using the Stuttgart tight-binding linear muffin-tin orbital (TB-LMTO) program. The curious name refers to the shape of the potential energy functions. Near the positively charged ions, the potential energy approaches negativity infinity, but the function is truncated to a finite value, thereby approximating the shape of muffin tins. An atomic spheres approximation is applied in which the potential function is ensured to be continuous by filling empty spaces between atoms as spheres with zero potential. The program generates DOS and crystal orbital Hamilton population (COHP) curves (instead of COOP curves) (**Figure 1-19**).

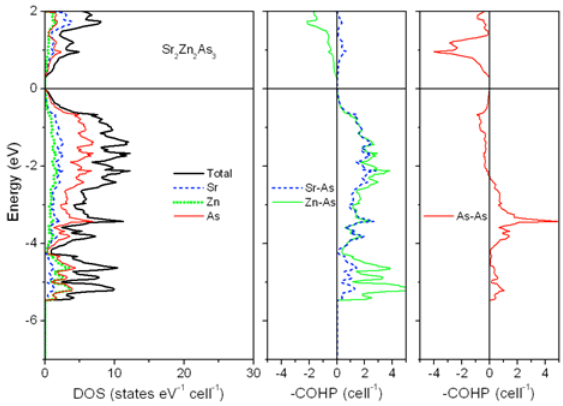

Figure 1-19. Schematic representation of Density of States curve (left); crystal orbital Hamiltonian population curve (middle and right) of $Sr_2Zn_2As_3$.

1.11. Objectives

The main goal of this thesis is to synthesize ternary and quaternary alkali-metal arsenides and antimonides, in combination with both transition metals and p-block metals, (e.g. tetrels) with the expectation that they will be Zintl phases. Because the structures of solid state compounds are generally unpredictable, it is important to determine the crystal structures of these new compounds. Structure types that are different from existing ones are valuable because they can lead to the discovery of new bonds between different kinds of elements. By using combinations of transition metals or p-block metals, or both, more complexity can be introduced which will generate different bonding interactions. These new compounds also allow the Zintl concept to be tested, to determine whether they satisfy the definition of normal valence compounds, or whether they exhibit polycationic or polyanionic bonds, to be evaluated in either metal-rich or pnicogen-rich phases, respectively.

A second goal is to examine the physical properties of these compounds. Generally, Zintl phases should be small band-gap semiconductors, but it is not obvious if this is always true, or whether semimetallic or metallic behavior is also possible. These property

measurements can be compared with predictions from band structure calculations, which will also be useful in evaluating the nature of bonding interactions in these compounds. A potential application for the pnictides prepared here is as thermoelectric materials, given that they are likely to exhibit small band gaps and complex frameworks. Unfortunately, because all the compounds were found to be moderately sensitive to air or moisture, the physical property measurements were not successful even after many attempts. Nevertheless, the discovery of new phases is an important part of research. Until a new phase is synthesized, it is impossible to confirm compositions, structures, bonding interactions, and physical properties.

To evaluate the applicability of the Zintl-Klemm concept, several series of compounds containing different elements and compositions were synthesized. The compounds containing transition metals in *A–M–Pn* systems are presented in Chapters 2 and 3. The compounds containing tetrels in *A–Tt*–As systems are reported in Chapters 4 and 5. The quaternary compounds containing both transition metals and tetrels in *A–M–Tt*–As systems are reported in Chapters 6 and 7.

1.12. References

1. Zintl, E. *Angew. Chem.* **1939**, *52*, 1–6.
2. Nesper, R. *Z. Anorg. Allg. Chem.* **2014**, *640*, 2639–2648.
3. Zintl, E.; Dullenkopf, W. *Z. Phys. Chem.* **1932**, *B16*, 183–194.
4. Zintl, E.; Brauer, G. *Z. Phys. Chem.* **1933**, *B20*, 245–271.
5. Schäfer, H.; Eisenmann, B.; Müller, W. *Angew. Chem., Intl. Ed. Engl.* **1973**, *12*, 694–712.
6. Schäfer, H.; Eisenmann, B. *Rev. Inorg. Chem.* **1981**, *3*, 29–101.
7. Schäfer, H. *Annu. Rev. Mater. Sci.* **1985***, 15*, 1–44.
8. Nesper, R. *Prog. Solid State Chem.* **1990**, *20*, 1–45.

9. Kauzlarich, S. M. *Chemistry, Structure, and Bonding of Zintl Phases and Ions,* Ed.; VCH: Weinheim, Germany, 1996.

10. Kanatzidis, M. G. *Recent Trends in Thermoelectric Materials Research I,* Series: *Semiconductors and Semimetals*; Academic: San Diego, 2001.

11. Gascoin, F.; Ottensmann, S.; Stark, D.; Haïle, S. M.; Snyder, G. J. *Adv. Funct. Mater.* **2005**, *15*, 1860–1864.

12. Shawna, R. B.; Kauzlarich, S. M.; Gascoin, F.; Snyder, G. J. *Chem. Mater.* **2006**, *18*, 1873–1877.

13. Condron, C. L.; Kauzlarich, S. M. *Inorg. Chem.* **2007**, *46*, 2556–2562.

14. Kauzlarich, S. M.; Brown, S. R.; Snyder, G. J. *Dalton Trans.* **2007**, 2099–2107.

15. Snyder, G. J.; Toberer, E. S. *Nat. Mater.* **2008**, *7*, 105–114.

16. Curro, N. J.; Caldwell, T.; Bauer, E. D.; Morales, L. A., Graf, M. J., Bang, Y.; Balatsky, A. V.; Thompson, J. D.; Sarrao, J. L. *Nature* **2005**, *434*, 622–625.

17. Gschneidner Jr., K. A.; Pecharsky, V. K.; Tsokol, A. O. *Rep. Prog. Phys.* **2005**, *68*, 1479–1539.

18. van Arkel, A. E. *Molecules and Crystals in Inorganic Chemistry,* Interscience: New York, 1956.

19. Ketelaar, J. A. A. *Chemical Constitution; An Introduction to the Theory of the Chemical Bond,* 2nd Ed.; Elsevier: Amsterdam, 1958.

20. Parthé, E. *Acta Crystallogr.*, *Sect. B* **1973**, *29,* 2808–2815.

21. Müller, U. *Inorganic Structural Chemistry*, 2nd Ed.; Wiley: Chichester, 2007.

22. Lewis, G. N. *J. Am. Chem. Soc.* **1916**, *38*, 762–785.

23. Kossel, W. *Ann. Phys*. **1916**, *354*, 229–362.

24. Klein, J.; Eisenmann, B. *Mater. Res. Bull*. **1988**, *23*, 587–594.

25. Hafner, P.; Range, K. J. *J. Alloys Compd*. **1994**, *216*, 7–10.

26. Smith, P. M.; Leadbetter, A. J.; Apling, A. J. *Philos. Ma*g. **1975**, *31*, 57–64.

27. Hönle, W.; von Schnering, H. G. *Acta Crystallogr.*, *Sect. A* **1978**, *34*, S152–156.

28. Iandelli, A.; Franceschi, E. A. *J. Less-Common Met*. **1973**, *30*, 211–216.

29. Hütz, A.; Nagorsen, G. *Z. Metallkd.* **1974**, *65*, 618–623.

30. Papoian, G. A.; Hoffmann, R. H. *Angew. Chem., Int. Ed.* **2000**, *39*, 2408–2448.

31. Hönle, W.; Buresch, J.; Peters, K.; Chang, J. H.; von Schnering, H. G. *Z. Kristallogr. – New Cryst. Struct*. **2002**, *217*, 487–488.

32. Emmerling, F.; Röhr, C. *Z. Naturforsch., B* **2002**, *57*, 963–975.

33. Gascoin, F.; Sevov, S. C. *Inorg. Chem*. **2001**, *40*, 5177–5181.

34. von Schnering, H. G.; Somer, M.; Kliche, G.; Hönle, W.; Meyer, T.; Wolf, J.; Ohse, L.; Kempa, P. B. *Z. Anorg. Allg. Chem.* **1991**, *601*, 13–30.

35. Hönle, W.; Krogull, G.; Peters, K.; von Schnering, H. G. *Z. Kristallogr. – New Cryst. Struct.* **1999**, *214*, 17–18.

36. Seifert-Lorenz, K.; Hafner, J. *Phys. Rev. B: Condens. Matter Mater. Phys.* **1999**, *59*, 829–842.

37. Senko, M. E.; Dunn, H. M.; Weidenborner, J. E.; Cole, H. *Acta Crystallogr.* **1959**, *12*, 76.

38. Wadsten, T. *Acta Chem. Scand*. **1967**, *21*, 593–594.

39. Rehr, A.; Guerra, F.; Parkin, S.; Hope, H.; Kauzlarich, S. M. *Inorg. Chem*. **1995**, *34*, 6218–6220.

40. Emmerling, F.; Hirschle, C.; Röhr, C. *Z. Anorg. Allg. Chem.* **2002**, *628*, 559–563.

41. Brice, J. F.; Courtois, A. *C. R. Seances Acad. Sci.*, *Ser. C* **1976**, *283*, 479–481.

42. Ferguson, M. J.; Hushagen, R. W.; Mar, A. *J. Alloys Compd.* **1997**, *249*, 191–198.

43. Brylak, M.; Möller, M. H.; Jeitschko, W. *J. Solid State Chem.* **1995**, *115*, 305–308.

44. Eschen, M.; Jeitschko, W. *Z. Naturforsch*., *B* **2003**, *58*, 399–409.

45. Lam, R.; McDonald, R.; Mar, A. *Inorg. Chem.* **2001**, *40*, 952–959.

46. Liu, Y.; Chen, L.; Li, L.-H.; Wu, L.-M; Zelinska, O. Ya.; Mar, A. *Inorg. Chem.* **2008**, *47*, 11930–11941.

47. Mills, A. M.; Mar, A. *Inorg. Chem.* **2000**, *39*, 4599–4607.

48. Mandrus, D.; Sefat, A. S.; McGuire, M. A.; Sales, B. C. *Chem. Mater.* **2010**, *22*, 715–723.

49. Stoyko, S. S.; Khatun, M.; Mar, A. *Inorg. Chem*. **2012**, *51*, 2621−2628.

50. Villars, P.; Cenzual, K. *Pearson's Crystal Data – Crystal Structure Database for Inorganic Compounds*, release 2015/16; ASM international: Materials Park, Ohio, USA.

51. Mentzen, B. F.; Hillel, R.; Michaelides, A.; Tranquard, A.; Bouix, J. *C. R. Acad. Sci., Ser. II* **1981**, *293*, 965–967.

52. Eisenmann, B.; Schäfer, H. *Z. Naturforsch., B* **1981**, *36*, 415–419.

53. Klein, J.; Eisenmann, B. *Mater. Res. Bull.* **1988**, *23*, 587–594.

54. Hurng, W.-M.; Corbett, J. D., Wang, S.-L.; Jacobson, R. A. *Inorg. Chem.* **1987**, *26*, 2392–2395.

55. Feng, K.; Yin, W.; He, R.; Lin, Z.; Jin, S.; Yao, J.; Fu, P.; Wu, Y. *Dalton Trans.* **2012**, *41*, 484–489.

56. Mewis, A. *Z. Naturforsch*., *B* **1980**, *35,* 141–145.

57. Kauzlarich, S. M.; Thomas, M. M.; Odink, D. A.; Olmstead, M. M. *J. Am. Chem. Soc.* **1991**, *113,* 7205–7208.

58. Rehr, A.; Kuromoto, T. Y.; Kauzlarich, S. M.; del Castillo, J.; Webb, D. J. *Chem. Mater.* **1994**, *6,* 93–99.

59. Cordier, G.; Müller V. *Z. Kristallogr*. **1993**, *203*, 152–153.

60. Dong, Z.-C.; Corbett, J. D. *Inorg. Chem.***1995**, *34*, 5042–5048.

61. Alemany, P.; Llunell, M.; Canadell, E. *Inorg. Chem.* **2006**, *45*, 7235–7241.

62. Ponou, S.; Fässler, T. F.; Tobías, G.; Canadell, E.; Cho, A.; Sevov, S. C. *Chem. -Eur. J.* **2004**, *10*, 3615–3621.

63. Guloy, A. M.; Corbett, J. D. *Inog. Chem*. **1996**, *35*, 2616–2622.

64. Birdwhistell, T. L. T.; Stevens, E. D.; O'Connor, C. J. *Inorg. Chem.* **1990**, *29*, 3892–3894.

65. Hutchins, P. T.; Leynaud, O.; O'Dell, L. A.; Smith, M. E.; Barnes, P.; McMillan, P. F. *Chem. Mater.* **2011**, *23*, 5160–5167.

66. Migas, D. B.; Shaposhnikov, V. L.; Borisenko, V. E. *Phys. Status Solidi B* **2007**, *244*, 2611–2618.

67. Baran, V. V.; Fischer, A.; Scherer, W.; Fässler, T. F. *Z. Anorg. Allg. Chem*. **2013**, *639*, 2125–2128.

68. Kalarasse, F.; Bennecer, B. *J. Phys. Chem. Solids* **2006**, *67*, 846–850.

69. He, H.; Tyson, C.; Bobev, S. *Inorg. Chem.* **2011**, *50*, 8375–8383.

70. Stoyko, S. S.; Khatun, M.; Mullen, C. S.; Mar, A. *J. Solid State Chem.* **2012**, *192*, 325–330.

71. He, H.; Zevalkink, A.; Gibbs, Z. M.; Snyder, G. J.; Bobev, S. *Chem. Mater.* **2012**, *24*, 3596–3603.

72. May, A. F.; McGuire, M. A.; Ma, J.; Delaire, O.; Huq, A.; Custelcean, R. *J. Appl. Phys.* **2012**, *111*, 033708-1–033708-7.

73. Young, D. M.; Kauzlarich, S. M. *Chem. Mater.* **1995**, *7*, 206–209.

74. Oh, H.; Moon, J.; Shin, D.; Moon, C.-Y.; Choi, H. J. *Prog. Supercond.* **2011**, *13*, 65–84.

75. Ettema, A. R. H. F.; de Groot, R. A. *J. Phys. Condens. Matter*. **1999**, *11*, 759–766.

76. Hirt, H.; Deiseroth, H. *Z. Anorg. Allg. Chem*. **2004**, *630*, 1357–1359.

77. Yan, J.-Q.; Nandi, S.; Zarestky, J. L.; Tian, W.; Kreyssig, A.; Jensen, B.; Kracher, A.; Dennis, K. W.; McQueeney, R. J.; Goldman, A. I.; McCallum, R. W.; Lograsso, T. A. *Appl. Phys. Lett*. **2009**, *95*, 222504-1–222504-3.

78. Chen, Z. G.; Yuan, R. H.; Dong, T.; Wang, N. L. *Phys. Rev. B* **2010**, *81*, 100502-1–100502-4.

79. Dong, T.; Chen, Z. G.; Yuan, R. H.; Hu, B. F.; Cheng, B.; Wang, N. L. *Phys. Rev. B* **2010**, *82*, 054522-1–054522-5.

80. Sangster, J.; Pelton, A. D. *J. Phase Equilib. Diffus*. **1993**, *14*, 240–242.

81. Voronin, G. F.; Bludova, L. N. *Vestnik Belorusskogo Gosudarstvennogo Universiteta*, *Seriya 2*: *Khimiya Biologiya*, *Geografiya* **1974**, *15*, 433–435.

82. Emmerling, F.; Röhr, C. *Z. Anorg. Allg. Chem.* **2003**, *629*, 467–472.

83. Hirschle, C.; Röhr, C. *Z. Anorg. Allg. Chem*. **2000**, *626*, 1992–1998.

84. Saparov, B.; Mitchell, J. E.; Sefat, A. S. *Supercond. Sci. Technol.* **2012**, *25*, 084016-1–084016-10.

85. Spitzer, D. P.; Castellion, G. A.; Haacke, G. *J. Appl. Phys.* **1966**, *37*, 3795–3801.

86. Wang, S.; Yang, J.; Wu, L.; Wei, P.; Yang, J.; Zhang, W.; Grin, Y. *Chem. Mater.* **2015**, *27*, 1071–1081.

87. Castillo-Ojeda, R.; Díaz-Reyes, J.; Galván-Arellano, M.; Peña-Sierra, R. *Adv. Mater. Res.* **2014**, *976*, 25–29.

88. Rau, J. W.; Kannewurf, C. R. *Phys. Rev. B* **1971**, *3*, 2581−2587.

89. Donohue, P. C.; Young, H. S. *J. Solid State Chem*. **1970**, *1*, 143–149.

90. Lee, K.; Kamali, S.; Ericsson, T.; Bellard, M.; Kovnir. K. *Chem. Mater*. **2016**, *28*, 2776−2785.

91. Wang, X. C.; Liu, Q. Q.; Lv, Y. X.; Gao, W. B.; Yang, L. X.; Yu, R. C.; Li, F. Y.; Jin, C. Q. *Solid State Commun.* **2008**, *148*, 538–540.

92. Rotter, M.; Tegel, M.; Johrendt, D. *Phys. Rev. Lett*. **2008**, *101*, 107006-1–107006-4.

93. Mittal, R.; Su, Y.; Rols, S.; Tegel, M.; Chaplot, S. L.; Schober, H.; Chatterji, T.; Johrendt, D.; Brueckel, Th. *Phys. Rev. B*. **2008**, *78*, 224518-1–224518-5.

94. Cortes-Gil, R.; Clarke, S. J. *Chem. Mater*. **2011**, *23*, 1009–1016.

95. Qi, Y.; Gao, Z.; Wang, L.; Wang, D.; Zhang, X.; Ma, Y. *New J. Phys.* **2008**, *10*, 123003-1–123003-6.

96. Jeitschko, W.; Glaum, R.; Boonk; L. *J. Solid State Chem*. **1987**, *69*, 93–100.

97. Guo, Q.; Pan, B. J.; Yu, J.; Ruan, B. B.; Chen, D. Y.; Wang, X. C.; Mu, Q. G.; Chen, G. F.; Ren, Z. A. *Sci. Bull.* **2016**, *61*, 921–924.

98. Lam, R.; Mar, A. *Inorg. Chem.* **1996**, 35*,* 6959–6963.

99. Deakin, L.; Lam, R.; Marsiglio, F.; Mar, A. *J. Alloys Compd.* **2002**, *388,* 69–72.

100. Fisher, I. R.; Wiener, T. A.; Bud'ko, S. L.; Canfield, P. C.; Chan, J. Y.; Kauzlarich, S. M. *Phys. Rev. B* **1999**, *59*, 13829–13834.

101. Klufers, P.; Mewis, A. *Z. Naturforsch*., *B* **1977**, *32*, 753–756.

102. Madsen, G. K. H. *J. Am. Chem. Soc.* **2006**, *128*, 12148–12146.

103. Lii, K.-H.; Haushalter, R. C. *J. Solid State Chem*. **1987**, *67*, 374–378.

104. Sharp, J. W.; Nolas, G. S.; Volckmann, E. H. *Mater*. *Res*. *Soc*. *Symp*. *Proc*. **1997**, *478*, 91–102.

105. Zhang, L.; Du, M.-H.; Singh, D. J. *Phys. Rev. B* **2010**, *81*, 075117-1–075117-8.

106. Brown, S. R.; Kauzlarich, S. M.; Gascoin, F.; Snyder, G. J. *Chem. Mater.* **2006**, *18*, 1873–1877.

107. Holm, A. P.; Kauzlarich, S. M.; Morton, S. A.; Waddill, G. D.; Pickett, W. E.; Tobin, J. G. *J. Am. Chem. Soc.* **2002**, *124*, 9894–9898.

108. Deng, Z.; Jin, C. Q.; Liu, Q. Q.; Wang, X. C.; Zhu, J. L.; Feng, S. M.; Chen, L. C.; Yu, R. C.; Arguello, C.; Goko, T.; Ning, F.; Zhang, J.; Wang, Y.; Aczel, A. A.; Munsie, T.; Williams, T. J.; Luke, G. M.; Kakeshita, T.; Uchida, S.; Higemoto, W.; Ito, T. U.; Gu, B.; Maekawa, S.; Morris, G. D.; Uemura, Y. J. *Nat. Commun.* **2011**, *2*, 1425-1–1425-5.

109. Yan, B.; Müchler, L.; Felser, C. *Phys. Rev. Lett.* **2012**, *109*, 116406-1–116406-5.

110. Guechi, A.; Merabet, A.; Chegaar, M.; Bouhemadou, A.; Guechi, N. *J. Alloys Compd*. **2015**, *623*, 219–228.

111. Pöttgen, R.; Johrendt, D. *Intermetallics: Synthesis*, *Structure*, *Function*, de Gruyter: Berlin, 2014.

112. Eckert, M. *Ann. Phys.* **2012**, *524*, A83–A85.

113. Bragg, W. H.; Bragg W. L. *Proc. R. Soc. Lond. A* **1913**, *88*, 428–438.

114. Sheldrick, G. M. *SHELXTL*, version 6.12; Bruker AXS Inc.: Madison, WI, 2001.

115. Brese, N. E; O'Keeffe, M. *Acta*. *Crystallogr., Sect. B* **1991**, *47*, 192–197.

116. Dronskowski, R. *Computational Chemistry of Solid State Materials*, Wiley-VCH: Weinheim, 2005.

117. Hoffman, R. *Angew*. *Chem*., *Int*. *Ed*. *Engl*. **1987**, *26*, 846–878.

Chapter 2

Ternary Arsenides $A_2Zn_5As_4$ (A = K, Rb): Zintl Phases Built from *Stellae Quadrangulae*

A version of this chapter has been published. Stoyko, S. S.; Khatun, M.; Mar, A. Inorg. Chem. 2012, 51, 9517–9521.

2.1 Introduction

Much of the current resurgence of interest in ternary arsenides *A*–*M*–As containing an electropositive metal *A* and a transition metal *M* can be traced to the discovery of useful materials properties, particularly superconductivity in $BaFe_2As_2$ and related compounds.[1] However, these arsenides are significant in their own right for their diverse structural chemistry, originating from the different ways that heteronuclear anionic units MAs_n can be linked to form complex extended frameworks; for the most part, they can be considered to be Zintl phases.[2] Given previous work on ternary rare-earth-metal zinc arsenides *RE*–Zn–As,[3–5] we and others have been interested in extending these studies to systems containing other electropositive components, such as alkaline-earth metals.[6–9] The alkali-metal-containing systems *A*–Zn–As remain sparsely investigated and examples of compounds have been so far limited to a few: LiZnAs (MgAgAs-type),[10–13] NaZnAs (MgAgAs- and PbFCl-types),[14–16] KZnAs (ZrBeSi- and LiBaSi-types),[15,17] $NaZn_4As_3$ ($RbCd_4As_3$-type),[18] AZn_4As_3 (A = K, Rb, Cs; KCu_4S_3-type),[18] and K_4ZnAs_2 (K_4CdP_2-type).[19] LiZnAs has been identified as a host material that can be doped to induce ferromagnetism.[20]

In this chapter the preparation of the ternary arsenides $K_2Zn_5As_4$ and $Rb_2Zn_5As_4$ is discussed. They adopt a new and unusual structure type which can be described through

stellae quadrangulae as the building units. Their relationships to other structures are drawn, and the bonding in these Zintl phases is examined through the use of band structure calculations.

2.2 Experimental

2.2.1 Synthesis

Starting materials were K pieces (99.95%, Alfa-Aesar), Rb pieces (99.75%, Alfa-Aesar), Zn shot (99.99%, Aldrich), and As lumps (99.999%, Alfa-Aesar). All reagents and products were handled within an argon-filled glovebox. Stoichiometric mixtures of the elements were loaded into alumina crucibles placed within fused-silica tubes, which were evacuated and sealed. The tubes were heated to 650 °C (for K samples) or 600 °C (for Rb samples) over 2 d, held at that temperature for 10 d, and cooled to room temperature over 2 d. The use of a lower annealing temperature for the Rb samples was prompted by the low boiling point for Rb metal (688 °C). Products were analyzed by powder X-ray diffraction (XRD) on an Inel diffractometer equipped with a curved position-sensitive detector (CPS 120) and a Cu $K\alpha_1$ radiation source operated at 40 kV and 20 mA. The powder XRD patterns revealed that the K-containing reactions gave nearly quantitative yields of $K_2Zn_5As_4$ along with small amounts (less than 5%) of KZnAs, whereas the Rb-containing reactions gave nearly equal proportions of $Rb_2Zn_5As_4$ and $RbZn_4As_3$ (**Figure A 1-1** in **Appendix 1**). The lower yields for $Rb_2Zn_5As_4$ are likely associated with partial evaporative loss of Rb metal from the open alumina crucibles and reaction with the fused-silica tubes. However, an alternative explanation for the differences in the reaction products for the K- vs. Rb-containing reactions is that the ternary compounds, once formed, may be prone to undergo

decomposition at high temperature. Single crystals of the title compounds are moderately air-sensitive, although they can be handled without any special precautions for several minutes before tarnishing. Crystals were selected under paraffin oil and examined by energy-dispersive X-ray (EDX) analysis on a JEOL JSM-6010LA scanning electron microscope. A representative SEM image is shown in **Figure A 1-2** in **Appendix 1**. The experimentally determined average compositions (in atomic %) were $K_{19(2)}Zn_{44(1)}As_{37(2)}$ and $Rb_{20(2)}Zn_{45(1)}As_{35(2)}$, which are in excellent agreement with expectations ($A_{18.2}Zn_{45.4}As_{36.4}$). Attempts were made to prepare the Na analogue of these compounds, under similar conditions as above, to no avail. Reactions with Cs were not attempted.

2.2.2 Structure Determination

Suitable single crystals were mounted within small droplets of paraffin oil on glass fibers and placed under a cold nitrogen gas stream on a Bruker D8 ($K_2Zn_5As_4$) or a Bruker PLATFORM ($Rb_2Zn_5As_4$) diffractometer, each equipped with a SMART APEX II CCD detector and a Mo $K\alpha$ radiation source. Full spheres of intensity data were collected at –100 °C using ω scans with a scan width of 0.3° and an exposure time of 15 s per frame in 7 ($K_2Zn_5As_4$) or 5 ($Rb_2Zn_5As_4$) batches. Face-indexed numerical absorption corrections were applied. Structure solution and refinement were carried out with use of the SHELXTL (version 6.12) program package.[21] Crystal data and further experimental details are given in **Table 2-1**. The centrosymmetric orthorhombic space group *Cmcm* was chosen on the basis of the Laue symmetry, systematic absences, and intensity statistics (mean $|E^2 - 1|$ of 0.920 for $K_2Zn_5As_4$ and 0.969 for $Rb_2Zn_5As_4$). Initial atomic positions were easily located by direct methods and refinements proceeded in a straightforward manner. All sites are fully

occupied and have reasonable displacement parameters. Atomic positions were standardized with the program STRUCTURE TIDY.[22] Final values of the positional and displacement parameters are given in **Table 2-2** and selected interatomic distances are listed in **Table 2-3**. Further crystallographic information can be found in CSD numbers 424848 to 424849.

Table 2-1. Crystallographic data for $A_2Zn_5As_4$ (A = K, Rb)

formula	$K_2Zn_5As_4$	$Rb_2Zn_5As_4$
formula mass (amu)	704.73	797.47
space group	*Cmcm* (No. 63)	*Cmcm* (No. 63)
a (Å)	11.5758(5)	11.6649(5)
b (Å)	7.0476(3)	7.0953(3)
c (Å)	11.6352(5)	11.7585(5)
V (Å^3)	949.22(7)	973.20(7)
Z	4	4
ρ_{calcd} (g cm^{-3})	4.931	5.443
T (K)	173(2)	173(2)
crystal dimensions (mm)	0.07 × 0.16 × 0.21	0.04 × 0.08 × 0.09
radiation	graphite-monochromated Mo $K\alpha$, λ = 0.71073 Å	
μ(Mo $K\alpha$) (mm^{-1})	27.09	35.50
transmission factors	0.032–0.264	0.134–0.386
2θ limits	6.76–66.32°	6.72–66.46°
data collected	$-17 \le h \le 17$, $-10 \le k \le 10$, $-17 \le l \le 17$	$-17 \le h \le 17$, $-10 \le k \le 10$, $-17 \le l \le 18$
no. of data collected	6481	6610
no. of unique data, including $F_o^2 < 0$	981 (R_{int} = 0.018)	1004 (R_{int} = 0.031)
no. of unique data, with $F_o^2 > 2\sigma(F_o^2)$	948	905
no. of variables	35	35
$R(F)$ for $F_o^2 > 2\sigma(F_o^2)$ [a]	0.014	0.016
$R_w(F_o^2)$ [b]	0.032	0.034
goodness of fit	1.28	1.08
$(\Delta\rho)_{max}$, $(\Delta\rho)_{min}$ (e Å^{-3})	0.77, –0.61	0.93, –0.70

[a] $R(F) = \sum||F_o| - |F_c|| / \sum|F_o|$. [b] $R_w(F_o^2) = [\sum[w(F_o^2 - F_c^2)^2] / \sum wF_o^4]^{1/2}$; $w^{-1} = [\sigma^2(F_o^2) + (Ap)^2 + Bp]$, where $p = [\max(F_o^2,0) + 2F_c^2] / 3$.

Table 2-2. Atomic coordinates and equivalent isotropic displacement parameters for $A_2Zn_5As_4$ (A = K, Rb)

Atom	Wyckoff position	*x*	*y*	*z*	U_{eq} (Å^2) [a]
$K_2Zn_5As_4$					
K	8*e*	0.21456(4)	0	0	0.01331(9)
Zn1	8*g*	0.14314(2)	0.38609(4)	¼	0.00968(6)
Zn2	8*f*	0	0.65236(4)	0.10852(2)	0.01013(6)
Zn3	4*c*	0	0.00784(5)	¼	0.01072(8)
As1	8*g*	0.34153(2)	0.25779(3)	¼	0.00756(6)
As2	8*f*	0	0.27484(3)	0.09769(2)	0.00759(6)
$Rb_2Zn_5As_4$					
Rb	8*e*	0.21769(2)	0	0	0.01061(7)
Zn1	8*g*	0.14335(3)	0.38326(5)	¼	0.00981(8)
Zn2	8*f*	0	0.65403(5)	0.10868(3)	0.00988(8)
Zn3	4*c*	0	0.00991(7)	¼	0.01091(10)
As1	8*g*	0.34319(2)	0.25739(4)	¼	0.00729(7)
As2	8*f*	0	0.27883(4)	0.09870(2)	0.00730(7)

[a] U_{eq} is defined as one-third of the trace of the orthogonalized U_{ij} tensor.

Table 2-3. Selected interatomic distances (Å) in $A_2Zn_5As_4$ (A = K, Rb)

	$K_2Zn_5As_4$	$Rb_2Zn_5As_4$
A–As2 (×2)	3.3485(4)	3.4219(3)
A–As1 (×2)	3.4346(2)	3.4798(2)
A–As1 (×2)	3.7312(2)	3.7576(2)
A–As2 (×2)	3.8377(4)	3.8280(3)
A–Zn1 (×2)	3.4379(3)	3.4576(2)
A–Zn2 (×2)	3.6966(5)	3.6976(3)
A–Zn2 (×2)	3.7102(4)	3.7560(3)
A–Zn3 (×2)	3.8253(3)	3.8852(2)
A–Zn1 (×2)	4.0680(2)	4.0973(3)
A–*A* (×2)	3.6181(3)	3.6268(2)
Zn1–As1	2.4682(3)	2.4963(4)
Zn1–As2 (×2)	2.5497(2)	2.5515(3)
Zn1–As1	2.6256(3)	2.6592(5)
Zn2–As2	2.4535(3)	2.4846(4)
Zn2–As1 (×2)	2.5743(2)	2.5778(3)
Zn2–As2	2.6636(3)	2.6648(5)
Zn3–As1 (×2)	2.5437(3)	2.5605(5)
Zn3–As2 (×2)	2.5848(3)	2.6088(5)
Zn1–Zn2 (×2)	2.9961(3)	3.0411(4)
Zn2–Zn3 (×2)	2.9977(4)	3.0228(6)
Zn1–Zn3	3.1387(4)	3.1327(6)

2.2.3. Band Structure Calculations

Tight-binding linear muffin tin orbital band structure calculations were performed on $K_2Zn_5As_4$ within the local density and atomic spheres approximation with use of the Stuttgart TB-LMTO-ASA program (version 4.7).[23] The basis sets included K 4s/4p/3d, Zn 4s/4p/3d, and As 4s/4p/4d orbitals, with the K 4p/3d and As 4d orbitals being downfolded. The unit cell contains two formula units. Calculations were performed with an increasing number of *k* points (ranging from 172 to 666 within the first Brillouin zone) until the total energy did not deviate by more than 10^{-5} eV/cell. Integrations in reciprocal space were carried out with an improved tetrahedron method over 666 irreducible *k* points within the first Brillouin zone. A similar calculation was conducted on $Rb_2Zn_5As_4$ to investigate how the band gap is influenced by a change in the alkali-metal substituent.

2.3 Result and Discussion

The preparation of the new arsenides $A_2Zn_5As_4$ (A = K, Rb) illustrates the richness of these ternary A–Zn–As systems. All known phases to date can be considered to be members of the pseudobinary join A_3As–Zn_3As_2: A_4ZnAs_2 (4/3 A_3As + 1/3 Zn_3As_2),[19] AZnAs (1/3 A_3As + 1/3 Zn_3As_2),[10–17] $A_2Zn_5As_4$ (2/3 A_3As + 5/3 Zn_3As_2), and AZn_4As_3 (1/3 A_3As + 4/3 Zn_3As_2).[18] This pattern reflects their shared features of being Zintl phases with structures built up from simple Zn-centred polyhedra and having no homoatomic As–As bonds. There are recent reports that analogous Cd-containing arsenides and antimonides isostructural to $A_2Zn_5As_4$ can also be formed: $Rb_2Cd_5As_4$,[18] $Rb_2Cd_5Sb_4$,[24] and $Cs_2Cd_5Sb_4$.[24,25]

The structure type (space group *Cmcm*, Pearson code *oC*44, Wyckoff sequence *g*2 *f*2 *e c*) is new. $ZnAs_4$ tetrahedra are linked through corner- and edge-sharing to form a three-dimensional framework, generating large channels extending along the *b*-direction within which lie the *A* atoms (**Figure 2-1**). Because the connectivity of the $ZnAs_4$ tetrahedra is a little difficult to visualize in a conventional ball-and-stick drawing, it is helpful to switch to a polyhedral representation (**Figure 2-2**). Now it becomes evident that two types of tetrahedra (centred by Zn1 and Zn2) are arranged in an interesting way to form a unit called a *stella quadrangula* (also tetrahedral star or tetraederstern), basically a tetracapped tetrahedron. Such units can be useful for describing complex crystal structures as diverse as silicates and alloys.[26–30] Here, two Zn1- and two Zn2-centred tetrahedra form the caps of these units, leaving the central tetrahedron empty. Another way to view this unit is as a heterocubane structure, with Zn_4As_4 as the central cube and additional As atoms attached to four corners. The *stellae* are extended along the *c*-direction through edge-sharing, and within the *ab*-plane through corner-sharing. The third type of tetrahedra (centred by Zn3 atoms) also serve to link these units within the *ab*-plane through edge-sharing. Although the presence of *A* cations enclosed in large 20-vertex coordination polyhedra (**Figure 2-3**) suggests some resemblance to clathrate structures of related antimonides,[24,25] these polyhedra are highly irregular and they interpenetrate each other along the *b*-direction. A more distant relationship that can be drawn is to $K_2Cu_2Te_5$, which has similar cell parameters and almost the same Wyckoff sequence as $A_2Zn_5As_4$ except that a 8*f* site is missing.[31] Both contain flat nets parallel to the *ab*-plane with similar topologies but different patterns of metal and nonmetal atoms (**Figure 2-4**).

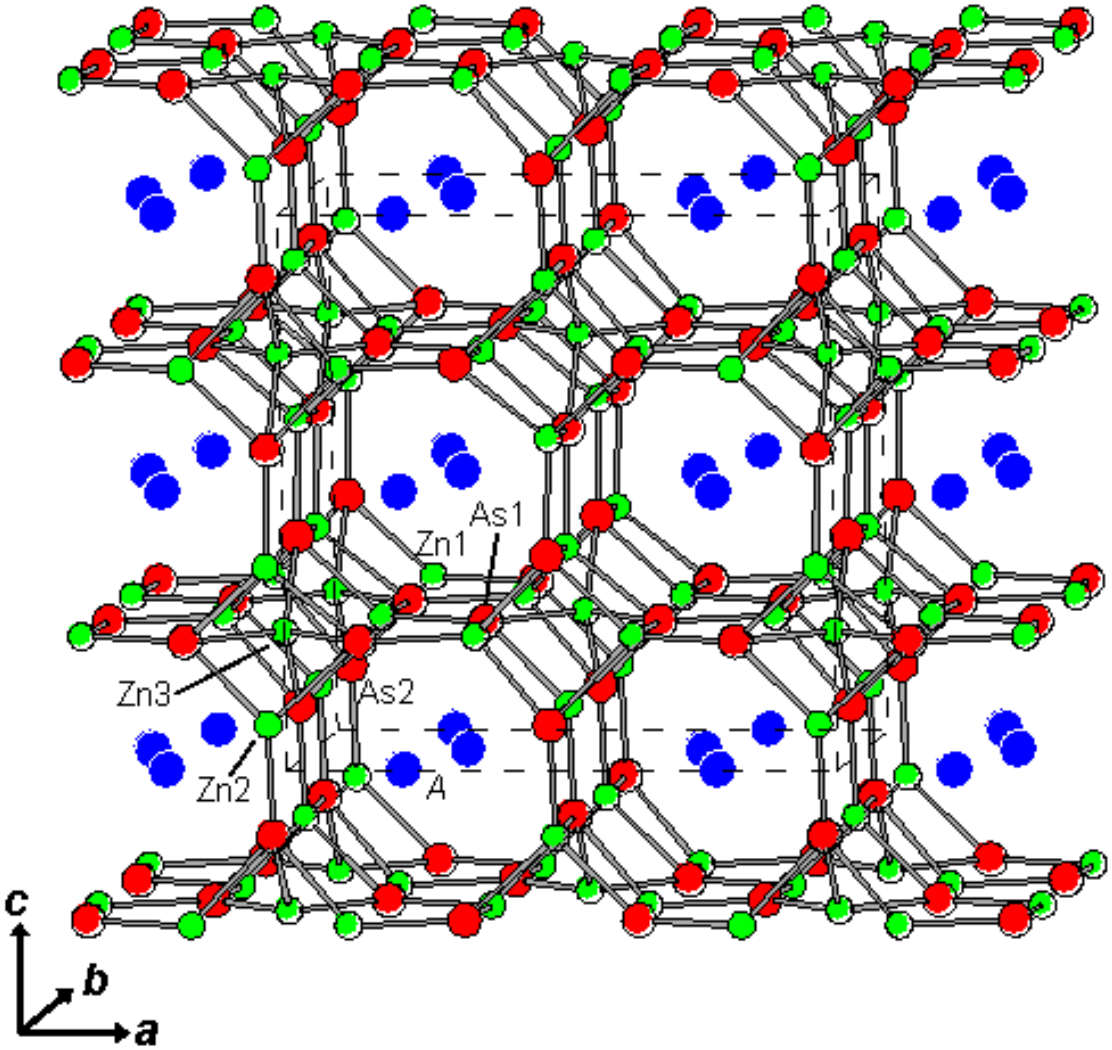

Figure 2-1. Structure of $A_2Zn_5As_4$ (A = K, Rb), viewed approximately down the b-direction, in a ball-and-stick representation. The large blue circles are A atoms, the small green circles are Zn atoms, and the medium red circles are As atoms.

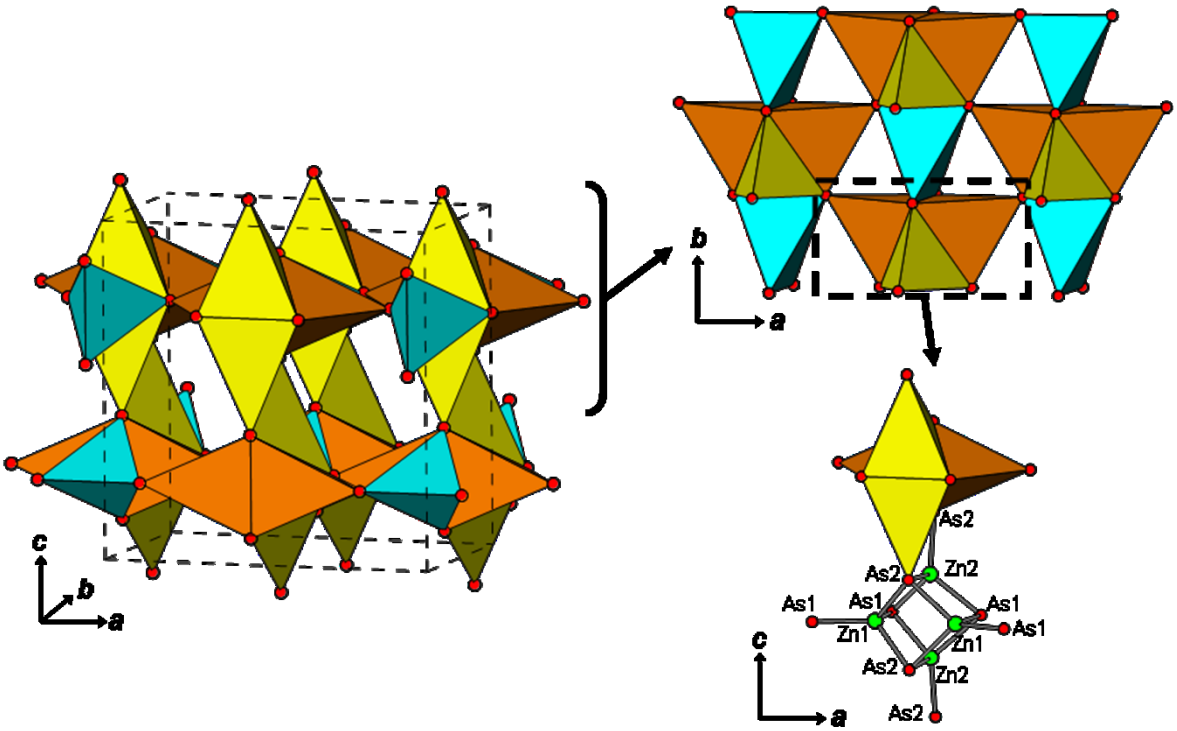

Figure 2-2. With the *A* atoms omitted for clarity, the 3D-framework of $A_2Zn_5As_4$ (*A* = K, Rb) can be built up from $ZnAs_4$ tetrahedra. Two Zn1- (orange) and two Zn2-centred tetrahedra (yellow) are connected to form a *stella quadrangula*; these units are further linked by Zn3-centred tetrahedra (cyan).

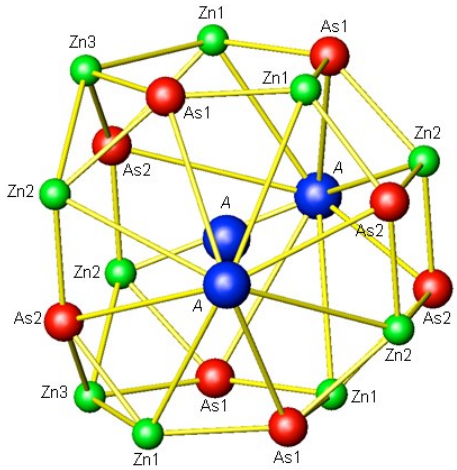

Figure 2-3. Coordination environment around an *A* atom in $A_2Zn_5As_4$ (*A* = K, Rb), forming a 20-vertex polyhedron.

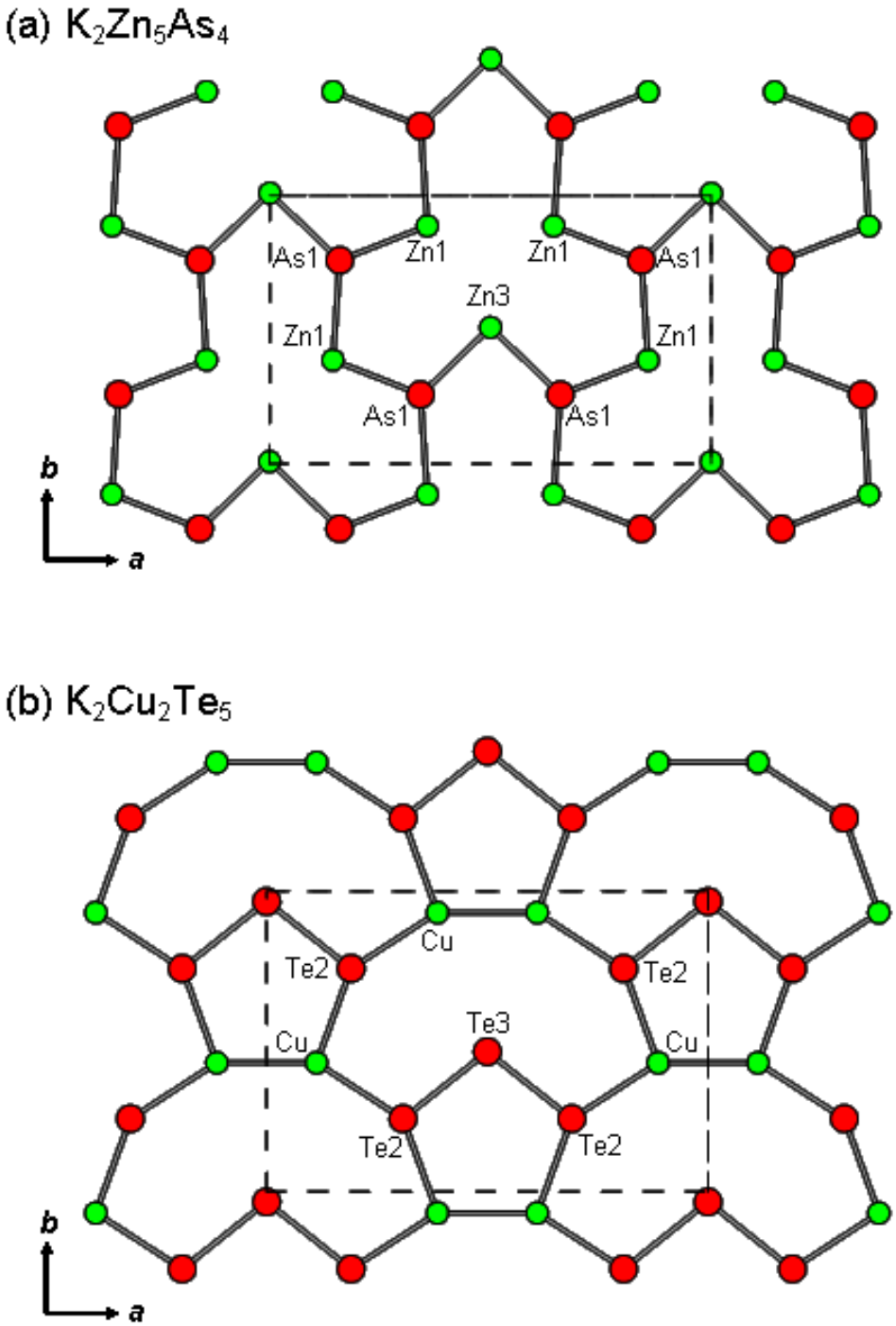

Figure 2-4. Comparison of nets parallel to the *ab*-plane present in (a) $K_2Zn_5As_4$ and (b) $K_2Cu_2Te_5$.

Inspection of interatomic distances (**Table 2-3**) indicates that the Zn–As contacts fall in the normal range (2.5–2.7 Å), the Zn–Zn contacts are probably too long to be bonding (3.0–3.1 Å), and As–As contacts are not present. Thus, these compounds are typical Zintl phases in which all atoms attain closed-shell electron configurations and charge balance is maintained: $(A^{+})_2(Zn^{2+})_5(As^{3-})_4$. Band structure calculations on $K_2Zn_5As_4$ (**Figure 2-5**) confirm these expectations, with the density of states (DOS) curve revealing nearly empty K-based states, completely filled Zn 3d states (the large spike between –7 and –8 eV), and nearly filled As-based states below the Fermi level. In fact, most of the bonding stability in the structure is derived from heteroatomic Zn–As contacts, which are perfectly optimized as seen by the occupation of all bonding and no antibonding levels in the crystal orbital Hamilton population (COHP) curve (**Figure 2-5**). These Zn–As bonds are strong (–ICOHP of 1.04 eV/bond and 12.5 eV/cell) and constitute >95% of the total covalent bonding energy in the structure, in contrast to the almost negligible contributions from K–As (–ICOHP of 0.02 eV/bond and 0.2 eV/cell) and Zn–Zn bonding (–ICOHP of 0.08 eV/bond and 0.3 eV/cell). The Zintl concept thus works well to account for the relatively minor role of the alkali-metal atoms as mere suppliers of electrons to the Zn–As framework, with the consequence that the analogous Rb-containing compound should also be expected to have a closely related electronic structure. Indeed, $K_2Zn_5As_4$ and $Rb_2Zn_5As_4$ have very similar band dispersion diagrams (**Figure A 1-3** in **Appendix 1**); both are predicted to be essentially direct band gap semiconductors with nearly the same gap energy of 0.4 eV between the valence and conduction bands.

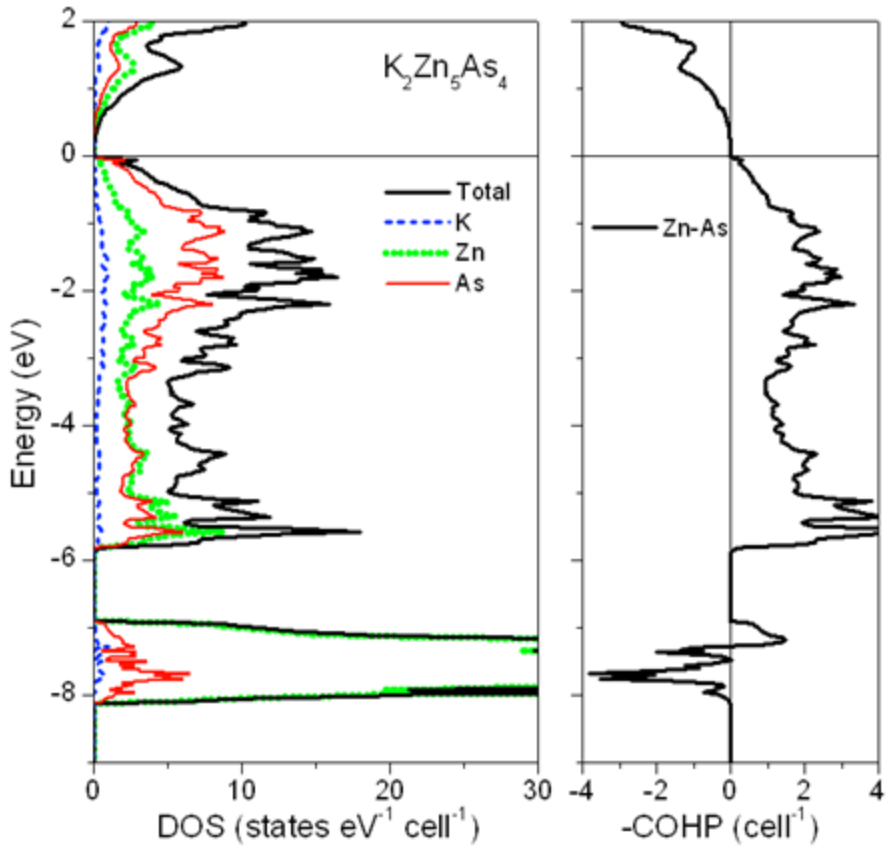

Figure 2-5. Density of states with atomic projections (left) and crystal orbital Hamilton population (COHP) curve for Zn–As contacts (right) in $K_2Zn_5As_4$. The horizontal line at 0 eV marks the Fermi level.

2.4 Conclusion

Adding to the growing family of ternary transition-metal arsenides, the compounds $A_2Zn_5As_4$ (A = K, Rb) exhibit a unique structure that can be described through *stellae quadrangulae* containing Zn-centred tetrahedra. They are likely amenable to substitution, not only through the obvious ones (e.g., Zn by Cd, or As by Sb),[18,24,25] but also through replacement with a d^5 transition-metal component such as Mn^{2+}. Compounds prepared by replacing Zn with Mn and Cd are presented in Chapter 3. Band structure calculations on $K_2Zn_5As_4$ support the bonding picture implied by the Zintl concept: K^+ cations interact

electrostatically with the anionic framework $[Zn_5As_4]^{2-}$, within which heteroatomic Zn–As covalent bonding predominates. If the modest air sensitivity of these compounds could be reduced, perhaps through appropriate chemical substitution of the alkali-metal component, it would be interesting to perform measurements of physical properties to determine if these compounds could be viable candidates for thermoelectric materials.

2.5 References

1. Mandrus, D.; Sefat, A. S.; McGuire, M. A.; Sales, B. C. *Chem. Mater.* **2010**, *22*, 715–723.
2. Eisenmann, B.; Cordier, G. In *Chemistry, Structure, and Bonding of Zintl Phases and Ions*; Kauzlarich, S. M., Ed.; VCH: New York, 1996; pp 61–137.
3. Stoyko, S. S.; Mar, A. *J. Solid State Chem.* **2011**, *184*, 2360–2367.
4. Stoyko, S. S.; Mar, A. *Inorg. Chem.* **2011**, *50*, 11152–11161.
5. Nientiedt, A. T.; Lincke, H.; Rodewald, U. Ch.; Pöttgen, R.; Jeitschko, W. *Z. Naturforsch., B: J. Chem. Sci.* **2011**, *66*, 221–226.
6. Hellman, A.; Löhken, A.; Wurth, A.; Mewis, A. *Z. Naturforsch., B: J. Chem. Sci.* **2007**, *62*, 155–161.
7. Saparov, B.; Bobev, S. *Inorg. Chem.* **2010**, *49*, 5173–5179.
8. Wilson, D. K.; Saparov, B.; Bobev, S. *Z. Anorg. Allg. Chem.* **2011**, *637*, 2018–2025.
9. Stoyko, S. S.; Khatun, M.; Mar, A. *Inorg. Chem.* **2012**, *51*, 2621–2628.
10. Nowotny, H.; Bachmeyer, K. *Monatsh. Chem.* **1949**, *8*, 734.
11. Kuriyama, K.; Nakamura, F. *Phys. Rev. B* **1987**, *36*, 4439–4441.
12. Kuriyama, K.; Kato, T.; Kawada, K. *Phys. Rev. B* **1994**, *49*, 11452–11455.
13. Kalarasse, F.; Bennecer, B. *J. Phys. Chem. Solids* **2006**, *67*, 846–850.
14. Nowotny, H.; Glatzl, B. *Monatsh. Chem.* **1951**, *82*, 720–722.
15. Kahlert, H.; Schuster, H.-U. *Z. Naturforsch., B: Anorg. Chem., Org. Chem.* **1976**, *31*, 1538–1539.
16. Jaganesh, G.; Merita Anto Britto, T.; Eithiraj, R. D.; Kalpana, G. *J. Phys.: Condens. Matter* **2008**, *20*, 085220-1–085220-8.
17. Vogel, R.; Schuster, H.-U. *Z. Naturforsch., B: Anorg. Chem., Org. Chem.* **1980**, *35*, 114–116.
18. He, H.; Tyson, C.; Bobev, S. *Inorg. Chem.* **2011**, *50*, 8375–8383.

19. Prots, Yu.; Aydemir, U.; Öztürk, S. S.; Somer, M. *Z. Kristallogr. – New Cryst. Struct.* **2007**, *222*, 163–164.

20. Deng, Z.; Jin, C. Q.; Liu, Q. Q.; Wang, X. C.; Zhu, J. L.; Feng, S. M.; Chen, L. C.; Yu, R. C.; Arguello, C.; Goko, T.; Ning, F.; Zhang, J.; Wang, Y.; Aczel, A. A.; Munsie, T.; Williams, T. J.; Luke, G. M.; Kakeshita, T.; Uchida, S.; Higemoto, W.; Ito, T. U.; Gu, B.; Maekawa, S.; Morris, G. D.; Uemura, Y. J. *Nat. Commun.* **2011**, *2*, No. 422.

21. Sheldrick, G. M. *SHELXTL*, version 6.12; Bruker AXS Inc.: Madison, WI, 2001.

22. Gelato, L. M.; Parthé, E. *J. Appl. Crystallogr.* **1987**, *20*, 139–143.

23. Tank, R.; Jepsen, O.; Burkhardt, A.; Andersen, O. K. *TB-LMTO-ASA Program*, version 4.7; Max Planck Institut für Festkörperforschung: Stuttgart, Germany, 1998.

24. Zheng, W.-Z.; Wang, P.; Wu, L.-M.; Liu, Y.; Chen, L. *Inorg. Chem.* **2010**, *49*, 5890–5896.

25. Liu, Y.; Wu, L.-M.; Li, L.-H.; Du, S.-W.; Corbett, J. D.; Chen, L. *Angew. Chem. Int. Ed.* **2009**, *48*, 5305–5308.

26. Nyman, H.; Andersson, S. *Acta Crystallogr., Sect. A* **1979**, *35*, 580–583.

27. Nyman, H.; Andersson, S. *Acta Crystallogr., Sect. A* **1979**, *35*, 934–937.

28. Nyman, H. *Acta Crystallogr., Sect. B* **1983**, *39*, 529–532.

29. Zheng, C.; Hoffmann, R.; Nelson, D. R. *J. Am. Chem. Soc.* **1990**, *112*, 3784–3791.

30. Häussermann, U.; Svensson, C.; Lidin, S. *J. Am. Chem. Soc.* **1998**, *120*, 3867–3880.

31. Chen, X.; Huang, X.; Li, J. *Inorg. Chem.* **2001**, *40*, 1341–1346.

Chapter 3

Electron-Deficient Ternary and Quaternary Pnictides $Rb_4Zn_7As_7$, $Rb_4Mn_{3.5}Zn_{3.5}Sb_7$, $Rb_7Mn_{12}Sb_{12}$, and $Rb_7Mn_4Cd_8Sb_{12}$ with Corrugated Anionic Layers

A version of this chapter has been published. Khatun, M.; Stoyko, S. S.; Mar, A. Inorg. Chem. 2013, 52, 12682–12690.

3.1. Introduction

Ternary arsenides and antimonides *A–M–Pn* containing an electropositive metal *A* and a d-block element *M* represent a growing category of solid-state compounds useful for materials applications. An important subset comprises charge-balanced Zintl phases forming isostructural series in which the *M* substituent has a d^5 or d^{10} configuration (*M* = Mn, Zn, Cd) and can be extended to include p-block metalloids (*M* = Al, Ga, In).[1] Among numerous examples, perhaps the most well-known is the $A_{14}MPn_{11}$ series (*A* = alkaline-earth and divalent rare-earth metal) adopting the $Ca_{14}AlSb_{11}$-type structure; in particular, $Yb_{14}MnSb_{11}$ has been examined extensively for its thermoelectric, magnetoresistive, and other transport properties.[2–4] Relatively fewer examples are known in which *A* is an alkali metal, but they also show interesting properties. They range from equiatomic phases *AMPn* (*A* = Li–Cs; *M* = Mn, Zn, Cd; *Pn* = As, Sb) adopting simple structures such as cubic MgAgAs- or tetragonal PbFCl-type,[5–8] to complex phases $A_8M_{18}Pn_{28}$ (*A* = K, Rb, Cs; *M* = Zn, Cd; *Pn* = As, Sb) crystallizing in clathrate structures.[9,10] LiZnSb and $A_8M_{18}Pn_{28}$ have been assessed for their thermoelectric properties;[10–13] KHgSb may be a suitable candidate as a weak topological

insulator;[14] and Mn-doped LiZnAs is a dilute half-metallic ferromagnetic semiconductor with potential applications in spintronics.[15]

Further investigations within these alkali-metal-containing systems have led to the discovery of ternary pnictides $A_2M_5Pn_4$ (A = K, Rb, Cs; M = Zn, Cd; Pn = As, Sb),[9,16–19] RbM_4As_3 (M = Zn, Cd),[17] and Cs_4MAs_{14} (M =Zn, Cd),[20] as well as quaternary arsenides $AM_{1.5}Tt_{0.5}As_2$ (A = Na, K, Rb; M = Zn, Cd; Tt = Si, Ge, Sn),[21] $A_2A'CdSb_2$ (A = Na, K; A' = Ca, Sr, Ba, Eu, Yb),[22] and $KA'_2Cd_2Sb_3$ (A' = Ca, Sr, Ba, Eu, Yb).[23] In continuation of these efforts, this chapter describes the preparation of four new rubidium-containing pnictides: $Rb_4Zn_7As_7$, $Rb_4Mn_{3.5}Zn_{3.5}Sb_7$, $Rb_7Mn_{12}Sb_{12}$, and $Rb_7Mn_4Cd_8Sb_{12}$. Their related crystal structures illustrate a principle for connecting edge-sharing tetrahedra to generate corrugated anionic layers not observed previously. Their electronic structures are also examined through band structure calculations, providing support for a one-electron deficiency observed in these compounds.

3.2. Experimental

3.2.1. Synthesis

Starting materials were Rb pieces (99.75%, Alfa-Aesar), Mn powder (99.6%, Alfa-Aesar), Zn shot (99.99%, Aldrich), Cd shot (99.95%, Alfa-Aesar), As lumps (99.999%, Alfa-Aesar), and Sb ingots (99.999%, Alfa-Aesar). All reagents and products were handled within an argon-filled glove box. $Rb_7Mn_{12}Sb_{12}$ was first identified in the course of attempts to prepare "$A_2Mn_5Pn_4$" (A = K, Rb; Pn = As, Sb). Substitution of the d-block component with Cd or Zn then led to the isostructural compound $Rb_7Mn_4Cd_8Sb_{12}$ as well as the different phase $Rb_4Mn_{3.5}Zn_{3.5}Sb_7$. Further substitution of the pnicogen component eventually

revealed the arsenide $Rb_4Zn_7As_7$. The title compounds were prepared from stoichiometric mixtures of the elements, which were loaded into alumina crucibles placed within fused-silica tubes. The tubes were evacuated and sealed; they were then heated to 600 °C over 2 d, kept at this temperature for 10 d, and cooled to room temperature over 2 d. The fused-silica tubes were not attacked, but became slightly turbid, likely a result of partial vaporization of Rb during the heat treatment. The resulting products were air-sensitive, visibly tarnishing within minutes, and were examined under paraffin oil. Products were analyzed by powder X-ray diffraction (XRD) patterns collected on an Inel diffractometer equipped with a curved position-sensitive detector (CPS 120) and a Cu $K\alpha_1$ radiation source operated at 40 kV and 20 mA. These XRD patterns suffered from a high background as a result of contributions from the paraffin oil and X-ray fluorescence from the Mn component within the samples. However, the title compounds generally constituted the major phase, as suggested by a representative XRD pattern for $Rb_7Mn_{12}Sb_{12}$ (**Figure A 2-1** in **Appendix 2**). Crystals of these compounds grew as thin needles (**Figure A 2-2** in **Appendix 2**). The chemical compositions of crystals selected for single-crystal X-ray diffraction experiments were determined by energy-dispersive X-ray (EDX) analysis on a JEOL JSM-6010LA scanning electron microscope and were in good agreement with expectations (**Table A 2-1** in **Appendix 2**). Attempts to prepare other permutations within the series $Rb_4M_7Pn_7$, $Rb_4M_{3.5}M'_{3.5}Pn_7$, $Rb_7M_{12}Pn_{12}$, and $Rb_7M_4M'_8Pn_{12}$ (M, M' = Mn, Zn, Cd; Pn = As, Sb) under the same synthetic conditions as above were unsuccessful.

3.2.2. Structure Determination

Single crystals were mounted within small droplets of paraffin oil on glass fibers and placed under a cold nitrogen gas stream on a Bruker PLATFORM diffractometer equipped with a SMART APEX II CCD detector and a Mo $K\alpha$ radiation source. Intensity data were collected at –100 °C using ω scans with a scan width of 0.3° and an exposure time of 12–20 s per frame at 6–7 different ϕ angles. Face-indexed numerical absorption corrections were applied. Structure solution and refinement were carried out with use of the SHELXTL (version 6.12) program package.[24] Full crystallographic details and interatomic distances are listed in **Tables A 2-2 to A 2-4** in **Appendix 2**. **Table 3-1** gives abbreviated details of the crystallographic data. **Table 3-2** listing atomic coordinates and equivalent isotropic displacement parameters are provided in the main text to facilitate discussion of the structure determinations below. **Table 3-3** lists ranges of interatomic distances.

Table 3-1. Crystallographic data for $Rb_4Zn_7As_7$, $Rb_4Mn_{3.5}Zn_{3.5}Sb_7$, $Rb_7Mn_{12}Sb_{12}$, and $Rb_7Mn_4Cd_8Sb_{12}$

	$\mathbf{Rb_4Zn_7As_7}$	$\mathbf{Rb_4Mn_{3.4(1)}Zn_{3.6(1)}Sb_7}$	$\mathbf{Rb_7Mn_{12}Sb_{12}}$	$\mathbf{Rb_7Mn_{4.2(1)}Cd_{7.8(1)}Sb_{12}}$
formula mass (amu)	1323.91	1615.22	2718.57	3178.25
space group	*Cmcm* (No. 63)	*Cmcm* (No. 63)	*C*2/*m* (No. 12)	*C*2/*m* (No. 12)
a (Å)	4.1883(4)	4.3911(8)	26.544(12)	27.009(4)
b (Å)	24.844(2)	26.546(5)	4.448(2)	4.5752(7)
c (Å)	17.6056(17)	18.743(4)	16.676(8)	16.727(3)
β (°)	90	90	103.183(8)	103.221(2)
V (Å^3)	1831.9(3)	2184.7(7)	1917(2)	2012.2(5)
Z	4	4	2	2
ρ_{calcd} (g cm^{-3})	4.800	4.911	4.710	5.246
T (K)	173(2)	173(2)	173(2)	173(2)
radiation	graphite monochromated Mo $K\alpha$, λ = 0.71073 Å			
μ (mm^{-1})	32.09	23.04	20.91	21.63
$R(F)$ [a]	0.061	0.034	0.068	0.034
$R_w(F_o^2)$ [b]	0.161	0.068	0.130	0.065

[a] $R(F) = \sum||F_o| - |F_c|| / \sum|F_o|$ for $F_o^2 > 2\sigma(F_o^2)$. [b] $R_w(F_o^2) = [\sum[w(F_o^2 - F_c^2)^2] / \sum wF_o^4]^{1/2}$; $w^{-1} = [\sigma^2(F_o^2) + (Ap)^2 + Bp]$, where $p = [\max(F_o^2,0) + 2F_c^2] / 3$.

Table 3-2. Atomic coordinates and equivalent isotropic displacement parameters for $Rb_4Zn_7As_7$, $Rb_4Mn_{3.5}Zn_{3.5}Sb_7$, $Rb_7Mn_{12}Sb_{12}$, and $Rb_7Mn_4Cd_8Sb_{12}$

Atom	Wyckoff position	Occupancy	*x*	*y*	*z*	U_{eq} (Å^2) [a]
$Rb_4Zn_7As_7$						
Rb1	8*f*	1	0	0.13577(7)	0.6173(1)	0.0242(4)
Rb2	4*c*	1	0	0.71912(9)	¼	0.0172(4)
Rb3	4*a*	1	0	0	0	0.0345(7)
Zn1	8*f*	1	0	0.14844(8)	0.1023(1)	0.0210(4)
Zn2	8*f*	1	0	0.28286(7)	0.5358(1)	0.0134(3)
Zn3	8*f*	1	0	0.57194(11)	0.1662(1)	0.0374(6)
Zn4	4*c*	1	0	0.00631(15)	¼	0.0509(11)
As1	8*f*	1	0	0.25245(6)	0.1050(1)	0.0132(3)
As2	8*f*	1	0	0.46937(10)	0.1829(2)	0.0671(10)
As3	8*f*	1	0	0.61089(6)	0.0389(1)	0.0147(3)
As4	4*c*	1	0	0.10990(9)	¼	0.0147(4)
$Rb_4Mn_{3.4(1)}Zn_{3.6(1)}Sb_7$						
Rb1	8*f*	1	0	0.13760(3)	0.61505(4)	0.0188(2)
Rb2	4*c*	1	0	0.71850(4)	¼	0.0149(2)
Rb3	4*a*	1	0	0	0	0.0229(2)
*M*1	8*f*	0.22(2) Mn, 0.78(2) Zn	0	0.15102(4)	0.10272(5)	0.0165(3)
*M*2	8*f*	0.59(2) Mn, 0.41(2) Zn	0	0.28362(4)	0.53403(5)	0.0132(3)
*M*3	8*f*	0.40(2) Mn, 0.60(2) Zn	0	0.57193(4)	0.16888(5)	0.0169(3)
*M*4	4*c*	1.00 Mn	0	0.00659(6)	¼	0.0131(3)
Sb1	8*f*	1	0	0.25351(2)	0.10677(3)	0.0123(1)
Sb2	8*f*	1	0	0.46912(2)	0.17359(3)	0.0151(1)
Sb3	8*f*	1	0	0.61074(2)	0.03802(3)	0.0124(1)
Sb4	4*c*	1	0	0.11146(3)	¼	0.0117(1)
$Rb_7Mn_{12}Sb_{12}$						
Rb1	4*i*	1	0.26148(9)	0	0.2902(1)	0.0203(5)
Rb2	4*i*	1	0.37933(8)	0	0.1281(1)	0.0217(5)
Rb3	4*i*	1	0.42081(9)	0	0.4386(1)	0.0263(5)

Rb4	2*b*	1	0	½	0	0.0268(7)
Mn1	4*i*	1	0.09996(12)	0	0.1983(2)	0.0173(7)
Mn2	4*i*	1	0.12592(12)	0	0.3826(2)	0.0158(7)
Mn3	4*i*	1	0.22071(12)	0	0.0400(2)	0.0154(7)
Mn4	4*i*	1	0.28944(12)	0	0.5408(2)	0.0154(7)
Mn5	4*i*	1	0.54519(12)	0	0.2896(2)	0.0146(7)
Mn6	4*i*	1	0.66523(12)	0	0.1226(2)	0.0166(7)
Sb1	4*i*	1	0.00416(6)	0	0.7985(1)	0.0183(3)
Sb2	4*i*	1	0.02101(6)	0	0.3790(1)	0.0183(3)
Sb3	4*i*	1	0.11533(5)	0	0.0442(1)	0.0152(3)
Sb4	4*i*	1	0.18426(5)	0	0.5387(1)	0.0161(3)
Sb5	4*i*	1	0.65123(5)	0	0.2915(1)	0.0141(3)
Sb6	4*i*	1	0.76950(5)	0	0.1230(1)	0.0155(3)
$Rb_7Mn_{4.2(1)}Cd_{7.8(1)}Sb_{12}$						
Rb1	4*i*	1	0.24992(3)	0	0.28824(5)	0.0158(2)
Rb2	4*i*	1	0.37660(3)	0	0.13414(5)	0.0186(2)
Rb3	4*i*	1	0.41946(3)	0	0.43942(6)	0.0217(2)
Rb4	2*b*	1	0	½	0	0.0283(3)
*M*1	4*i*	0.135(5) Mn, 0.865(5) Cd	0.08959(3)	0	0.18721(4)	0.0173(2)
*M*2	4*i*	0.282(5) Mn, 0.718(5) Cd	0.12215(3)	0	0.39183(4)	0.0150(2)
*M*3	4*i*	0.345(5) Mn, 0.655(5) Cd	0.22206(3)	0	0.03947(4)	0.0132(2)
*M*4	4*i*	0.239(5) Mn, 0.761(5) Cd	0.29067(3)	0	0.53668(4)	0.0138(2)
*M*5	4*i*	1.00 Mn	0.53803(5)	0	0.29253(8)	0.0130(2)
*M*6	4*i*	0.105(5) Mn, 0.895(5) Cd	0.66281(2)	0	0.11603(4)	0.0142(2)
Sb1	4*i*	1	0.01209(2)	0	0.79352(4)	0.0162(1)
Sb2	4*i*	1	0.01598(2)	0	0.38242(3)	0.0151(1)
Sb3	4*i*	1	0.11147(2)	0	0.03292(3)	0.0136(1)
Sb4	4*i*	1	0.18519(2)	0	0.55002(3)	0.0144(1)
Sb5	4*i*	1	0.64346(2)	0	0.29102(3)	0.0113(1)
Sb6	4*i*	1	0.77067(2)	0	0.12948(3)	0.0137(1)

[a] U_{eq} is defined as one-third of the trace of the orthogonalized U_{ij} tensor.

Table 3-3. Ranges of interatomic distances (Å) for $Rb_4Zn_7As_7$, $Rb_4Mn_{3.5}Zn_{3.5}Sb_7$, $Rb_7Mn_{12}Sb_{12}$, and $Rb_7Mn_4Cd_8Sb_{12}$

	$Rb_4Zn_7As_7$	**$Rb_4Mn_{3.5}Zn_{3.5}Sb_7$**
Rb1–*Pn* (CN6)	3.485(1)–3.541(2)	3.633(1)–3.748(1)
Rb2–*Pn* (CN6)	3.405(1)–3.428(3)	3.590(1)–3.591(1)
Rb3–*Pn* (CN8)	3.528(1)–3.916(3)	3.738(1)–4.010(1)
*M*1–*Pn* (CN4)	2.549(1)–2.772(4)	2.722(1)–2.953(1)
*M*2–*Pn* (CN4)	2.576(1)–2.640(2)	2.758(1)–2.806(1)
*M*3–*Pn* (CN4)	2.441(3)–2.729(2)	2.660(1)–2.870(1)
*M*4–*Pn* (CN5)	2.574(4)–2.574(2)	2.784(2)–2.804(1)
M–*M*	2.940(2)–3.044(2)	3.041(2)–3.281(1)
*Pn*2–*Pn*2	2.363(7)	2.864(1)
	$Rb_7Mn_{12}Sb_{12}$	**$Rb_7Mn_4Cd_8Sb_{12}$**
Rb1–Sb (CN6)	3.611(2)–3.680(2)	3.644(1)–3.683(1)
Rb2–Sb (CN6)	3.652(2)–3.779(2)	3.650(1)–3.751(1)
Rb3–Sb (CN6)	3.653(3)–3.799(3)	3.672(1)–3.844(1)
Rb4–Sb (CN8)	3.719(2)–4.051(2)	3.720(1)–4.217(1)
*M*1–Sb (CN4)	2.692(4)–2.872(2)	2.776(1)–3.035(1)
*M*2–Sb (CN4)	2.709(3)–2.858(2)	2.800(1)–2.975(1)
*M*3–Sb (CN4)	2.779(2)–2.814(4)	2.877(1)–2.964(1)
*M*4–Sb (CN4)	2.759(2)–2.880(3)	2.862(1)–3.021(1)
*M*5–Sb (CN5)	2.808(4)–2.832(2)	2.853(1)–2.874(1)
*M*6–Sb (CN4)	2.761(2)–2.924(4)	2.865(1)–3.089(1)
M–*M*	2.993(5)–3.246(3)	3.188(1)–3.412(1)
Sb1–Sb2	2.883(2)	2.866(1)

On the basis of Laue symmetry, systematic absences, and intensity statistics, the space groups chosen were either *Cmcm* for $Rb_4Zn_7As_7$ and $Rb_4Mn_{3.5}Zn_{3.5}Sb_7$, or *C*2/*m* for $Rb_7Mn_{12}Sb_{12}$ and $Rb_7Mn_4Cd_8Sb_{12}$. In general, structure solution and refinement for the ternary compounds $Rb_4Zn_7As_7$ and $Rb_7Mn_{12}Sb_{12}$ were straightforward, but the treatment of disorder in the quaternary compounds $Rb_4Mn_{3.5}Zn_{3.5}Sb_7$ and $Rb_7Mn_4Cd_8Sb_{12}$ required special attention. In $Rb_4Mn_{3.5}Zn_{3.5}Sb_7$, four sites for the *M* component were identified. Refinements were performed in which each *M* site was allowed to be occupied by a mixture of Mn and Zn atoms, with the constraint that the occupancies sum to unity but with no restriction placed on the overall formula. The occupancies converged to 0.22(2) Mn / 0.78(2) Zn in *M*1, 0.60(2) Mn / 0.40(2) Zn in *M*2, and 0.40(2) Mn / 0.60(2) Zn in *M*3; in contrast, *M*4 tended towards an occupancy of >1.00 Mn (accompanied by a physically meaningless negative Zn occupancy), which we interpret as evidence for this site being exclusively occupied by Mn atoms. If Zn mixing is not allowed in the *M*4 site, its occupancy converges to 0.999(6) Mn. These refinements are stable and converge to the same occupancies when different starting values are introduced. In a similar manner, six *M* sites were available in $Rb_7Mn_4Cd_8Sb_{12}$ to be occupied by mixtures of Mn and Cd atoms. Here, the occupancies converged to 0.134(5) Mn / 0.866(5) Cd in *M*1, 0.280(5) Mn / 0.720(5) Cd in *M*2, 0.343(5) Mn / 0.657(5) Cd in *M*3, 0.237(5) Mn / 0.763(5) Cd in *M*4, 0.986(5) Mn / 0.014(5) Cd in *M*5, and 0.106(5) Mn / 0.894(5) Cd in *M*6. The *M*5 site was thus assigned to be exclusively occupied by Mn atoms. The resulting formulas from these refinements were "$Rb_4Mn_{3.4(1)}Zn_{3.6(1)}Sb_7$" and "$Rb_7Mn_{4.2(1)}Cd_{7.8(1)}Sb_{12}$", which are consistent with the loaded

compositions and the EDX analyses. For brevity, we use the simplified formulas $Rb_4Mn_{3.5}Zn_{3.5}Sb_7$ and $Rb_7Mn_4Cd_8Sb_{12}$ in subsequent discussion.

The displacement parameters for atoms in these four structures were reasonable (with U_{eq} values generally ranging from 0.01 to 0.03 Å^2), but they appeared to be somewhat elevated for the Zn4 site (0.051(1) Å^2) and especially the As2 site (0.067(1) Å^2) in $Rb_4Zn_7As_7$. However, the displacement parameters were not significantly reduced when partial occupancy was introduced into these sites (0.043(1) Å^2 for Zn4 at 0.89(1) occupancy and 0.054(1) Å^2 for As2 at 0.85(1) occupancy). Refinements of the occupancies of all other sites confirmed that they are fully occupied. A comparison of the fully stoichiometric model "$Rb_4Zn_7As_7$" and the substoichiometric model "$Rb_4Zn_{6.90(1)}As_{6.70(2)}$" is provided in **Table A 2-5** in **Appendix 2**. Because the agreement factors do improve ($R(F)$ for $F_o^2 > 2\sigma(F_o^2)$ decreasing from 0.0614 to 0.0565) upon introduction of two occupancy parameters, we cannot definitively rule out the substoichiometric model. In both cases, the As2 site exhibits a somewhat elongated displacement ellipsoid but refinements in which it was split into two sites were unstable. Closer inspection suggests that this feature is likely intrinsic to the structure, given the unusual coordination environments around these atoms, as discussed later.

Atomic positions were standardized with the program STRUCTURE TIDY.[25] Further data, in the form of crystallographic information files (CIFs) are available in CSD number 426459 to 426462.

3.2.3. Band Structure Calculations

Tight-binding linear muffin tin orbital band structure calculations were performed on $Rb_4Zn_7As_7$ and $Rb_7Mn_{12}Sb_{12}$ within the local density and atomic spheres approximation with use of the Stuttgart TB-LMTO-ASA program (version 4.7).[26] Cell parameters and atomic positions were taken directly from the refined crystal structures. The basis sets included Rb 5s/5p/4d/4f, Mn 4s/4p/3d, Zn 4s/4p/3d, As 4s/4p/4d, and Sb 5s/5p/4d/4f orbitals, with the Rb 5p/4d/4f, As 4d, and Sb 5d/4f orbitals being downfolded. Integrations in reciprocal space were carried out with an improved tetrahedron method over 63 ($Rb_4Zn_7As_7$) or 78 ($Rb_7Mn_{12}Sb_{12}$) irreducible *k* points within the first Brillouin zone.

3.3. Results and Discussion

The four rubidium transition-metal pnictides prepared here belong to two series adopting new orthorhombic ($Rb_4Zn_7As_7$ and $Rb_4Mn_{3.5}Zn_{3.5}Sb_7$ in space group *Cmcm*) and monoclinic structures ($Rb_7Mn_{12}Sb_{12}$ and $Rb_7Mn_4Cd_8Sb_{12}$ in space group *C*2/*m*), with the ternary compounds conveniently serving as names of the structure types. There are 3 Rb, 4 *M*, and 4 *Pn* sites in the $Rb_4Zn_7As_7$-type structure, and 4 Rb, 6 *M*, and 6 *Pn* sites in the $Rb_7Mn_{12}Sb_{12}$-type structure. Viewed down the short crystallographic axis (~4 Å), these closely related structures consist of corrugated anionic layers separated by Rb cations (**Figure 3-1**). In $Rb_4Zn_7As_7$, the layers extend parallel to the *ac*-plane and stack along the *b*-direction; in $Rb_7Mn_{12}Sb_{12}$, they extend parallel to the *bc*-plane and stack along the *a*-direction. These layers are built up of *M*-centred tetrahedra, which share edges to form infinite four- or six-tetrahedra-wide ribbons, as well as *M*-centred square pyramids, which share opposite edges to form an infinite chain (**Figure 3-2a**). The ribbons of tetrahedra are

connected in a zigzag-like manner, and the chains of square pyramids are located at the hinges. The layers contain a uniform sequence of six-tetrahedra-wide ribbons in $Rb_4Zn_7As_7$ but an alternating sequence of four- and six-tetrahedra-wide ribbons in $Rb_7Mn_{12}Sb_{12}$ (**Figure 3-2b**), resulting in an oblique layer stacking associated with the lower monoclinic symmetry in the latter. Such ribbons, of course, can be considered to be fragments of PbO-type layers of edge-sharing tetrahedra which are common in many structures.[27]

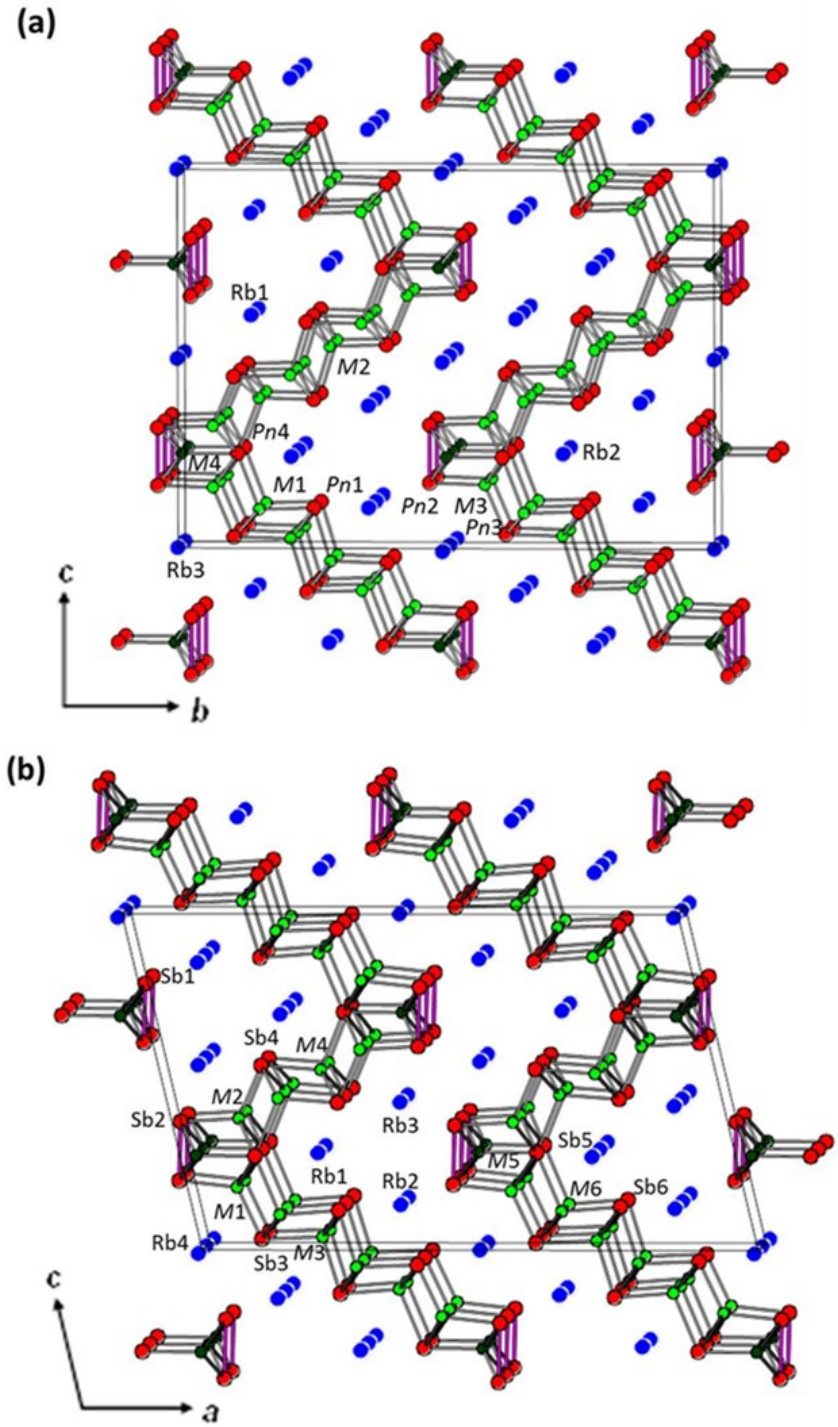

Figure 3-1. (a) Orthorhombic $Rb_4Zn_7As_7$-type and (b) monoclinic $Rb_7Mn_{12}Sb_{12}$-type structures, viewed down the short-axis directions. The large blue circles are Rb atoms, the small green circles are transition-metal atoms (*M* = Mn, Zn, Cd), and the medium red circles are pnicogen atoms (*Pn* = As, Sb).

In the quaternary compounds $Rb_4Mn_{3.5}Zn_{3.5}Sb_7$ and $Rb_7Mn_4Cd_8Sb_{12}$, the presence of two different transition metals introduces the possibility of disorder within the tetrahedral or square pyramidal *M* sites. Structural refinements indicate that the square pyramidal sites are occupied exclusively by Mn atoms in both compounds, whereas the tetrahedral sites are occupied by a mixture of Mn and Zn or Cd atoms. The site distribution within the tetrahedral sites is irregular. In order of decreasing occupancy, the Zn atoms prefer the *M*1 (0.78), *M*3 (0.60), and *M*2 (0.41) tetrahedral sites in $Rb_4Mn_{3.5}Zn_{3.5}Sb_7$. In contrast, the site preference of the Cd atoms is more muted in $Rb_7Mn_4Cd_8Sb_{12}$: *M*6 (0.90), *M*1 (0.86), *M*4 (0.76), *M*2 (0.72), *M*3 (0.66). There does not appear to be a simple trend that relates the site distribution to the patterns of tetrahedra within the ribbons (**Figure 3-2b**) or size effects as gauged by the observed bond distances (**Table 3-2**). On the basis of Pauling metallic radii (R_1 of 2.39 Å for Mn, 2.42 Å for Zn, and 2.59 Å for Cd)[28] or other scales of radii, it is difficult to distinguish between the similar-sized Mn and Zn atoms, but it may be possible to identify the larger Cd atoms. In the parent ternary structures ($Rb_4Zn_7As_7$, $Rb_7Mn_{12}Sb_{12}$) as well as in $Rb_4Mn_{3.5}Zn_{3.5}Sb_7$, there is no obvious segregation of *M*–*Pn* bond lengths within the tetrahedral or square pyramidal sites. In $Rb_7Mn_4Cd_8Sb_{12}$, the average *M*–Sb bond length within the square pyramidal site occupied by Mn atoms is only marginally shorter (2.87 Å) compared with those within the tetrahedral sites occupied by a mixture of Mn and Cd atoms (2.89–2.92 Å).

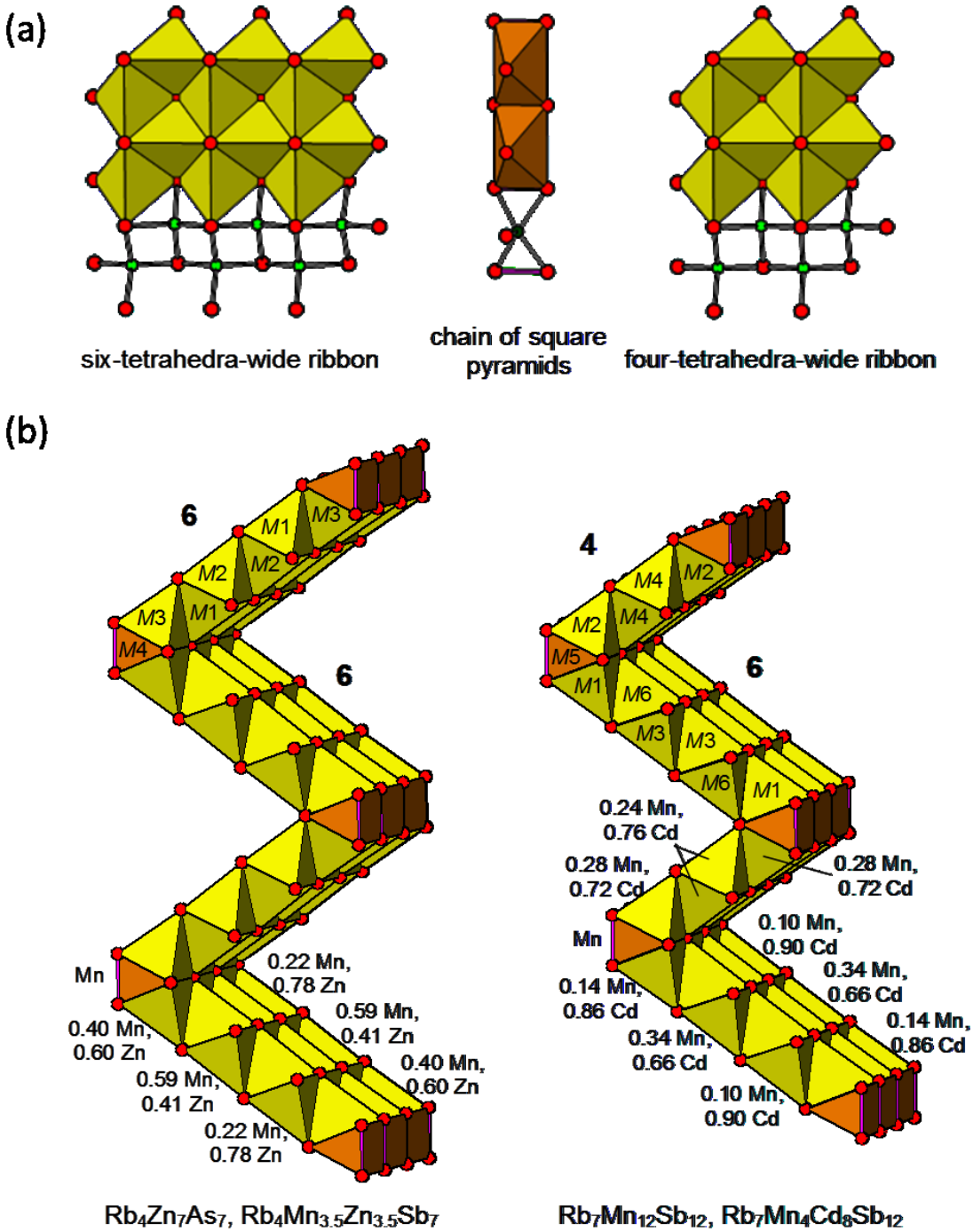

Figure 3-2. (a) Building units composed of edge-sharing M-centred tetrahedra or square pyramids. (b) Connectivity of building units to form the corrugated anionic layers found in the $Rb_4Zn_7As_7$- (in 6–6–… sequence) and $Rb_7Mn_{12}Sb_{12}$-type structures (in 4–6–… sequence) Site occupancies for the *M* sites are shown for the quaternary derivatives $Rb_4Mn_{3.5}Zn_{3.5}Sb_7$ (left) and $Rb_7Mn_4Cd_8Sb_{12}$ (right).

Some of the coordination environments around the Rb atoms are unusual (**Figure 3-3**). Although a trigonal prism (CN6) is a common geometry, it becomes highly distorted around Rb1 in the $Rb_4Zn_7As_7$-type structure and around Rb2 and Rb3 in the $Rb_7Mn_{12}Sb_{12}$-type structure, with the central atom displaced nearly on a quadrilateral face. Remarkably, there are no close contacts to any surrounding atoms above this face until another Rb atom about 5 Å away. The coordination geometry around Rb3 in the $Rb_4Zn_7As_7$-type structure and around Rb4 in the $Rb_7Mn_{12}Sb_{12}$-type structure appears at first glance to be approximately cubic (CN8). However, the distances to four of the eight surrounding As or Sb atoms are very long (more than 4 Å in the antimonides), so the coordination may be more properly described as [4+4]. In the course of the structure determination, it was noted that the displacement parameters for the As2 site in $Rb_4Zn_7As_7$ were elevated. This As2 site is common to the asymmetric coordination around Rb1 and the long distances to Rb3. Strong As–As homoatomic bonding develops to form an As_2 pair (2.36 Å), which is responsible for the distortion of the Mn-centred pyramids so that the base becomes compressed into a rectangle (**Figure 3-2a**). Close inspection of the displacement ellipsoids around the As2 site suggests a tendency to shift towards the open quadrilateral face of Rb1-centred trigonal prism, reducing the asymmetry, and to expand the As_2 pair. The As–As distance in this pair is close to some of the shortest values observed in other polyarsenides (e.g., 2.32–2.43 Å in Rb_3As_7, 2.38–2.48 Å in Rb_3As_{11}).[29,30] Vibrational spectroscopy to probe for the presence of this As–As pair would be interesting to perform, but is unfortunately precluded here because of the high air-sensitivity of the compounds. Similarly, Sb_2 pairs are present in the title antimonides, but the Sb–Sb distances (2.86–2.88 Å) are more typical of the median values

found in many polyantimonides.[31] The Sb2 site in $Rb_4Mn_{3.5}Zn_{3.5}Sb_7$ also exhibits slightly more elevated displacement parameters but the effect is less pronounced compared to the As2 site in $Rb_4Zn_7As_7$.

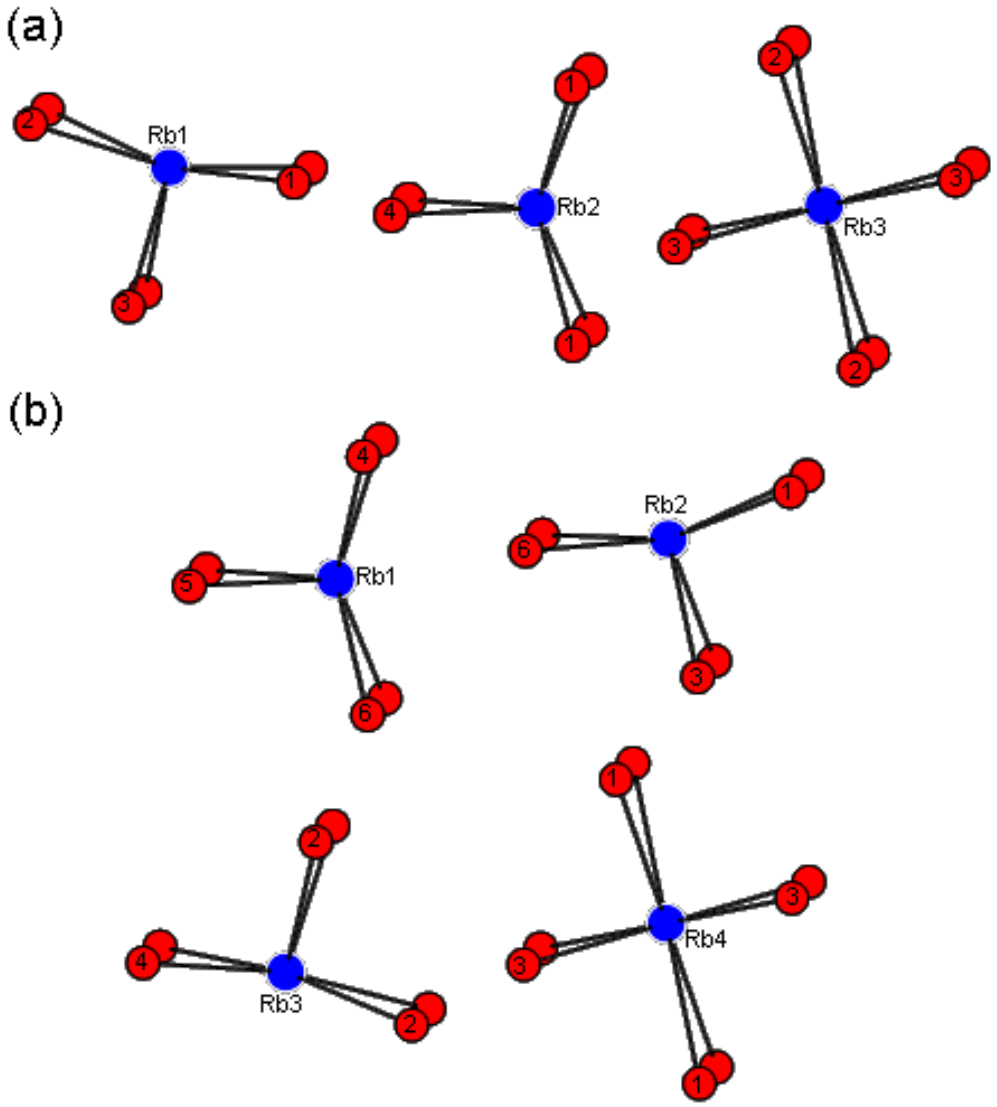

Figure 3-3. Coordination environments around Rb atoms in (a) $Rb_4Zn_7As_7$- and (b) $Rb_7Mn_{12}Sb_{12}$-type structures. Rb1 is coordinated to one of the atoms in the As_2 pair in the $Rb_4Zn_7As_7$-type structure; Rb2 and Rb3 are each coordinated to one of the atoms in the Sb_2 pair in the $Rb_7Mn_{12}Sb_{12}$-type structure.

The structures resemble those of many other Zintl phases whose frameworks are built up by condensing tetrahedral units.[32] Normally, Zintl phases are electronically charge-balanced with closed-shell configurations for all atoms. Relatively rarely, however, electron-deficient (e.g., $Ba_5In_4Bi_5$)[33] or electron-excessive phases (e.g., $Ba_7Ga_4Sb_9$)[34,35] have been identified; they are interesting because they provide test cases for probing the limits of the Zintl concept. In the title compounds presented here, any reasonable assignment of charges leads to the conclusion of an electron deficiency. The transition-metal atoms (Mn, Zn, Cd) are assumed to be divalent. The *Pn*–*Pn* contacts within the Pn_2 pairs appear to correspond to normal single-bond distances, so these *Pn* atoms are assumed to be not fully reduced, each with a formal charge of 2–. The formulations $(Rb^+)_4(M^{2+})_7(h^+)(Pn^{2-})_2(Pn^{3-})_5$ and $(Rb^+)_7(M^{2+})_{12}(h^+)(Sb^{2-})_4(Sb^{3-})_8$, where h^+ represents a hole, suggests that these compounds are one electron short of complete charge balance. However, it is important to consider arguments that can be made against the presence of an electron deficiency. First, the electron deficiency could be eliminated if vacancies are introduced into some of the atom sites. In the only all-Zn compound prepared here, $Rb_4Zn_7As_7$, refinement of site occupancies suggests a substoichiometric model in which the Zn4 and As2 sites may be partially occupied. Nevertheless, the resulting formula, "$Rb_4Zn_{6.90(1)}As_{6.70(2)}$", still leads to an electron deficiency, albeit diminished, of 0.6 e^-. Second, the square pyramidal sites (*M*4 in the $Rb_4Zn_7As_7$-type and *M*5 in the $Rb_7Mn_{12}Sb_{12}$-type structures) are always the ones that are exlusively occupied by Mn-atoms in the quaternary derivatives ($Rb_4Mn_{3.5}Zn_{3.5}Sb_7$ and $Rb_7Mn_4Cd_8Sb_{12}$). It is tempting to assign Mn atoms that occupy these square pyramidal sites to be trivalent Mn^{3+} species, which would recover charge balance in the formulas. An

appropriate basis for comparison is to ternary Mn-containing Zintl phases *A*–Mn–Sb (*A* = electropositive metal), for which *A*MnSb (*A* = Li–Cs),[6–8] *A*$MnSb_2$ (*A* = Ca, Sr, Ba),[36,37] *A*Mn_2Sb_2 (*A* = Ca, Sr, Ba, Yb),[38–42] $A_{14}MnSb_{11}$ (*A* = Ca, Sr, Ba, Yb),[2–4,43] $A_{21}Mn_4Sb_{18}$ (*A* = Ca, Sr),[44–46] and $Yb_9Mn_{4+x}Sb_9$ [47] are known. Except for $A_{14}MnSb_{11}$, all these compounds contain formally divalent Mn^{2+} species, in tetrahedral and sometimes square pyramidal coordination (in *A*MnSb). The case of $A_{14}MnSb_{11}$ is interesting: the initial assignment of trivalent Mn^{3+} species was subsequently overturned in favour of divalent Mn^{2+} species, as supported by X-ray magnetic circular dichroism measurements on $Yb_{14}MnSb_{11}$.[48] Comparison of Mn–Sb bond lengths do not provide much guidance because they fall in the same range (2.7–2.9 Å) among these compounds. Experimental measurements (such as magnetic susceptibility or X-ray spectroscopy) to probe the oxidation state of Mn in the title compounds would be helpful, but are hampered by their high air-sensitivity. There is growing consensus in the literature that high oxidation states for Mn are simply unlikely in antimonides.[41]

To investigate the electronic structure in more detail, band structure calculations were performed on the parent ternary compounds $Rb_4Zn_7As_7$ and $Rb_7Mn_{12}Sb_{12}$, for which the problem of metal site disorder can be avoided (**Figure 3-4**). Inspection of the density of states (DOS) curves shows that the Rb-based states are mostly empty and found well above the Fermi level; below the Fermi level, the Rb projection is not zero but is very small. As gauged by the integrated crystal orbital Hamilton population values (–ICOHP), the covalent portion of Rb–*Pn* bonding interactions is nearly negligible in both compounds (–ICOHP of 0.07 eV/bond for Rb–As contacts in $Rb_4Zn_7As_7$ and 0.05 eV/bond for Rb–Sb contacts in

$Rb_7Mn_{12}Sb_{12}$). Thus, the usual notion is confirmed that the highly electropositive alkali-metal atoms tend to transfer their valence electrons to the rest of the anionic framework. The bonding around the [4+4]-coordinated Rb3 atoms in $Rb_4Zn_7As_7$ or the Rb4 atoms in $Rb_7Mn_{12}Sb_{12}$ can also be evaluated. In both compounds, the four longer Rb–*Pn* distances are confirmed to be essentially non-bonding (–ICOHP of <0.02 eV/bond) compared to the four shorter ones (–ICOHP of 0.07–0.08 eV/bond), suggesting that the coordination geometry should really be described as square planar.

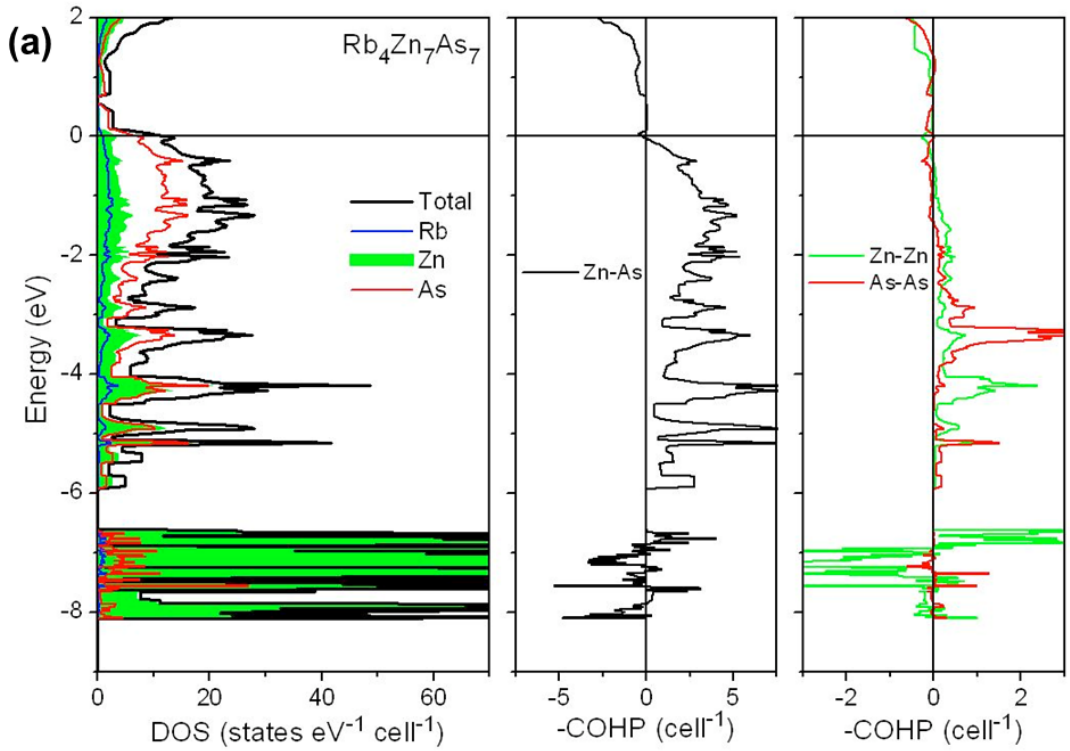

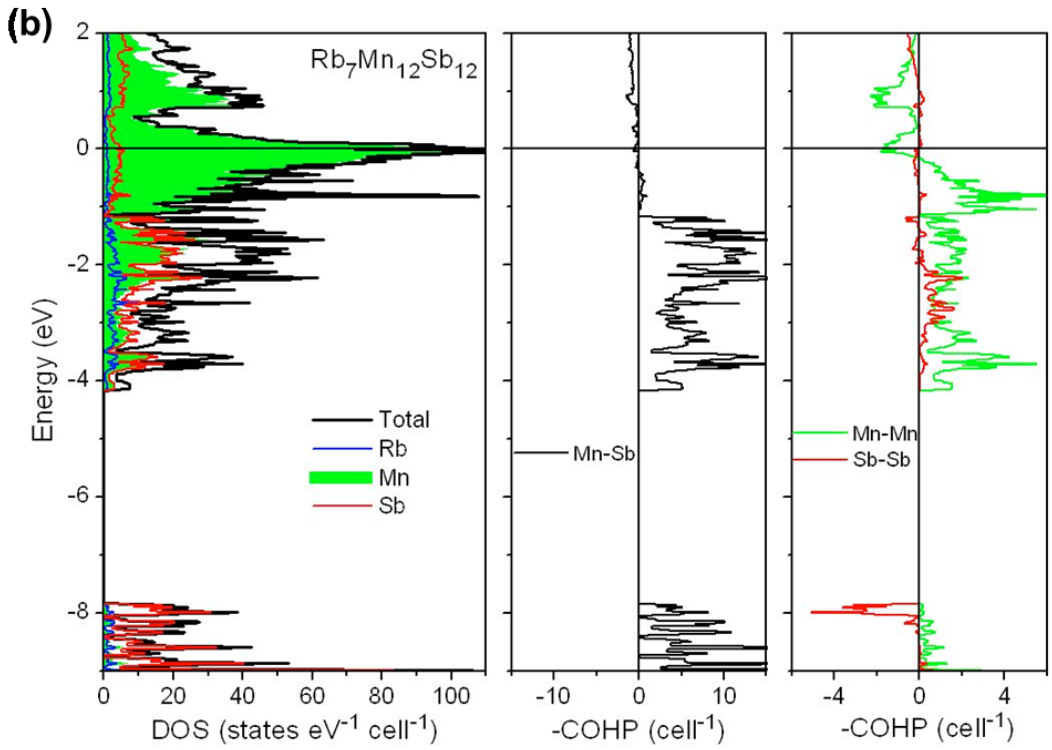

Figure 3-4. Density of states with atomic projections (left) and crystal orbital Hamilton population (COHP) curves (centre and right) for (a) $Rb_4Zn_7As_7$ and (b) $Rb_7Mn_{12}Sb_{12}$. The horizontal line at 0 eV marks the Fermi level.

In $Rb_4Zn_7As_7$ (**Figure 3-4a**), the filled Zn 3d states are clustered mostly in a narrow band found well below the Fermi level, from –8 to –7 eV. The valence band appears as a wide manifold extending from –6 eV to +0.5 eV and results largely from mixing of Zn hybridized 4s/4p states with As 4p states; it is separated from the conduction band at higher energies by a small gap of 0.1 eV. The Zn–As bonding interactions are perfectly optimized up to the Fermi level and they constitute the dominant contributions (>78% of the bonding energy in the entire structure), with an –ICOHP value of 1.11 eV/bond. The lowering of the Fermi level from the band gap at +0.5 eV to just below the top of the valence band at 0 eV corresponds precisely to the one-electron deficiency identified earlier. Interestingly, the

origin of this electron deficiency is derived from As-based states, which constitute most of the DOS near the Fermi level. The occurrence of an As_2 pair in the structure results in bands that mimic the usual pattern of molecular orbitals for diatomic molecules. The σ_s and σ_s* levels are found very deep in energy at –13 and –10 eV (not shown). The bonding σ_p and π_p levels are separated from the antibonding π_p* and σ_p* levels at around –1.5 eV. The As–As COHP curve reveals the large bonding spike at –3.5 eV; the corresponding antibonding spike starts near +2 eV and maximizes at +3 eV above the scale shown. A singly bonded $(As_2)^{4-}$ pair is isoelectronic to a neutral diatomic halogen molecule in which only the σ_p* levels are unoccupied. The implication of the electron deficiency in $Rb_4Zn_7As_7$ is that the antibonding π_p* levels are slightly depopulated, which strengthens the As–As bond within this pair and accounts for the short 2.36 Å distance observed experimentally. The large –ICOHP value of 2.58 eV/bond for this As–As contact is also consistent with strong bonding. The other type of homoatomic bonding that could potentially occur in this structure comes from Zn–Zn contacts in the range of 2.9–3.0 Å, presumably through so-called d^{10}-d^{10} interactions in which hybridization with s orbitals must be invoked.[49] Inspection of the Zn–Zn COHP curve confirms that some bonding is indeed present, but it is rather weak, with an –ICOHP value of 0.15 eV/bond.

In $Rb_7Mn_{12}Sb_{12}$, the electronic situation is quite different because the Mn component introduces a partially filled 3d-subshell, which the Fermi level cuts in the DOS (**Figure 3-4b**). Moreover, the gap between the valence and conduction bands has closed to become a pseudogap near +0.5 eV. The crystal field splitting experienced by Mn atoms, which are mostly in tetrahedral coordination geometries, is clearly manifested in the segregation of *e*

and t_2 levels, the former mostly participating in Mn–Sb (–4 to –1 eV) and the latter in Mn–Mn bonding interactions (–1 eV upwards), as seen in the COHP curves. As expected, the Mn–Sb interactions are strong (–ICOHP of 1.46 eV/bond) but now the Mn–Mn interactions also become significant (–ICOHP of 0.43 eV/bond). Sb–Sb interactions are present, with a similar pattern in the COHP curve as before (the σ_s* levels are now visible at –8 eV) and a resulting –ICOHP value of 1.37 eV/bond. It appears that the driving force for the electron deficiency is no longer the depletion of antibonding Sb–Sb levels, but rather Mn–Mn ones, which dominate near the Fermi level. Spin-polarized calculations will be important to perform to ascertain if the Mn-based states shift away from the Fermi level, depending on the magnetic properties yet to be determined for this compound.

The site preference (or "colouring problem") within the mixed-metal compounds $Rb_4Mn_{3.5}Zn_{3.5}Sb_7$ and $Rb_7Mn_4Cd_8Sb_{12}$ is not easy to rationalize. Apart from the existent compound $Rb_7Mn_{12}Sb_{12}$ which was already treated above, additional band structure calculations were performed on model compounds that would correspond to the ternary end-members of these quaternary systems but without changing the structural parameters, i.e. "$Rb_4Mn_7Sb_7$", "$Rb_4Zn_7Sb_7$", and "$Rb_7Cd_{12}Sb_{12}$" (**Figure A 2-3** in **Appendix 2**). The most straightforward way to assess site preferences is to compare the integrated electron densities within the Wigner-Seitz spheres surrounding specified atoms, called QVAL in the LMTO calculations performed here.[50] For the metal sites in $Rb_4Mn_7Sb_7$ and $Rb_4Zn_7Sb_7$, these values in decreasing order are (respectively for the two models): 6.78 / 11.76 for *M*4, 6.75 / 11.69 for *M*2, 6.72 / 11.54 for *M*1, and 6.56 / 11.47 for *M*3. Sites with higher QVAL are preferred by more electronegative atoms (or alternatively, by less easily ionized atoms),

namely Zn in this case. However, the trend in QVAL is almost the reverse to the observed occupancy of Zn atoms in $Rb_4Mn_{3.5}Zn_{3.5}Sb_7$: 0.00 in *M*4, 0.41 in *M*2, 0.60 in *M*3, and 0.78 in *M*1. A similar assessment of QVAL for the metal sites in $Rb_7Mn_{12}Sb_{12}$ and $Rb_7Cd_{12}Sb_{12}$ also leads to inconsistency with the observed occupancies in $Rb_7Mn_4Cd_8Sb_{12}$. It would be helpful to perform higher-level calculations in which the total energies of alternative ordered model structures are compared. One crystal chemical principle which does seem to be respected is that more electronegative atoms prefer sites with lower CNs, accounting for the observation that the tetrahedral sites suffer from Mn/Zn or Mn/Cd disorder while the square pyramidal sites are restricted to Mn atoms only. Investigations of other members with different Mn:Zn or Mn:Cd ratios will also be important to understand trends in the site preferences and to establish limits of solid solubility.

3.4. Conclusions

Orthorhombic $Rb_4Zn_7As_7$ and monoclinic $Rb_7Mn_{12}Sb_{12}$ represent new structure types built up by connecting ribbons of edge-sharing metal-centred tetrahedra in different ways to generated corrugated anionic layers. This *aufbau* suggests possibilities for envisioning compounds belonging to homologous series in which the anionic layers contain analogous ribbons but of different widths. Given the preparation of quaternary mixed-metal derivatives $Rb_4Mn_{3.5}Zn_{3.5}Sb_7$ and $Rb_7Mn_4Cd_8Sb_{12}$, it will be necessary to evaluate the extent of the phase width and to target missing ternary end-members; these investigations may also shed light on the site preferences of transition-metal atoms. These syntheses may be challenging because there exist several compounds close in composition to the targeted compounds that may be more thermodynamically stable under the conditions used. The origin of the one-

electron deficiency can be traced to the depopulation of antibonding *Pn–Pn* states in the $Rb_4Zn_7As_7$ or of antibonding *M–M* states in $Rb_7Mn_{12}Sb_{12}$; in effect, an internal oxidation of the *Pn* or *M* atoms takes place. Metallic behaviour is predicted for these compounds. The Mn-containing compounds will be especially interesting to examine for their magnetic properties.

To further explore the structural variety of alkali-metal pnictides, we have carried out investigations in which the second component *M* is now replaced by a tetrel in ternary systems *A–Tt–Pn*, as reported in the next two chapters.

3.5. References

1. Kauzlarich, S. M. In *Chemistry, Structure, and Bonding of Zintl Phases and Ions*; Kauzlarich, S. M., Ed.; VCH: New York, 1996; pp 245–274.
2. Fisher, I. R.; Wiener, T. A.; Bud'ko, S. L.; Canfield, P. C.; Chan, J. Y.; Kauzlarich, S. M. *Phys. Rev. B* **1999**, *59*, 13829–13834.
3. Brown, S. R.; Kauzlarich, S. M.; Gascoin, F.; Snyder, G. J. *Chem. Mater.* **2006**, *18*, 1873–1877.
4. Kauzlarich, S. M.; Brown, S. R.; Snyder, G. J. *Dalton Trans.* **2007**, 2009–2107.
5. Juza, R.; Bohmann, T. *Z. Anorg. Allg. Chem.* **1961**, *308*, 159–178.
6. Achenbach, G.; Schuster, H.-U. *Z. Anorg. Allg. Chem.* **1981**, *475*, 9–17.
7. Bronger, W.; Müller, P.; Höppner, R.; Schuster, H.-U. *Z. Anorg. Allg. Chem.* **1986**, *539*, 175–182.
8. Schucht, F.; Dascoulidou, A.; Müller, R.; Jung, W.; Schuster, H.-U.; Bronger, W.; Müller, P. *Z. Anorg. Allg. Chem.* **1999**, *625*, 31–36.
9. Liu, Y.; Wu, L.-M.; Li, L.-H.; Du, S.-W.; Corbett, J. D.; Chen, L. *Angew. Chem. Int. Ed.* **2009**, *48*, 5305–5308.
10. He, H.; Zevalkink, A.; Gibbs, Z. M.; Snyder, G. J.; Bobev, S. *Chem. Mater.* **2012**, *24*, 3596–3603.
11. Madsen, G. K. H. *J. Am. Chem. Soc.* **2006**, *128*, 12148–12146.
12. Toberer, E. S.; May, A. F.; Scanlon, C. J.; Snyder, G. J. *J. Appl. Phys.* **2009**, *105*, 063701-1–063701-5.
13. Li, L.-H.; Chen, L.; Li, J.-Q.; Wu, L.-M. *Chem. Mater.* **2010**, *22*, 4007–4018.

14. Yan, B.; Müchler, L.; Felser, C. *Phys. Rev. Lett.* **2012**, *109*, 116406-1–116406-5.

15. Deng, Z.; Jin, C. Q.; Liu, Q. Q.; Wang, X. C.; Zhu, J. L.; Feng, S. M.; Chen, L. C.; Yu, R. C.; Arguello, C.; Goko, T.; Ning, F.; Zhang, J.; Wang, Y.; Aczel, A. A.; Munsie, T.; Williams, T. J.; Luke, G. M.; Kakeshita, T.; Uchida, S.; Higemoto, W.; Ito, T. U.; Gu, B.; Maekawa, S.; Morris, G. D.; Uemura, Y. J. *Nat. Commun.* **2011**, *2*, 1425-1–1425-5.

16. Zheng, W.-Z.; Wang, P.; Wu, L.-M.; Liu, Y.; Chen, L. *Inorg. Chem.* **2010**, *49*, 5890–5896.

17. He, H.; Tyson, C.; Bobev, S. *Inorg. Chem.* **2011**, *50*, 8375–8383.

18. Stoyko, S. S.; Khatun, M.; Mar, A. *Inorg. Chem.* **2012**, *51*, 9517–9521.

19. He, H.; Stoyko, S. S.; Mar, A.; Bobev, S. *Acta Crystallogr., Sect. C* **2013**, *69*, 455–459.

20. He, H.; Tyson, C.; Bobev, S. *Crystals* **2011**, *1*, 87–98.

21. Khatun, M.; Stoyko, S. S.; Mar, A. *Inorg. Chem.* **2013**, *52*, 3148–3158.

22. Saparov, B.; Saito, M.; Bobev, S. *J. Solid State Chem.* **2011**, *184*, 432–440.

23. Saparov, B.; Broda, M.; Ramanujachary, K. V.; Bobev, S. *Polyhedron* **2010**, *29*, 456–462.

24. Sheldrick, G. M. *SHELXTL*, version 6.12; Bruker AXS Inc.: Madison, WI, 2001.

25. Gelato, L. M.; Parthé, E. *J. Appl. Crystallogr.* **1987**, *20*, 139–143.

26. Tank, R.; Jepsen, O.; Burkhardt, A.; Andersen, O. K. *TB-LMTO-ASA Program*, version 4.7; Max Planck Institut für Festkörperforschung: Stuttgart, Germany, 1998.

27. Lin, X.; Stoyko, S. S.; Mar, A. *J. Solid State Chem.* **2013**, *199*, 189–195.

28. Pauling, L. *The Nature of the Chemical Bond*, 3rd ed.; Cornell University Press: Ithaca, NY, 1960.

29. Emmerling, F.; Röhr, C. *Z. Naturforsch. B: Chem. Sci.* **2002**, *57*, 963–975.

30. Emmerling, F.; Röhr, C. *Z. Anorg. Allg. Chem.* **2003**, *629*, 467–472.

31. Papoian, G. A.; Hoffmann, R. *Angew. Chem. Int. Ed.* **2000**, *39*, 2408–2448.

32. Eisenmann, B.; Cordier, G. In *Chemistry, Structure, and Bonding of Zintl Phases and Ions*; Kauzlarich, S. M., Ed.; VCH: New York, 1996; pp 61–137.

33. Ponou, S.; Fässler, T. F.; Tobías, G.; Canadell, E.; Cho, A.; Sevov, S. C. *Chem. Eur. J.* **2004**, *10*, 3615–3621.

34. Alemany, P.; Alvarez, S.; Hoffmann, R. *Inorg. Chem.* **1990**, *29*, 3070–3073.

35. Alemany, P.; Llunell, M.; Canadell, E. *Inorg. Chem.* **2006**, *45*, 7235–7241.

36. Cordier, G.; Schäfer, H. *Z. Naturforsch. B: Anorg. Chem., Org. Chem.* **1977**, *32*, 383–386.

37. Brechtel, E.; Cordier, G.; Schäfer, H. *J. Less-Common Met.* **1981**, *79*, 131–138.

38. Brechtel, E.; Cordier, G.; Schäfer, H. *Z. Naturforsch. B: Anorg. Chem., Org. Chem.* **1979**, *34*, 921–925.

39. Morozkin, A. V.; Isnard, O.; Henry, P.; Granovsky, S.; Nirmala, R.; Manfrinetti, P. *J. Alloys Compd.* **2006**, *420*, 34–36.

40. Bobev, S.; Merz, J.; Lima, A.; Fritsch, V.; Thompson, J. D.; Sarrao, J. L.; Gillessen, M.; Dronskowski, R. *Inorg. Chem.* **2006**, *45*, 4047–4054.

41. Xia, S.-Q.; Myers, C.; Bobev, S. *Eur. J. Inorg. Chem.* **2008**, 4262–4269.

42. An, J.; Sefat, A. S.; Singh, D. J.; Du, M.-H. *Phys. Rev. B* **2009**, *79*, 075120-1–075120-6.

43. Rehr, A.; Kuromoto, T. Y.; Kauzlarich, S. M.; Del Castillo, J.; Webb, D. J. *Chem. Mater.* **1994**, *6*, 93–99.

44. Kim, H.; Condron, C. L.; Holm, A. P.; Kauzlarich, S. M. *J. Am. Chem. Soc.* **2000**, *122*, 10720–10721.

45. Holm, A. P.; Olmstead, M. M.; Kauzlarich, S. M. *Inorg. Chem.* **2003**, *42*, 1973–1981.

46. Xia, S.-Q.; Bobev, S. *Inorg. Chem.* **2007**, *46*, 874–883.

47. Xia, S.-Q.; Bobev, S. *Chem. Mater.* **2010**, *22*, 840–850.

48. Holm, A. P.; Kauzlarich, S. M.; Morton, S. A.; Waddill, G. D.; Pickett, W. E.; Tobin, J. G. *J. Am. Chem. Soc.* **2002**, *124*, 9894–9898.

49. Jansen, M. *Angew. Chem. Int. Ed. Engl.* **1987**, *26*, 1098–1110.

50. Misra, S.; Miller, G. J. *J. Am. Chem. Soc.* **2008**, *130*, 13900–13911.

Chapter 4

Ternary Arsenides ATt_3As_3 (A = K, Rb; Tt = Ge, Sn) with Layered Structures.

A version of this chapter has been published. Khatun, M.; Stoyko, S. S.; Mar, A. J. Solid State Chem. 2016, 238, 229–235.

4.1. Introduction

Ternary pnictides *A–M–Pn* (*A* = electropositive metal; *M* = group 13 or 14 metalloid or metal; *Pn* = P, As, Sb, Bi) constitute a diverse class of compounds, most of which can be considered to be Zintl phases.[1] Electron transfer is assumed to take place from *A* to the other components so that the structures contain A^{n+} cations embedded within a framework built up of heteronuclear $[M_xPn_y]^{n-}$ anions. For a given electron count, additional *M–M* or *Pn–Pn* bonds may form to satisfy the 8–*N* rule. The closed-shell configurations of all atoms generally results in a small band gap in the electronic structure, although in unusual situations, valence and conduction bands may overlap to form so-called metallic Zintl phases. This small band-gap semiconducting behaviour, together with the presence of a rigid anionic framework to enhance electronic conduction and weakly bonded A cations that can be "alloyed" to impede lattice vibrations, has led to the proposal that such Zintl phases could be good candidates for thermoelectric materials.[2,3] In addition to well established materials such as those based on the $Ca_{14}AlSb_{11}$-type structure, theoretical studies suggest that other compounds are worthwhile examining;[4] for example, Zintl phases in the *A*–Sn–Sb (*A* = Na, K) systems have been identified as promising candidates.[5]

The *A–Tt–Pn* (*A* = alkali metal; *Tt*, tetrel = Si, Ge, Sn; *Pn* = P, As, Sb) systems exhibit a very rich chemistry, consisting of well over 40 compounds so far, many serving as structural prototypes. The vast majority of these structures contain simple anionic units with the normal oxidation states adopted by all atoms (A^+, Tt^{+4}, Pn^{-3}). The most common are *Tt*-centred tetrahedra that can be

isolated (e.g., Na_8SnSb_4-type),[6] corner-sharing (e.g., Na_2SnAs_2- and Na_5SnSb_3-types),[7,8] or edge-sharing (e.g., Na_5GeP_3- and K_2SiP_2-types).[9,10] Isolated Tt-centred trigonal planes are found in the Cs_5SiP_3-type.[11] Lower oxidation states for the Tt atoms are encountered in the more unusual cases of KSnAs with Sn-centred trigonal pyramids that share corners to form puckered layers, [12–14] Rb_4SnSb_6 with $[SnSb_6]^{4-}$ clusters isostructural to P_4S_3,[15] and $K_6Sn_3As_5$ with $[Sn_2As_6]^{10-}$ edge-sharing tetrahedral dimers and $[Sn_2As_6]^{12-}$ trigonal prismatic groups (containing a Sn–Sn bond) forming a complex three-dimensional framework.[13] Mixed valence is invoked in the remarkable compounds KSi_3As_3 and $NaGe_3P_3$, which adopt related layered structures that differ in their topology.[16,17]

This chapter represents the discovery of the new series of ternary arsenides ATt_3As_3 (A = K, Rb; Tt = Ge, Sn), examine their structural relationships to other compounds, and evaluate their electronic structures.

4.2. Experimental

4.2.1. Synthesis

Starting materials were Na pieces (99.99%), K pieces (99.95%), Rb pieces (99.75%), Ge ingot (99.999%), Sn granules (99.99%), and As lumps (99.999%), all obtained from Alfa-Aesar. All samples were handled within an argon-filled glovebox. KGe_3As_3 was originally identified as a byproduct in a reaction intended to prepare "$K_2CdGe_3As_4$" in the course of exploratory investigations of quaternary arsenide systems; subsequently, further reactions were attempted to examine the range of substitution of the alkali-metal and tetrel component. Mixtures of the elements A (= Na, K, Rb), Tt (= Ge, Sn), and As combined in a 1:3:3 ratio were loaded into alumina crucibles placed within fused-silica tubes, which were evacuated and sealed. The tubes were heated to 650 °C (for samples containing Na or K) or 600 °C (for samples containing Rb) over 2 d, held at that temperature for 10 d, and cooled to room temperature over 2 d. (The lower temperature in the Rb-

containing reactions was used to minimize volatilization of Rb metal, which boils at 688 °C.) The products were ground, mixed with paraffin oil, and analyzed by powder X-ray diffraction (XRD) carried out on an Inel diffractometer equipped with a curved position-sensitive detector (CPS 120) and a Cu $K\alpha_1$ radiation source operated at 40 kV and 20 mA. For A = K and Rb, the products consisted of the title compounds as the major phase and typically unreacted Ge or Sn as minor phases (**Figure A 3-1** in **Appendix 3**). The yields were variable because under the reaction conditions used, it was difficult to avoid volatilization loss of the alkali-metal component, as evidenced by the fused-silica tubes turning slightly brown. Further efforts are required to optimize the synthesis, including use of excess alkali metal or placement of the reactants in a welded metal tube. For A = Na, the reactions led instead to a new compound $NaGe_6As_6$ with a layered structure, which has been reported separately in Chapter 5,[18] or the previously known compound $NaSn_2As_2$.[19] Needle-shaped crystals of ATt_3As_3 were selected under paraffin oil and examined by energy-dispersive X-ray (EDX) analysis on a JEOL JSM-6010LA scanning electron microscope. The experimentally determined compositions (in atomic %), averaged over 4–5 crystals per compound, were $K_{14(1)}Ge_{41(2)}As_{45(2)}$, $Rb_{16(1)}Ge_{40(2)}As_{44(2)}$, $K_{13(1)}Sn_{43(2)}As_{44(2)}$, and $Rb_{13(1)}Sn_{46(2)}As_{41(2)}$, which are in good agreement with the expected composition $A_{14}Tt_{43}As_{43}$.

4.2.2. Structure Determination

Each single crystal was mounted on a glass fiber within a small droplet of paraffin oil and placed under a cold nitrogen gas stream on a Bruker PLATFORM diffractometer equipped with a SMART APEX II CCD area detector and a graphite-monochromated Mo $K\alpha$ radiation source. Full spheres of intensity data were collected at –80 ºC (for Ge-containing compounds) or –100 ºC (for Sn-containing compounds) using ω scans at 5–8 different ϕ angles with a frame width of 0.3º and an exposure time of 15–30 s per frame. Face-indexed numerical absorption corrections were applied.

Structure solution and refinement were carried out with use of the SHELXTL (version 6.12) program package. [20] Intensity statistics, Laue symmetry, and systematic absences led to the choice of the centrosymmetric orthorhombic space group *Pnma*. Initial locations for seven sites – one *A*, three *Tt*, and three As, all in Wyckoff position 4*c* – were found by direct methods. For the Sn-containing compounds, refinements in which the sites were allowed to be occupied by a mixture of Sn and As atoms clearly supported an ordered model. For example, in KSn_3As_3, the sites assigned as Sn contained 0.99(1) to 1.00(1) Sn and 0.00(1) to 0.01(1) As whereas those assigned as As contained – 0.04(1) to 0.00(1) Sn and 1.00(1) to 1.04(1) As. Displacement parameters for all atoms were reasonable and all sites were confirmed to be fully occupied. For the Ge-containing compounds, the similar scattering factors of Ge and As posed problems in convergence when analogous refinements involving disorder of the two atoms were attempted. In KGe_3As_3, for example, although two of the sites later assigned as Ge atoms had occupancies of 0.8(2) Ge / 0.2(2) As or 0.7(2) Ge / 0.3(2) As, refinements of the other sites were unstable. Therefore, we assumed the same ordered model as for the Sn-containing compounds. In $RbGe_3As_3$, the displacement ellipsoid for the Rb site appeared to be quite elongated along the *b*-direction (U_{22} = 0.259(7) Å^2, compared to U_{11} = 0.041(2) Å^2 and U_{33} = 0.049(2) Å^2). This site was thus split into two half-occupied ones 0.6 Å apart from each other off the mirror plane (from 4*c* (0.21, ¼, 0.46) to 8*d* (0.21, 0.16, 0.46)), with an ISOR restraint applied to approximate isotropic behaviour (**Figure A 3-2** in **Appendix 3**). Refinement of the split model gave a more reasonable displacement ellipsoid for the Rb site (U_{22} = 0.077(3) Å^2, compared to U_{11} = 0.048(2) Å^2 and U_{33} = 0.053(2) Å^2), although the agreement factors were slightly worse. In KGe_3As_3, the K site also exhibited a displacement ellipsoid that was elongated, albeit to a lesser degree. Refinement of a similar model containing half-occupied split K sites, now only 0.4 Å apart, also led to more isotropic displacement parameters but no improvement in agreement factors.

Reasons for why these Ge-containing compounds but not the Sn-containing ones suffer from this problem are discussed later.

Atomic positions were standardized with the program STRUCTURE TIDY.[21] Crystal data and experimental details are listed in **Table 4-1**, positional and displacement parameters in **Table 4-2**, and interatomic distances in **Table 4-3**. Results for both the unsplit and split models for KGe_3As_3 and $RbGe_3As_3$ are provided in these tables. Further data in CIF format are available in CSD number 430747 to 430750.

Table 4-1. Crystallographic data for ATt_3As_3 (A = K, Rb; Tt = Ge, Sn)[a]

formula	KGe_3As_3	$RbGe_3As_3$	KSn_3As_3	$RbSn_3As_3$
formula mass (amu)	481.63	528.00	619.93	666.30
space group	*Pnma* (No. 62)	*Pnma* (No. 62)	*Pnma* (No. 62)	*Pnma* (No. 62)
a (Å)	9.9931(11)	10.1657(19)	10.1990(12)	10.3211(11)
b (Å)	3.7664(4)	3.7595(7)	4.0840(5)	4.0917(4)
c (Å)	18.607(2)	19.028(4)	19.240(2)	19.570(2)
V (Å^3)	700.34(13)	727.2(2)	801.41(16)	826.46(15)
Z	4	4	4	4
ρ_{calcd} (g cm^{-3})	4.568	4.823	5.138	5.355
T (K)	193(2)	193(2)	173(2)	173(2)
crystal dimensions (mm)	0.29 × 0.03 × 0.02	0.11 × 0.04 × 0.03	0.16 × 0.04 × 0.02	0.25 × 0.03 × 0.03
radiation	graphite monochromated Mo $K\alpha$, λ = 0.71073 Å			
μ(Mo $K\alpha$) (mm^{-1})	27.33	32.40	21.98	26.66
transmission factors	0.122–0.596	0.069–0.492	0.133–0.697	0.135–0.635
2θ limits	4.38–66.09°	4.28–66.36°	4.23–66.50°	4.16–66.48°
data collected	$-15 \le h \le 15$, –5	$-15 \le h \le 15$, –5	$-15 \le h \le 15$, –6	$-15 \le h \le 15$, –6

	$\leq k \leq 5, -28 \leq l \leq 28$		$\leq k \leq 5, -28 \leq l \leq 29$		$\leq k \leq 6, -28 \leq l \leq 28$	$\leq k \leq 6, -30 \leq l \leq 30$
no. of data collected	9750		10233		10718	11165
no. of unique data, including $F_o^2 < 0$	1497 (R_{int} = 0.078)		1566 (R_{int} = 0.136)		1697 (R_{int} = 0.079)	1757 (R_{int} = 0.062)
no. of unique data, with $F_o^2 > 2\sigma(F_o^2)$	1092		957		1313	1424
no. of variables	44	47	44	47	44	44
$R(F)$ for $F_o^2 > 2\sigma(F_o^2)$ [b]	0.039	0.039	0.062	0.065	0.034	0.027
$R_w(F_o^2)$ [c]	0.096	0.098	0.188	0.198	0.074	0.060
goodness of fit	1.084	1.073	1.052	1.049	1.020	1.017
$(\Delta\rho)_{max}$, $(\Delta\rho)_{min}$ (e Å^{-3})	1.96, –2.33	1.96, –2.53	2.93, –3.56	3.00, –3.87	2.08, –2.18	1.56, –1.48

[a] The shaded entries refer to alternative models containing split sites for the *A* atoms.

[b] $R(F) = \sum||F_o| - |F_c|| / \sum|F_o|$.

[c] $R_w(F_o^2) = [\sum[w(F_o^2 - F_c^2)^2] / \sum wF_o^4]^{1/2}$; $w^{-1} = [\sigma^2(F_o^2) + (Ap)^2 + Bp]$, where $p = [\max(F_o^2,0) + 2F_c^2] / 3$.

Table 4-2. Positional and displacement parameters for ATt_3As_3 (A = K, Rb; Tt = Ge, Sn)[a]

Atom	Wyckoff position	x	y	z	U_{eq} (Å^2) [b]
KGe_3As_3					
K	4*c*	0.2202(3)	¼	0.45727(18)	0.0713(12)
K	8*d*	0.2201(4)	0.1913(18)	0.4572(2)	0.0490(14)
Ge1	4*c*	0.30819(9)	¼	0.15689(5)	0.01194(19)
Ge2	4*c*	0.41421(9)	¼	0.75660(5)	0.01276(19)
Ge3	4*c*	0.52037(10)	¼	0.63181(5)	0.0165(2)
As1	4*c*	0.04405(8)	¼	0.63048(4)	0.01128(18)
As2	4*c*	0.11350(9)	¼	0.07913(5)	0.01413(19)
As3	4*c*	0.23867(9)	¼	0.28121(5)	0.01278(19)
$RbGe_3As_3$					
Rb	4*c*	0.2137(3)	¼	0.45971(17)	0.116(2)
Rb	8*d*	0.2135(3)	0.1640(12)	0.45960(19)	0.0595(12)
Ge1	4*c*	0.29552(15)	¼	0.16066(9)	0.0166(4)
Ge2	4*c*	0.42561(16)	¼	0.75740(9)	0.0180(4)
Ge3	4*c*	0.52687(17)	¼	0.63529(10)	0.0216(4)
As1	4*c*	0.05905(14)	¼	0.63417(9)	0.0159(3)
As2	4*c*	0.10422(15)	¼	0.08359(9)	0.0191(4)
As3	4*c*	0.22500(14)	¼	0.28219(9)	0.0174(4)
KSn_3As_3					
K	4*c*	0.21476(19)	¼	0.45854(11)	0.0196(4)
Sn1	4*c*	0.32879(5)	¼	0.14869(3)	0.01055(12)
Sn2	4*c*	0.39021(5)	¼	0.75813(3)	0.01116(12)
Sn3	4*c*	0.51891(5)	¼	0.62159(3)	0.01258(12)
As1	4*c*	0.01512(8)	¼	0.62022(4)	0.01045(16)

As2	4*c*	0.12616(8)	¼	0.06768(4)	0.01172(17)
As3	4*c*	0.27428(8)	¼	0.28142(4)	0.01133(16)
$RbSn_3As_3$					
Rb	4*c*	0.21148(6)	¼	0.45983(3)	0.01619(13)
Sn1	4*c*	0.31911(4)	¼	0.15156(2)	0.00965(9)
Sn2	4*c*	0.39856(4)	¼	0.75851(2)	0.01032(9)
Sn3	4*c*	0.52323(4)	¼	0.62419(2)	0.01153(9)
As1	4*c*	0.02685(6)	¼	0.62355(3)	0.00948(12)
As2	4*c*	0.11928(6)	¼	0.07152(3)	0.01081(13)
As3	4*c*	0.26369(6)	¼	0.28165(3)	0.01039(13)

[a] The shaded entries refer to alternative models containing split sites for the *A* atoms. Positional and displacement parameters for the other atoms in the split models are identical within standard uncertainties to those in the unsplit models.

[b] U_{eq} is defined as one-third of the trace of the orthogonalized U_{ij} tensor.

Table 4-3. Interatomic distances (Å) in ATt_3As_3 (A = K, Rb; Tt = Ge, Sn)

	KGe_3As_3		**$RbGe_3As_3$**	
A–As3	3.281(3)	3.287(4)	3.380(4)	3.393(4)
A–As2 (×2)	3.384(3)	3.268(5)/3.513(5)	3.538(3)	3.380(4)/3.722(4)
A–As1 (×2)	3.632(3)	3.520(5)/3.749(5)	3.796(3)	3.644(4)/3.964(4)
A–As1	3.673(4)	3.680(4)	3.673(4)	3.687(4)
A–Ge3 (×2)	3.607(3)	3.497(5)/3.728(5)	3.709(3)	3.557(4)/3.883(4)
A–*A* (×2)	3.7664(4)	(3.32(1))/4.21(1)	3.7595(7)	(3.11(1))/4.41(1)
Ge1–As3	2.4153(12)		2.421(2)	
Ge1–As2	2.4246(13)		2.436(2)	
Ge1–As1 (×2)	2.4430(8)		2.4440(14)	
Ge2–As3 (×2)	2.4678(8)		2.4699(15)	
Ge2–As1	2.4694(13)		2.469(2)	
Ge3–As2 (×2)	2.5093(9)		2.5055(16)	
Ge2–Ge3	2.5529(14)		2.541(3)	
	KSn_3As_3		**$RbSn_3As_3$**	
A–As2 (×2)	3.3484(17)		3.4661(7)	
A–As1 (×2)	3.4588(17)		3.5915(7)	
A–As3	3.462(2)		3.5284(10)	
A–As1	3.718(2)		3.7277(10)	
A–Sn3 (×2)	3.7316(18)		3.7930(7)	
A–*A* (×2)	4.0840(5)		4.0917(4)	
Sn1–As2	2.5885(10)		2.5898(8)	
Sn1–As3	2.6134(10)		2.6094(8)	
Sn1–As1 (×2)	2.6466(6)		2.6483(5)	
Sn2–As1	2.6649(10)		2.6609(7)	
Sn2–As3 (×2)	2.6805(7)		2.6824(5)	
Sn3–As2 (×2)	2.7267(7)		2.7224(5)	
Sn2–Sn3	2.9366(8)		2.9266(6)	

[a] The shaded entries refer to alternative models containing split sites for the *A* atoms.

4.2.3. Band Structure Calculations

Tight-binding linear muffin tin orbital band structure calculations were performed on KGe_3As_3 and KSn_3As_3 within the local density and atomic spheres approximation with use of the Stuttgart TB-LMTO-ASA program (version 4.7). [22] The basis set consisted of K 4s/4p/3d, Ge 4s/4p/4d or Sn 5s/5p/5d/4f, and As 4s/4p/4d orbitals, with the K 4p/3d, Ge 4d or Sn 5d/4f and As 4d orbitals being downfolded. Integrations in reciprocal space were carried out with an improved tetrahedron method over 63 irreducible *k* points within the first Brillouin zone.

4.3. Result and Dicussion

Previously known ternary phases were limited in the *A*–Ge–As (*A* = alkali metal) systems ($Li_{1.67}Ge_{0.33}As$, A_5GeAs_3 (*A* = Na, Cs), K_2GeAs_2) [11, 23–25] but more numerous in the *A*–Sn–As systems ($NaSn_2As_2$, A_2SnAs_2 (*A* = Na, K, Rb), A_5SnAs_3 (*A* = Na, K), KSnAs, $K_6Sn_3As_5$).[7,12–14,19,25–28] The isostructural arsenides ATt_3As_3 (*A* = K, Rb; *Tt* = Ge, Sn) are new phases in these systems. They adopt an orthorhombic structure (space group *Pnma*) consisting of 7 independent sites – one *A*, three *Tt*, and three As – all in Wyckoff position 4*c*. The structure contains corrugated [Tt_3As_3] layers separated by *A* cations stacked along the *c*-direction (**Figure. 4-1a**). Each layer is built from characteristic building blocks of five-membered rings (*Tt*1–As3–*Tt*2–*Tt*3–As2) decorated with handles of As1 atoms (**Figure. 4-1b**). The coordination geometry is tetrahedral around *Tt*1 and *Tt*2, but trigonal pyramidal around *Tt*3; the *Tt*2 and *Tt*3 atoms are connected by a homoatomic bond. All three types of As atoms are surrounded by *Tt* atoms in trigonal pyramidal geometry. The *A* atom is surrounded by six As atoms in roughly octahedral geometry that is distorted to accommodate additional interactions to two *Tt* atoms, resulting in a bicapped trigonal prismatic coordination (CN8) overall (**Figure. 4-1c**).

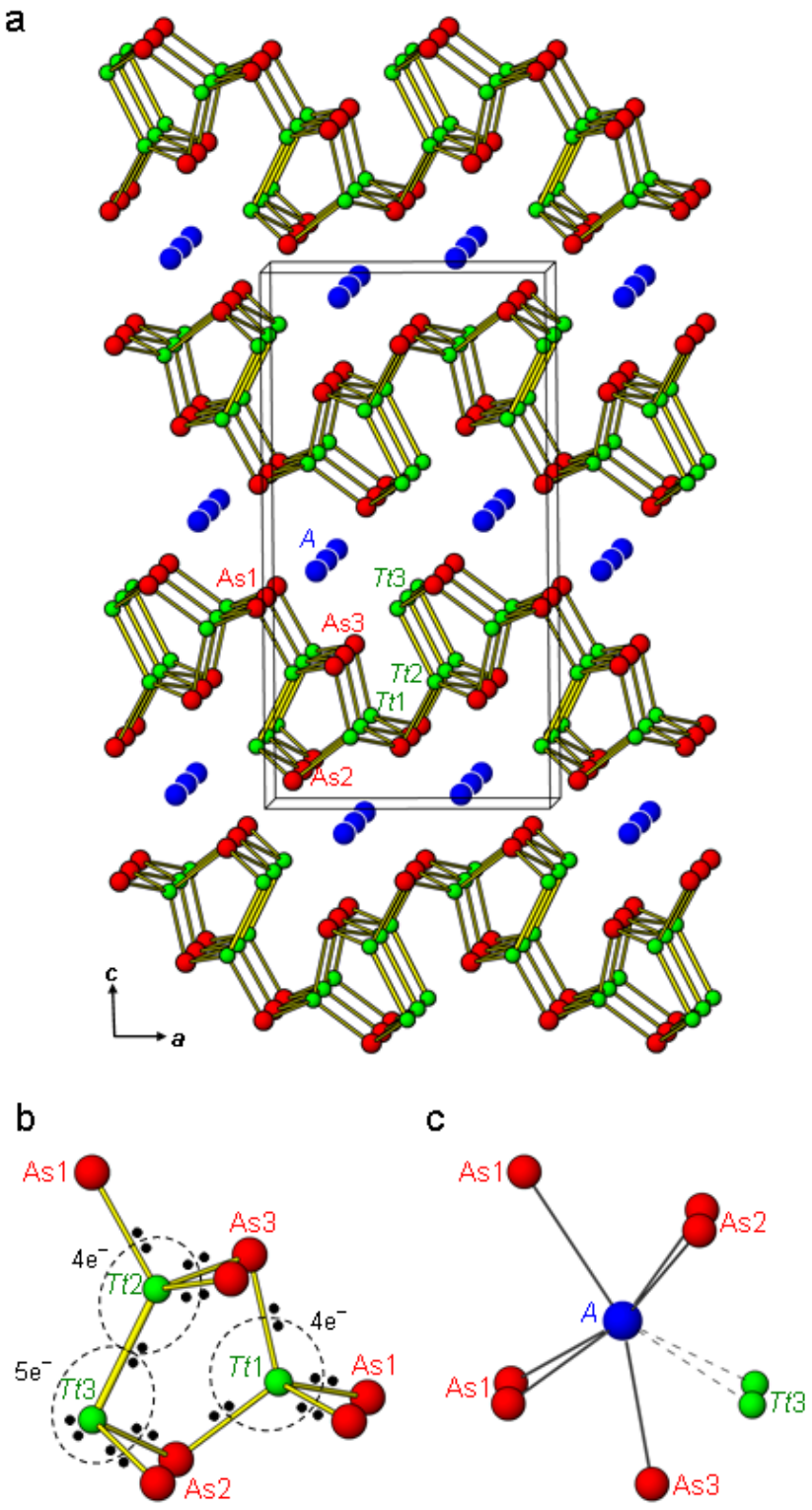

Figure 4-1. (a) Structure of ATt_3As_3 (A = K, Rb; Tt = Ge, Sn) viewed down the b-direction. (b) Building block consisting of five-membered rings with As handles, with the electron counting shown around the three different Tt sites. (c) Coordination environment around A sites.

In the Sn-containing compounds KSn_3As_3 and $RbSn_3As_3$, the structures displayed clear ordering of Sn and As atoms as evidenced by occupancy refinements. Consistent with trends seen in the literature, the Sn–As bonds are shorter within Sn-centred tetrahedra (2.588(1)–2.6805(7) Å in KSn_3As_3; cf. 2.588(1)–2.644(1) Å in Na_2SnAs_2 [7], 2.630(1)–2.712(1) Å in K_5SnAs_3 [28]) than within Sn-centred trigonal pyramids (2.7267(7) Å in KSn_3As_3; cf. 2.710(3) Å in KSnAs,[13] 2.700(1)–2.727(1) Å in $K_6Sn_3As_5$.[13] The homoatomic Sn–Sn bond (2.9366(8) Å in KSn_3As_3; cf. 2.984(1) Å in $K_6Sn_3As_5$ [13]) is slightly greater than the sum of the metallic radii of Sn (1.42 + 1.42 = 2.84 Å).[29] In the Ge-containing compounds KGe_3As_3 and $RbGe_3As_3$, the Ge and As atoms were assumed to be similarly ordered. The Ge–As bonds within tetrahedra (2.4153(12)–2.4694(13) Å in KGe_3As_3; cf. 2.457(3) Å in K_2GeAs_2,[25] 2.442(1)–2.510(2) Å in Na_5GeAs_3 [24]) are also shorter than within trigonal pyramids (2.5093(9) Å in KGe_3As_3); the Ge–Ge bond (2.5529(14) Å in KGe_3As_3; cf. 2.476(6)–2.568(6) Å in $BaGe_2As_2$ [30]) is just slightly longer than the sum of the metallic radii (1.24 + 1.24 = 2.48 Å) [29].

The alkali metal sites were well behaved in the Sn-containing compounds but exhibited elongated displacement ellipsoids (which can be modeled as closely spaced split sites) along the *b*-direction in the Ge-containing ones, being more pronounced in $RbGe_3As_3$ (**Figure. A 3-2** in **Appendix 3)**. If covalent bonding interactions within the anionic framework $[Tt_3As_3]^{3-}$ are assumed to be more important than the ionic interactions between *A* cations and this framework, then the substitution of smaller Ge atoms in the *Tt* site can be expected to contract the entire structure, as confirmed by inspection of the cell parameters. It is informative to compare the closest *A*–*A* contact, which corresponds to the *b*-parameter, to the sum of the metallic radii (K–K, 4.05 Å; Rb–Rb, 4.32 Å)[29]. The *b*-parameters are not too far off from the expected separation of the *A* atoms in KSn_3As_3 and $RbSn_3As_3$ (4.08–4.09 Å), but they are considerably shorter in KGe_3As_3 and especially $RbGe_3As_3$

(3.76 Å). The elongated displacement ellipsoids in the latter may thus manifest a tendency of the *A* atoms to distort from their ideal sites to counteract these short *A*–*A* contacts. This feature probably occurs in the related layered structure of KSi_3As_3 (with K–K separation of 3.66 Å), which also exhibits elevated displacement parameters for the K atoms.[16]

The corrugated [Tt_3As_3] layers resemble those found in only a few other structures. For concreteness, we arbitrarily designate KSn_3As_3 as the prototype of the title compounds. The binary arsenide $GeAs_2$ crystallizes in space group *Pbam*, with the short axis along *c*, and contains neutral layers lying parallel to the *ab*-plane, without any cations between them (**Figure. 4-2a**).[31] The Ge atoms in these layers reside exclusively in tetrahedral coordination; homoatomic As–As bonds are formed instead of Ge–Ge bonds. Insertion of cations between analogous anionic layers results in the structure of $BaIn_2Sb_4$, which crystallizes in space group *Pnma*, with the short axis along *b* (**Figure. 4-2b**).[32] There are still subtle differences, but the relationship can be made clearer if the formula of $GeAs_2$ ($Z = 8$) is doubled to Ge_2As_4 ($Z = 4$) and the *b*- and *c*-axes are interchanged so that the space group is in the non-standard setting *Pcma*. The neutral [Ge_2As_4] layers in $GeAs_2$ correspond exactly to the anionic $[In_2Sb_4]^{2-}$ layers in $BaIn_2Sb_4$, which contain homoatomic Sb–Sb bonds. However, the stacking of the layers along the *a*-direction is slightly different: successive layers are related by *c*-glide in $GeAs_2$ but by *n*-glide in $BaIn_2Sb_4$. In KSn_3As_3, which also crystallizes in space group *Pnma*, the layers are stacked in the same way as in $BaIn_2Sb_4$, but the site distribution (or "colouring") within the layers differs to form Sn–Sn bonds but no As–As bonds (**Figure. 4-2c**). A limiting model substructure resembling KSn_3As_3 with the anionic composition "$[BaSn_3As_3]^{2-}$" is found in the remarkable case of $Ba_3Sn_4As_6$, which exhibits an unusual type of twinning.[33] Finally, $NaGe_3P_3$ shows an identical site distribution of *Tt* and *Pn* atoms as in KSn_3As_3, but now the layers always point in the same orientation along the stacking direction, aligned parallel to a polar 2_1-axis

(**Figure. 4-2d**).[17] Interestingly, KSi_3As_3 is not isostructural to KGe_3As_3 or KSn_3As_3, notwithstanding their identical compositions and layered structures.[16] Although there are similar pentagonal tubes made of five-membered rings (Si–As–Si–Si–As), they are connected quite differently in KSi_3As_3.

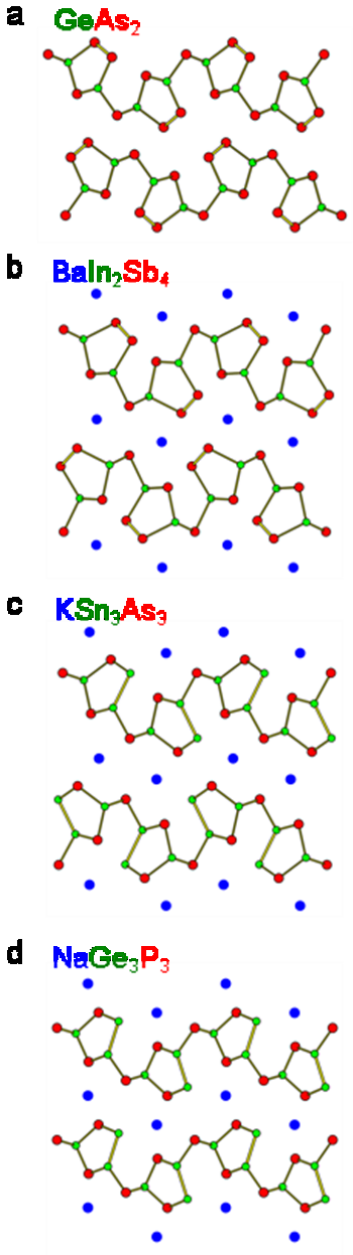

Figure 4-2. Comparison of structures of (a) $GeAs_2$, (b) $BaIn_2Sb_4$, (c) KSn_3As_3, and (d) $NaGe_3P_3$, built up of similar types of corrugated layers.

KSn_3As_3 and isostructural arsenides show a definite relationship between electronic and crystal structures, satisfying the conditions for being Zintl phases with all atoms attaining closed-shell electron configurations. Assignment of formal charges, in which electrons in covalent bonds are split evenly in half, results in the charge-balanced formulation $(K^+)(Sn^{1-})(Sn^0)_2(As^0)_3$ (**Figure. 4-1b**). Alternatively, assignment of oxidation states, in which electrons in covalent bonds are given to the more electronegative atom, results in the formulation $(K^{+1})(Sn^{+1})(Sn^{+3})(Sn^{+4})(As^{-3})_3$. The formal charge assignment is more realistic in cases where electronegativity differences are small, as they are here, but the oxidation state assignment does draw attention to the presence of different valence states for the tetrel atoms. Thus, KSn_3As_3 can be considered to be a mixed-valent compound containing Sn atoms in three different oxidation states. In a simple electron dot diagram, the most electron-rich Sn site, in trigonal pyramidal coordination, would have a lone pair of electrons that is directed towards the K cation. Although the occurrence of Sn with a stereochemically active lone pair is normal, the analogous situation of Ge containing lone pairs as implied in KGe_3As_3 and $RbGe_3As_3$ is uncommon. Interactions between Ge lone pairs and alkali metal cations have been evidenced in charge density maps for the related compound $NaGe_3P_3$,[17] and are likely operative in KGe_3As_3 and $RbGe_3As_3$ as well. The mixed valence is also reflected in the bond valence sums [34] evaluated for the *Tt* atoms: 4.0 for Sn1, 3.2 for Sn2, and 2.1 for Sn3 in KSn_3As_3; 4.0 for Ge1, 3.4 for Ge2, and 2.3 for Ge3 in KGe_3As_3. It may be interesting to attempt X-ray photoelectron spectroscopy or Mössbauer spectroscopy to ascertain if this mixed valence can be experimentally confirmed.

Electronic band structures were calculated for KGe_3As_3 and KSn_3As_3 as representative members of this series of arsenides. The density of states (DOS) curve for KGe_3As_3 confirms the presence of a small band gap (0.71 eV), expected for a Zintl phase, between valence and conduction bands (**Figure. 4-3a**). The filled levels are derived primarily from strong mixing of Ge and As

states, with mostly 4s character at lower energy (–13.5 to –10.5 eV), both 4s and 4p character at intermediate energy (–9.1 to –6.3 eV), and mostly 4p character at higher energy (–4.8 to 0 eV). The heteroatomic Ge–As interactions are perfectly optimized, with all bonding and no antibonding levels filled, as seen in the crystal orbital Hamilton population (COHP) curves. Although less significant, the homoatomic Ge–Ge interactions are similarly optimized. As gauged by the integrated COHP values (–ICOHP), the Ge–Ge bonds are slightly weaker (1.74 eV/bond) than the Ge–As bonds (2.49 eV/bond). In the structure determination of KGe_3As_3, the assignment of Ge and As atoms was assumed by analogy to the ordered structure found for KSn_3As_3 and by inspection of bond distances. The chief ambiguity is in the occupation of Ge3 and As2 sites, both in trigonal pyramidal coordination. However, the possibility that the Ge3 and As2 sites are interchanged can be ruled out because a band structure calculation based on this model shows that it is less stable by 0.12 eV per formula unit. The K atoms are not completely innocent of bonding but do participate in rather weak covalent interactions with the As and Ge atoms, as seen in the COHP curves. The –ICOHP values are 0.10 eV/bond for K–As and 0.09 eV/bond for K–Ge contacts. Thus, the covalent bonding energy in the structure is provided mostly by the Ge–As interactions (–ICOHP of 22.5 eV/cell, or 90%) and to a much smaller extent from the Ge–Ge interactions (–ICOHP of 1.7 eV/cell, or 7%), and K–Ge and K–As interactions (–ICOHP of 0.8 eV/cell, or 3%).

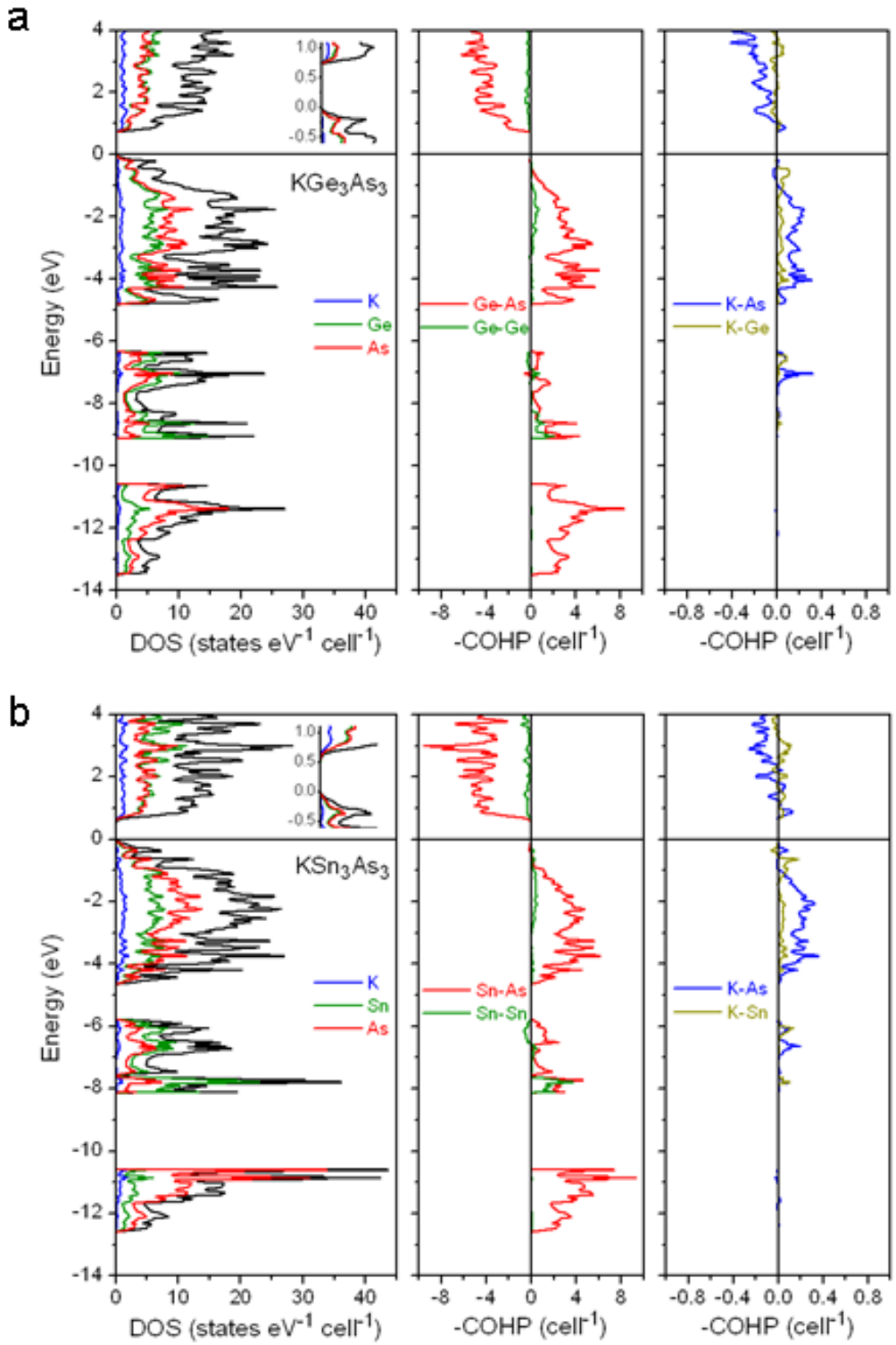

Figure 4-3. Density of states (DOS) and crystal orbital Hamilton population (–COHP) curves for (a) KGe_3As_3 and KSn_3As_3. Magnified views of the DOS curves near the Fermi level are shown. Note the different scales for the –COHP values in the middle vs. right panels.

On proceeding from KGe_3As_3 to KSn_3As_3, the band gap narrows to 0.50 eV (**Figure. 4-3b**). Most of the features in the DOS curve remain preserved, except that the lowest energy bands are somewhat narrower (by about 0.5 eV), indicative of weaker s/p hybridization within both Sn and As atoms. Thus, reflecting the greater p-character in the bonds, the angles around the Sn3 atom (95.61(2)–96.99(3)°) in KSn_3As_3 are slightly narrower than those around the Ge3 atom (97.26(5)–97.69(4)°) in KGe_3As_3. The bond strengths as quantified by –ICOHP values follow the same pattern as before: 2.23 eV/bond for Sn–As, 2.00 eV/bond for Sn–Sn, 0.11 eV/bond for K–As, and 0.08 eV/bond for K–Sn contacts. Similarly, the covalent bonding energy is dominated by Sn–As interactions (–ICOHP of 20.1 eV/cell, or 89%). Calculations performed for the Rb-containing compounds gave similar results (not shown here), the main effect being a widening of the band gap (1.22 eV in $RbGe_3As_3$, 0.73 eV in $RbSn_3As_3$) relative to the K-containing compounds.

4.4. Conclusion

The new series of compounds KGe_3As_3, KSn_3As_3, $RbGe_3As_3$, and $RbSn_3As_3$ expands considerably the number of ternary alkali-metal tetrel pnictides with the composition ATt_3Pn_3, which were previously limited to two well-characterized representatives, $NaGe_3P_3$ and KSi_3As_3, each with different layered structures. However, all have *Tt*–*Tt* bonds, in the form of Tt_2 dimers in KSn_3As_3 and $NaGe_3P_3$, or a combination of Tt_2 dimers and Tt_4 strings in KSi_3As_3. The flexibility in the distribution of *Tt* vs *Pn* atoms and the possibility for different stacking arrangements of layers suggest that other chemical substitutions are worthwhile investigating. Moreover, given that ion exchange of the K atoms (with Li and Na) has been demonstrated in KSi_3As_3,[16] this may also be feasible in the other compounds. Physical property measurements on these compounds would also be worthwhile but it will be important to first optimize their syntheses and evaluate their air-

sensitivity. The Na-containing compound $NaGe_6As_6$ was formed as a byproduct in the $NaGe_3As_3$ sample, and is presented in Chapter 5.

4.5. References

1. Eisenmann, B.; Cordier, G. In *Chemistry, Structure, and Bonding of Zintl Phases and Ions*; Kauzlarich, S. M. Ed.; VCH: New York, 1996; pp 61–137.
2. Kauzlarich, S. M.; Brown, S. R.; Snyder, G. J. *Dalton Trans*. **2007**, 2099–2107.
3. Toberer, E. S.; May, A. F.; Snyder, G. J. *Chem. Mater.***2010**, *22*, 624–634.
4. Yan, J.; Gorai, P.; Ortiz, B.; Miller, S.; Barnett, S. A.; Mason, T.; Stevanović, V.; Toberer, E. S. *Energy Environ. Sci.* **2015**, *8*, 983–994.
5. Zhang, L.; Du, M.–H.; Singh, D. J. *Phys. Rev. B* **2010**, *81*, 075117-1–075117-8.
6. Eisenmann, B.; Klein, J. *Z. Naturforsch., B* **1988**, *43*, 69–71.
7. Asbrand, M.; Eisenmann, B. *Z. Naturforsch., B* **1993**, *48*, 452–456.
8. Eisenmann, B.; J. Klein, J. *Z. Naturforsch., B* **1988**, *43*, 1156–1160.
9. Eisenmann, B.; Somer, M. *Z. Naturforsch., B* **1985**, *40*, 886–890.
10. Eisenmann, B.; Somer, M. *Z. Naturforsch., B* **1984**, *39*, 736–738.
11. Eisenmann, B.; Klein, J.; Somer, M. *Angew. Chem., Int. Ed. Engl.* **1990**, *29*, 87–88.
12. Lii, K.-H.; Haushalter, R. C. *J. Solid State Chem.* **1987**, *67*, 374–378.
13. Klein, J.; Eisenmann, B. *Mater. Res. Bull.* **1988**, *23*, 587–594.
14. Schmidt, P. C.; Stahl, D.; Eisenmann, B.; Kniep, R.; Eyert, V.; Kübler, J. *J. Solid State Chem.* **1992**, *97*, 93–104.
15. Asbrand, M.; Eisenmann, B. *Z. Kristallogr.* **1992**, *198*, 309–310.
16. Hurng, W.-M.; Corbett, J. D., Wang, S.-L.; Jacobson, R. A. *Inorg. Chem.* **1987**, *26*, 2392–2395.
17. Feng, K.; Yin, W.; He, R.; Lin, Z.; Jin, S.; Yao, J.; Fu, P.; Wu, Y. *Dalton Trans.* **2012**, *41* 484–489.
18. Khatun, M.; Mar, A. *Z. Naturforsch., B* **2016**, *71*, 375-380.
19. Asbrand, M.; Eisenmann, B.; Klein, J. *Z. Anorg. Allg. Chem.* **1995,** *621*, 576–582.
20. Sheldrick, G. M. *SHELXTL*, version 6.12; Bruker AXS Inc.: Madison, WI, 2001.
21. Gelato, L.M.; Parthé, E. *J. Appl. Crystallogr.* **1987**, *20*, 139–143.
22. Tank, R.; Jepsen, O.; Burkhardt, A.; Andersen, O. K. *TB-LMTO-ASA Program*, version 4.7; Max Planck Institut für Festkörperforschung: Stuttgart, Germany, 1998.
23. Juza, R.; Schulz, W. *Z. Anorg. Allg. Chem.* **1954**, *275*, 65–78.
24. Eisenmann, B.; Klein, J.; Somer, M. *Z. Kristallogr.* **1991**, *197*, 265–266.
25. Eisenmann, B.; Klein, J. *J. Less-Common Met.* **1991**, *175*, 109–117.

26. Burtzlaff, S.; Hołyńska, M.; Dehnen, S. *Z. Anorg. Allg. Chem.* **2010**, *636*, 1691–1693.

27. Eisenmann, B.; Klein, J. *Z. Kristallogr.* **1991**, *196*, 213–229.

28. Eisenmann, B.; Rössler, U.; Kristallogr Z. – *New Cryst. Struct.* **2000**, *215*, 347–348.

29. Pauling, L. *The Nature of the Chemical Bond*, 3rd ed., Cornell University Press: Ithaca, NY, 1960.

30. Eisenmann, B.; Schäfer, H. *Z. Naturforsch., B* **1981**, *36*, 415–419.

31. Bryden, J. H. *Acta Crystallogr.* **1962**, *15*, 167–171.

32. Kim, S.-J. Hu, S.; Uher, C.; Kanatzidis, M. G. *Chem. Mater.* **1999**, *11*, 3154–3159.

33. Lam, R.; Mar, A. *Solid State Sci.* **2001**, *3*, 503–512.

34. Brese, N. E.; O'Keeffe, M. *Acta Crystallogr., Sect. B* **1991**, *47*, 192–197.

Chapter 5

$NaGe_6As_6$: Insertion of Sodium into the Layered Semiconductor Germanium Arsenide GeAs

A version of this chapter has been published. Khatun, M.; Mar, A. Z. Naturforsch., B 2016, 71, 375–380.

5.1. Introduction

A large number of ternary pnictides *A*-*M*-*Pn* (*A* = electropositive metal; *M* = metal or metalloid from group 13 or 14; *Pn* = P, As, Sb, Bi) exhibit structures in which *A* cations are found in conjunction with heteronuclear anionic $[M_xPn_y]^{n-}$ units.[1] Most of these compounds satisfy the Zintl concept so that there is a definite relationship between the electron count and the crystal structure. In cases where the *Pn* atoms experience a deficiency of electrons with respect to the 8–*N* rule, polyanionic networks containing *Pn*–*Pn* bonds must necessarily develop. Less commonly, there is a surplus of electrons, which are assumed to reside on the *M* atoms, leading to formation of polycationic networks containing *M*–*M* bonds. Within the *A*-Ge-As (*A* = alkali or alkaline-earth metal) systems, the only known phases reported so far are Na_5GeAs_3,[2] K_2GeAs_2,[3] and $BaGe_2As_2$[4]. The latter is a polycationic compound with Ge atoms in homoatomic bonding arrangements of infinite *cis*-*trans* chains, consistent with the presence of Ge^{2+} species if oxidation states are assigned. A gas-phase molecular species $NaGeAs_3$ has also been proposed.[5]

As part of a broader investigation of other *A*-Ge-As phases, this chapter decribes the preparation and structure determination of the new compound $NaGe_6As_6$. Remarkably, it is related to the binary arsenide GeAs, a charge-balanced semiconducting compound that has so far been relatively little studied,[6–14] through intercalation of Na atoms between layers. We examine the implications of this relationship for the electronic structure.

5.2 Experimental

5.2.1. Synthesis

Na pieces (99.99 %), Ge ingots (99.999 %), and As lumps (99.999 %), all obtained from Alfa-Aesar and handled within an argon-filled glovebox, were combined in a 1:3:3 molar ratio (in an attempt to prepare "$NaGe_3As_3$"), loaded into an alumina crucible, and placed within a fused-silica tube which was evacuated and sealed. The tube was heated to 650 °C, held at this temperature for 10 d, and cooled to room temperature over 2 d. The product contained small needle-shaped crystals (typically 0.2 mm in length) which were selected under paraffin oil. Energy-dispersive X-ray (EDX) analysis of these crystals on a JEOL JSM-6010LA scanning electron microscope indicated a composition of $Na_{0.8(1)}Ge_{6.7(5)}As_{5.5(5)}$, which is close to the composition $NaGe_6As_6$ obtained from the structure determination. After this composition was established, the compound could also be prepared through reaction of a stoichiometric ratio (1:6:6) of the elements under the same heating conditions as above.

5.2.2. Structure Determination

A crystal of $NaGe_6As_6$ was mounted within a small droplet of paraffin oil and placed under a cold nitrogen gas stream on a Bruker PLATFORM diffractometer equipped with a SMART APEX II CCD area detector and a graphite-monochromated Mo $K\alpha$ radiation source. Intensity data were collected at –80 °C using ω scans with a width of 0.3° and an exposure time of 15 s per frame at 6 different ϕ angles. Face-indexed numerical absorption corrections were applied. Structure solution and refinement were carried out with use of the SHELXTL (version 6.12) program package.[15] The centrosymmetric monoclinic space group $C2/m$ was chosen on the basis of Laue symmetry, systematic absences, and intensity statistics. The initial positions for seven sites were located by Direct Methods. Of these sites, one (at 2*a*) was assigned as Na, three (at 4*i*) as Ge, and three (at 4*i*)

as As atoms on the basis of their coordination geometries; this model is the most chemically reasonable because it places the more electronegative As atoms as the coordinating atoms around the Na atoms. Because the scattering factors of Ge and As are similar, refinements of occupancies were generally unstable when sites were allowed to be mixed with both Ge and As. However, these refinements tended towards all Ge in the first set of three sites and all As in the second set of three sites. All sites were found to be fully occupied and had reasonable displacement parameters. Atomic positions were standardized with the program STRUCTURE TIDY.[16] The final refinement led to good agreement factors and a featureless difference electron density map. Crystal data and experimental details are listed in **Table 5-1**, positional and displacement parameters in **Table 5-2**, and interatomic distances in **Table 5-3**. Further details of the crystal structure investigation are available in CSD number 430531.

Table 5-1. Crystallographic data for $NaGe_6As_6$

formula	$NaGe_6As_6$
formula mass (amu)	908.05
space group	$C2/m$ (No. 12)
a, Å	22.063(2)
b, Å	3.8032(4)
c, Å	7.2020(8)
β, (º)	92.7437(15)
V, Å^3	603.64(11)
Z	2
ρ_{calcd}, g cm^{-3}	5.00
T, K	193(2)
crystal dimensions, mm^3	0.22 × 0.04 × 0.03
radiation	graphite monochromated Mo $K\alpha$, λ = 0.71073 Å
μ(Mo $K\alpha$), mm^{-1}	31.1
transmission factors	0.128–0.547
2θ limits, (º)	3.70–66.44
data collected	$-33 \le h \le 32$, $-5 \le k \le 5$, $-10 \le l \le 10$
no. of data collected	4333
no. of unique data, including $F_o^2 < 0$	1270 (R_{int} = 0.034)
no. of unique data, with $F_o^2 > 2\sigma(F_o^2)$	1039
no. of variables	42
$R(F)$ for $F_o^2 > 2\sigma(F_o^2)$ [a]	0.026
$R_w(F_o^2)$ [b]	0.063
goodness of fit	1.040
$(\Delta\rho)_{max}$, $(\Delta\rho)_{min}$, e Å^{-3}	1.91, –2.35

[a] $R(F) = \sum||F_o| - |F_c|| / \sum|F_o|$. [b] $R_w(F_o^2) = [\sum[w(F_o^2 - F_c^2)^2] / \sum wF_o^4]^{1/2}$; $w^{-1} = [\sigma^2(F_o^2) + (Ap)^2 + Bp]$, where $p = [\max(F_o^2,0) + 2F_c^2] / 3$.

Table 5-2. Atomic coordinates and equivalent isotropic displacement parameters for $NaGe_6As_6$

Atom	**Wyckoff position**	***x***	***y***	***z***	U_{eq}, Å^2 [a]
Na	2*a*	0	0	0	0.0473(13)
Ge1	4*i*	0.05379(3)	0	0.46855(9)	0.0106(1)
Ge2	4*i*	0.31904(3)	0	0.33205(8)	0.0109(1)
Ge3	4*i*	0.31982(3)	0	0.67334(9)	0.0111(1)
As1	4*i*	0.11796(3)	0	0.76009(8)	0.0122(1)
As2	4*i*	0.22100(3)	0	0.15772(9)	0.0131(1)
As3	4*i*	0.57094(2)	0	0.25992(8)	0.0109(1)

[a] U_{eq} is defined as one-third of the trace of the orthogonalized U_{ij} tensor.

Table 5-3. Interatomic distances (Å) for $NaGe_6As_6$

Na–As3 (×4)	3.0478(5)	Ge2–Ge3	2.4572(9)
Na–As1 (×2)	3.1921(6)	Ge2–As2	2.4487(8)
Ge1–Ge1	2.4376(11)	Ge2–As1 (×2)	2.4651(6)
Ge1–As3 (×2)	2.4640(6)	Ge3–As3	2.4349(8)
Ge1–As1	2.4755(9)	Ge3–As2 (×2)	2.4520(6)

5.2.3. Band Structure Calculations

Tight-binding linear muffin tin orbital band structure calculations were performed on GeAs and $NaGe_6As_6$ within the local density and atomic spheres approximation with use of the Stuttgart TB-LMTO-ASA program (version 4.7).[17] The basis set consisted of Na 3s/3p/3d, Ge 4s/4p/4d, and As 4s/4p/4d orbitals, with the Na 3p/3d, Ge 4d, and As 4d orbitals being downfolded. Integrations in

reciprocal space were carried out with an improved tetrahedron method over 164 (for GeAs) or 242 irreducible *k* points (for $NaGe_6As_6$) within the first Brillouin zone.

5.3. Results and Discussion

$NaGe_6As_6$ is a new phase in the Na-Ge-As system, in which Na_5GeAs_3 and $NaGeAs_3$ were the only previously reported representatives. Na_5GeAs_3 is a Zintl phase that contains Na^+ cations and $[Ge_2As_6]^{10-}$ anions in the form of discrete edge-sharing tetrahedral units.[2] $NaGeAs_3$ was prepared in a Knudsen cell and is proposed to consist of gaseous "Zintl molecules" that are aggregates of Na^+ cations and $[GeAs_3]^-$ anions in the form of tetrahedral clusters isoelectronic to As_4.[5]

The structure of $NaGe_6As_6$ is of a new monoclinic type (space group *C*2/*m*) containing $[Ge_6As_6]$ layers alternately stacked with Na atoms along the *c* direction (**Figure 5-1a**). Each layer is built by condensing chains of edge-sharing octahedra, each centred by Ge–Ge dumbbells, extending along the *b* direction (**Figure 5-1b**). There are two types of Ge_2As_6 units, each of which resembles ethane in staggered conformation. These units are oriented so that Ge1–Ge1 pairs lie roughly parallel to the layers whereas Ge2–Ge3 pairs lie perpendicular to the layers. The sequence of these pairs (one horizontal Ge1–Ge1 pair followed by two vertical Ge2–Ge3 pairs) as they propagate along the *a* direction leads to a characteristic motif of two five-membered rings fused to opposite sides of a central six-membered ring. The Na atoms lying between the layers are surrounded by six As atoms in octahedral coordination. Other structures containing ethane-like Ge_2As_6 units have been previously reported in only a few examples: GeAs,[12] $A_3Ge_2As_4$ (*A* = Ca, Sr),[18] $ACdGeAs_2$ (*A* = K, Rb),[19] $K_5In_5Ge_5As_{14}$,[20] and $K_8In_8Ge_5As_{17}$[20] (the latter two exhibit disorder of In and Ge atoms). Similar motifs of fused 5-6-5 rings are found in $K_5In_5Ge_5As_{14}$[20] and Ga_3Te_3I[21].

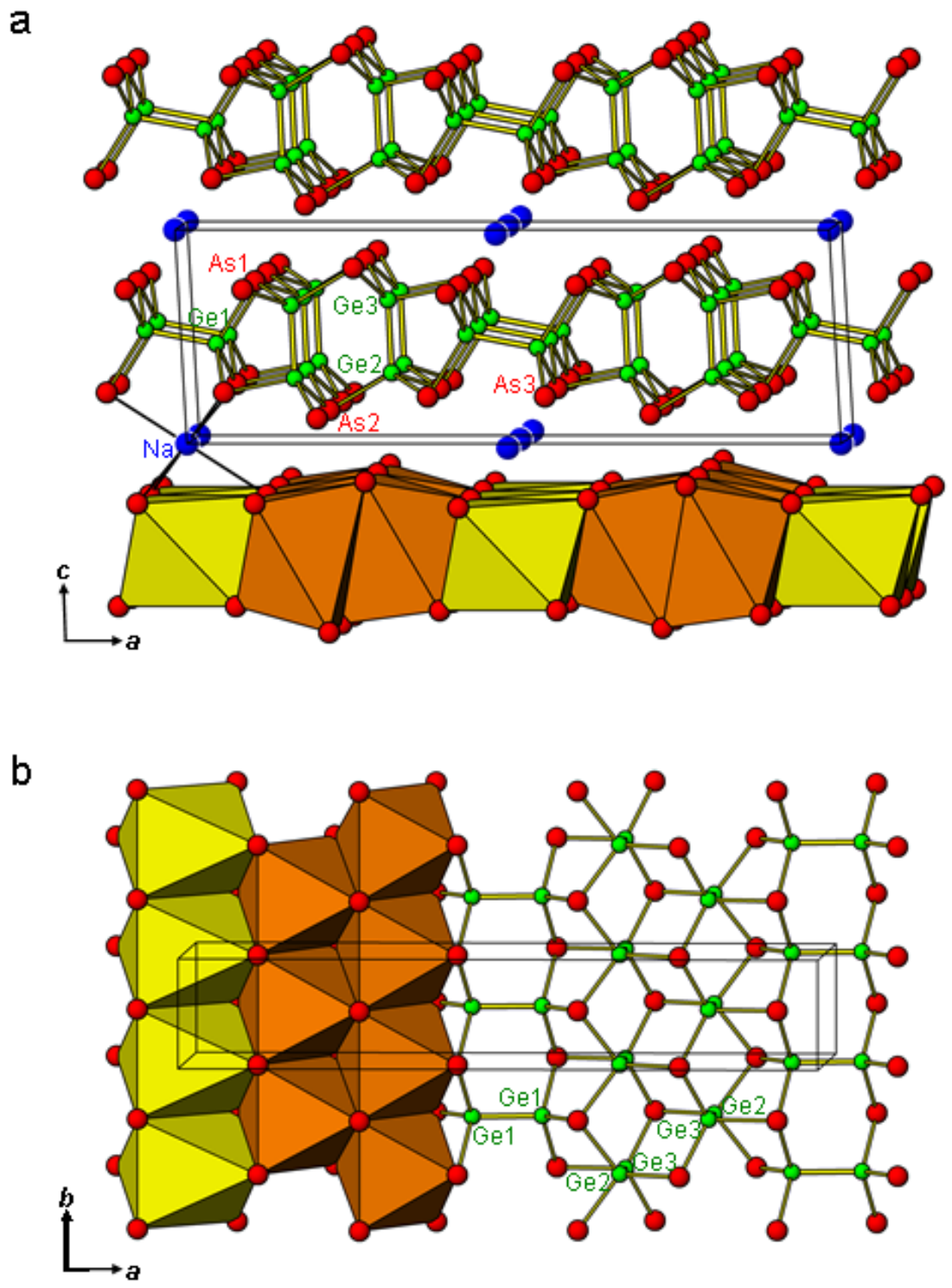

Figure 5-1. Structure of $NaGe_6As_6$ viewed (a) down the b direction, showing the stacking of layers and (b) down the c direction, showing a layer built up of edge-sharing octahedra centred by Ge–Ge dumbbells. The octahedral coordination geometry is highlighted around one of the Na atoms in (a).

The $[Ge_6As_6]$ layers in $NaGe_6As_6$ are the same as those found in the binary arsenide GeAs (**Figure 5-2**). As the layers are stacked, they are in perfect registry in $NaGe_6As_6$ but they are displaced with respect to each other in GeAs. Both structures can also be regarded as being built from rumpled close-packed nets of As atoms stacked in an hcp (AB) arrangement, with Ge–Ge dumbbells centred in the octahedral sites between alternate pairs of layers. This viewpoint draws an analogy to the CdI_2-type structure: when half of all available octahedral sites are filled with Ge–Ge dumbbells within a close-packed array of As atoms, the resulting formula is $\square_{1/2}(Ge_2)_{1/2}(As)$, or GeAs. When a third of the remaining vacant octahedral sites between the GeAs layers is occupied by Na atoms, the resulting formula is $\square_{2/6}(Na)_{1/6}(Ge_2)_{1/2}(As)$, or $NaGe_6As_6$. This relationship is similar to the intercalation of guest atoms within layered transition-metal dichalcogenides.[22]

The possibility that the Ge and As atoms are not ordered, as was assumed in the structure refinement, must be considered given their similar X-ray scattering factors. Evidence to support the ordered model comes from an analysis of the bond valence sums,[23] which are 1.3 for the Na atom, 3.5–3.6 for the Ge atoms, and 2.6–3.0 for the As atoms, in agreement with the expected valences. If the assignments of Ge and As atoms are reversed, the bond valence sums would show worse agreement.

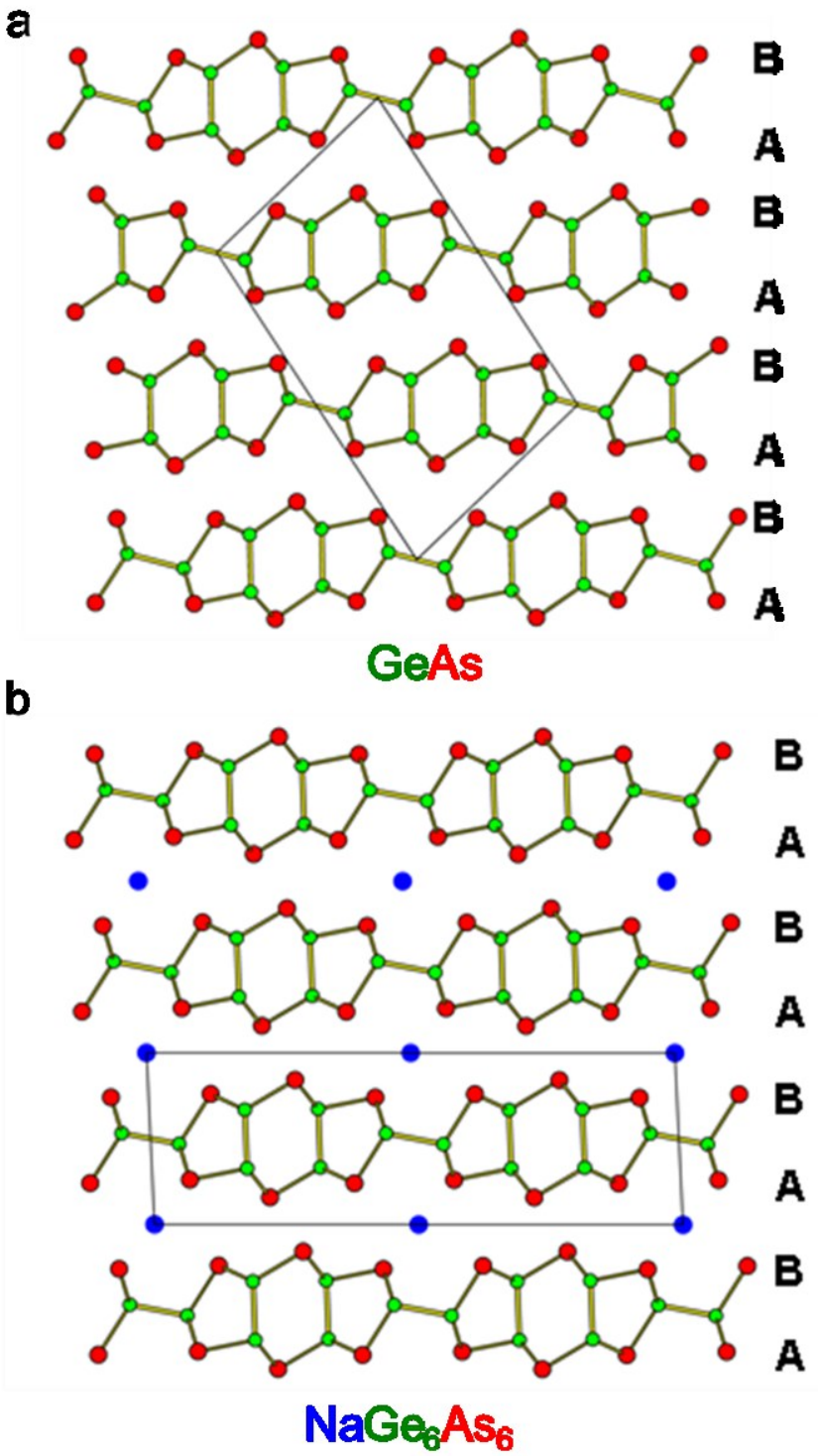

Figure 5-2. Comparison of the monoclinic structures of (a) GeAs and (b) $NaGe_6As_6$, both built from similar layers formed by filling octahedral sites with Ge–Ge dumbbells within an hcp stacking of rumpled close-packed As nets.

The derivation of $NaGe_6As_6$ by insertion of Na atoms into GeAs poses interesting questions about how the electronic structure is affected. GeAs itself can be considered to be a polycationic Zintl phase, attaining the charge-balanced formulation $(Ge^{3+})(As^{3-})$ consistent with the presence of homoatomic Ge–Ge bonds within the dumbbells. (SiAs,[10, 24, 25] GeP,[10, 26] and GaTe[27] are the only other known compounds isostructural to GeAs.) On proceeding from GeAs[12] to $NaGe_6As_6$, there is virtually no change in the Ge–As (2.44(1)–2.47(1) vs. 2.4349(8)–2.4755(9) Å) and Ge–Ge distances (2.43(1)–2.46(1) vs. 2.4376(11)–2.4572(9) Å). It is reasonable to propose that electron transfer will take place from the Na atoms to the rest of the framework to give the formulation $Na^+[Ge_6As_6]^-$. If this increase in electron count is assumed to cause local chemical reduction of the Ge atoms, corresponding to the formulation $(Na^+)(Ge^{2.83+})_6(As^{3-})_6$, one expects a strengthening of the Ge–Ge bonds, but this is not reflected in the observed distances. Interestingly, although insertion of Na atoms pries the layers further apart (the centre-to-centre distance between the layers expands from 6.4 to 7.2 Å), the closest As–As separation in the gap between the layers actually decreases slightly from 3.34(1) Å in GeAs to 3.270(1) Å in $NaGe_6As_6$. These As–As distances are certainly too long to be considered as fully covalent bonds, but it is notable that they are quite a bit shorter than twice the van der Waals radius of As (4.0 Å).[28]

The absence of significant structural changes within the layers implies that the major electronic effect of introducing Na atoms into GeAs is to essentially produce an *n*-doped semiconductor. This picture is confirmed by comparing the electronic band structures of GeAs and $NaGe_6As_6$. The density of states (DOS) curve for GeAs clearly reveals valence and conduction bands separated by a gap of 0.58 eV (**Figure 5-3a**), which agrees fortuitously well with an optical band gap of 0.65 eV reported in early experimental measurements.[11] The atomic projections of the DOS show that, as a result of the similar energies of Ge and As atomic orbitals, there is a strong

hybridization of these states, which are dominated by 4s character at lowest energy (–14 to –6 eV) and by 4p character at higher energy (–5 to 0 eV). The crystal orbital Hamilton population (COHP) curves indicate that the filled valence bands correspond to Ge–As and Ge–Ge bonding levels. If a rigid band model is applied and the electron count is increased by one, corresponding to $NaGe_6As_6$, the Fermi level would be raised so that it lies at the bottom of the conduction band. Because antibonding levels now start to be occupied, the expectation is that Ge–As and Ge–Ge bonds will be weakened, or the structure may undergo distortion to avoid this situation. The DOS curve for the actual structure of $NaGe_6As_6$ (**Figure 5-3b**) is very similar to that of GeAs. The calculated band gap is slightly larger (0.64 eV) and the Fermi level just cuts the bottom of the conduction band. The bonds do weaken, but only very slightly; the integrated COHP values (–ICOHP) change from 2.61 to 2.56 eV/bond for the Ge–As contacts and from 2.74 to 2.66 eV/bond for the Ge–Ge contacts on proceeding from GeAs to $NaGe_6As_6$. This small destabilization will, of course, be compensated by ionic bonding interactions between the Na atoms and the layers. The situation is reminiscent of $Ba_7Ga_4Sb_9$, an "electron-rich metallic Zintl phase" in which the apparent violation of charge balance can be reconciled by recognizing the important stabilizing role of the cations.[29, 30] Except for the region around the Na atoms in $NaGe_6As_6$, the layers are non-interacting and held together only by van der Waals forces, as confirmed by the small and negative –ICOHP values for the interlayer As–As contacts (–0.03 eV/bond in GeAs and –0.10 eV/bond in $NaGe_6As_6$).

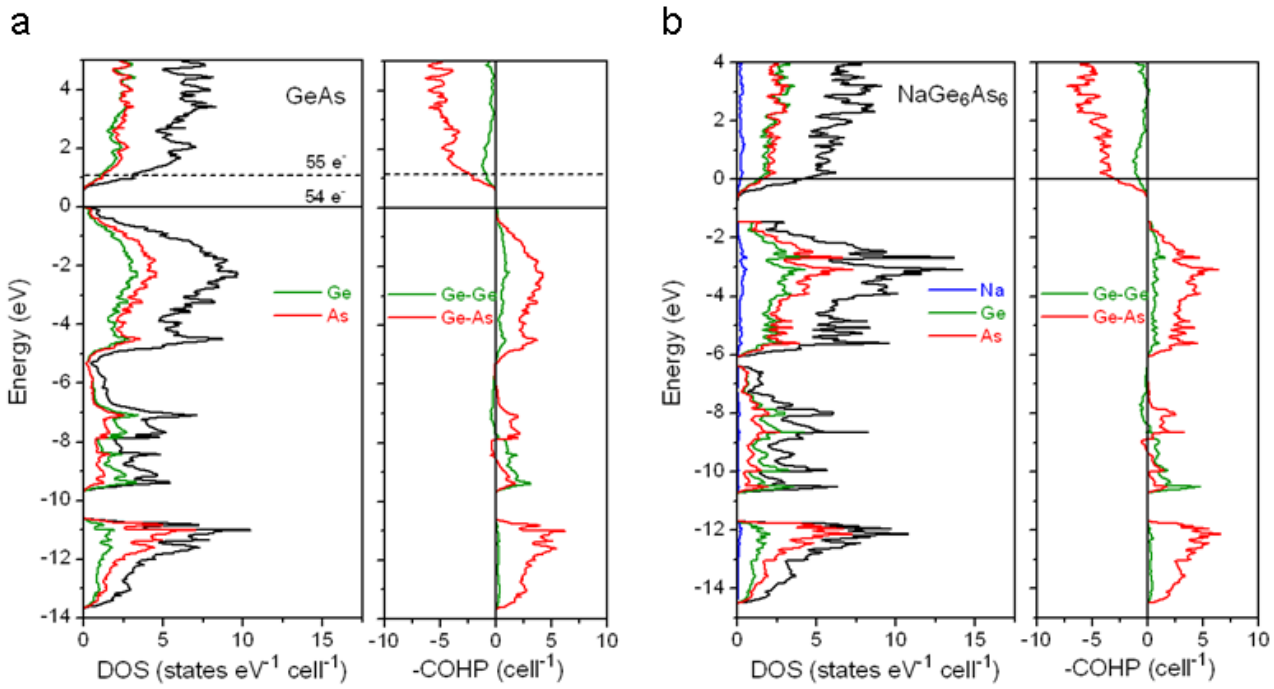

Figure 5-3. Density of states (DOS) and crystal orbital Hamilton population (–COHP) curves for (a) GeAs and (b) $NaGe_6As_6$.

5.4. Conclusion

The successful preparation of $NaGe_6As_6$ suggests that the GeAs structure can tolerate modest changes of its electron count; it may thus be amenable to doping within layers or intercalation between layers by other elements. To establish if the proposed description of intercalation is accurate, it will be important to perform experiments to attempt deintercalation of $NaGe_6As_6$. Moreover, the physical properties will be expected to be modified; for example, metallic-like electrical conductivity can be predicted for $NaGe_6As_6$. It will be worthwhile to examine other compounds that are isostructural to GeAs, such as SiAs, or those with related layered structures, such as GaS and GaSe,[31–35] to see if they can also accommodate guest atoms between the layers.

The crystal and electronic structures of ternary pnictides in *A–M–Pn* and *A–Tt–Pn* systems are highly varied. Compounds having an *A*-to-*Pn* ratio of 1:2 to 1:3 follow the Zintl concept, but those having an *A*-to-*Pn* ratio of less than 2 are electron-deficient and those having an *A*-to-*Pn* ratio

greater than 3 are electron-rich. To introduce further complexity, quaternary alkali-metal pnictides containing both transition metals and tetrels in the *A–M–Tt–Pn* systems have been investigated, as presented in the next two chapters.

5.5. References

1. Eisenmann, B.; Cordier, G. In *Chemistry, Structure, and Bonding of Zintl Phases and Ions*; Kauzlarich, S. M., Ed.; VCH: New York, 1996; pp 61–137.
2. Eisenmann, B.; Klein, J.; Somer, M. *Z. Kristallogr.* **1991**, *197*, 265–266.
3. Eisenmann, B.; Klein, J. *J. Less-Common Met.* **1991**, *175*, 109–117.
4. Eisenmann, B.; Schäfer, H. *Z. Naturforsch.* **1981**, *36b*, 415–419.
5. Poth, L.; Weil, K. G. *Ber. Bunsenges. Phys. Chem.* **1992**, *96*, 1621–1626.
6. Stöhr, H.; Klemm, W. *Z. Anorg. Allg. Chem.* **1940**, *244*, 205–223.
7. Schubert, K.; Dörre, E.; Günzel, E. *Naturwissenschaften* **1954**, *41*, 448.
8. Hulliger, F.; Mooser, E. *J. Phys. Chem. Solids* **1963**, *24*, 283–295.
9. Bryden, J. H. *Acta Crystallogr.* **1962**, *15*, 167–171.
10. Wadsten, T. *Acta Chem. Scand.* **1967**, *21*, 593–594.
11. Rau, J. W.; Kannewurf, C. R. *Phys. Rev. B* **1971**, *3*, 2581–2587.
12. Mentzen, B. F.; Hillel, R.; Michaelides, A.; Tranquard, A.; Bouix, J. *C. R. Acad. Sci., Ser. II* **1981**, *293*, 965–967.
13. Mead, D. G. *Infrared Phys.* **1982**, *22*, 209–213.
14. Olesinski, R. W.; Abbaschian, G. J. *Bull. Alloy Phase Diagrams* **1985**, *6*, 250–254.
15. Sheldrick, G. M. *SHELXTL*, version 6.12; Bruker AXS Inc.: Madison, WI, 2001.
16. Gelato, L. M.; Parthé, E. *J. Appl. Crystallogr.* **1987**, *20*, 139–143.
17. Tank, R.; Jepsen, O.; Burkhardt, A.; Andersen, O. K. *TB-LMTO-ASA Program*, version 4.7; Max Planck Institut für Festkörperforschung: Stuttgart, Germany, 1998.
18. Eisenmann, B.; Schäfer, H. *Z. Anorg. Allg. Chem.* **1982**, *484*, 142–152.
19. Khatun, M.; Stoyko, S. S.; Mar, A. *Inorg. Chem.* **2014**, *53*, 7756–7762.
20. Shreeve-Keyer, J. L.; Haushalter, R. C.; Lee, Y.-S.; Li, S.; O'Connor, C. J.; Seo, D.-K.; Whangbo, M.-H. *J. Solid State Chem.* **1997**, *130*, 234–249.
21. Paashaus, S.; Kniep, R. *Angew. Chem., Int. Ed. Engl.* **1986**, *25*, 752–753.
22. Yuan, H.; Wang, H.; Cui, Y. *Acc. Chem. Res.* **2015**, *48*, 81–90.
23. O'Keeffe, M.; Brese, N. E. *J. Am. Chem. Soc.* **1991**, *113*, 3226–3229.
24. Wadsten, T. *Acta Chem. Scand.* **1965**, *19*, 1232–1238.
25. Wadsten, T. *Acta Chem. Scand.* **1969**, *23*, 331–333.

26. Lee, K.; Synnestvedt, S.; Bellard, M.; Kovnir, K. *J. Solid State Chem.* **2015**, *224*, 62–70.

27. Blachnik, R.; Irle, E. *J. Less-Common Met.* **1985**, *113*, L1–L3.

28. Pauling, L. *The Nature of the Chemical Bond*, 3rd ed.; Cornell University Press: Ithaca, NY, 1960.

29. Alemany, P.; Alvarez, S.; Hoffmann, R. *Inorg. Chem.* **1990**, *29*, 3070–3073.

30. Alemany, P.; Llunell, M.; Canadell, E. *Inorg. Chem.* **2006**, *45*, 7235–7241.

31. Hahn, H.; Frank, G. *Z. Anorg. Allg. Chem.* **1955**, *278*, 340–348.

32. Kuhn, A.; Chevalier, R.; Rimsky, A. *Acta Crystallogr., Sect. B* **1975**, *31*, 2841–2842.

33. Kuhn, A.; Chevy, A. *Acta Crystallogr.* **1976**, *B32*, 983–984.

34. d'Amour, H.; Holzapfel, W. B.; Polian, A.; Chevy, A. *Solid State Commun.* **1982**, *44*, 852–855.

35. Benazeth, S.; Dung, N.-H.; Guittard, M.; Laruelle, P. *Acta Crystallogr., Sect. C* **1988**, *44*, 234–236.

Chapter 6

Quaternary Arsenides $AM_{1.5}Tt_{0.5}As_2$ (A = Na, K, Rb; M = Zn, Cd; Tt = Si, Ge, Sn): Size Effects in $CaAl_2Si_2$- and $ThCr_2Si_2$-Type Structures

A version of this chapter has been published. Khatun, M.; Stoyko, S. S.; Mar, A. Inorg. Chem. 2013, 52, 3148–3158.

6.1 Introduction

Ternary phases AB_2X_2 are formed for many combinations of components A (alkali, alkaline-earth, or rare-earth metal), B (transition metal or main-group metalloid), and X (element from groups 13–16).[1] Most adopt the tetragonal $ThCr_2Si_2$-type structure, which serves as the prototype for many materials with interesting physical properties such as superconductivity (e.g. doped $BaFe_2As_2$).[2] However, many also adopt the trigonal $CaAl_2Si_2$-type structure, which appears to be more limited because of stricter electronic requirements. With few exceptions, the valence electron count must satisfy 16 e^-/f.u. and the B component should have filled or half-filled d-electron configurations (d^0, d^5, or d^{10}).[3–10] Because these conditions typically lead to small band gap semiconducting behaviour, these compounds have been identified as promising candidates for thermoelectric materials (e.g. doped $YbZn_2Sb_2$ and $YbCd_2Sb_2$).[11–15] Notwithstanding these restrictions, there is still a wide variety of A, B, and X components that can be chosen while maintaining charge balance. In fact, quaternary representatives of the $CaAl_2Si_2$-type structure can be prepared through appropriate aliovalent substitution, as exemplified by our recent investigation of the quaternary rare-earth phosphides $RECuZnP_2$ in which Cu and Zn atoms are disordered over

the single *B* site.[16] In hopes of expanding the versatility of the $CaAl_2Si_2$-type structure, we are interested in exploring what other combinations of metal components *A* and *B* could be successful in affording further quaternary representatives.

This chapter represents the synthesis of new quaternary arsenides $AM_{1.5}Tt_{0.5}As_2$ derived from combinations of an alkali metal (*A* = Na, K, Rb), a group-12 metal (*M* = Zn, Cd), and a tetrel (*Tt* = Si, Ge, Sn). They segregate into two groups, adopting either $CaAl_2Si_2$- or $ThCr_2Si_2$-type structures. Because the valence electron count is constant (16 e^-/f.u.), an attractive opportunity is available to examine the size effects that influence the formation of the $CaAl_2Si_2$- vs. $ThCr_2Si_2$-type structures in this series of compounds. Their bonding and electronic structures are further analyzed through band structure calculations.

6.2 Experimental

6.2.1. Synthesis

Starting materials were Na, K, and Rb pieces, Zn and Cd shot, Si, Ge, and Sn ingots or granules, and As lumps, all with purities greater than 99.9% and obtained from Alfa-Aesar, Aldrich, or other local sources. All reagents and products were handled within an argon-filled glovebox. Stoichiometric mixtures of the elements were loaded into alumina crucibles placed within fused-silica tubes, which were evacuated and sealed. The tubes were heated to 650 °C (for Na and K samples) or 600 °C (for Rb samples) over 2 d, held at that temperature for 10 d, and cooled to room temperature over 2 d. A different annealing temperature was used for the Rb samples because of the low boiling point for Rb metal (688 °C). The products were moderately air-sensitive, with the surfaces of crystals becoming visibly tarnished within minutes, and were thus handled under paraffin oil. Powder X-ray

diffraction (XRD) patterns were collected on an Inel diffractometer equipped with a curved position-sensitive detector (CPS 120) and a Cu $K\alpha_1$ radiation source operated at 40 kV and 20 mA. They confirmed that the quaternary arsenides $AM_{1.5}Tt_{0.5}As_2$ were generally formed as the major phase in each reaction, with ternary arsenides AM_4As_3 and $A_2M_5As_4$ found as the most common secondary phases.[17,18] Representative powder XRD patterns are provided in **Figure A 4-1** in **Appendix 4**. Quantitative yields were difficult to achieve because many of the elemental components (particularly the alkali metals, Zn, Cd, Sn, and As) as well as possible intermediate binary phases (e.g. Zn_3As_2, Cd_3As_2, $ZnAs_2$, $CdAs_2$) are highly volatile, which posed problems in maintaining the correct overall composition of the melt. To account for mass balance, Si- or Ge-containing phases may be present in amorphous form, but these would be masked under the large background (subtracted from the patterns) resulting from the paraffin oil. Single crystals of the title compounds were selected under paraffin oil and their chemical compositions were determined by energy-dispersive X-ray (EDX) analysis on a JEOL JSM-6010LA scanning electron microscope. Representative SEM images of these crystals are shown in **Figure A 4-2** in **Appendix 4**. The EDX results, averaged over multiple spectra for several crystals of each compound, are summarized in **Table A 4-1** in **Appendix 4**. In those cases where peaks belonging to different elements overlap in the EDX spectra, the combined atomic percentages were calculated. In general, the experimental compositions for $AM_{1.5}Tt_{0.5}As_2$ were within 1–2 at. % of the expected values (20% *A*, 30% *M*, 10% *Tt*, 40% As). The observation of precise compositions for these crystals, which were selected from products containing mixtures of phases, implies that the quaternary arsenides $AM_{1.5}Tt_{0.5}As_2$ do not exhibit homogeneity ranges.

6.3.1. Structure Determination

Single crystals were selected under paraffin oil, mounted on glass fibers, and placed under a cold nitrogen gas stream on a Bruker PLATFORM diffractometer equipped with a SMART APEX II CCD detector and a Mo $K\alpha$ radiation source. Full spheres of intensity data were collected at –100 °C using ω scans with a scan width of 0.3° and an exposure time of 12–15 s per frame in 5–7 batches. Face-indexed numerical absorption corrections were applied. Structure solution and refinement were carried out with use of the SHELXTL (version 6.12) program package.[19]

Table 6-1. Crystallographic data for $AM_{1.5}Tt_{0.5}As_2$ compounds with $CaAl_2Si_2$-type structure

formula	$NaZn_{1.47(2)}Si_{0.53(2)}As_2$	$NaZn_{1.50}Ge_{0.50}As_2$	$NaZn_{1.49(6)}Sn_{0.49(3)}As_2$	$NaCd_{1.48(1)}Sn_{0.50}As_2$
formula mass (amu)	284.93	307.18	330.23	400.77
space group	$P\bar{3}m1$ (No. 164)	$P\bar{3}m1$ (No. 164)	$P\bar{3}m1$ (No. 164)	$P\bar{3}m1$ (No. 164)
a (Å)	4.0662(3)	4.0948(3)	4.1637(2)	4.3726(2)
c (Å)	7.4120(5)	7.4463(5)	7.5090(4)	7.4647(4)
V (Å^3)	106.13(1)	108.13(1)	112.74(1)	123.60(1)
Z	1	1	1	1
ρ_{calcd} (g cm^{-3})	4.458	4.717	4.864	5.384
T (K)	173(2)	173(2)	173(2)	173(2)
crystal dimensions (mm)	0.04 × 0.06 × 0.12	0.03 × 0.20 × 0.20	0.05 × 0.08 × 0.10	0.08 × 0.13 × 0.14
radiation	graphite monochromated Mo $K\alpha$, λ = 0.71073 Å			
μ(Mo $K\alpha$) (mm^{-1})	24.03	26.85	25.19	22.15
transmission factors	0.178–0.494	0.066–0.520	0.198–0.419	0.130–0.291
2θ limits	5.50–66.00°	5.48–66.18°	5.42–66.28°	5.46–66.18°
data collected	$-6 \le h \le 6$, $-6 \le k \le 6$, $-11 \le l \le 11$	$-6 \le h \le 6$, $-6 \le k \le 6$, $-11 \le l \le 11$	$-6 \le h \le 6$, $-6 \le k \le 6$, $-11 \le l \le 11$	$-6 \le h \le 6$, $-6 \le k \le 6$, $-11 \le l \le 11$
no. of data collected	1473	1488	1571	1724
no. of unique data, including $F_o^2 < 0$	189 (R_{int} = 0.027)	191 (R_{int} = 0.025)	198 (R_{int} = 0.020)	215 (R_{int} = 0.009)
no. of unique data, with $F_o^2 > 2\sigma(F_o^2)$	183	187	190	211
no. of variables	11	10	15	14
$R(F)$ for $F_o^2 > 2\sigma(F_o^2)$ [a]	0.023	0.032	0.014	0.024
$R_w(F_o^2)$ [b]	0.048	0.085	0.034	0.060
goodness of fit	1.20	1.35	1.16	1.27
$(\Delta\rho)_{max}$, $(\Delta\rho)_{min}$ (e Å^{-3})	1.88, –2.03	2.09, –2.68	0.55, –0.87	1.01, –2.21

formula	$KZn_{1.54(1)}Sn_{0.46(1)}As_2$	$KCd_{1.50}Sn_{0.50}As_2$	$RbCd_{1.50}Sn_{0.50}As_2$
formula mass (amu)	346.34	416.89	463.26
space group	$P\bar{3}m1$ (No. 164)	$P\bar{3}m1$ (No. 164)	$P\bar{3}m1$ (No. 164)
a (Å)	4.1985(5)	4.4174(3)	4.4263(7)
c (Å)	8.1471(9)	8.1638(5)	8.4586(14)
V (Å^3)	124.37(3)	137.96(2)	143.52(4)
Z	1	1	1
ρ_{calcd} (g cm^{-3})	4.624	5.018	5.360
T (K)	173(2)	173(2)	173(2)
crystal dimensions (mm)	0.07 × 0.14 × 0.16	0.04 × 0.10 × 0.10	0.04 × 0.04 × 0.12
radiation	graphite monochromated Mo $K\alpha$, λ = 0.71073 Å		
μ(Mo $K\alpha$) (mm^{-1})	23.59	20.52	27.43
transmission factors	0.106–0.348	0.254–0.514	0.200–0.491
2θ limits	5.00–66.18°	4.98–66.26°	4.82–65.86°
data collected	$-6 \le h \le 6$, $-6 \le k \le 6$, $-12 \le l \le 12$	$-6 \le h \le 6$, $-6 \le k \le 6$, $-12 \le l \le 12$	$-6 \le h \le 6$, $-6 \le k \le 6$, $-12 \le l \le 12$
no. of data collected	1776	1966	2034
no. of unique data, including $F_o^2 < 0$	219 (R_{int} = 0.019)	236 (R_{int} = 0.017)	246 (R_{int} = 0.014)
no. of unique data, with $F_o^2 > 2\sigma(F_o^2)$	216	230	242
no. of variables	12	10	10
$R(F)$ for $F_o^2 > 2\sigma(F_o^2)$ [a]	0.013	0.018	0.023
$R_w(F_o^2)$ [b]	0.032	0.044	0.061
goodness of fit	1.17	1.22	1.19
$(\Delta\rho)_{max}$, $(\Delta\rho)_{min}$ (e Å^{-3})	1.76, –0.78	1.72, –2.45	3.63, –1.75

[a] $R(F) = \sum||F_o| - |F_c|| / \sum|F_o|$. [b] $R_w(F_o^2) = [\sum[w(F_o^2 - F_c^2)^2] / \sum wF_o^4]^{1/2}$; $w^{-1} = [\sigma^2(F_o^2) + (Ap)^2 + Bp]$, where $p = [\max(F_o^2,0) + 2F_c^2] / 3$

For seven of the quaternary arsenides $AM_{1.5}Tt_{0.5}As_2$, the trigonal space group $P\bar{3}m1$ was chosen and the initial atomic positions found by direct methods were consistent with the $CaAl_2Si_2$-type structure.[20] In this structure type normally adopted by ternary phases AB_2X_2, there are three sites available to accommodate the *A*, *B*, and *X* components. We assumed that the group-12 transition metal (*M* = Zn, Cd) and tetrel (*Tt* = Si, Ge, Sn) atoms were disordered within the single available *B* site (at Wyckoff position 2*d*: 1/3, 2/3, ~0.6). However, the appropriate treatment of disorder depended on the particular combination of *M* and *Tt* atoms, which we detail separately on a case-by-case basis below. Each case is instructive for the crystallographic problems posed. Crystal data and further experimental details are given in **Table 6-1**.

For $NaZn_{1.5}Ge_{0.5}As_2$, $KCd_{1.5}Sn_{0.5}As_2$, and $RbCd_{1.5}Sn_{0.5}As_2$, the *M* and *Tt* components differ by only two in atomic number and their X-ray scattering factors are too similar to permit discrimination. If the occupancies of *M* and *Tt* atoms within the *B* site were allowed to vary freely, with the constraint that they sum to unity but with no consideration placed on overall charge balance in the formula, the refinements were generally unstable. In some cases, carefully introducing damping in the refinements eventually led to convergence, but the uncertainties in the occupancies were either large or the resulting formula deviated significantly from expectations (e.g., "$KCd_{1.67(2)}Sn_{0.33(2)}As_2$"), in contradiction to the EDX results. Thus, the occupancies were fixed to be exactly 0.75 *M* and 0.25 *Tt* within this *B* site in the final refinements of these structures.

For $NaZn_{1.5}Si_{0.5}As_2$ and $KZn_{1.5}Sn_{0.5}As_2$, the *M* and *Tt* components should be easily distinguishable by their X-ray scattering factors. When their occupancies within the *B* site

were freed, they converged to 0.736(5) Zn / 0.264(5) Si and 0.816(15) Zn / 0.184(15) Sn, resulting in the formulas $NaZn_{1.47(1)}Si_{0.53(1)}As_2$ and $KZn_{1.63(3)}Sn_{0.37(3)}As_2$, respectively. The former is reasonable whereas the latter deviates a bit far from expectations. Subsequently, an analysis of the crystallographic data (including structure factors) through checkCIF alerted us to the possibility of merohedral twinning (related by reflection normal to the *c*-axis). This twin component was minor (BASF of 0.03) but its inclusion dramatically cleaned up the difference electron density map and led to occupancies within the *B* site of 0.769(6) Zn / 0.232(6) Sn, corresponding to a formula, $KZn_{1.54(1)}Sn_{0.46(1)}As_2$, that is closer to expectations.

For $NaZn_{1.5}Sn_{0.5}As_2$ and $NaCd_{1.5}Sn_{0.5}As_2$, a further complication emerged in which a residual peak (6.0–8.0 $e^-/Å^3$) in the difference electron density map is found close to the *B* site. This site was thus split into two closely separated ones, now labeled *B*1 (the original site at 1/3, 2/3, ~0.6 with tetrahedral coordination) and *B*2 (a minor site at 1/3, 2/3, ~0.7 with trigonal planar coordination). Taking into account reasonable bond lengths, we proposed a structural model in which the *B*1 site, with its higher CN, is occupied by a mixture of Zn (or Cd) and Sn atoms, whereas the *B*2 site, with its lower CN, is occupied solely by Zn (or Cd) atoms. A restraint was applied such that the sum of the occupancies over these two sites is unity but none was placed on the sum of the charges. Furthermore, in the case of $NaCd_{1.5}Sn_{0.5}As_2$, the occupancy of Sn atoms entering the *B*1 site was fixed at exactly 0.25, because Cd and Sn cannot be easily distinguished by their scattering factors. Displacement parameters were kept isotropic for the *B*2 site. Reassuringly, the refinements led to formulas of $NaZn_{1.49(6)}Sn_{0.49(3)}As_2$ and $NaCd_{1.48(1)}Sn_{0.50}As_2$.

The structure determinations for the three remaining quaternary arsenides ($KZn_{1.5}Si_{0.5}As_2$, $KZn_{1.5}Ge_{0.5}As_2$, and $RbZn_{1.5}Ge_{0.5}As_2$) were more straightforward. The tetragonal space group *I*4/*mmm* was chosen and the initial atomic positions found by direct methods were consistent with the $ThCr_2Si_2$-type structure.[21,22] Ternary phases AB_2X_2 adopting this structure type have three sites available to be occupied. The Zn and Si (or Ge) atoms were assumed to disorder over the single available *B* site at 4*d* (0, 1/2, 1/4). As before, because Zn and Si can be distinguished but not Zn and Ge, we allowed the occupancies to vary in the former case (which led to the formula $KZn_{1.47(1)}Si_{0.53(1)}As_2$), but fixed them in the two latter cases. Crystal data and further experimental details are given in **Table 6-2**.

Table 6-2. Crystallographic data for $AM_{1.5}Tt_{0.5}As_2$ compounds with $ThCr_2Si_2$-type structure

formula	$KZn_{1.47(1)}Si_{0.53(1)}As_2$	$KZn_{1.50}Ge_{0.50}As_2$	$RbZn_{1.50}Ge_{0.50}As_2$
formula mass (amu)	301.04	323.29	369.66
space group	*I*4/*mmm* (No. 139)	*I*4/*mmm* (No. 139)	*I*4/*mmm* (No. 139)
a (Å)	4.0613(10)	4.0872(4)	4.1157(5)
c (Å)	14.258(3)	14.312(2)	14.662(2)
V (Å^3)	235.18(10)	239.08(4)	248.36(5)
Z	2	2	2
ρ_{calcd} (g cm^{-3})	4.251	4.491	4.943
T (K)	173(2)	173(2)	173(2)
crystal dimensions (mm)	0.04 × 0.04 × 0.15	0.03 × 0.08 × 0.10	0.02 × 0.09 × 0.11
radiation	graphite monochromated Mo $K\alpha$, λ = 0.71073 Å		
μ(Mo $K\alpha$) (mm^{-1})	22.48	25.07	33.03
transmission factors	0.137–0.558	0.191–0.634	0.113–0.526
2θ limits	5.72–66.50°	5.70–66.22°	5.56–66.50°
data collected	$-6 \le h \le 6$, $-6 \le k \le 6$, $-21 \le l \le 22$	$-6 \le h \le 6$, $-6 \le k \le 6$, $-22 \le l \le 22$	$-6 \le h \le 6$, $-6 \le k \le 6$, $-22 \le l \le 22$
no. of data collected	1639	1691	1744

no. of unique data, including $F_o^2 < 0$	171 (R_{int} = 0.019)	171 (R_{int} = 0.019)	176 (R_{int} = 0.030)
no. of unique data, with $F_o^2 > 2\sigma(F_o^2)$	158	160	161
no. of variables	10	9	9
$R(F)$ for $F_o^2 > 2\sigma(F_o^2)$ [a]	0.015	0.020	0.022
$R_w(F_o^2)$ [b]	0.034	0.038	0.043
goodness of fit	1.18	1.18	1.10
$(\Delta\rho)_{max}$, $(\Delta\rho)_{min}$ (e Å^{-3})	1.05, –0.72	1.23, –1.08	1.61, –1.63

[a] $R(F) = \sum||F_o| - |F_c|| / \sum|F_o|$. [b] $R_w(F_o^2) = [\sum[w(F_o^2 - F_c^2)^2] / \sum wF_o^4]^{1/2}$; $w^{-1} = [\sigma^2(F_o^2) + (Ap)^2 + Bp]$, where $p = [\max(F_o^2,0) + 2F_c^2] / 3$.

In all the treatments above, we have assumed that *Tt* and As atoms do not disorder within the *X* site in either the $CaAl_2Si_2$- or $ThCr_2Si_2$-type structures. However, there have been some precedents in the literature for mixing of Si or Ge with As atoms (such as our own earlier work on $Zr(Si_xAs_{1-x})As$ and $Zr(Ge_xAs_{1-x})As$).[23,24] The appropriate candidates for testing the possibility of *Tt*/As disorder are $NaZn_{1.5}Si_{0.5}As_2$ and $KZn_{1.5}Sn_{0.5}As_2$ among the $CaAl_2Si_2$-type phases and $KZn_{1.5}Si_{0.5}As_2$ among the $ThCr_2Si_2$-type phases, because the *Tt* and As components provide sufficient contrast in their X-ray scattering and there are no further complications from split sites. Refinements were then performed on models in which *Tt* atoms are allowed to enter *both* the *B* and *X* sites. The occupancies converged to the following values for the *B* and *X* sites, respectively: 0.71(1) Zn / 0.29(3) Si and 0.03(3) Si / 0.97(3) As for $NaZn_{1.5}Si_{0.5}As_2$; 0.75(1) Zn / 0.25(1) Sn and 0.02(1) Sn / 0.98(1) As for $KZn_{1.5}Sn_{0.5}As_2$; 0.75(1) Zn / 0.25(1) Si and 0.00(1) Si / 1.00(1) As for $KZn_{1.5}Si_{0.5}As_2$. These results provide convincing evidence that the *X* site is essentially occupied only by As atoms, and we extrapolate this conclusion to all members of the quaternary arsenides $AM_{1.5}Tt_{0.5}As_2$.

Atomic positions were standardized with the program STRUCTURE TIDY.[25] Final values of the positional and displacement parameters are given in **Tables 6-3 and 6-4**, and selected interatomic distances are listed in **Tables 6-5 and 6-6**. Further data in the form of crystallographic information files (CIFs) are available in CSD number 425474 to 425483.

Table 6-3. Atomic coordinates and equivalent isotropic displacement for $AM_{1.5}Tt_{0.5}As_2$ compounds with $CaAl_2Si_2$-type structure

Atom	Wyckoff position	Occupancy	*x*	*y*	*z*	U_{eq} (Å^2) [a]
$NaZn_{1.47(2)}Si_{0.53(2)}As_2$						
Na	1*a*	1	0	0	0	0.0207(8)
B	2*d*	0.733(8) Zn, 0.267(8) Si	1/3	2/3	0.6294(1)	0.0182(3)
As	2*d*	1	1/3	2/3	0.27155(9)	0.0187(3)
$NaZn_{1.50}Ge_{0.50}As_2$						
Na	1*a*	1	0	0	0	0.0202(11)
B	2*d*	0.75 Zn, 0.25 Ge	1/3	2/3	0.6287(2)	0.0199(4)
As	2*d*	1	1/3	2/3	0.2689(1)	0.0150(4)
$NaZn_{1.49(6)}Sn_{0.49(3)}As_2$						
Na	1*a*	1	0	0	0	0.0228(4)
*B*1	2*d*	0.64(3) Zn, 0.24(2) Sn	1/3	2/3	0.6286(1)	0.0171(2)
*B*2	2*d*	0.106(4) Zn	1/3	2/3	0.704(1)	0.012(1)
As	2*d*	1	1/3	2/3	0.26329(4)	0.0135(2)
$NaCd_{1.48(1)}Sn_{0.50}As_2$						
Na	1*a*	1	0	0	0	0.0253(9)
*B*1	2*d*	0.692(5) Cd, 0.25 Sn	1/3	2/3	0.6358(1)	0.0212(3)
*B*2	2*d*	0.050(4) Cd	1/3	2/3	0.721(2)	0.021(3)
As	2*d*	1	1/3	2/3	0.25018(9)	0.0188(3)
$KZn_{1.54(1)}Sn_{0.46(1)}As_2$						
K	1*a*	1	0	0	0	0.0170(2)
B	2*d*	0.769(6) Zn, 0.232(6) Sn	1/3	2/3	0.62324(5)	0.0154(2)
As	2*d*	1	1/3	2/3	0.28507(5)	0.0133(1)
$KCd_{1.50}Sn_{0.50}As_2$						
K	1*a*	1	0	0	0	0.0172(3)
B	2*d*	0.75 Cd, 0.25 Sn	1/3	2/3	0.62761(6)	0.0169(2)

As	2*d*	1	1/3	2/3	0.27332(9)	0.0164(2)
$RbCd_{1.50}Sn_{0.50}As_2$						
Rb	1*a*	1	0	0	0	0.0159(3)
B	2*d*	0.75 Cd, 0.25 Sn	1/3	2/3	0.62313(6)	0.0154(2)
As	2*d*	1	1/3	2/3	0.2824(1)	0.0155(3)

[a] U_{eq} is defined as one-third of the trace of the orthogonalized U_{ij} tensor.

Table 6-4. Atomic coordinates and equivalent isotropic displacement for $AM_{1.5}Tt_{0.5}As_2$ compounds with $ThCr_2Si_2$-type structure

Atom	**Wyckoff position**	**Occupancy**	***x***	***y***	***z***	**U_{eq} (Å^2) [a]**
$KZn_{1.47(1)}Si_{0.53(1)}As_2$						
K	2*a*	1	0	0	0	0.0217(3)
B	4*d*	0.736(5) Zn, 0.264(5) Si	0	1/2	1/4	0.0215(2)
As	4*e*	1	0	0	0.35483(3)	0.0237(2)
$KZn_{1.50}Ge_{0.50}As_2$						
K	2*a*	1	0	0	0	0.0205(4)
B	4*d*	0.75 Zn, 0.25 Ge	0	1/2	1/4	0.0244(2)
As	4*e*	1	0	0	0.35629(4)	0.0197(2)
$RbZn_{1.50}Ge_{0.50}As_2$						
Rb	2*a*	1	0	0	0	0.0188(3)
B	4*d*	0.75 Zn, 0.25 Ge	0	1/2	1/4	0.0241(3)
As	4*e*	1	0	0	0.35284(6)	0.0192(2)

[a] U_{eq} is defined as one-third of the trace of the orthogonalized U_{ij} tensor

Table 6-5. Interatomic distances (Å) in $AM_{1.5}Tt_{0.5}As_2$ compounds with $CaAl_2Si_2$-type structure [a]

	$NaZn_{1.47(2)}Si_{0.53(2)}As_2$	**$NaZn_{1.50}Ge_{0.50}As_2$**
A–As (×6)	3.0923(5)	3.0980(6)
A–*B* (×6)	3.6133(7)	3.6378(9)
B–As (×3)	2.4597(4)	2.4842(5)
B–As	2.6524(12)	2.6793(14)
B–*B* (×3)	3.0317(12)	3.0434(14)
	$NaZn_{1.49(6)}Sn_{0.49(3)}As_2$	**$NaCd_{1.48(1)}Sn_{0.50}As_2$**
A–As (×6)	3.1125(2)	3.1402(4)
A–*B*1 (×6) / *A*–*B*2 (×6)	3.6817(7) / 3.273(5)	3.7103(6) / 3.272(10)
*B*1–As (×3) / *B*2–As (×3)	2.5372(3) / 2.4162(7)	2.6643(3) / 2.5336(14)
*B*1–As	2.7433(9)	2.8781(10)
*B*1–*B*1 (×3)	3.0839(11)	3.2373(10)
	$KZn_{1.54(1)}Sn_{0.46(1)}As_2$	**$KCd_{1.50}Sn_{0.50}As_2$**
A–As (×6)	3.3571(4)	3.3887(5)
A–*B* (×6)	3.9112(4)	3.9682(4)
B–As (×3)	2.5365(3)	2.6756(3)
B–As	2.7551(6)	2.8924(9)
B–*B* (×3)	3.1478(6)	3.2933(6)
	$RbCd_{1.50}Sn_{0.50}As_2$	
A–As (×6)	3.4982(7)	
A–*B* (×6)	4.0857(6)	
B–As (×3)	2.6775(5)	
B–As	2.8819(11)	
B–*B* (×3)	3.2969(8)	

[a] Site *B* is occupied by a mixture of *M* (Zn or Cd) and *Tt* (Si, Ge, or Sn) atoms.

Table 6-6. Interatomic distances (Å) in $AM_{1.5}Tt_{0.5}As_2$ compounds with $ThCr_2Si_2$-type structure [a]

	$KZn_{1.47(1)}Si_{0.53(1)}As_2$	$KZn_{1.50}Ge_{0.50}As_2$	$RbZn_{1.50}Ge_{0.50}As_2$
A–As (×8)	3.5400(7)	3.5472(5)	3.6228(6)
A–*A* (×4)	4.0613(10)	4.0872(4)	4.1157(5)
B–As (×4)	2.5214(5)	2.5476(4)	2.5512(5)
B–*B* (×4)	2.8718(7)	2.8901(3)	2.9102(4)

[a] Site *B* is occupied by a mixture of *M* (Zn) and *Tt* (Si or Ge) atoms.

6.2.3. Band Structure Calculations

Tight-binding linear muffin tin orbital band structure calculations were performed within the local density and atomic spheres approximation with use of the Stuttgart TB-LMTO-ASA program (version 4.7).[26] The basis sets included Na 3s/3p/3d, K 4s/4p/3d, Zn 4s/4p/3d, Cd 5s/5p/4d/4f, Si 3s/3p/3d, Ge 4s/4p/4d, Sn 5s/5p/5d/4f, and As 4s/4p/4d orbitals, with the Na 3p/3d, K 4p/3d, Cd 4f, Si 3d, Ge 4d, Sn 5d/4f, and As 4d orbitals being downfolded. Integrations in reciprocal space were carried out with an improved tetrahedron method over 131 irreducible *k* points within the first Brillouin zone for $CaAl_2Si_2$-type superstructures, as described below.

Because the arsenides $AM_{1.5}Tt_{0.5}As_2$ exhibit site disorder of the *M* and *Tt* atoms, it was necessary to develop ordered model structures for these calculations. For both $CaAl_2Si_2$- and $ThCr_2Si_2$-type structures, the 0.25 *Tt* occupancy could be modeled by distributing *Tt* atoms in an ordered fashion in: (i) half of the *B* sites within every other slab of edge-sharing tetrahedra, or (ii) a quarter of the *B* sites within every slab (**Figure A 4-3** in **Appendix 4**). The latter was found to be more stable than the former by 0.48 eV/f.u. for

$NaZn_{1.5}Si_{0.5}As_2$ ($CaAl_2Si_2$-type) and by 0.18 eV/f.u. for $KZn_{1.5}Si_{0.5}As_2$ ($ThCr_2Si_2$-type). Thus, subsequent calculations were made on this type of site distribution ($CaAl_2Si_2$-type in space group $P\bar{3}m1$ with a $2\boldsymbol{a} \times 2\boldsymbol{b} \times \boldsymbol{c}$ superstructure, or $ThCr_2Si_2$-type in space group $P4_2/mcm$ with a $\sqrt{2}\boldsymbol{a} \times \sqrt{2}\boldsymbol{b} \times \boldsymbol{c}$ superstructure). To gauge the reliability of these calculations, the $ThCr_2Si_2$-type superstructure model for $KZn_{1.5}Si_{0.5}As_2$ was optimized by varying the c'/a' ($= c/(\sqrt{2}a)$) ratio and the z-coordinate of the As atom, while the cell volume was kept constant, and identifying the total energy minima. The resulting cell parameters and bond distances in the optimized structure were within 2% of the observed values. In view of this good agreement, calculations on other compounds were made using cell and positional parameters taken from the experimentally determined crystal structures. Further details of these calculations are provided in the context of the discussion of the results.

6.3 Results and Discussion

6.3.1. Crystal Structures

Within the series of quaternary arsenides $AM_{1.5}Tt_{0.5}As_2$ (A = Na, K, Rb; M = Zn, Cd; Tt = Si, Ge, Sn), 10 compounds out of the 18 possible permutations could be prepared by stoichiometric reactions of the elements at 650 °C (Na and K samples) or 600 °C (Rb samples). Seven of them adopt the trigonal $CaAl_2Si_2$-type structure (space group $P\bar{3}m1$),[20] and the remaining three adopt the tetragonal $ThCr_2Si_2$-type structure (space group $I4/mmm$),[21,22] both commonly found for AB_2X_2 phases (**Tables 6-1 and 6-2**). In either structure, only one main crystallographic site is available for each of the A, B, and X atoms. The B site is thus occupied by a disordered mixture of 75% M and 25% Tt atoms (**Tables 6-3 and 6-4**).

Both structures are generated by a stacking along the *c*-direction of [B_2As_2] slabs (B = 0.75 M + 0.25 Tt), built up of edge-sharing BAs_4 tetrahedra and interleaved with nets of the *A* cations (**Figure 6-1**). The structure of the $CaAl_2Si_2$-type compounds can also be described as consisting of an arrangement of hexagonal nets of As atoms (in hcp stacking sequence **AB**), with half the octahedral interstices filled by *A* atoms and half the tetrahedral interstices by *B* atoms. The [B_2As_2] slabs thus contain both up- and down-pointing BAs_4 tetrahedra with their threefold rotation axes aligned parallel to *c*. Correspondingly, the structure of the $ThCr_2Si_2$-type compounds could be viewed as an arrangement of square nets of As atoms, but in a stacking sequence **ABBA**. The *B* atoms occupy tetrahedral interstices within **AB** pairs of nets to form the [B_2As_2] slabs in which BAs_4 tetrahedra are aligned with their fourfold improper rotation axes ($\bar{4}$) parallel to *c*, and the *A* atoms occupy square prismatic (nearly cubic) interstices within **AA** (or **BB**) pairs of nets.

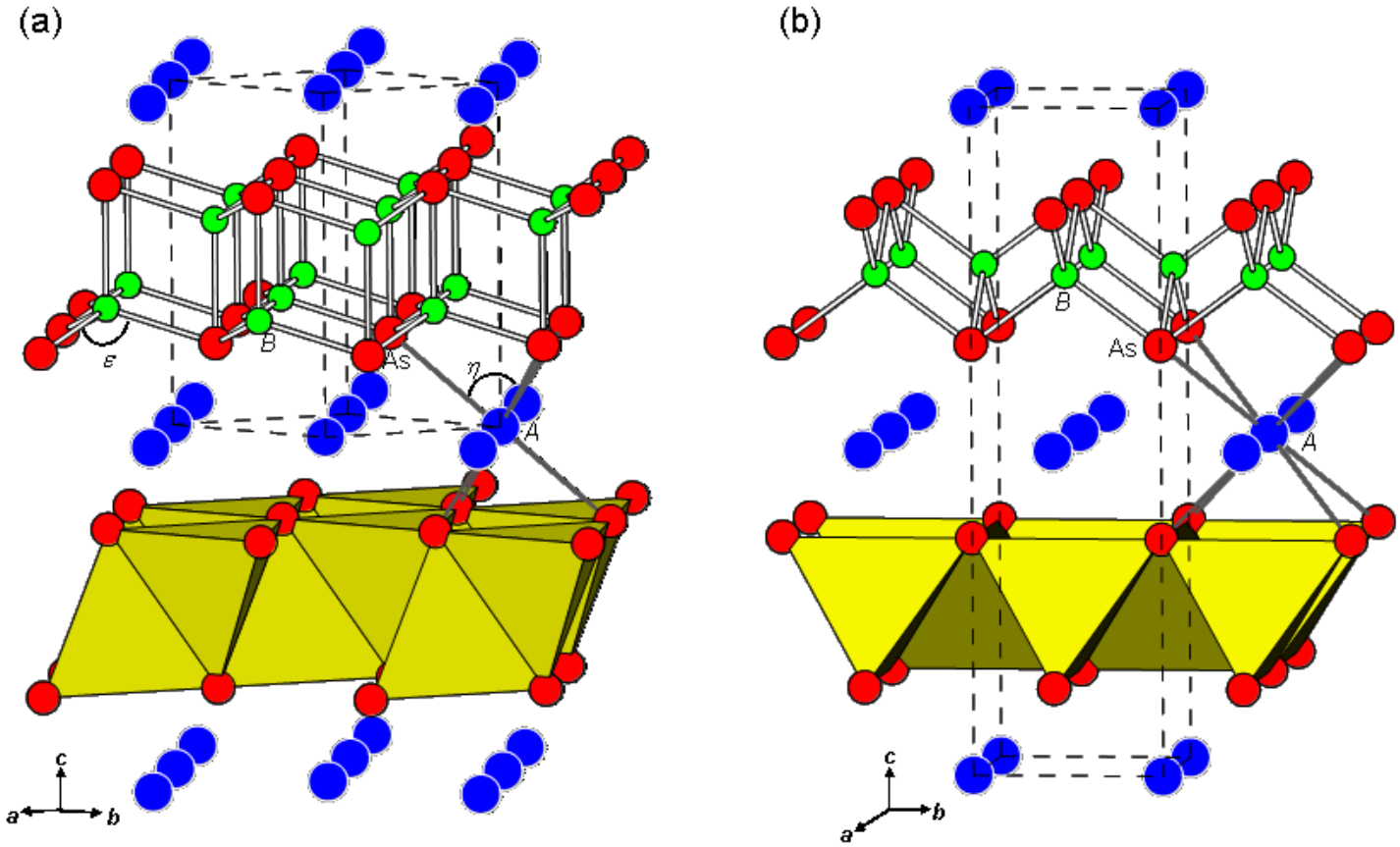

Figure 6-1. (a) $CaAl_2Si_2$-type or (b) $ThCr_2Si_2$-type structures of quaternary arsenides $AM_{1.5}Tt_{0.5}As_2$ (A = Na, K, Rb; M = Zn, Cd; Tt = Si, Ge, Sn), with the slabs of edge-sharing BAs_4 tetrahedra (B = 0.75 M and 0.25 Tt) and the coordination of A atoms highlighted. In (a), the bond angles around the A atom (η = ∠As–A–As) and the B atom (ε = ∠As–B–As) are defined as shown.

On proceeding from the $CaAl_2Si_2$- to the $ThCr_2Si_2$-type structure, the increase in coordination number (CN) of the *A* atom from 6 to 8 is consistent with the tendency of the former structure to form with the smaller alkali metals (Na- and K-containing members) and the latter with the larger alkali metals (K- and Rb-containing members). The higher CN is also accompanied by an expansion of *A*–As distances, as seen by comparing the K–As distances in $KZn_{1.5}Sn_{0.5}As_2$ ($CaAl_2Si_2$-type, 3.3571(4) Å) vs. $KZn_{1.5}Si_{0.5}As_2$ ($ThCr_2Si_2$-type, 3.5400(7) Å), or the Rb–As distances in $RbCd_{1.5}Sn_{0.5}As_2$ ($CaAl_2Si_2$-type, 3.4982(7) Å) vs. $RbZn_{1.5}Ge_{0.5}As_2$ ($ThCr_2Si_2$-type, 3.6228(6) Å), for example. Whereas the *A*–As distances are unextraordinary, the *B*–As distances within the BAs_4 tetrahedral groups deserve closer examination given the disorder of different *M* and *Tt* atoms that occurs within the *B* site. In general, the *B*–As distances (**Tables 6-5 and 6-6**) agree well with literature values for compounds containing similar BAs_4 tetrahedra (e.g., Zn–As, 2.5629(7) Å in $LaZn_{0.66}As_2$;[27] Cd–As, 2.547(9)–2.752(2) Å in $LaCd_3As_3$;[28] Si–As, 2.351(1)–2.441(1) Å in Na_5SiAs_3;[29] Ge–As, 2.433(1)–2.520(1) Å in Na_5GeAs_3;[30] Sn–As, 2.630(1)–2.712(1) Å in K_5SnAs_3 [31]) and can be compared with the sum of Pauling metallic radii (R_1) (Zn–As, 2.42 Å; Cd–As, 2.59 Å; Si–As, 2.38 Å; Ge–As, 2.45 Å; Sn–As 2.63 Å).[32] Among the possible combinations of *M* and *Tt* atoms, all but Cd–Si and Cd–Ge are observed, which is not unexpected considering the disparate atomic sizes within these pairs of elements. However, the formation of compounds with the Zn–Sn combination is a little surprising. Of course, this analysis of distances neglects the charge transfer that would take place to modify the sizes of atoms within the solid. It is interesting to note that two of the compounds, $NaZn_{1.5}Sn_{0.5}As_2$ and $NaCd_{1.5}Sn_{0.5}As_2$, exhibit a minor site, with trigonal planar (CN3) coordination, split off from

the main tetrahedrally coordinated *B* site (**Figure A 4-4** in **Appendix 4**). Occupation of this site at a low level (<11%) by the smaller Zn or, to a lesser extent, Cd atoms perhaps reflects the preference to recover shorter distances that are more suitable for these atoms.

With the *X* component fixed to be As within the AB_2X_2 compounds of $CaAl_2Si_2$-type, it is possible to examine structural trends more closely as a function of the *A* or *B* component. **Figure 6-2** shows plots of the *c*/*a* ratio as the *A* component is changed in $ACd_{1.5}Sn_{0.5}As_2$ and as the *B* component is changed in $NaM_{1.5}Tt_{0.5}As_2$. The *c*/*a* ratio is a measure of the expansion or compression of the structure along the *c* axis. In turn, this is caused by distortions of the coordination polyhedra around the *A* or *B* atoms, as expressed by the bond angles η (∠As–*A*–As) and ε (∠As–*B*–As), according to the notation established by Klüfers and Mewis.[3] In the series $ACd_{1.5}Sn_{0.5}As_2$, the *B* component (mixture of Cd and Sn atoms) is fixed while the *A* component is varied (*A* = Na, K, Rb). Substitution with a larger alkali metal on progressing from $NaCd_{1.5}Sn_{0.5}As_2$ to $RbCd_{1.5}Sn_{0.5}As_2$ leads to an expansion along *c*, caused primarily by the elongation of the AAs_6 octahedra along the threefold rotation axes parallel to *c* (**Figure 6-2a**). The As–*A*–As bond angle deviates away from the ideal value of 90° and becomes more acute (from 88° to 78°) to accommodate longer *A*–As distances, while respecting the need to maintain constant *B*–As distances of ~2.7 Å within the $[Cd_{1.5}Sn_{0.5}As_2]$ slabs. In the series $NaM_{1.5}Tt_{0.5}As_2$, the *A* component is fixed while the *B* component (mixture of *M* and *Tt* atoms) is varied (*B* = Zn–Si, Zn–Ge, Zn–Sn, Cd–Sn). Substitution with a set of larger *M* and *Tt* atoms on progressing from $NaZn_{1.5}Si_{0.5}As_2$ to $NaCd_{1.5}Sn_{0.5}As_2$ leads to a compression along *c* (**Figure 6-2b**). Interestingly, the dominant cause for this compression is still the identity of the *A* component, for which the As–Na–As

angles gradually increase (from 82° to 88°), while the geometry around the *B* component reaches a limit in which the As–*B*–As angles do not decrease below 110°. These observations are consistent with the expectation that the geometric requirements for $CaAl_2Si_2$-type phases AB_2X_2 will be more rigid within the $[B_2X_2]$ slab because of the directional character of covalent *B*–*X* bonds, in contrast to the greater flexibility allowed around the *A* atoms which participate in more ionic *A*–*X* bonds.

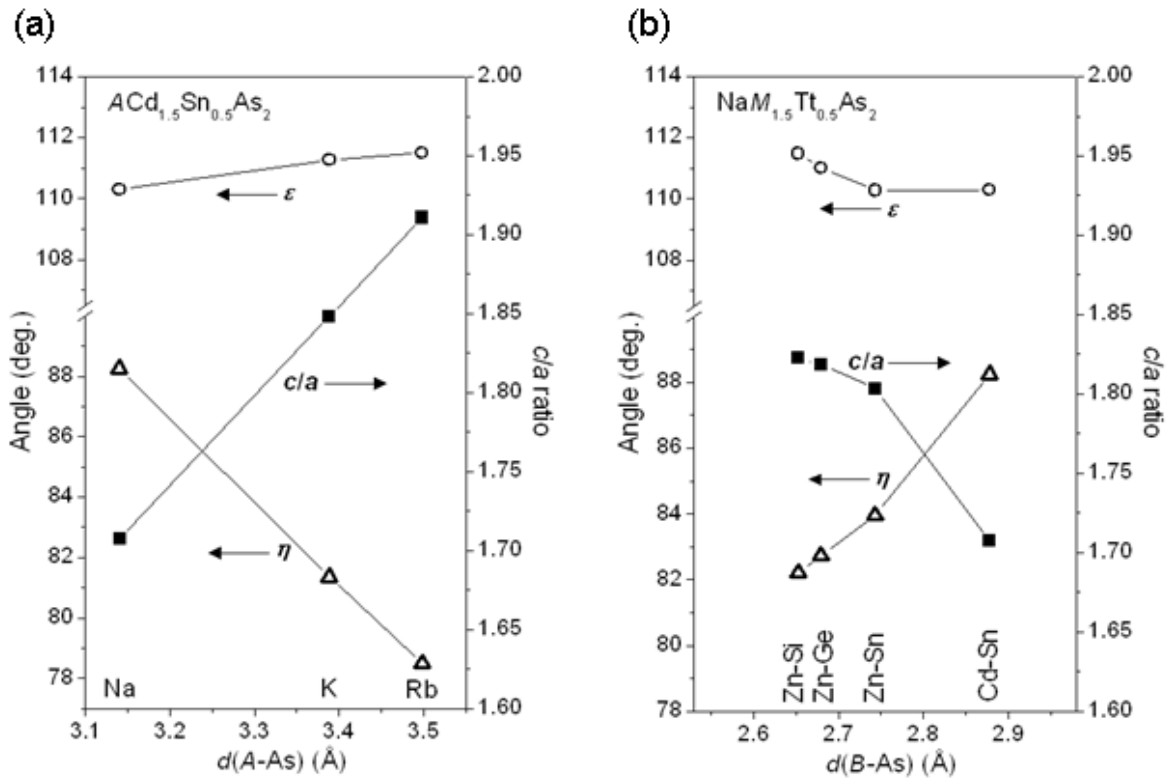

Figure 6-2. Plots of c/a ratio and bond angles (around *A* atoms (η) and *B* atoms (ε), as defined in Figure 1) for two series of $CaAl_2Si_2$-type phases: (a) $ACd_{1.5}Sn_{0.5}As_2$ (*A* = Na, K, Rb) and (b) $NaM_{1.5}Tt_{0.5}As_2$ (*B* = 0.75 *M* and 0.25 *Tt*, with Zn–Si, Zn–Ge, Zn–Sn, Cd–Sn combinations).

A structure map has been previously developed to define the limits of stability of the $CaAl_2Si_2$-type structure for ternary AB_2X_2 phases, on the basis of the average principal

quantum number $\bar{n}$ and a parameter f that is a weighted function of Slater atomic radii for A, B, and X ($f = r_A / (r_B + 0.2r_X)$).[3] To establish a similar structure map applicable for the quaternary arsenides $AM_{1.5}Tt_{0.5}As_2$, it will be important to introduce the radius ratio r_M/r_{Tt} to take into account the relative sizes of M and Tt atoms disordered over the B site, with the expectation that the structure will not be stable if these atoms are too disparate in size. Because the X component is fixed to be As in these quaternary arsenides but the B component contains two types of atoms, we omit consideration of the radius of the X atom and replace the parameter f by the radius ratio r_A/r_B where r_B is the weighted average of the M and Tt radii. We have also opted to use Pauling metallic radii (R_1)[32] instead of Slater atomic radii,[33] although either set will probably do. A plot of these two radius ratios is sufficient to reveal a good demarcation of those compounds that adopt the $CaAl_2Si_2$-type vs. $ThCr_2Si_2$-type structures, as well as those that do not form (**Figure 6-3**). Inspection of this plot confirms that smaller alkali-metal atoms that occupy the A site favour the $CaAl_2Si_2$-type structure (with CN6 for A). When larger alkali-metal atoms are present so that r_A/r_B exceeds 1.6, the $ThCr_2Si_2$-type structure becomes preferred because the A site now has CN8. The nonexistent compound $RbZn_{1.5}Si_{0.5}As_2$ lies at the highest r_A/r_B point of 1.8, which represents the limiting value beyond which even the $ThCr_2Si_2$-type structure does not form within this series of quaternary arsenides. For both structure types, r_M/r_{Tt} does not generally stray far from 1.0 except for the unexpected formation of $NaZn_{1.5}Sn_{0.5}As_2$ and $KZn_{1.5}Sn_{0.5}As_2$ noted earlier. This anomaly might be rectified through use of Slater atomic radii, according to which Zn and Sn have more similar radii ($r_M/r_{Tt} = 0.93$) than in the case of Pauling metallic radii ($r_M/r_{Tt} = 0.84$).[32,33] The drawback of this choice is that the radius ratio then becomes

too large for the Zn–Si combination (r_M/r_{Tt} = 1.23). In any event, this analysis neglects the charge transfer that would be expected to occur from the electropositive to electronegative components, so that in the ionic extreme, the nominal charges would be Zn^{2+} and Sn^{4+} and their radii would be modified from those of the neutral atoms. $RbZn_{1.5}Sn_{0.5}As_2$ is a potential $CaAl_2Si_2$-type phase but it lies at the boundaries of low r_M/r_{Tt} and high r_A/r_B values; its non-existence may be attributed to significant distortions that would take place around the Rb atoms, giving extremely acute η angles, which are already at 77.41(1)° in $KZn_{1.5}Sn_{0.5}As_2$.

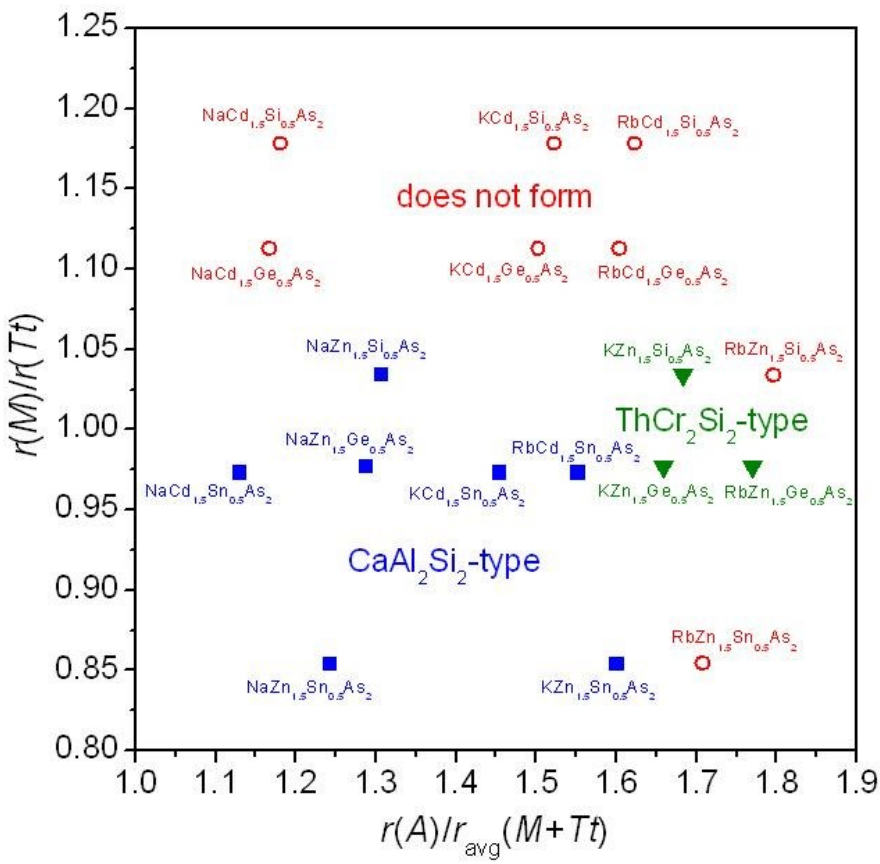

Figure 6-3. Structure map for quaternary arsenides $AM_{1.5}Tt_{0.5}As_2$ (A = Na, K, Rb; M = Zn, Cd; Tt = Si, Ge, Sn) showing the demarcation of $CaAl_2Si_2$-type structures (blue squares), $ThCr_2Si_2$-type structures (green triangles), and non-existent members to date (red circles) on the basis of radius ratios.

6.3.2. Electronic Structure and Bonding

The charge-balanced formulation $(A^{+})(M^{2+})_{1.5}(Tt^{4+})_{0.5}(As^{3-})_2$, obtained in the extreme picture of ionic bonding when the Zintl concept is applied, corresponds to closed-shell electron configurations for all atoms. For the $AM_{1.5}Tt_{0.5}As_2$ compounds with the $CaAl_2Si_2$-type structure, the occurrence of fully reduced As atoms implied by this formulation indicates that no As–As bonding takes place. The interslab As–As distances in these compounds are all very long (ranging from 4.661(1) Å in $NaZn_{1.5}Si_{0.5}As_2$ to 5.418(1) Å in $RbCd_{1.5}Sn_{0.5}As_2$). In $ThCr_2Si_2$-type phases, however, it is well known that anion-anion bonds can potentially form between $[B_2X_2]$ slabs, depending on the electron count controlled by the choice of the transition-metal component *B*. This bond formation was first proposed to occur through an internal redox process in which electrons flow back to the transition-metal component to alleviate antibonding *X–X* interactions.[34] Although this elegant explanation has been popular,[35,36] it was later shown to be oversimplified because the position and population of the antibonding *X–X* levels are intimately linked with intralayer *B–B* and *B–X* interactions.[37,38] In particular, the importance of the metal-metal (*B–B*) interactions has since been corroborated by others.[39–41] For the three $AM_{1.5}Tt_{0.5}As_2$ compounds with the $ThCr_2Si_2$-type structure, the interslab As–As distances are far too long to be bonding (ranging from 4.114(1) Å in $KZn_{1.5}Ge_{0.5}As_2$ to 4.315(1) Å in $RbZn_{1.5}Ge_{0.5}As_2$), as are the intralayer *B–B* distances (>3.1 Å). Much of the literature of $ThCr_2Si_2$-type phases has focused on examining the effect of d-electron count of the transition-metal component, with the *A* component generally being neglected from consideration or serving a primarily geometric role in separating the $[B_2X_2]$ layers.[5,34,37]

However, there is growing recognition that the nature of the *A* component can strongly influence the physical properties of $ThCr_2Si_2$-type phases,[42,43] and that cation-anion interactions, as well as other factors such as the spin state of the transition-metal, are important in determining the adoption of the $CaAl_2Si_2$- vs. $ThCr_2Si_2$-type structures, as has been shown for AMn_2P_2 (*A* = Ca, Sr, Ba).[10,44]

Given the closed-shell configurations of the M^{2+} and Tt^{4+} species, the $AM_{1.5}Tt_{0.5}As_2$ series provides the possibility to isolate the role of the *A* cation in the adoption of $CaAl_2Si_2$- vs. $ThCr_2Si_2$-type structures. This is a challenging problem in which alternative hypothetical structures must be constructed to give reasonable bond lengths. Extended Hückel methods have been previously applied to investigate the stability of isolated $[Mn_2P_2]$ slabs in $CaAl_2Si_2$- and $ThCr_2Si_2$-type structures as a function of band filling, with the assumption that both structures have the same Mn–Mn and Mn–P distances.[5] However, it would be expected that geometrical differences between $CaAl_2Si_2$- and $ThCr_2Si_2$-type polymorphs of a given compound would render these distances to be not identical. Comparison of the observed distances in $AM_{1.5}Tt_{0.5}As_2$ (**Tables 6-5 and 6-6**) reveals trends which we can exploit to define hypothetical model structures. First, on proceeding from $CaAl_2Si_2$- to $ThCr_2Si_2$-type structures, the *A*–As distances expand in accordance with the change in CN from 6 to 8, close to the difference in Shannon ionic radii for A^+ cations ($\Delta r_{CN6\rightarrow CN8}$ of 0.16 Å for Na^+, 0.13 Å for K^+, and 0.09 Å for Rb^+).[45] Second, although there are two inequivalent sets of *B*–As distances, typically designated the three shorter lateral "rib" and one longer vertical "handle" bonds,[4] within the BAs_4 tetrahedra in the $CaAl_2Si_2$-type structures, the average *B*–As distance is retained in the $ThCr_2Si_2$-type structures, all other things being equal. Third,

the *B*–*B* distances tend to be 0.1–0.2 Å shorter in the $ThCr_2Si_2$-type structures for a fixed combination of *M* and *Tt*. We have chosen $KZn_{1.5}Ge_{0.5}As_2$ as a test case in which the $[Zn_{1.5}Ge_{0.5}As_2]$ slabs, containing an ordered distribution of Zn and Ge atoms, were taken from the experimental $ThCr_2Si_2$-type structure and constructed in a hypothetical $CaAl_2Si_2$-type polymorph so as to exhibit differences that are consistent with the changes seen in the rest of the $AM_{1.5}Tt_{0.5}As_2$ series. The $[Zn_{1.5}Ge_{0.5}As_2]$ slabs were then kept invariant while the effect of a change in the alkali-metal component was mimicked by expanding or contracting the structure along the *c*-direction, which is a good approximation in view of the interpretation of **Figure 6-2(a)** discussed earlier. Plots of the relative total energy determined from LMTO calculations (**Figure 6-4(a)**) confirm that the $ThCr_2Si_2$-type structure is favoured at long K–As separations whereas the $CaAl_2Si_2$-type structure is favoured at short ones, a result that is consistent, of course, with the coordination preferences of large vs. small *A* cations. Similar calculations were performed on $KCd_{1.5}Sn_{0.5}As_2$ with fixed $[Cd_{1.5}Sn_{0.5}As_2]$ slabs taken from the experimental $CaAl_2Si_2$-type structure and constructed in a hypothetical $ThCr_2Si_2$-type polymorph. The substitution with larger *M* and *Tt* atoms increases the in-plane distances so that the $[Cd_{1.5}Sn_{0.5}As_2]$ slabs in $KCd_{1.5}Sn_{0.5}As_2$ are expanded relative to the $[Zn_{1.5}Ge_{0.5}As_2]$ slabs in $KZn_{1.5}Ge_{0.5}As_2$. To compensate for the weakening in K–As interactions accompanying this expansion, it would be expected that the K cations would prefer the lower CN and shorter K–As distances available in the $CaAl_2Si_2$-type structure. Plots of the relative total energy confirm that at shorter K–As distances, the $ThCr_2Si_2$-type structure becomes highly disfavoured while the $CaAl_2Si_2$-type structure becomes more stable (**Figure 6-4(b)**).

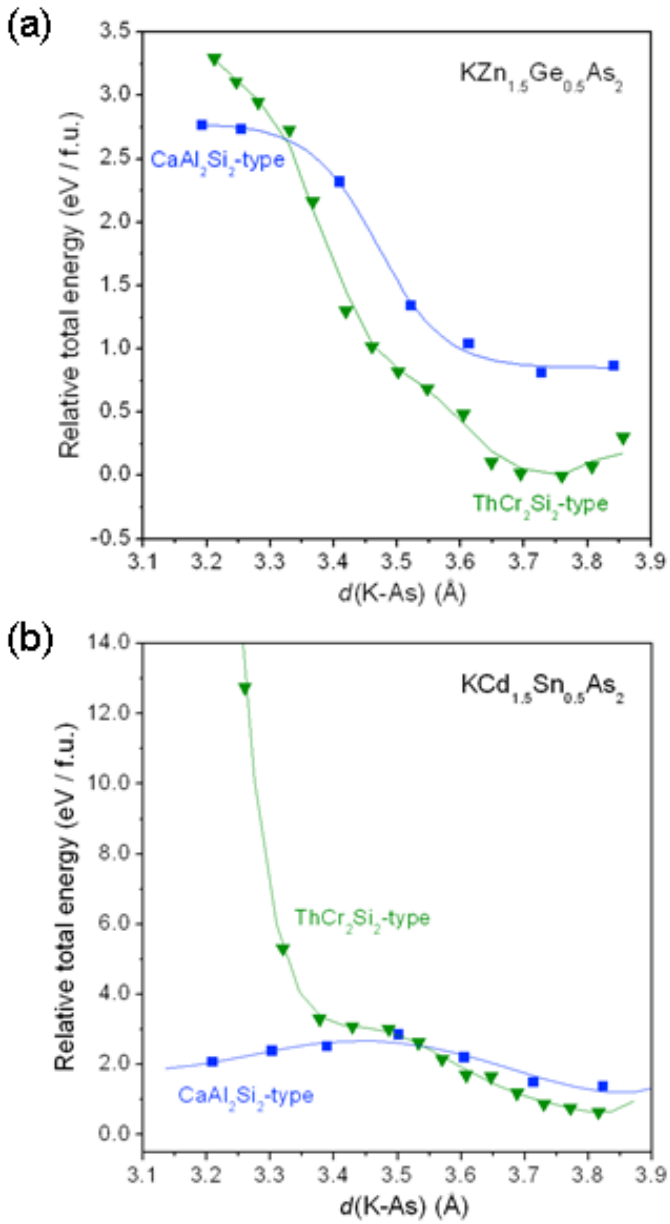

Figure 6-4. Plots of relative total energy for ordered (a) $KZn_{1.5}Ge_{0.5}As_2$ and (b) $KCd_{1.5}Sn_{0.5}As_2$ models with fixed [$M_{1.5}Tt_{0.5}As_2$] slabs in $CaAl_2Si_2$- vs. $ThCr_2Si_2$-type structures, as a function of K–As distances as the structures are expanded or contracted along the *c*-direction.

The closed-shell electron configurations in $AM_{1.5}Tt_{0.5}As_2$ also lead to the prediction of semiconducting behaviour. Unfortunately these compounds are moderately air-sensitive

and we have been unable to perform electrical resistivity measurements. There have been many studies of the electrical properties of $ThCr_2Si_2$-type phases, but relatively few on $CaAl_2Si_2$-type phases.[46] The band structure was calculated for one of the $CaAl_2Si_2$-type phases presented here, $NaZn_{1.5}Si_{0.5}As_2$. In fact, the band dispersion diagram reveals that there is no band gap and that the valence and conduction bands overlap slightly (**Figure 6-5(a)**). When the calculations were repeated with the intervening Na^+ cations removed between the $[Zn_{1.5}Si_{0.5}As_2]^-$ slabs, the overlap remains (**Figure 6-5(b)**). These results indicate that the absence of a band gap is intrinsic to the slabs themselves, confirming similar conclusions made previously on other $CaAl_2Si_2$-type phases (including $CaAl_2Si_2$ itself) in which the controlling factor is the difference in electronegativity between the *B* and *X* atoms within the $[B_2X_2]$ slabs.[7–10] A lower electronegativity difference leads to greater energy dispersion of the bands, such that the top of the valence band and the bottom of the conduction band approach each other and eventually overlap. This proposal can be tested within the series $NaZn_{1.5}Si_{0.5}As_2$, $NaZn_{1.5}Ge_{0.5}As_2$, and $NaZn_{1.5}Sn_{0.5}As_2$, which all adopt the $CaAl_2Si_2$-type structure but differ only in the *Tt* component to give $\Delta\chi_{Tt\text{–As}} = 0.28$, 0.17, and 0.22, respectively. The calculated densities of states (DOS) at the Fermi level are 2.0, 3.5, and 0.9 states/eV per cell for $NaZn_{1.5}Si_{0.5}As_2$, $NaZn_{1.5}Ge_{0.5}As_2$, and $NaZn_{1.5}Sn_{0.5}As_2$, respectively. Because the DOS depends on several factors (slopes of bands, number of bands crossed by Fermi level), the agreement is not perfect. However, it is clear that $NaZn_{1.5}Ge_{0.5}As_2$, which corresponds to the combination with the smallest electronegativity difference, gives rise to the greatest overlap of valence and conduction bands.

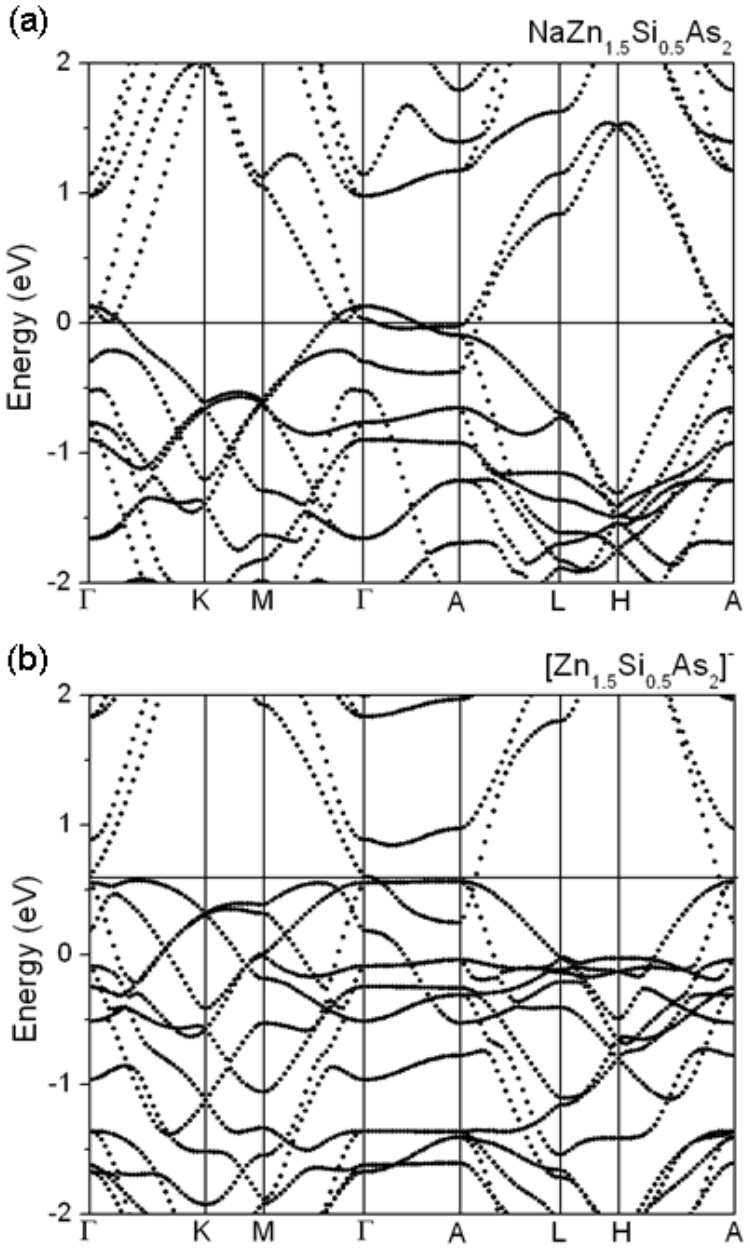

Figure 6-5. Band dispersion diagrams for ordered models of (a) $NaZn_{1.5}Si_{0.5}As_2$ (with Na atoms included in calculation) and (b) $[Zn_{1.5}Si_{0.5}As_2]$– (with Na atoms omitted from calculation).

Table 6-7. Comparison of –ICOHP values in $NaZn_{1.5}Tt_{0.5}As_2$ (*Tt* = Si, Ge, Sn)

Contact	–ICOHP (eV bond^{-1})	–ICOHP (eV cell^{-1})	Contribution (%)
$NaZn_{1.5}Si_{0.5}As_2$			
Na–As	0.14	1.66	9.6
Zn–As	1.63	6.55	37.7
Si–As	2.28	9.14	52.7
$NaZn_{1.5}Ge_{0.5}As_2$			
Na–As	0.13	1.53	9.6
Zn–As	1.42	5.70	35.8
Ge–As	2.17	8.70	54.6
$NaZn_{1.5}Sn_{0.5}As_2$			
Na–As	0.17	2.07	13.0
Zn–As	1.22	4.89	30.8
Sn–As	2.22	8.91	56.1

Implicit in the discussion above is that the *A* cations participate in some degree of covalent bonding, notwithstanding the ionic bonding picture presented in the Zintl formulation. Even though they do not directly influence the electrical properties and provide only small contributions to the DOS at the Fermi level (e.g., 5% for $NaZn_{1.5}Si_{0.5}As_2$ and 8% for $NaZn_{1.5}Ge_{0.5}As_2$), they would be expected to have some orbital interactions with the surrounding As atoms. As shown in the atomic projections of the DOS for $NaZn_{1.5}Si_{0.5}As_2$ (**Figure 6-6(a)**), there is a small mixing of Na 3s with As 4p states primarily in the region from –6 to 0 eV. The mixing leads to weak bonding interactions, as verified by the crystal

orbital Hamilton population (COHP) curve (**Figure 6-6(b)**), with an integrated –COHP value (–ICOHP) of 0.14 eV/bond. The sharp spike in the DOS from –8 to –6.5 eV corresponds to the filled 3d band of the Zn atoms. The most important bonding interactions come from mixing of Zn 4s/4p and Si 3s/3p with As 4p states, with all the bonding levels filled just up to the Fermi level. The Zn–As bonds in the three shorter ribs are stronger (–ICOHP of 1.63 eV/bond) than in the longer handle (–ICOHP of 1.18 eV/bond). At the same distances, the Si–As bonds are even stronger (–ICOHP of 2.43 eV/bond for the ribs and 1.84 eV/bond for the handle). When the Na^+ cations are omitted from the calculation, these Zn–As and Si–As bonds are strengthened by 27%, which lends further support to the non-innocent role of these cations. Summed over the unit cell, the contributions to covalent bonding decrease in the order Si–As, Zn–As, and Na–As. **Table 6-7** compares these bonding contributions for the series $NaZn_{1.5}Tt_{0.5}As_2$ (*Tt* = Si, Ge, Sn). Introducing larger *Tt* atoms into the tetrahedral sites necessarily lengthens the Zn–As bonds as well, which gradually become weaker. The observed crystal structure of $NaZn_{1.5}Sn_{0.5}As_2$ reveals that the response to this bond weakening is to relegate a proportion of the smaller Zn atoms to a new split site with trigonal planar coordination (CN3) consistent with more appropriate Zn–As bond lengths.

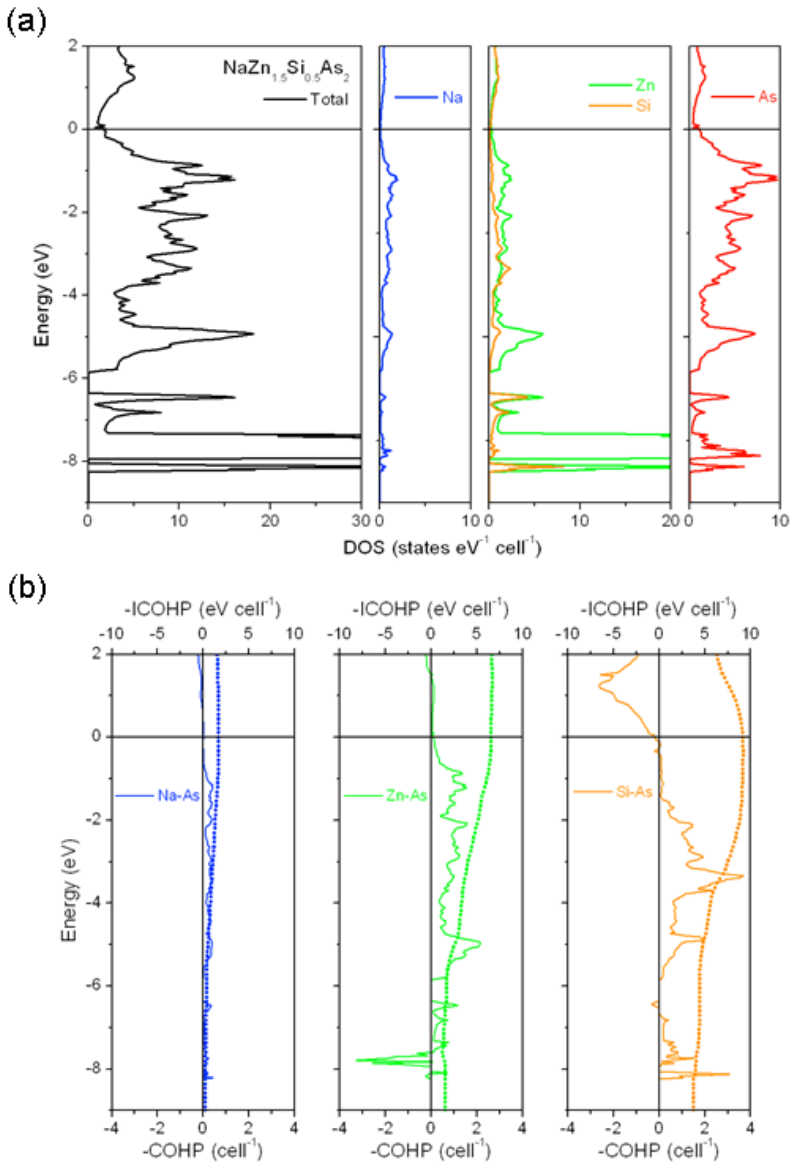

Figure 6-6. (a) Density of states (DOS) and its atomic projections for $NaZn_{1.5}Si_{0.5}As_2$. (b) Crystal orbital Hamilton population (COHP) curves for Na–As, Zn–As, and Si–As contacts. The Fermi level is at 0 eV.

6.4 Conclusion

Several quaternary arsenides $AM_{1.5}Tt_{0.5}As_2$ with $CaAl_2Si_2$- or $ThCr_2Si_2$-type structures can be prepared in which the combination of *A*, *M*, and *Tt* components satisfies

simple radius ratio rules. Because the *M* and *Tt* components necessarily disorder over the same *B* site with tetrahedral coordination, their sizes should not differ greatly and r_M/r_{Tt} is close to 1.0. Consistent with the increase in CN from 6 to 8 for the *A* site, the $CaAl_2Si_2$-type structure is preferred by smaller *A* cations, whereas the $ThCr_2Si_2$-type structure is preferred by larger *A* cations. However, this size preference for the *A* component must be compatible with the geometric requirements of $[M_{1.5}Tt_{0.5}As_2]$ slab, as expressed by the ratio $r_A/r_{avg(M+Tt)}$. It would be interesting to change experimental conditions (e.g. pressure) that might overcome these restrictions to favour the formation of the currently nonexistent $AM_{1.5}Tt_{0.5}As_2$ members. The electronic structure is largely dominated by these $[M_{1.5}Tt_{0.5}As_2]$ slabs, which can be viewed as relatively rigid and which contain strong covalent bonds, while the *A* cations participate mostly in ionic interactions with these slabs. Band structure calculations confirm that despite being charge-balanced Zintl phases, these arsenides are predicted to exhibit semimetallic behaviour resulting from a small overlap of valence and conduction bands.

The structure map suggested that some phases will not form with the $AM_{1.5}Tt_{0.5}As_2$ composition because of the disparate sizes of the *M* and *Tt* atoms. Although these phases could not be formed, such as $ACd_{1.5}Ge_{0.5}As_2$ perhaps other phases with different compositions can be prepared. The next chapter discusses the formation of $ACdGeAs_2$ (*A* = K, Rb).

6.5 References

1. Villars, P.; Cenzual, K. *Pearson's Crystal Data – Crystal Structure Database for Inorganic Compounds*, release 2010/11; ASM International: Materials Park, OH, 2010.

2. Mandrus, D.; Sefat, A. S.; McGuire, M. A.; Sales, B. C. *Chem. Mater.* **2010**, *22*, 715–723.

3. Klüfers, P.; Mewis, A. *Z. Kristallogr.* **1984**, *169*, 135–147.

4. Zheng, C.; Hoffmann, R.; Nesper, R.; von Schnering, H.-G. *J. Am. Chem. Soc.* **1986**, *108*, 1876–1884.

5. Zheng, C.; Hoffmann, R. *J. Solid State Chem.* **1988**, *72*, 58–71.

6. Burdett, J. K.; Miller, G. J. *Chem. Mater.* **1990**, *2*, 12–26.

7. Kranenberg, C.; Johrendt, D.; Mewis, A. *Z. Anorg. Allg. Chem.* **1999**, *625*, 1787–1793.

8. Kranenberg, C.; Johrendt, D.; Mewis, A. *Solid State Sci.* **2002**, *4*, 261–265.

9. Wartenberg, F.; Kranenberg, C.; Pocha, R.; Johrendt, D.; Mewis, A.; Hoffmann, R.-D.; Mosel, B. D.; Pöttgen, R. *Z. Naturforsch. B: J. Chem. Sci.* **2002**, *57*, 1270–1276.

10. Alemany, P.; Llunell, M.; Canadell, E. *J. Comput. Chem.* **2008**, *29*, 2144–2153.

11. Gascoin, F.; Ottensmann, S.; Stark, D.; Haïle, S. M.; Snyder, G. J. *Adv. Funct. Mater.* **2005**, *15*, 1860–1864.

12. Wang, X.-J.; Tang, M.-B.; Chen, H.-H.; Yang, X.-X.; Zhao, J.-T.; Burkhardt, U.; Grin, Yu. *Appl. Phys. Lett.* **2009**, *94*, 092106-1–092106-3.

13. Flage-Larsen, E.; Diplas, S.; Prytz, Ø.; Toberer, E. S.; May, A. F. *Phys. Rev. B* **2010**, *81*, 205204-1–205204-7.

14. Guo, K.; Cao, Q.-G.; Feng, X.-J.; Tang, M.-B.; Chen, H.-H.; Guo, X.; Chen, L.; Grin, Yu.; Zhao, J.-T. *Eur. J. Inorg. Chem.* **2011**, 4043–4048.

15. May, A. F.; McGuire, M. A.; Singh, D. J.; Ma, J.; Delaire, O.; Huq, A.; Cai, W.; Wang, H. *Phys. Rev. B* **2012**, *85*, 035202-1–035202-10.

16. Blanchard, P. E. R.; Stoyko, S. S.; Cavell, R. G.; Mar, A. *J. Solid State Chem.* **2011**, *184*, 97–103.

17. He, H.; Tyson, C.; Bobev, S. *Inorg. Chem.* **2011**, *50*, 8375–8383.

18. Stoyko, S. S.; Khatun, M.; Mar, A. *Inorg. Chem.* **2012**, *51*, 9517–9521.

19. Sheldrick, G. M. *SHELXTL*, version 6.12; Bruker AXS Inc.: Madison, WI, 2001.

20. Gladyshevskii, E. I.; Kripyakevich, P. I.; Bodak, O. I. *Ukr. Fiz. Zh.* **1967**, *12*, 447–452.

21. Ban, Z.; Sikirica, M. *Acta Crystallogr.* **1965**, *18*, 594–599.

22. Leciejewicz, J.; Siek, S.; Szytuła, A. *J. Less-Common Met.* **1988**, *144*, L9–L13.

23. Gaultois, M. W.; Grosvenor, A. P.; Blanchard, P. E. R.; Mar, A. *J. Alloys Compd.* **2010**, *492*, 19–25.

24. Blanchard, P. E. R.; Cavell, R. G.; Mar, A. *J. Alloys Compd.* **2010**, *505*, 17–22.

25. Gelato, L. M.; Parthé, E. *J. Appl. Crystallogr.* **1987**, *20*, 139–143.

26. Tank, R.; Jepsen, O.; Burkhardt, A.; Andersen, O. K. *TB-LMTO-ASA Program*, version 4.7; Max Planck Institut für Festkörperforschung: Stuttgart, Germany, 1998.

27. Stoyko, S. S.; Mar, A. *J. Solid State Chem.* **2011**, *184*, 2360–2367.

28. Stoyko, S. S.; Mar, A. *Inorg. Chem.* **2011**, *50*, 11152–11161.

29. Eisenmann, B.; Klein, J.; Somer, M. *Z. Kristallogr.* **1991**, *197*, 267–268.

30. Eisenmann, B.; Klein, J.; Somer, M. *Z. Kristallogr.* **1991**, *197*, 265–266.

31. Eisenmann, B.; Rössler, U. *Z. Kristallogr. – New Cryst. Struct.* **2000**, *215*, 347.

32. Pauling, L. *The Nature of the Chemical Bond*, 3rd ed.; Cornell University Press: Ithaca, NY, 1960.

33. Slater, J. C. *J. Chem. Phys.* **1964**, *41*, 3199–3204.

34. Hoffmann, R.; Zheng, C. *J. Phys. Chem.* **1985**, *89*, 4175–4181.

35. Hoffmann, R. *Solids and Surfaces: A Chemist's View of Bonding in Extended Structures*; VCH Publishers: New York, 1998.

36. Huheey, J. E.; Keiter, E. A.; Keiter, R. L. *Inorganic Chemistry: Principles of Structure and Reactivity*, 4th ed.; Harper Collins: New York, 1993.

37. Johrendt, D.; Felser, C.; Jepsen, O.; Andersen, O. K.; Mewis, A.; Rouxel, J. *J. Solid State Chem.* **1997**, *130*, 254–265.

38. Gustenau, E.; Herzing, P.; Neckel, A. *J. Solid State Chem.* **1997**, *129*, 147–156.

39. Kang, D.-B. *Bull. Korean Chem. Soc.* **2003**, *24*, 1215–1218.

40. An, J.; Sefat, A. S.; Singh, D. J.; Du, M.-H. *Phys. Rev. B* **2009**, *79*, 075120-1–075120-6.

41. Singh, D. J. *Phys. Rev. B* **2009**, *79*, 153102-1–153102-4.

42. Chefki, M.; Abd-Elmeguid, M. M.; Micklitz, H.; Huhnt, C.; Schlabitz, W.; Reehuis, M.; Jeitschko, W. *Phys. Rev. Lett.* **1998**, *80*, 802–805.

43. Kovnir, K.; Thompson, C. M.; Zhou, H. D.; Wiebe, C. R.; Shatruk, M. *Chem. Mater.* **2010**, *22*, 1704–1713.

44. Brock, S. L.; Greedan, J. E.; Kauzlarich, S. M. *J. Solid State Chem.* **1994**, *109*, 416–418.

45. Shannon, R. D. *Acta Crystallogr., Sect. A* **1976**, *32*, 751–767.

46. Imai, M.; Abe, H.; Yamada, K. *Inorg. Chem.* **2004**, *43*, 5186–5188.

Chapter 7

Quaternary Arsenides ACdGeAs$_2$ (A = K, Rb) Built of Ethane-Like Ge$_2$As$_6$ Units

A version of this chapter has been published. Khatun, M.; Stoyko, S. S.; Mar, A. Inorg. Chem. 2014, 53, 7756–7762.

7.1. Introduction

Ternary pnictides *A–M–Pn* (*A* = electropositive metal; *M* = metalloid from groups 13 or 14; *Pn* = P, As, Sb, Bi) form an extremely numerous set of compounds.[1,2] They conform well to the Zintl concept, namely that their structures can be understood in terms of the attainment of closed-shell configurations for all atoms, with the assumption of complete electron transfer from the *A* component to the other components. The structures are characterized by complex networks built from heteronuclear anionic units $[M_xPn_y]^{n-}$ containing localized 2c–2e$^-$ bonds between *M* and *Pn* atoms, typically *M*-centred tetrahedra or trigonal planes. The many different ways in which such units can be connected suggest a structural diversity that has the potential to rival that of silicates or chalcogenides. These ternary pnictides can be considered to be the forerunners to many analogues that contain transition metals with d^0, d^5, or d^{10} configuration and have attracted attention for their physical properties, such as thermoelectric materials (e.g., Yb$_{14}$MnSb$_{11}$ with the Ca$_{14}$AlSb$_{11}$-type structure).[3] More complex quaternary pnictides can be envisioned containing both transition-metal and metalloid components, as we have recently demonstrated in the preparation of arsenides $AM_{1.5}Tt_{0.5}$As$_2$ (A = Na, K, Rb; M = Zn, Cd; Tt = Si, Ge, Sn).[4] They are charge-balanced Zintl phases with *M* and *Tt* atoms disordering over the same site in either CaAl$_2$Si$_2$- and ThCr$_2$Si$_2$-type structures, depending on the relative atomic sizes of the different components. Not all combinations of *M* and *Tt* are possible, however, if their sizes are too disparate. For example, we observed that "ACd$_{1.5}$Ge$_{0.5}$As$_2$" phases did not form; rather, as we report here, the phases ACdGeAs$_2$ (A = K, Rb)

were found whose formula would not be charge-balanced unless oxidation states were different from normal expectations. It is interesting to note the similarity of this formula to the ternary arsenide $CdGeAs_2$, a well-known chalcopyrite semiconductor with applications in nonlinear optical, spintronic, and possibly thermoelectric materials.[5–7] The resolution of the crystal structures of ACdGeAs$_2$ (A = K, Rb), as described in this chapter, reveals some unusual features, including the formation of rare ethane-like Ge_2As_6 units that are reminiscent of the much more prevalent thiophosphate anions P_2S_6,[8] the presence of Cd atoms in low coordination (CN3),[9] and an unintuitive close relationship to the ternary arsenides $A_3Ge_2As_4$ (A = Ca, Sr).[10] The electronic band structure of $KCdGeAs_2$ is also presented.

7.2. Experimental

7.2.1. Synthesis

Starting materials were K pieces (99.95%), Rb pieces (99.75%), Cd shot (99.95%), Ge ingot (99.999%), and As lumps (99.999%), all obtained from Alfa-Aesar. All manipulations were carried out within an argon-filled glovebox. Stoichiometric mixtures of the elements were loaded into alumina crucibles placed within fused-silica tubes, which were evacuated and sealed. The tubes were heated to 650 °C (for the K sample) or 600 °C (for the Rb sample) over 2 d, kept at that temperature for 10 d, and cooled to room temperature over 2 d. The lower initial temperature was used for the Rb sample to avoid excessive volatilization due to the low boiling point of Rb metal (688 °C). The products contained grey plate- or prism-shaped crystals which were moderately air-sensitive and handled under paraffin oil. Powder X-ray diffraction (XRD) patterns were collected on an Inel diffractometer equipped with a curved position-sensitive detector (CPS 120) and a Cu $K\alpha_1$ radiation source operated at 40 kV and 20 mA. The K-containing reaction resulted in nearly phase pure $KCdGeAs_2$ along with <5% of unidentified phase, whereas the Rb-containing reaction gave

~70% of $RbCdGeAs_2$ along with $RbCd_4As_3$ [11] and elemental Ge as secondary phases (**Figure A 5-1** in **Appendix 5**). The chemical compositions of single crystals of these quaternary arsenides were determined by energy-dispersive X-ray (EDX) analysis on a JEOL JSM-6010LA scanning electron microscope **(Figure A 5-2** in **Appendix 5**). The experimental compositions, averaged over 3–4 crystals with 4–5 point analyses per crystal, were $K_{19(1)}Cd_{20(1)}Ge_{20(1)}As_{41(1)}$ and $Rb_{22(1)}Cd_{22(1)}Ge_{19(1)}As_{37(1)}$, in good agreement with expectations (20% *A*, 20% Cd, 20% Ge, 40% As).

7.2.2. Structure Determination

Single crystals were selected under paraffin oil, mounted on glass fibers, and placed under a cold nitrogen gas stream on a Bruker PLATFORM diffractometer equipped with a SMART APEX II CCD detector and a Mo $K\alpha$ radiation source. Full spheres of intensity data were collected at –100 °C using ω scans in 6 batches at different ϕ angles with a frame width of 0.3° and an exposure time of 12–15 s per frame. Face-indexed numerical absorption corrections were applied. Structure solution and refinement were carried out with use of the SHELXTL (version 6.12) program package.[12] The centrosymmetric triclinic space group $P\bar{1}$ was chosen on the basis of Laue symmetry and intensity statistics; no transformation to higher lattice symmetry was evident, as confirmed by the checkCIF/PLATON validation of the final structure.[13] Initial atomic positions were easily located by direct methods. A possible ambiguity arises from the similar scattering factors of Ge and As, but the only chemical meaningful model places the more electronegative As atoms as the coordinating ligands around the Cd atoms. In fact, refinements in which the Ge1 or Ge2 site was allowed to be disordered with As atoms did indeed permit discrimination; for example, in $KCdGeAs_2$, the occupancies converged to 0.98(7) Ge / 0.02(7) As in the Ge1 site and 0.87(7) Ge / 0.13(7) As in the Ge2 site. However, similar refinements in which any of the As sites was allowed

to be disordered with Ge atoms were unstable. We interpret these results as evidence for supporting the ordering of the Ge and As atoms. Atomic positions were standardized with the program STRUCTURE TIDY.[14] Refinements proceeded in a straightforward manner, leading to reasonable displacement parameters for all atoms and no evidence for partial occupancies. Agreement factors were acceptable and the difference electron density maps were featureless. Crystal data are given in **Table 7-1**, final values of the positional and displacement parameters are given in **Table 7-2**, and selected interatomic distances are listed in **Table 7-3**. Further data in the form of crystallographic information files (CIFs) are available in CSD number 427769 to 427770.

Table 7-1. Crystallographic data for ACdGeAs$_2$ (A = K, Rb)

formula	KCdGeAs$_2$	RbCdGeAs$_2$
fw (amu)	373.93	420.30
space group	$P\bar{1}$ (No. 2)	$P\bar{1}$ (No. 2)
a (Å)	8.0040(18)	8.2692(13)
b (Å)	8.4023(19)	8.4519(13)
c (Å)	8.703(2)	8.7349(13)
α (°)	71.019(3)	71.163(2)
β (°)	75.257(3)	75.601(2)
γ (°)	73.746(3)	73.673(2)
V (Å^3)	522.7(2)	546.04
Z	4	4
ρ_{calcd} (g cm^{-3})	4.752	5.113
T (K)	173(2)	173(2)
crystal dimensions (mm)	0.04 × 0.06 × 0.18	0.04 × 0.06 × 0.06
radiation	graphite monochromated Mo $K\alpha$, λ = 0.71073 Å	
μ(Mo $K\alpha$) (mm^{-1})	23.00	30.11
transmission factors	0.106–0.547	0.278–0.454
2θ limits	5.04–66.58°	5.00–66.54°
data collected	$-12 \le h \le 12$, $-12 \le k \le 12$, $-13 \le l \le 13$	$-12 \le h \le 12$, $-12 \le k \le 12$, $-13 \le l \le 13$
no. of data collected	7236	7771
no. of unique data, including $F_o^2 < 0$	3808 (R_{int} = 0.025)	4037 (R_{int} = 0.036)
no. of unique data, with $F_o^2 > 2\sigma(F_o^2)$	3249	3124
no. of variables	92	92
$R(F)$ for $F_o^2 > 2\sigma(F_o^2)$ [a]	0.024	0.030
$R_w(F_o^2)$ [b]	0.046	0.055
goodness of fit	1.00	0.97
$(\Delta\rho)_{max}$, $(\Delta\rho)_{min}$ (e Å^{-3})	1.03, –0.88	1.25, –1.44

[a] $R(F) = \sum||F_o| - |F_c|| / \sum|F_o|$. [b] $R_w(F_o^2) = [\sum[w(F_o^2 - F_c^2)^2] / \sum wF_o^4]^{1/2}$; $w^{-1} = [\sigma^2(F_o^2) + (Ap)^2 + Bp]$, where $p = [\max(F_o^2,0) + 2F_c^2] / 3$.

Table 7-2. Atomic coordinates and equivalent isotropic displacement for ACdGeAs$_2$ (A = K, Rb)

Atom [a]	***x***	***y***	***z***	U_{eq} (Å^2) [b]
KCdGeAs$_2$				
K1	0.54318(11)	0.23215(11)	0.67684(10)	0.01810(16)
K2	0.55834(11)	0.19480(10)	0.19075(10)	0.01703(15)
Cd1	0.00614(3)	0.10236(3)	0.31500(3)	0.01151(6)
Cd2	0.02515(3)	0.17290(3)	0.83388(3)	0.01316(6)
Ge1	0.04585(5)	0.41453(4)	0.40079(4)	0.00876(7)
Ge2	0.84076(5)	0.55190(4)	0.02600(4)	0.00858(7)
As1	0.20674(5)	0.12778(4)	0.53488(4)	0.00981(7)
As2	0.22797(5)	0.59126(4)	0.67993(4)	0.00972(7)
As3	0.24063(5)	0.12951(4)	0.03622(4)	0.01026(7)
As4	0.24921(5)	0.55556(4)	0.16681(4)	0.00968(7)
RbCdGeAs$_2$				
Rb1	0.54631(6)	0.22985(6)	0.67800(6)	0.01662(10)
Rb2	0.55888(6)	0.19570(6)	0.18861(6)	0.01528(10)
Cd1	0.00481(5)	0.10276(4)	0.31445(4)	0.01172(8)
Cd2	0.02767(5)	0.17510(4)	0.83191(4)	0.01330(8)
Ge1	0.04357(6)	0.41440(6)	0.40123(6)	0.00884(10)
Ge2	0.84630(6)	0.55200(6)	0.02475(6)	0.00879(10)
As1	0.19785(6)	0.12851(6)	0.53545(6)	0.00988(10)
As2	0.21939(6)	0.59107(6)	0.68289(6)	0.00976(10)
As3	0.23124(6)	0.13200(6)	0.03766(6)	0.01015(10)
As4	0.23799(6)	0.55531(6)	0.16892(6)	0.00976(10)

[a] All atoms are in Wyckoff position 2i. [a] U_{eq} is defined as one-third of the trace of the orthogonalized U_{ij} tensor.

Table 7-3. Interatomic distances (Å) in ACdGeAs$_2$ (A = K, Rb)

	KCdGeAs$_2$	**RbCdGeAs$_2$**
*A*1–As2	3.2904(10)	3.3930(8)
*A*1–As2	3.3507(11)	3.4666(8)
*A*1–As3	3.4569(10)	3.5783(8)
*A*1–As4	3.4905(10)	3.5835(8)
*A*1–As3	3.5754(10)	3.6207(7)
*A*1–As1	3.6423(11)	3.8010(8)
*A*1–As1	3.8609(11)	3.8998(8)
*A*2–As4	3.3177(10)	3.4151(8)
*A*2–As2	3.3823(10)	3.4724(7)
*A*2–As3	3.4025(10)	3.5248(8)
*A*2–As4	3.4027(10)	3.4839(8)
*A*2–As1	3.4360(10)	3.5231(7)
*A*2–As1	3.5647(10)	3.7092(8)
*A*2–As3	3.6531(10)	3.7035(8)
Cd1–As3	2.6500(6)	2.6524(7)
Cd1–As1	2.7235(6)	2.7280(6)
Cd1–As2	2.7334(6)	2.7302(7)
Cd1–As1	2.8822(6)	2.8847(7)
Cd2–As3	2.6428(6)	2.6332(6)
Cd2–As4	2.6872(6)	2.6834(7)
Cd2–As1	2.7268(7)	2.7158(7)
Ge1–As4	2.4542(6)	2.4524(7)
Ge1–As1	2.4544(6)	2.4540(7)
Ge1–As2	2.4829(7)	2.4785(8)
Ge2–As2	2.4393(7)	2.4422(7)
Ge2–As4	2.4726(6)	2.4704(7)
Ge2–As3	2.4787(8)	2.4723(8)
Ge1–Ge1	2.4417(8)	2.4492(10)
Ge2–Ge2	2.4266(9)	2.4214(11)

7.2.3. Band Structure Calculations

Tight-binding linear muffin tin orbital band structure calculations were performed on $KCdGeAs_2$ within the local density and atomic spheres approximation with use of the Stuttgart TB-LMTO-ASA program (version 4.7).[15] The basis set included K 4s/4p/3d, Cd 5s/5p/4d/4f, Ge 4s/4p/4d, and As 4s/4p/4d orbitals, with the K 4p/3d, Cd 4f, Ge 4d, and As 4d orbitals being downfolded. Integrations in reciprocal space were carried out with an improved tetrahedron method over 132 irreducible *k* points within the first Brillouin zone.

7.2.4. Physical Property Measurement

Measurements of dc magnetic susceptibility were made on nearly phase-pure samples of $KCdGeAs_2$ between 2 and 300 K on a Quantum Design 9T-PPMS (Physical Property Measurement System) under an applied field of 0.5 T. The susceptibility was corrected for contributions from the holder and sample ion-core diamagnetism. Attempts were also made to mount single crystals of $KCdGeAs_2$ for four-probe electrical resistivity measurements, but unfortunately good electrical contacts could not be established, probably because of rapid surface oxidation of these crystals.

7.3. Result and Discussion

The arsenides $ACdGeAs_2$ (A = K, Rb) are the first examples of quaternary phases in the A–Cd–Ge–As systems. Previously reported quaternary arsenides A–M–Ge–As (A = alkali metal, M = any other metal) are $Na_{4.3}Eu_{1.7}GeAs_4$,[16] $K_5In_5Ge_5As_{14}$,[17] $K_8In_8Ge_5As_{17}$,[17] and $NaZn_{1.5}Ge_{0.5}As_2$.[4] Known ternary arsenide phases in the related A–Cd–As, A–Ge–As, and Cd–Ge–As systems include KCdAs,[18] K_4CdAs_2,[19] ACd_4As_3 (A = K, Rb),[11] $Rb_2Cd_5As_4$,[20] K_2GeAs_2,[21] and $CdGeAs_2$,[22] all of which have structures built from Cd- or Ge-centred tetrahedra and contain only heteroatomic bonds, as can be predicted by their adherence to charge-balanced formulations involving normal oxidation

states (A^+, Cd^{2+}, Ge^{4+}, and As^{3-}). An exception is Cd_2GeAs_4, which contains a bent As_3^{5-} unit with homoatomic As–As bonds, in addition to an isolated As^{3-} anion.[23]

The low-symmetry structure (space group $P\bar{1}$) of ACdGeAs$_2$ presents interesting differences from the ternary arsenides above and contains 10 crystallographically unique sets of atoms (**Figure 7-1**). Anionic layers $[CdGeAs_2]^-$ lying parallel to the *bc*-plane are alternately stacked with nets of A^+ cations (**Figure 7-2a**). These layers can be regarded as being built up from two types of chains extending along the *c*-direction: (i) a linear chain formed by sharing opposite edges of As octahedra enclosing Ge_2 dumbbells, and (ii) a zigzag chain formed by sharing edges of As tetrahedra centred by Cd atoms (**Figure 7-2b**). The Ge_2As_6 units that comprise the linear chain adopt a conformation similar to staggered ethane, and the Ge_2 dumbbells alternate in orientation as they propagate along the chain. The Ge–As bonds of 2.45–2.48 Å are within the ranges of distances found in GeAs (2.44–2.48 Å)[24] and $GeAs_2$ (2.42–2.51) Å.[25] The Ge–Ge bonds of 2.42–2.45 Å agree well with the sum of Pauling covalent or metallic radii (2.45 Å),[26] as well as with distances found in other compounds containing Ge_2 dumbbells (GeAs, 2.43–2.46 Å; $Ca_3Ge_2As_4$, 2.42 Å; $Sr_3Ge_2As_4$, 2.45 Å).[10,24] The linear $[Ge_2As_4]$ chains (= $[Ge_2As_{4/2}As_{2/1}]$) are linked by intervening Cd atoms in tetrahedral sites. The four surrounding As atoms are arranged more regularly around Cd1 (2.65–2.88 Å) than Cd2 atoms (2.63–2.73 Å for the closest three distances and much longer, 3.49–3.55 Å, for the fourth distance), such that the latter are more accurately described as being in trigonal pyramidal geometry (CN3). A similar disparity, though not as pronounced, is observed in $RbCd_4As_3$, which also contains Cd atoms in a tetrahedral (2.64 (×1), 2.83 Å (×3)) vs. a nearly trigonal pyramidal environment (2.65 (×3), 3.19 Å (×1)).[11] The Cd–Cd distances exceed ~3.1 Å in ACdGeAs$_2$ and are probably insignificant.

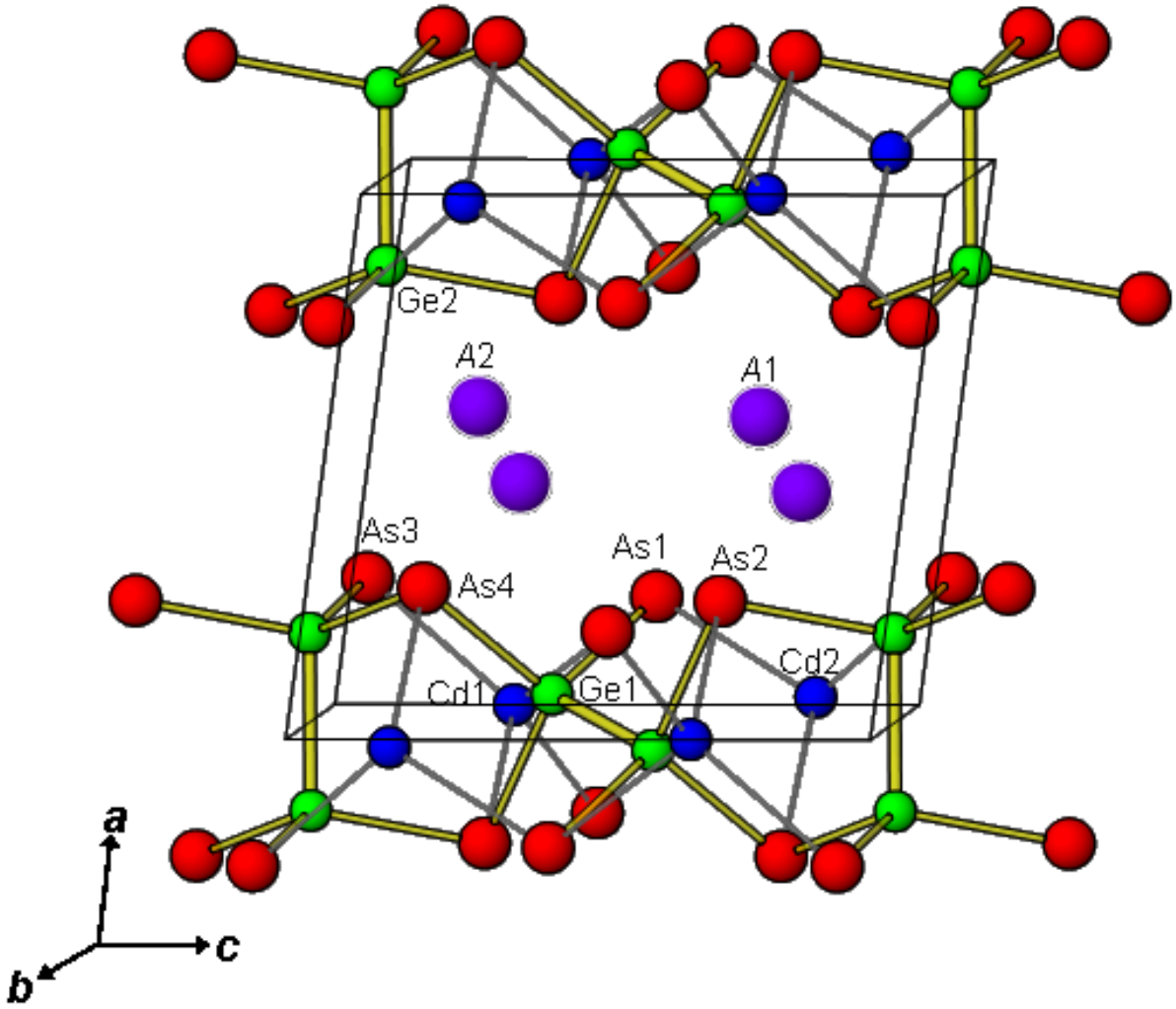

Figure 7-1. Structure of ACdGeAs$_2$ (A = K, Rb) in a ball-and-stick representation. The large violet circles are A atoms, the small blue circles are Cd atoms, the small green circles are Ge atoms, and the medium red circles are As atoms.

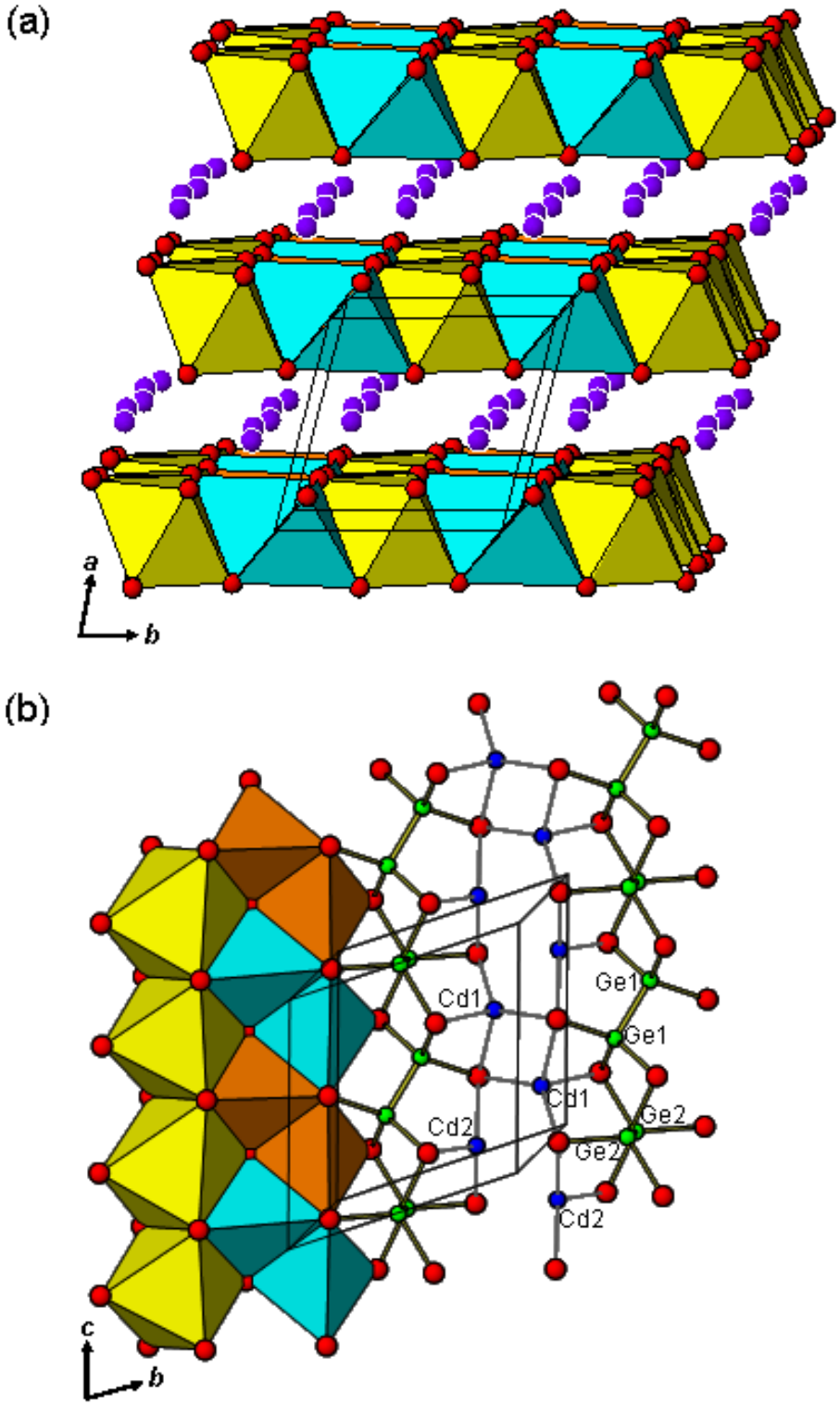

Figure 7-2. Polyhedral representation of ACdGeAs$_2$ (A = K, Rb) viewed (a) approximately down the c-direction, showing the stacking of [CdGeAs$_2$] layers, and (b) approximately down the a-direction, showing an individual layer built up of chains of octahedra filled with Ge$_2$ dumbbells (yellow) and chains of tetrahedra filled with Cd atoms (orange and blue).

The structural model assumes that the Ge and As atoms do not disorder with each other, consistent with the majority of previously known Zintl phases containing these elements. Nevertheless, given that a few examples of Ge/As disorder have been previously observed, such as in the clathrate compound $I_8As_{21}Ge_{25}$,[27] it is important to rule out that such a situation occurs in ACdGeAs$_2$. First, notwithstanding the similar X-ray scattering factors of Ge and As, structure refinements indicated that there is little mixing of As atoms into the Ge sites. We did attempt to prepare the isostructural phosphide "KCdGeP$_2$", which would have permitted clearer distinction between Ge and P atoms, but were unsuccessful under the same synthetic conditions used to obtain the arsenides. Second, bond valence sums evaluated for all atoms in the structure agree with expected valences (**Table A 5-1** in **Appendix 5**). In particular, the bond valence sums are 3.68–3.75 for the Ge atoms and 2.56–3.04 for the As atoms. Because the bond valence parameters for Ge–Ge, Ge–As, and As–As contacts are nearly identical (R_{ij} = 2.42–2.43),[28] switching the assignment of Ge and As atoms will not change the bond valence sums significantly. In fact, reversing the roles of the Ge and As atoms as formally cationic and anionic species, respectively, would only exacerbate deviations of the bond valence sums from expected values.

The ethane-like Ge_2As_6 unit is unusual but has been previously observed in GeAs,[24] $A_3Ge_2As_4$ (A = Ca, Sr),[10] $K_5In_5Ge_5As_{14}$,[17] and $K_8In_8Ge_5As_{17}$.[17] There do exist other $[M_xPn_y]^{n-}$ (M = group 13 or 14) pnictide polyanions, such as $Sn_2P_6^{12-}$, which contain formally low oxidation states for M and thus the presence of M–M bonds within these anions,[1,29–37] but they remain relatively rare compared to chalcogenide polyanions such as $P_2S_6^{4-}$.[8] The structure of ACdGeAs$_2$ bears a cursory resemblance to those of $K_5In_5Ge_5As_{14}$ and $K_8In_8Ge_5As_{17}$, only to the extent that the latter also consist of layers, but having a much more complicated connectivity of Ge_2As_6 units, which suffer from partial disordering of Ge and In atoms.[17] The binary arsenide GeAs consists of neutral layers

held together by van der Waals forces and built up of edge-sharing octahedra filled by Ge_2 dumbbells, which can be contrasted with the anionic $[CdGeAs_2]^-$ layers built up of edge-sharing octahedra and tetrahedra in ACdGeAs$_2$ (**Figure A 5-3** in **Appendix 5**). A better comparison is to $Sr_3Ge_2As_4$ (or $Ca_3Ge_2As_4$),[10] for which the arrangement of Ge_2As_6 units occurring in isolated chains is more easily related to those present in the layers in ACdGeAs$_2$ (**Figure 7-3**). The chain in ACdGeAs$_2$ is linear because the octahedra share edges in a *trans* fashion, whereas the chain is zigzag in $Sr_3Ge_2As_4$ ($Ca_3Si_2As_4$-type) because the octahedra share edges in a *cis* fashion. In both cases, five-membered rings are formed. Changes in the orientation of the dumbbells within the octahedra in the zigzag chains give rise to four- or six-membered rings, as seen in the $Sr_3Si_2As_4$ and $Ba_3Sn_2P_4$-type structures.[10,37] The relationship between the structures of ACdGeAs$_2$ and $Sr_3Ge_2As_4$ is more evident if the charge-balanced formula for the former is doubled, $(A^+)_2(Cd^{2+})_2(Ge^{3+})_2(As^{3-})_4$, and compared to the latter, $(Sr^{2+})_3(Ge^{3+})_2(As^{3-})_4$. These formulations provide a simple way to understand the bonding in these compounds. The set of two A^+ and two Cd^{2+} cations in ACdGeAs$_2$ provides the equivalent positive charge as three Sr^{2+} cations in $Sr_3Ge_2As_4$. The $[Ge_2As_4]^{6-}$ chains, which are isolated in $Sr_3Ge_2As_4$, then become connected by Cd^{2+} cations to form the $[Cd_2Ge_2As_4]^{2-}$ layers, which in turn are held together by the A^+ cations in ACdGeAs$_2$. The coordination geometry of As atoms around the A atoms can be described as monocapped trigonal prismatic (CN7) (**Figure 7-4**), with the distance to the furthest As atom around $A1$ being quite long. These trigonal prisms share opposite triangular faces to form columns extending along the c-direction.

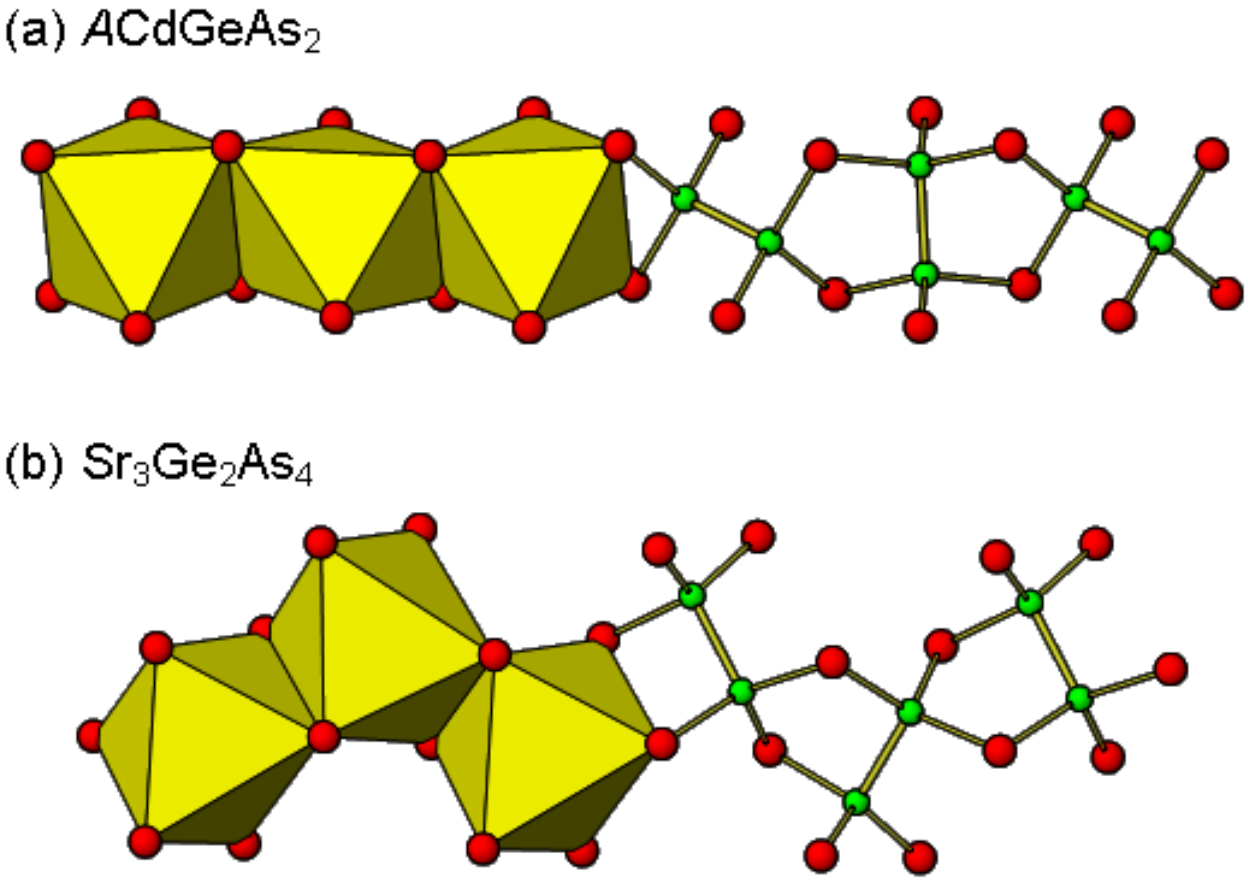

Figure 7-3. Arrangements of Ge_2As_6 units forming (a) linear chains in ACdGeAs$_2$ (A = K, Rb) and (b) zigzag chains in $Sr_3Ge_2As_4$.

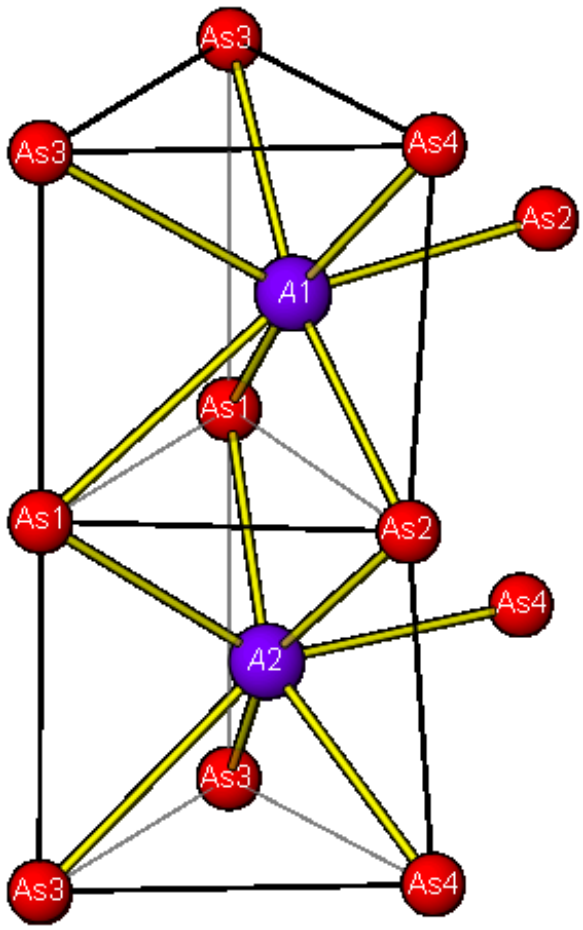

Figure 7-4. Monocapped trigonal prismatic coordination environments of As atoms around A atoms in ACdGeAs$_2$ (A = K, Rb).

The electron-precise formulation for ACdGeAs$_2$ implies that they are Zintl phases and are thus expected to be semiconducting. This is confirmed by a band structure calculation on KCdGeAs$_2$, for which the density of states (DOS) curve reveals a band gap of 0.80 eV (**Figure 7-5a**). The assumption of complete electron transfer from K atoms is consistent with the nearly insignificant contribution of K-based states below the Fermi level. The valence band extending from –5 to 0 eV is derived by mixing of Cd 5s/5p, Ge 4p, and As 4p states. Lying below in energy are filled Cd 4d (near –8 eV), Ge 4s, and As 4s states. The presence of Cd 5s/5p states below the Fermi level seems to suggest a contradiction with the oxidation state assignment of Cd^{2+}; however, the mixing of these states with As 4p states implies strongly covalent character of the Cd–As bonds,

which is to be contrasted with the more ionic character of the K–As bonds. Typical of Zintl phases, heteroatomic Cd–As and Ge–As bonds provide the dominant contribution (over 80% of the covalent bonding energy), with perfect optimization attained through filling of all bonding and no antibonding states, as seen in the crystal orbital Hamilton population (COHP) curves (**Figure 7-5b**). The integrated COHP values (–ICOHP) are 1.2 eV/bond for Cd–As contacts and 2.5 eV/bond for Ge–As contacts. Although the atomic projections of the DOS for the Cd1 (CN4) and Cd2 atoms (CN3) are similar, close inspection of the COHP curves for the Cd–As contacts reveals that the extremely long 3.49 Å distance to the fourth As atom around Cd2 is almost completely devoid of bonding, corresponding to an –ICOHP value of 0.1 eV/bond (**Figure A 5-4** in **Appendix 5**). The strong homoatomic 2.4 Å Ge–Ge bonds found in the Ge_2As_6 units are associated with the separation of filled bonding and empty antibonding states, resulting in a large and maximized –ICOHP value of 2.5 eV/bond. In contrast, the closest separations between Cd atoms (Cd1–Cd2, 3.087 Å; Cd1–Cd1, 3.109 Å) correspond to nearly negligible bonding, with a very small –ICOHP value of 0.3 eV/bond (**Figure A 5-4** in **Appendix 5**).

Magnetic susceptibility measurements on powder samples of $KCdGeAs_2$ reveal essentially temperature-independent diamagnetism ($\chi_0 = -1 \times 10^{-3}$ emu/mol) (**Figure A 5-5** in **Appendix 5**), consistent with the absence of unpaired electrons and the closed-shell (or subshell) configurations of all atoms.

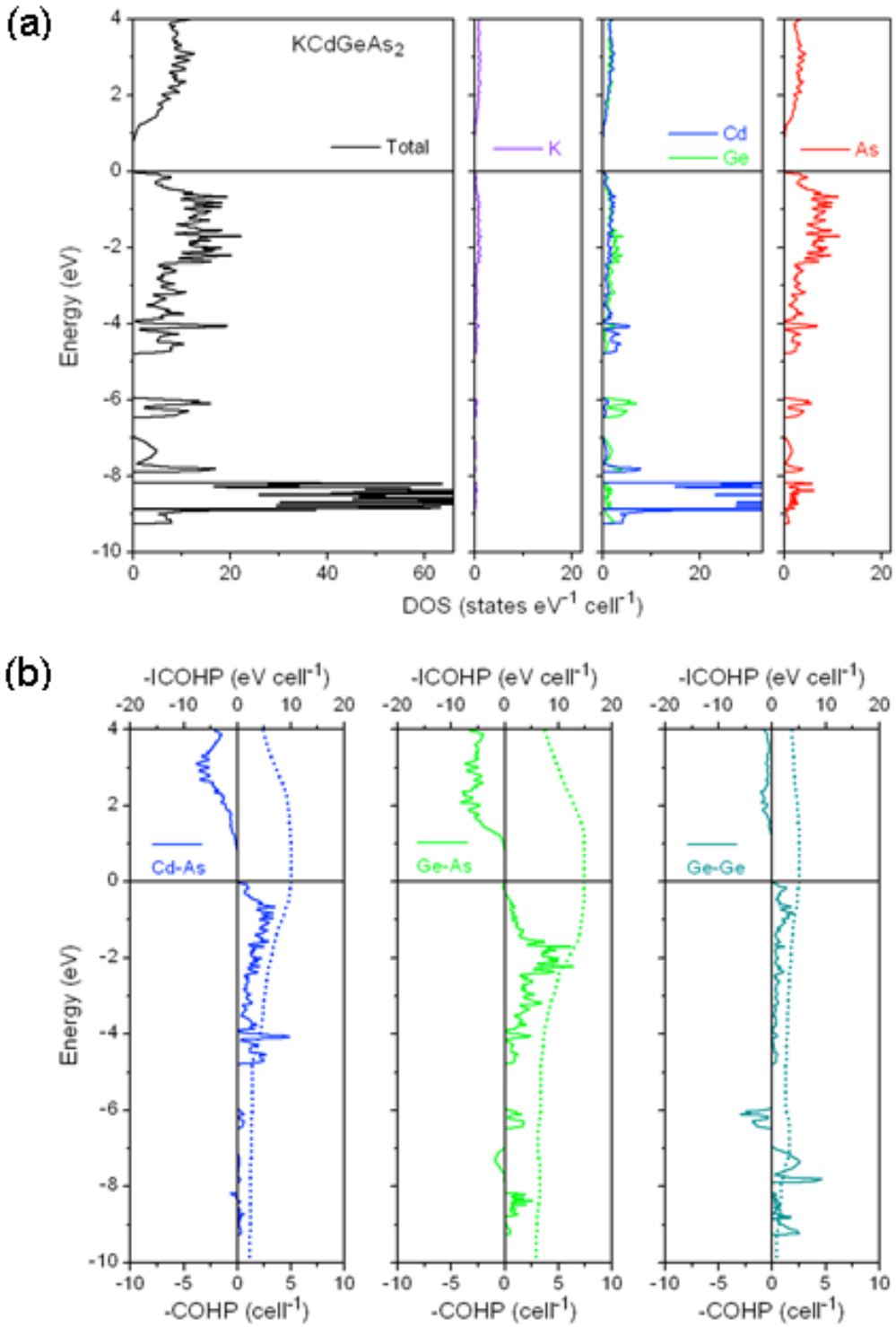

Figure 7-5. (a) Density of states (DOS) and its atomic projections for $KCdGeAs_2$. (b) Crystal orbital Hamilton population (COHP) curves for Cd–As, Ge–As, and Ge–Ge contacts. The Fermi level is at 0 eV.

7.4. Conclusion

The structure of the quaternary arsenides ACdGeAs$_2$ (A = K, Rb) consists of heteroatomic pnictide polyanions $Ge_2As_6^{12-}$ coordinating onto Cd^{2+} centres. This viewpoint is useful because it draws attention to the similarity to the more extensive examples of chalcogenide polyanions, such as $P_2S_6^{4-}$, which form the basis of a rich chemistry of multinary chalcogenides.[8] There appear to be attractive opportunities to develop analogous complex pnictides, and efforts are underway to explore the substitution of Cd with other divalent transition metals (such as Mn, Fe, Co, Ni) in the systems A–M–Ge–As.

7.5. References

1. Eisenmann, B.; Cordier, G. In *Chemistry, Structure, and Bonding of Zintl Phases and Ions*; Kauzlarich, S. M.; Ed.; VCH: New York, 1996; pp. 61–137.
2. Villars, P.; Cenzual, K. *Pearson's Crystal Data – Crystal Structure Database for Inorganic Compounds*, release 2010/11; ASM International: Materials Park, OH, 2010.
3. Brown, S. R.; Kauzlarich, S. M.; Gascoin, F.; Snyder, G. J. *Chem. Mater.* **2006**, *18*, 1873–1877.
4. Khatun, M.; Stoyko, S. S.; Mar, A. *Inorg. Chem.* **2013**, *52*, 3148–3158.
5. Schunemann, P. G.; Schepler, K. L.; Budni, P. A. *MRS Bull.* **1998**, *23(7)*, 45–49.
6. Novotortsev, V. M.; Kalinnikov, V. T.; Koroleva, L. I.; Demin, R. V.; Marenkin, S. F.; Aminov, T. G.; Shabunina, G. G.; Boichuk, S. V.; Ivanov, V. A. *Zh. Neorg. Khim.* **2005**, *50*, 552–557.
7. Parker, D.; Singh, D. J. *Phys. Rev. B* **2012**, *85*, 125209-1–125209-7.
8. Wu, Y.; Bensch, W. *CrystEngComm* **2010**, *12*, 1003–1015.
9. Eller, P. G.; Bradley, D. C.; Hursthouse, M. B.; Meek, D. W. *Coord. Chem. Rev.* **1977**, *24*, 1–95.
10. Eisenmann, B.; Schäfer, H. *Z. Anorg. Allg. Chem.* **1982**, *484*, 142–152.
11. He, H.; Tyson, C.; Bobev, S. *Inorg. Chem.* **2011**, *50*, 8375–8383.
12. Sheldrick, G. M. *SHELXTL*, version 6.12; Bruker AXS Inc.: Madison, WI, 2001.
13. Spek, A. L. *Acta Crystallogr., Sect. D: Biol. Crystallogr.* **2009**, *65*, 148–155.
14. Gelato, L. M.; Parthé, E. *J. Appl. Crystallogr.* **1987**, *20*, 139–143.
15. Tank, R.; Jepsen, O.; Burkhardt, A.; Andersen, O. K. *TB-LMTO-ASA Program*, version 4.7; Max Planck Institut für Festkörperforschung: Stuttgart, Germany, 1998.

16. Nuss, J.; Kalpen, H.; Hönle, W.; Hartweg, M.; von Schnering, H. G. *Z. Anorg. Allg. Chem.* **1997**, *623*, 205–211.

17. Shreeve-Keyer, J. L.; Haushalter, R. C.; Lee, Y.-S.; Li, S.; O'Connor, C. J.; Seo, D.-K.; Whangbo, M.-H. *J. Solid State Chem.* **1997**, *130*, 234–249.

18. Kahlert, H.; Schuster, H. U. *Z. Naturforsch. B: Anorg. Chem., Org. Chem.* **1976**, *31*, 1538–1539.

19. Eisenmann, B.; Klein, J.; Somer, M. *Z. Kristallogr.* **1991**, *197*, 271–272.

20. He, H.; Stoyko, S. S.; Mar, A.; Bobev, S. *Acta Crystallogr., Sect. C: Cryst. Struct. Commun.* **2013**, *69*, 455–459.

21. Eisenmann, B.; Klein, J. *J. Less-Common Met.* **1991**, *175*, 109–117.

22. Novotortsev, V. M.; Palkina, K. K.; Mikhailov, S. G.; Molchanov, A. V.; Ochertyanova, L. I.; Marenkin, S. F. *Inorg. Mater.* **2005**, *41*, 439–442.

23. Mikkelsen, Jr., J. C.; Hong, H. Y.-P. *Mater. Res. Bull.* **1974**, *9*, 1209–1218.

24. Mentzen, B. F.; Hillel, R.; Michaelides, A.; Tranquard, A.; Bouix, J. *C. R. Seances Acad. Sci., Ser. 2* **1981**, *293*, 965–967.

25. Bryden, J. H. *Acta Crystallogr.* **1962**, *15*, 167–171.

26. Pauling, L. *The Nature of the Chemical Bond*, 3rd ed.; Cornell University Press: Ithaca, NY, 1960.

27. Ayouz, K.; Kars, M.; Rebbah, A.; Rebbah, H. *Acta Crystallogr., Sect. E* **2009**, *65*, i15.

28. O'Keeffe, M.; Brese, N. E. *J. Am. Chem. Soc.* **1991**, *113*, 3226–3229.

29. Eisenmann, B.; Schäfer, H. *Z. Naturforsch. B: Anorg. Chem., Org. Chem.* **1981**, *36*, 415–419.

30. Eisenmann, B.; Jordan, H.; Schäfer, H. *Z. Naturforsch. B: Anorg. Chem., Org. Chem.* **1982**, *37*, 1564–1568.

31. Eisenmann, B.; Jordan, H.; Schäfer, H. *Z. Naturforsch. B: Anorg. Chem., Org. Chem.* **1983**, *38*, 404–406.

32. Cordier, G.; Ochmann, H.; Schäfer, H. *Mater. Res. Bull.* **1986**, *21*, 331–336.

33. Hurng, W.-M.; Corbett, J. D.; Wang, S.-L.; Jacobson, R. A. *Inorg. Chem.* **1987**, *26*, 2392–2395.

34. Klein, J.; Eisenmann, B. *Mater. Res. Bull.* **1988**, *23*, 587–594.

35. Kim, S.-J.; Kanatzidis, M. G. *Inorg. Chem.* **2001**, *40*, 3781–3785.

36. Park, S.-M.; Kim, S.-J.; Kanatzidis, M. G. *J. Solid State Chem.* **2003**, *175*, 310–315.

37. Dong, Y.; Ranjan, C.; DiSalvo, F. J. *J. Alloys Compd.* **2007**, *430*, 54–59.

Chapter 8

Conclusions

8.1 Conclusions

In accordance with the goals set out in the introduction, several series of new ternary and quaternary arsenides and antimonides were synthesized and characterized by X-ray diffraction methods. The main focus was on the synthesis of new phases that extend the limit of Zintl's definition and show the structural diversity of pnictides. As summarized in **Table 8-1**, these new compounds exhibit various crystal structures, bonding character, and electronic structures.

Table 8-1. Ternary and quaternary pnictides synthesized

Compounds	Structure type	Homoatomic bonds	Structure classification	Properties
$A_2Zn_5As_4$ (A = K, Rb)	own type	absent	normal valence Zintl phases	semiconductor
$Rb_4Zn_7As_7$ ($Rb_4Mn_{3.5}Zn_{3.5}Sb_7$)	own type	*Pn–Pn* bonds	polyanionic or electron deficient Zintl phases	metallic
$Rb_7Mn_{12}Sb_{12}$ ($Rb_7Mn_4Cd_8Sb_{12}$)	own type	Sb–Sb bonds	polyanionic or electron deficient Zintl phases	metallic
ATt_3As_3 (A = K, Rb, Tt = Ge, Sn)	own type, related to $NaGe_3P_3$ structure	*Tt–Tt* bonds	polycationic Zintl phases	semiconductor
$NaGe_6As_6$	own type	*Tt–Tt* bonds	polycationic or electron rich Zintl phases	*n*-doped semiconductor
$AM_{1.5}Tt_{0.5}As_2$ (A = Na, K, Rb; M = Zn, Cd; Tt = Si, Ge, Sn)	$CaAl_2Si_2$-type or $ThCr_2Si_2$-type structure	absent	simple valence Zintl phase	semimetallic
$ACdGeAs_2$ (A = K, Rb)	own type	Ge–Ge	polycationic Zintl phases	semiconductor

The compounds listed in **Table 8-1** can be broadly grouped into three categories: (1) *A–M–Pn* system: $A_2Zn_5As_4$ (*A* = K, Rb), $Rb_4Zn_7As_7$ ($Rb_4Mn_{3.5}Zn_{3.5}Sb_7$), and $Rb_7Mn_{12}Sb_{12}$ ($Rb_7Mn_4Cd_8Sb_{12}$); (2) *A–Tt–Pn* system: ATt_3As_3 and $NaGe_6As_6$; (3) *A–M–Tt–Pn* system: $AM_{1.5}Tt_{0.5}As_2$ and ACdGeAs_2.

The compounds $A_2Zn_5As_4$ (A = K, Rb) are normal valence compounds (*VEC* = (2+10+20)/4 = 8, no homoatomic bond) whereas $Rb_4Zn_7As_7$ and $Rb_7Mn_{12}Sb_{12}$ are unusual examples of electron-deficient Zintl phases. The valence electron count, *VEC*, is 7.6 for $Rb_4Zn_7As_7$ and $Rb_7Mn_{12}Sb_{12}$, implying that homoatomic *Pn–Pn* bonds are present in these pnicogen-rich phases. The closed-shell formulations $(Rb^+)_4(M^{2+})_7(h^+)(Pn^{2-})_2(Pn^{3-})_5$ and $(Rb^+)_7(M^{2+})_{12}(h^+)(Sb^{2-})_4(Sb^{3-})_8$, where h^+ represents a hole, indicate that they have one electron less than required for completely charge balance. Band structure calculations reveal that the electron deficiency originates from the depopulation of antibonding *Pn–Pn* states in the $Rb_4Zn_7As_7$ and *M–M* states in $Rb_7Mn_{12}Sb_{12}$. As a result, an internal oxidation of *Pn* or *M* takes place.

The electron counting rules discussed in the introduction can be applied for compounds in the *A–Tt–Pn* system to give *VEC* = (1+12+15)/3 = 9.33 for ATt_3As_3 and *VEC* = (1+24+30)/6 = 9.16 for $NaGe_6As_6$. Because *VEC*(*X*) exceeds 8, these compounds are metal-rich phases that contain polycationic *Tt–Tt* bonds. In ATt_3As_3 phases, the *Tt* atoms reside in three different crystallographic positions. The coordination geometry around *Tt*1 and *Tt*2 are tetrahedral whereas it is trigonal pyramidal around *Tt*3. The *Tt*2 and *Tt*3 atoms, which have formal charges of 3+ and 1+ respectively, are connected via a homoatomic bond. On the other hand, the $NaGe_6As_6$ phase contains two types of ethane-like Ge_2As_6 units, each containing Ge–Ge homoatomic bonds. Three different As atoms, with formal charge of 3–, are connected to the remaining *Tt* atoms. Band structure calculations on

these pnictides confirm the presence of homoatomic *Tt–Tt* interactions. They are termed as polycationic Zintl phases.

The electron counting rules can be extended to the quaternary phases in the *A–M–Tt–Pn* systems. For $AM_{1.5}Tt_{0.5}As_2$ (*A* = Na, K, Rb; *M* = Zn, Cd; *Tt* = Si, Ge, Sn), the *VEC* is 8, which implies that they are normal valance compounds. However, X-ray diffraction reveals that they have $ThCr_2Si_2$-type structures ($KZn_{1.5}Si_{0.5}As_2$, $KZn_{1.5}Ge_{0.5}As_2$, and $RbZn_{1.5}Ge_{0.5}As_2$), which contain weak *M–M* and *Pn–Pn* interactions. Another quaternary phase, $ACdGeAs_2$ (*VEC* = 8.5), contains the ethane-like Ge_2As_6 units seen previously in $NaGe_6As_6$ in which Ge atoms with formal charge of 3+ participate in homoatomic Ge–Ge bonds. This compound contains only homoatomic Ge–Ge but no As–As bonds, as confirmed using bond valence sum calculations.

All pnictides synthesized are confirmed to be Zintl phases and satisfy the definition provided earlier. In general, they form complex anionic slabs or networks $[M_mTt_bPn_x]^{a-}$ with A^{a+} cations residing between layers or within channels as a space-filler. However, the bonding patterns of anionic fragments are different in each type of structure, which is not something that can be explained from the Zintl concept alone. Possible factors that influence the particular structure formed include relative atomic sizes, electronegativity differences, variable oxidation states, and elemental composition. Some of the bonding patterns are unique and interesting. The structure of $A_2Zn_5As_4$ contains a unit where four $ZnAs_4$ tetrahedra are connected in a special way through edge- and corner-sharing to form a complex 3*D* network. $Rb_4Zn_7As_7$ ($Rb_4Mn_{3.5}Zn_{3.5}Sb_7$), and $Rb_7Mn_{12}Sb_{12}$ ($Rb_7Mn_4Cd_8Sb_{12}$) structures contain zigzag corrugated infinite ribbons that are built of six-membered-wide and alternating six- and four-member-wide MAs_4 tetrahedra. Quaternary derivatives of these compounds were made to examine site preferences. The square pyramidal sites are preferred by Mn atoms and the tetrahedral sites contain a disordered mixture of Mn and Zn/Cd

atoms. Reactions to prepare similar phases containing Na, K, Fe, Co, Ni, or Cu elements were unsuccessful. Such a study leads to the conclusion that the size of the *A* atoms is important and that the *M* sites only accommodate d^5 and d^{10} metals.

The ATt_3As_3 structure contains corrugated anionic layers which are built from five-membered rings (*Tt*–As–*Tt*–*Tt*–As) containing *Tt* atoms in variable oxidation states (+4, +3, and +1). The anionic $[Ge_6As_6]$ layer in $NaGe_6As_6$ is built by condensing chains of edge-sharing octahedra, each centred by Ge–Ge dumbbells. Although the structure is derived by the insertion of Na between GeAs layers, we are unable to prepare the same phases using K and Rb; analogous investigations with Li are underway. It appears that the size of the guest atom is important for entering the empty space between layers.

The $AM_{1.5}Tt_{0.5}As_2$ compounds crystallize in either $CaAl_2Si_2$-type or $ThCr_2Si_2$-type structures, which opens a door to study the structural flexibility of these parent-type structures. $CaAl_2Si_2$-type and $ThCr_2Si_2$-type compounds have been studied widely for thermoelectricity and superconductivity, respectively. The preference for forming $CaAl_2Si_2$-type vs $ThCr_2Si_2$-type has been explained using a structure map as a function of relative atomic sizes (**Figure 8-1**). Cations whose radius ratios r_A/r_B are less than 1.6 (where r_B is the weighted average of the *M* and *Tt* radii) prefer to form $CaAl_2Si_2$-type structure, whereas those with r_A/r_B greater than 1.6 prefer $ThCr_2Si_2$-type structures; larger ratios, $r_A/r_B > 1.8$, lead to different structures. $ACd_{1.5}Ge_{0.5}As_2$ (*A*= K, Rb) do not exist but $ACdGeAs_2$ phases exist adopting a new structure type. However, a structure map is a good resource to evaluate the possible existence of phases. Similar reactions failed using Fe, Co, Ni, which further confirmed that the *M*-positions in $CaAl_2Si_2$-type structures are limited to d^0, d^5 and d^{10} metals. This study also concluded that pnictides in **Table 8-1** could be used for further structural flexibility studies and Zintl

rule is a guideline to explain the bonding and structure but crystal structure determination is a strong tool to visualize real structure pattern.

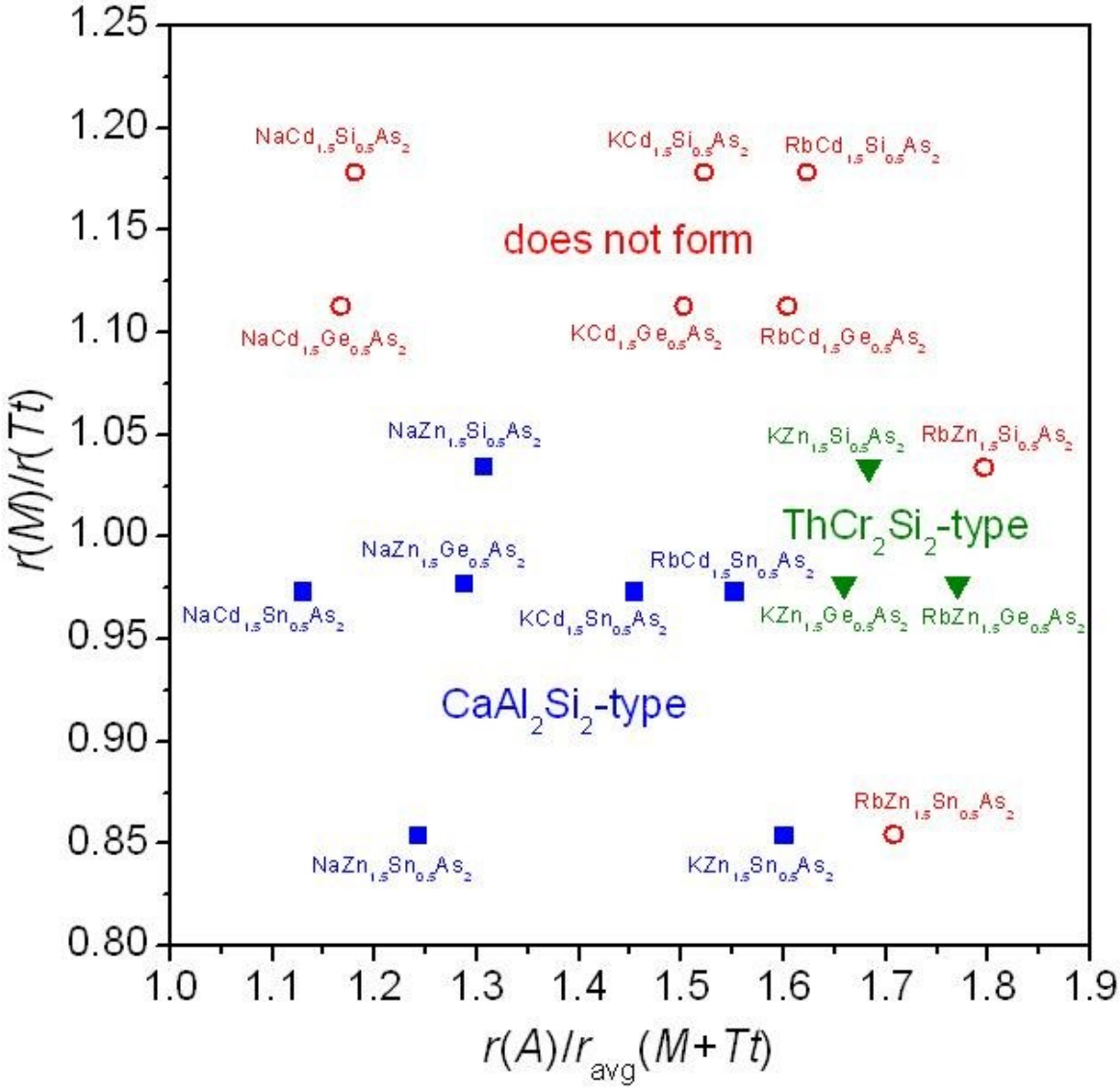

Figure 8-1. Structure map for quaternary arsenides $AM_{1.5}Tt_{0.5}As_2$ (A = Na, K, Rb; M = Zn, Cd; Tt = Si, Ge, Sn).

The band structure calculation suggested all synthesized pnictides in **Table 8-1** are either semiconductors or semimetals, which agrees with expectation. The complex anionic fragments contain interesting hybrid bonding character: covalent (*Tt–Tt* and *Pn–Pn*) character which increases the mobility of the charge carrier species, polar covalent (*M–Pn*), and metallic (*M–M*) bonds). The

overall complex structure reduces the lattice thermal conductivity via phonon scattering; therefore they behave as a "phonon-glass electron-crystal" material, which combined with the presence of a small band gap, fulfill the conditions for good thermoelectric materials. All pnictides **Table 8-1** are potential candidates for good thermoelectric materials. The study also suggests that there is a relation between total *VEC* and band gap. Pnictides containing d-block metals have *VEC* of 8 and exhibit small or pseudo band gaps. Pnictides containing tetrels have *VEC* of greater than 8 and exhibit wider band gaps. Therefore the introduction of d-block metals or tetrels in alkali-metal pnictides can be a way to tune the band-gap.

Table 8-2. Pnictides with their *VEC* and band gap (eV)

Compounds	***VEC***	**Band gap (eV)**
$Rb_4Zn_7As_7$	7.57	small gap above Fermi level
$Rb_7Mn_{12}Sb_{12}$	7.58	pseudo gap above Fermi level
$K_2Zn_5As_4$	8	0.40
$NaZn_{1.5}Tt_{0.5}As_2$	8	small overlap at Fermi level
KSn_3As_3	9.33	0.50
KGe_3As_3	9.33	0.71
$KCdGeAs_2$	8.5	0.80

8.2 Future Work

This work has brought a great opportunity to investigate new and exciting structures in solid state chemistry. Because binary and ternary metal arsenides have been poorly studied, further investigation on these compounds is worthwhile. Combined with previous results, as reviewed in the introduction, the work in this thesis reveals that (1) pnictides with early and late transition metals are rarely reported, and (2) pnictides with Group 13 elements are limited to only two to three

different compositions. It would be good to investigate new phases in *A–M–Pn*, *A–Tr–Pn*, and *A–RE–M–Pn* systems. The physical properties for alkali-metal pnictides are not well studied because of their air and moisture sensitivity. To improve the air stability of these compounds, we can modify them in different ways:

1. The $A_2Zn_5As_4$-type structure can be modified by replacing alkali metal *A* with alkaline-earth metal *AE* (Ca, Sr, Ba) and the rare-earth element Eu, which may result in air-stable compounds. Because they are small band-gap semiconductors and they have complex structures, they are potential candidates for thermoelectric materials. Wang et al. suggested that low level hole-doping on $A_2Zn_5As_4$ would improve their thermopower.[1] To do this, it would be good to partially substitute Ag or Cu at the Zn-positions.
2. Many compounds crystallize in $CaAl_2Si_2$- and $ThCr_2Si_2$-type structures. The preference for forming them can be evaluated using a structure map. There are many ways to modify quaternary $AM_{1.5}Tt_{0.5}As_2$ phases: by changing elements (either *A* or *M* or *Tt*) and by changing compositions. Some new compounds identified are $Na_2MGe_3As_4$, $A_2CdTt_3As_4$, $A_2ZnGe_4As_5$, $A_2ZnSn_{2.5}As_{3.5}$, $A_2CdGe_3As_6$, and $A_9M_2Ge_{12}As_{22}$.
3. The layered $NaGe_6As_6$ structure suggests that the GeAs layer can tolerate a small change in its electronic structure. Doping of other elements like Li or transition metals between GeAs layers would be interesting to study properties.
4. All of the new structures contain complex anionic fragments. Band structure calculations suggest either semiconducting or semimetallic behavior. It is important to examine their physical properties (e.g., electrical and thermal conductivity) because they may be good candidates for thermoelectric materials.

8.3 References

1. Yang, G.; Yang, J.; Yan, Y.; Wang, Y. *Phys. Chem. Chem. Phys.* **2014**, *16*, 5661–5666.

Bibliography

1. Zintl, E. *Angew. Chem.* **1939**, *52*, 1–6.
2. Nesper, R. *Z. Anorg. Allg. Chem.* **2014**, *640*, 2639–2648.
3. Zintl, E.; Dullenkopf, W. *Z. Phys. Chem.* **1932**, *B16*, 183–194.
4. Zintl, E.; Brauer, G. *Z. Phys. Chem.* **1933**, *B20*, 245–271.
5. Schäfer, H.; Eisenmann, B.; Müller, W. *Angew. Chem., Intl. Ed. Engl.* **1973**, *12*, 694–712.
6. Schäfer, H.; Eisenmann, B. *Rev. Inorg. Chem.* **1981**, *3*, 29–101.
7. Schäfer, H. *Annu. Rev. Mater. Sci.* **1985***, 15*, 1–44.
8. Nesper, R. *Prog. Solid State Chem.* **1990**, *20*, 1–45.
9. Kauzlarich, S. M. In *Chemistry, Structure, and Bonding of Zintl Phases and Ions;* Ed.; VCH: Weinheim, Germany, 1996.
10. Kanatzidis, M. G. *Recent Trends in Thermoelectric Materials Research I;* Series: *Semiconductors and Semimetals*; Academic: San Diego, 2001.
11. Gascoin, F.; Ottensmann, S.; Stark, D.; Haïle, S. M.; Snyder, G. J. *Adv. Funct. Mater.* **2005**, *15*, 1860–1864.
12. Shawna, R. B.; Kauzlarich, S. M.; Gascoin, F.; Snyder, G. J. *Chem. Mater.* **2006**, *18*, 1873–1877.
13. Condron, C. L.; Kauzlarich, S. M. *Inorg. Chem.* **2007**, *46*, 2556–2562.
14. Kauzlarich, S. M.; Brown, S. R.; Snyder, G. J. *Dalton Trans.* **2007**, 2099–2107.
15. Snyder, G. J.; Toberer, E. S. *Nat. Mater.* **2008**, *7*, 105–114.
16. Curro, N. J.; Caldwell, T.; Bauer, E. D.; Morales, L. A., Graf, M. J., Bang, Y.; Balatsky, A. V.; Thompson, J. D.; Sarrao, J. L. *Nature* **2005**, *434*, 622–625.
17. Gschneidner Jr., K. A.; Pecharsky, V. K.; Tsokol, A. O. *Rep. Prog. Phys.* **2005**, *68*, 1479–1539.
18. van Arkel, A. E. *Molecules and Crystals in Inorganic Chemistry.* Interscience: New York, 1956.
19. Ketelaar, J. A. A. *Chemical Constitution; An Introduction to the Theory of the Chemical Bond,* 2nd Ed.; Elsevier: Amsterdam, 1958.
20. Parthé, E. *Acta Crystallogr.*, *Sect. B* **1973**, *29,* 2808–2815.
21. Müller, U. *Inorganic Structural Chemistry*, 2nd Ed.; Wiley: Chichester, 2007.
22. Lewis, G. N. *J. Am. Chem. Soc.* **1916**, *38*, 762–785.
23. Kossel, W. *Ann. Phys.* **1916**, *354*, 229–362.
24. Klein, J.; Eisenmann, B. *Mater. Res. Bull.* **1988**, *23*, 587–594.

25. Hafner, P.; Range, K. J. *J. Alloys Compd*. **1994**, *216*, 7–10.

26. Smith, P. M.; Leadbetter, A. J.; Apling, A. J. *Philos. Mag*. **1975**, *31*, 57–64.

27. Hönle, W.; von Schnering, H.G. *Acta Crystallogr., Sect. A* **1978**, *34*, S152–156.

28. Iandelli, A.; Franceschi, E. A. *J. Less-Common Met*. **1973**, *30*, 211–216.

29. Hütz, A.; Nagorsen, G. *Z. Metallkd.* **1974**, *65*, 618–623.

30. Papoian, G. A.; Hoffmann, R. H. *Angew. Chem., Int. Ed.* **2000**, *39*, 2408–2448.

31. Hönle, W.; Buresch, J.; Peters, K.; Chang, J. H.; von Schnering, H. G. *Z. Kristallogr. – New Cryst. Struct*. **2002**, *217*, 487–488.

32. Emmerling, F.; Röhr, C. *Z. Naturforsch., B* **2002**, *57*, 963–975.

33. Gascoin, F.; Sevov, S. C. *Inorg. Chem*. **2001**, *40*, 5177–5181.

34. von Schnering, H. G.; Somer, M.; Kliche, G.; Hönle, W.; Meyer, T.; Wolf, J.; Ohse, L.; Kempa, P. B. *Z. Anorg. Allg. Chem.* **1991**, *601*, 13–30.

35. Hönle, W.; Krogull, G.; Peters, K.; von Schnering, H. G. *Z. Kristallogr. – New Cryst. Struct.* **1999**, *214*, 17–18.

36. Seifert-Lorenz, K.; Hafner, J. *Phys. Rev. B: Condens. Matter Mater. Phys.* **1999**, *59*, 829–842.

37. Senko, M. E.; Dunn, H. M.; Weidenborner, J. E.; Cole, H. *Acta Crystallogr.* **1959**, *12*, 76.

38. Wadsten, T. *Acta Chem. Scand*. **1967**, *21*, 593–594.

39. Rehr, A.; Guerra, F.; Parkin, S.; Hope, H.; Kauzlarich, S. M. *Inorg. Chem*. **1995**, *34*, 6218–6220.

40. Emmerling, F.; Hirschle, C.; Röhr, C. *Z. Anorg. Allg. Chem.* **2002**, *628*, 559–563.

41. Brice, J. F.; Courtois, A. *C. R. Seances Acad. Sci.*, *Ser. C* **1976**, *283*, 479–481.

42. Ferguson, M. J.; Hushagen, R. W.; Mar, A. *J. Alloys Compd.* **1997**, *249*, 191–198.

43. Brylak, M.; Möller, M. H.; Jeitschko, W. *J. Solid State Chem.* **1995**, *115*, 305–308.

44. Eschen, M.; Jeitschko, W. *Z. Naturforsch*., *B* **2003**, *58*, 399–409.

45. Lam, R.; McDonald, R.; Mar, A. *Inorg. Chem.* **2001**, *40*, 952–959.

46. Liu, Y.; Chen, L.; Li, L.-H.; Wu, L.-M; Zelinska, O. Ya.; Mar, A. *Inorg. Chem.* **2008**, *47*, 11930–11941.

47. Mills, A. M.; Mar, A. *Inorg. Chem.* **2000**, *39*, 4599–4607.

48. Mandrus, D.; Sefat, A. S.; McGuire, M. A.; Sales, B. C. *Chem. Mater.* **2010**, *22*, 715–723.

49. Stoyko, S. S.; Khatun, M.; Mar, A. *Inorg. Chem*. **2012**, *51*, 2621−2628.

50. Villars, P.; Cenzual, K. *Pearson's Crystal Data – Crystal Structure Database for Inorganic Compounds*, release 2015/16; ASM international: Materials Park, Ohio, USA.

51. Mentzen, B. F.; Hillel, R.; Michaelides, A.; Tranquard, A.; Bouix, J. *C. R. Acad. Sci., Ser. II* **1981**, *293*, 965–967.

52. Eisenmann, B.; Schäfer, H. *Z. Naturforsch., B* **1981**, *36*, 415–419.

53. Klein, J.; Eisenmann, B. *Mater. Res. Bull.* **1988**, *23*, 587–594.

54. Hurng, W.-M.; Corbett, J. D., Wang, S.-L.; Jacobson, R. A. *Inorg. Chem.* **1987**, *26*, 2392–2395.

55. Feng, K.; Yin, W.; He, R.; Lin, Z.; Jin, S.; Yao, J.; Fu, P.; Wu, Y. *Dalton Trans.* **2012**, *41*, 484–489.

56. Mewis, A. *Z. Naturforsch*., *B* **1980**, *35,* 141–145.

57. Kauzlarich, S. M.; Thomas, M. M.; Odink, D. A.; Olmstead, M. M. *J. Am. Chem. Soc.* **1991**, *113,* 7205–7208.

58. Rehr, A.; Kuromoto, T. Y.; Kauzlarich, S. M.; del Castillo, J.; Webb, D. J. *Chem. Mater.* **1994**, *6,* 93–99.

59. Cordier, G.; Müller V. *Z. Kristallogr*. **1993**, *203*, 152–153.

60. Dong, Z.-C.; Corbett, J. D. *Inorg. Chem.***1995**, *34*, 5042–5048.

61. Alemany, P.; Llunell, M.; Canadell, E. *Inorg. Chem.* **2006**, *45*, 7235–7241.

62. Ponou, S.; Fässler, T. F.; Tobías, G.; Canadell, E.; Cho, A.; Sevov, S. C. *Chem. -Eur. J.* **2004**, *10*, 3615–3621.

63. Guloy, A. M.; Corbett, J. D. *Inog. Chem*. **1996**, *35*, 2616–2622.

64. Birdwhistell, T. L. T.; Stevens, E. D.; O'Connor, C. J. *Inorg. Chem.* **1990**, *29*, 3892–3894.

65. Hutchins, P. T.; Leynaud, O.; O'Dell, L. A.; Smith, M. E.; Barnes, P.; McMillan, P. F. *Chem. Mater.* **2011**, *23*, 5160–5167.

66. Migas, D. B.; Shaposhnikov, V. L.; Borisenko, V. E. *Phys. Status Solidi B* **2007**, *244*, 2611–2618.

67. Baran, V. V.; Fischer, A.; Scherer, W.; Fässler, T. F. *Z. Anorg. Allg. Chem*. **2013**, *639*, 2125–2128.

68. Kalarasse, F.; Bennecer, B. *J. Phys. Chem. Solids* **2006**, *67*, 846–850.

69. He, H.; Tyson, C.; Bobev, S. *Inorg. Chem.* **2011**, *50*, 8375–8383.

70. Stoyko, S. S.; Khatun, M.; Mullen, C. S.; Mar, A. *J. Solid State Chem.* **2012**, *192*, 325–330.

71. He, H.; Zevalkink, A.; Gibbs, Z. M.; Snyder, G. J.; Bobev, S. *Chem. Mater.* **2012**, *24*, 3596–3603.

72. May, A. F.; McGuire, M. A.; Ma, J.; Delaire, O.; Huq, A.; Custelcean, R. *J. Appl. Phys.* **2012**, *111*, 033708-1–033708-7.

73. Young, D. M.; Kauzlarich, S. M. *Chem. Mater.* **1995**, *7*, 206–209.

74. Oh, H.; Moon, J.; Shin, D.; Moon, C-. Y.; Choi, H. J. *Prog. Supercond.* **2011**, *13*, 65–84.

75. Ettema, A. R. H. F.; de Groot, R. A. *J. Phys. Condens. Matter*. **1999**, *11*, 759–766.

76. Hirt, H.; Deiseroth, H. *Z. Anorg. Allg. Chem*. **2004**, *630*, 1357–1359.

77. Yan, J-. Q.; Nandi, S.; Zarestky, J. L.; Tian, W.; Kreyssig, A.; Jensen, B.; Kracher, A.; Dennis, K. W.; McQueeney, R. J.; Goldman, A. I.; McCallum, R. W.; Lograsso, T. A. *Appl. Phys. Lett*. **2009**, *95*, 222504-1–222504-3.

78. Chen, Z. G.; Yuan, R. H.; Dong, T.; Wang, N. L. *Phys. Rev. B* **2010**, *81*, 100502-1–100502-4.

79. Dong, T.; Chen, Z. G.; Yuan, R. H.; Hu, B. F.; Cheng, B.; Wang, N. L. *Phys. Rev. B* **2010**, *82*, 054522-1–054522-5.

80. Sangster, J.; Pelton, A. D. *J. Phase Equilib. Diffus*. **1993**, *14*, 240–242.

81. Voronin, G. F.; Bludova, L. N. *Vestnik Belorusskogo Gosudarstvennogo Universiteta*, *Seriya 2*: *Khimiya Biologiya*, *Geografiya,* **1974**, *15*, 433–435.

82. Emmerling, F.; Röhr, C. *Z. Anorg. Allg. Chem.* **2003**, *629*, 467–472.

83. Hirschle, C.; Röhr, C. *Z. Anorg. Allg. Chem*. **2000**, *626*, 1992–1998.

84. Saparov, B.; Mitchell, J. E.; Sefat, A. S. *Supercond. Sci. Technol.* **2012**, *25*, 084016-1–084016-10.

85. Spitzer, D. P.; Castellion, G. A.; Haacke, G. *J. Appl. Phys.* **1966**, *37*, 3795–3801.

86. Wang, S.; Yang, J.; Wu, L.; Wei, P.; Yang, J.; Zhang, W.; Grin, Y. *Chem. Mater.* **2015**, *27*, 1071–1081.

87. Castillo-Ojeda, R.; Díaz-Reyes, J.; Galván-Arellano, M.; Peña-Sierra, R. *Adv. Mater. Res.* **2014**, *976*, 25–29.

88. Rau, J. W.; Kannewurf, C. R. *Phys. Rev. B* **1971**, *3*, 2581−2587.

89. Donohue, P. C.; Young, H. S. *J. Solid State Chem*. **1970**, *1*, 143–149.

90. Lee, K.; Kamali, S.; Ericsson, T.; Bellard, M.; Kovnir. K. *Chem. Mater*. **2016**, *28*, 2776−2785.

91. Wang, X. C.; Liu, Q. Q.; Lv, Y. X.; Gao, W. B.; Yang, L. X.; Yu, R. C.; Li, F. Y.; Jin, C. Q. *Solid State Commun.* **2008**, *148*, 538–540.

92. Rotter, M.; Tegel, M.; Johrendt, D. *Phys. Rev. Lett*. **2008**, *101*, 107006-1–107006-4.

93. Mittal, R.; Su, Y.; Rols, S.; Tegel, M.; Chaplot, S. L.; Schober, H.; Chatterji, T.; Johrendt, D.; Brueckel, Th. *Phys. Rev. B*. **2008**, *78*, 224518-1–224518-5.

94. Cortes-Gil, R.; Clarke, S. J. *Chem. Mater*. **2011**, *23*, 1009–1016.

95. Qi, Y.; Gao, Z.; Wang, L.; Wang, D.; Zhang, X.; Ma, Y. *New J. Phys.* **2008**, *10*, 123003-1–123003-6.

96. Jeitschko, W.; Glaum, R.; Boonk; L. *J. Solid State Chem*. **1987**, *69*, 93–100.

97. Guo, Q.; Pan, B. J.; Yu, J.; Ruan, B. B.; Chen, D. Y.; Wang, X. C.; Mu, Q. G.; Chen, G. F.; Ren, Z. A. *Sci. Bull.* **2016**, *61*, 921–924.

98. Lam, R.; Mar, A. *Inorg. Chem.* **1996**, 35*,* 6959–6963.

99. Deakin, L.; Lam, R.; Marsiglio, F.; Mar, A. *J. Alloys Compd.* **2002**, *388,* 69–72.

100. Fisher, I. R.; Wiener, T. A.; Bud'ko, S. L.; Canfield, P. C.; Chan, J. Y.; Kauzlarich, S. M. *Phys. Rev. B* **1999**, *59*, 13829–13834.

101. Klufers, P.; Mewis, A. *Z. Naturforsch*., *B* **1977**, *32*, 753–756.

102. Madsen, G. K. H. *J. Am. Chem. Soc.* **2006**, *128*, 12148–12146.

103. Lii, K.-H.; Haushalter, R. C. *J. Solid State Chem*. **1987**, *67*, 374–378.

104. Sharp, J. W.; Nolas, G. S.; Volckmann, E. H. *Mater*. *Res*. *Soc*. *Symp*. *Proc*. **1997**, *478*, 91–102.

105. Zhang, L.; Du, M.-H.; Singh, D. J. *Phys. Rev. B* **2010**, *81*, 075117-1–075117-8.

106. Brown, S. R.; Kauzlarich, S. M.; Gascoin, F.; Snyder, G. J. *Chem. Mater.* **2006**, *18*, 1873–1877.

107. Holm, A. P.; Kauzlarich, S. M.; Morton, S. A.; Waddill, G. D.; Pickett, W. E.; Tobin, J. G. *J. Am. Chem. Soc.* **2002**, *124*, 9894–9898.

108. Deng, Z.; Jin, C. Q.; Liu, Q. Q.; Wang, X. C.; Zhu, J. L.; Feng, S. M.; Chen, L. C.; Yu, R. C.; Arguello, C.; Goko, T.; Ning, F.; Zhang, J.; Wang, Y.; Aczel, A. A.; Munsie, T.; Williams, T. J.; Luke, G. M.; Kakeshita, T.; Uchida, S.; Higemoto, W.; Ito, T. U.; Gu, B.; Maekawa, S.; Morris, G. D.; Uemura, Y. J. *Nat. Commun.* **2011**, *2*, 1425-1–1425-5.

109. Yan, B.; Müchler, L.; Felser, C. *Phys. Rev. Lett.* **2012**, *109*, 116406-1–116406-5.

110. Guechi, A.; Merabet, A.; Chegaar, M.; Bouhemadou, A.; Guechi, N. *J. Alloys Compd*. **2015**, *623*, 219–228.

111. Pöttgen, R.; Johrendt, D. *Intermetallics: Synthesis, Structure, Function*, de Gruyter: Berlin, 2014.

112. Eckert, M. *Ann. Phys.* **2012**, *524*, A83–A85.

113. Bragg, W. H.; Bragg W. L. *Proc. R. Soc. Lond. A* **1913**, *88*, 428–438.

114. Sheldrick, G. M. *SHELXTL*, version 6.12; Bruker AXS Inc.: Madison, WI, 2001.

115. Brese, N. E; O'Keeffe, M. *Acta*. *Crystallogr., Sect. B* **1991**, *47*, 192–197.

116. Dronskowski, R. *Computational Chemistry of Solid State Materials*, Wiley-VCH: Weinheim, 2005.

117. Hoffman, R. *Angew*. *Chem*., *Int*. *Ed*. *Engl*. **1987**, *26*, 846–878.

118. Eisenmann, B.; Cordier, G. In *Chemistry, Structure, and Bonding of Zintl Phases and Ions*; Kauzlarich, S. M., Ed.; VCH: New York, 1996; pp 61–137.

119. Stoyko, S. S.; Mar, A. *J. Solid State Chem.* **2011**, *184*, 2360–2367.

120. Stoyko, S. S.; Mar, A. *Inorg. Chem.* **2011**, *50*, 11152–11161.

121. Nientiedt, A. T.; Lincke, H.; Rodewald, U. Ch.; Pöttgen, R.; Jeitschko, W. *Z. Naturforsch., B: J. Chem. Sci.* **2011**, *66*, 221–226.

122. Hellman, A.; Löhken, A.; Wurth, A.; Mewis, A. *Z. Naturforsch., B: J. Chem. Sci.* **2007**, *62*, 155–161.

123. Saparov, B.; Bobev, S. *Inorg. Chem.* **2010**, *49*, 5173–5179.

124. Wilson, D. K.; Saparov, B.; Bobev, S. *Z. Anorg. Allg. Chem.* **2011**, *637*, 2018–2025.

125. Nowotny, H.; Bachmeyer, K. *Monatsh. Chem.* **1949**, *8*, 734.

126. Kuriyama, K.; Nakamura, F. *Phys. Rev. B* **1987**, *36*, 4439–4441.

127. Kuriyama, K.; Kato, T.; Kawada, K. *Phys. Rev. B* **1994**, *49*, 11452–11455.

128. Kalarasse, F.; Bennecer, B. *J. Phys. Chem. Solids* **2006**, *67*, 846–850.

129. Nowotny, H.; Glatzl, B. *Monatsh. Chem.* **1951**, *82*, 720–722.

130. Kahlert, H.; Schuster, H.-U. *Z. Naturforsch., B: Anorg. Chem., Org. Chem.* **1976**, *31*, 1538–1539.

131. Jaganesh, G.; Merita Anto Britto, T.; Eithiraj, R. D.; Kalpana, G. *J. Phys.: Condens. Matter* **2008**, *20*, 085220-1–085220-8.

132. Vogel, R.; Schuster, H.-U. *Z. Naturforsch., B: Anorg. Chem., Org. Chem.* **1980**, *35*, 114–116.

133. Prots, Yu.; Aydemir, U.; Öztürk, S. S.; Somer, M. *Z. Kristallogr. – New Cryst. Struct.* **2007**, *222*, 163–164.

134. Deng, Z.; Jin, C. Q.; Liu, Q. Q.; Wang, X. C.; Zhu, J. L.; Feng, S. M.; Chen, L. C.; Yu, R. C.; Arguello, C.; Goko, T.; Ning, F.; Zhang, J.; Wang, Y.; Aczel, A. A.; Munsie, T.; Williams, T. J.; Luke, G. M.; Kakeshita, T.; Uchida, S.; Higemoto, W.; Ito, T. U.; Gu, B.; Maekawa, S.; Morris, G. D.; Uemura, Y. J. *Nat. Commun.* **2011**, *2*, No. 422.

135. Sheldrick, G. M. *SHELXTL*, version 6.12; Bruker AXS Inc.: Madison, WI, 2001.

136. Gelato, L. M.; Parthé, E. *J. Appl. Crystallogr.* **1987**, *20*, 139–143.

137. Tank, R.; Jepsen, O.; Burkhardt, A.; Andersen, O. K. *TB-LMTO-ASA Program*, version 4.7; Max Planck Institut für Festkörperforschung: Stuttgart, Germany, 1998.

138. Zheng, W.-Z.; Wang, P.; Wu, L.-M.; Liu, Y.; Chen, L. *Inorg. Chem.* **2010**, *49*, 5890–5896.

139. Liu, Y.; Wu, L.-M.; Li, L.-H.; Du, S.-W.; Corbett, J. D.; Chen, L. *Angew. Chem. Int. Ed.* **2009**, *48*, 5305–5308.

140. Nyman, H.; Andersson, S. *Acta Crystallogr., Sect. A* **1979**, *35*, 580–583.

141. Nyman, H.; Andersson, S. *Acta Crystallogr., Sect. A* **1979**, *35*, 934–937.

142. Nyman, H. *Acta Crystallogr., Sect. B* **1983**, *39*, 529–532.

143. Zheng, C.; Hoffmann, R.; Nelson, D. R. *J. Am. Chem. Soc.* **1990**, *112*, 3784–3791.

144. Häussermann, U.; Svensson, C.; Lidin, S. *J. Am. Chem. Soc.* **1998**, *120*, 3867–3880.

145. Chen, X.; Huang, X.; Li, J. *Inorg. Chem.* **2001**, *40*, 1341–1346.

146. Juza, R.; Bohmann, T. *Z. Anorg. Allg. Chem.* **1961**, *308*, 159–178.

147. Achenbach, G.; Schuster, H.-U. *Z. Anorg. Allg. Chem.* **1981**, *475*, 9–17.

148. Bronger, W.; Müller, P.; Höppner, R.; Schuster, H.-U. *Z. Anorg. Allg. Chem.* **1986**, *539*, 175–182.

149. Schucht, F.; Dascoulidou, A.; Müller, R.; Jung, W.; Schuster, H.-U.; Bronger, W.; Müller, P. *Z. Anorg. Allg. Chem.* **1999**, *625*, 31–36.

150. Liu, Y.; Wu, L.-M.; Li, L.-H.; Du, S.-W.; Corbett, J. D.; Chen, L. *Angew. Chem. Int. Ed.* **2009**, *48*, 5305–5308.

151. Madsen, G. K. H. *J. Am. Chem. Soc.* **2006**, *128*, 12148–12146.

152. Toberer, E. S.; May, A. F.; Scanlon, C. J.; Snyder, G. J. *J. Appl. Phys.* **2009**, *105*, 063701-1–063701-5.

153. Li, L.-H.; Chen, L.; Li, J.-Q.; Wu, L.-M. *Chem. Mater.* **2010**, *22*, 4007–4018.

154. Yan, B.; Müchler, L.; Felser, C. *Phys. Rev. Lett.* **2012**, *109*, 116406-1–116406-5.

155. Zheng, W.-Z.; Wang, P.; Wu, L.-M.; Liu, Y.; Chen, L. *Inorg. Chem.* **2010**, *49*, 5890–5896.

156. He, H.; Stoyko, S. S.; Mar, A.; Bobev, S. *Acta Crystallogr. Sect. C* **2013**, *69*, 455–459.

157. He, H.; Tyson, C.; Bobev, S. *Crystals* **2011**, *1*, 87–98.

158. Khatun, M.; Stoyko, S. S.; Mar, A. *Inorg. Chem.* **2013**, *52*, 3148–3158.

159. Saparov, B.; Saito, M.; Bobev, S. *J. Solid State Chem.* **2011**, *184*, 432–440.

160. Saparov, B.; Broda, M.; Ramanujachary, K. V.; Bobev, S. *Polyhedron* **2010**, *29*, 456–462.

161. Gelato, L. M.; Parthé, E. *J. Appl. Crystallogr.* **1987**, *20*, 139–143.

162. Lin, X.; Stoyko, S. S.; Mar, A. *J. Solid State Chem.* **2013**, *199*, 189–195.

163. Pauling, L. *The Nature of the Chemical Bond*, 3rd ed.; Cornell University Press: Ithaca, NY, 1960.

164. Emmerling, F.; Röhr, C. *Z. Naturforsch. B: Chem. Sci.* **2002**, *57*, 963–975.

165. Papoian, G. A.; Hoffmann, R. *Angew. Chem. Int. Ed.* **2000**, *39*, 2408–2448.

166. Ponou, S.; Fässler, T. F.; Tobías, G.; Canadell, E.; Cho, A.; Sevov, S. C. *Chem. Eur. J.* **2004**, *10*, 3615–3621.

167. Alemany, P.; Alvarez, S.; Hoffmann, R. *Inorg. Chem.* **1990**, *29*, 3070–3073.

168. Alemany, P.; Llunell, M.; Canadell, E. *Inorg. Chem.* **2006**, *45*, 7235–7241.

169. Cordier, G.; Schäfer, H. *Z. Naturforsch. B: Anorg. Chem., Org. Chem.* **1977**, *32*, 383–386.

170. Brechtel, E.; Cordier, G.; Schäfer, H. *J. Less-Common Met.* **1981**, *79*, 131–138.

171. Brechtel, E.; Cordier, G.; Schäfer, H. *Z. Naturforsch. B: Anorg. Chem., Org. Chem.* **1979**, *34*, 921–925.

172. Morozkin, A. V.; Isnard, O.; Henry, P.; Granovsky, S.; Nirmala, R.; Manfrinetti, P. *J. Alloys Compd.* **2006**, *420*, 34–36.

173. Bobev, S.; Merz, J.; Lima, A.; Fritsch, V.; Thompson, J. D.; Sarrao, J. L.; Gillessen, M.; Dronskowski, R. *Inorg. Chem.* **2006**, *45*, 4047–4054.

174. Xia, S.-Q.; Myers, C.; Bobev, S. *Eur. J. Inorg. Chem.* **2008**, 4262–4269.

175. An, J.; Sefat, A. S.; Singh, D. J.; Du, M.-H. *Phys. Rev. B* **2009**, *79*, 075120-1–075120-6.

176. Kim, H.; Condron, C. L.; Holm, A. P.; Kauzlarich, S. M. *J. Am. Chem. Soc.* **2000**, *122*, 10720–10721.

177. Holm, A. P.; Olmstead, M. M.; Kauzlarich, S. M. *Inorg. Chem.* **2003**, *42*, 1973–1981.

178. Xia, S.-Q.; Bobev, S. *Inorg. Chem.* **2007**, *46*, 874–883.

179. Xia, S.-Q.; Bobev, S. *Chem. Mater.* **2010**, *22*, 840–850.

180. Jansen, M. *Angew. Chem. Int. Ed. Engl.* **1987**, *26*, 1098–1110.

181. Misra, S.; Miller, G. J. *J. Am. Chem. Soc.* **2008**, *130*, 13900–13911.

182. Toberer, E. S.; May, A. F.; Snyder, G. J. *Chem. Mater.***2010**, *22*, 624–634.

183. Yan, J.; Gorai, P.; Ortiz, B.; Miller, S.; Barnett, S. A.; Mason, T.; Stevanović, V.; Toberer, E. S. *Energy Environ. Sci.* **2015**, *8*, 983–994.

184. Zhang, L.; Du, M.-H.; Singh, D. J. *Phys. Rev. B* **2010**, *81*, 075117-1–075117-8.

185. Eisenmann, B.; Klein, J. *Z. Naturforsch., B* **1988**, *43*, 69–71.

186. Asbrand, M.; Eisenmann, B. *Z. Naturforsch., B* **1993**, *48*, 452–456.

187. Eisenmann, B.; J. Klein, J. *Z. Naturforsch., B* **1988**, *43*, 1156–1160.

188. Eisenmann, B.; Somer, M. *Z. Naturforsch., B* **1985**, *40*, 886–890.

189. Eisenmann, B.; Somer, M. *Z. Naturforsch., B* **1984**, *39*, 736–738.

190. Eisenmann, B.; Klein, J.; Somer, M. *Angew. Chem. Int. Ed. Engl.* **1990**, *29*, 87–88.

191. Lii, K.-H.; Haushalter, R. C. *J. Solid State Chem.* **1987**, *67*, 374–378.

192. Schmidt, P. C.; Stahl, D.; Eisenmann, B.; Kniep, R.; Eyert, V.; Kübler, J. *J. Solid State Chem.* **1992**, *97*, 93–104.

193. Asbrand, M.; Eisenmann, B. *Z. Kristallogr.* **1992**, *198*, 309–310.

194. Hurng, W.-M.; Corbett, J. D., Wang, S.-L.; Jacobson, R. A. *Inorg. Chem.* **1987**, *26*, 2392–2395.

195. Feng, K.; Yin, W.; He, R.; Lin, Z.; Jin, S.; Yao, J.; Fu, P.; Wu, Y. *Dalton Trans.* **2012**, *41* 484–489.

196. Khatun, M.; Mar, A. *Z. Naturforsch., B* **2016**, *71*, 375–380.

197. Asbrand, M.; Eisenmann, B.; Klein, J. *Z. Anorg. Allg. Chem.* **1995,** *621*, 576–582.

198. Gelato, L. M.; Parthé, E. *J. Appl. Crystallogr.* **1987**, *20*, 139–143.

199. Juza, R.; Schulz, W. *Z. Anorg. Allg. Chem.* **1954**, *275*, 65–78.

200. Eisenmann, B.; Klein, J.; Somer, M. *Z. Kristallogr.* **1991**, *197*, 265–266.

201. Eisenmann, B.; Klein, J. *J. Less-Common Met.* **1991**, *175*, 109–117.

202. Burtzlaff, S.; Hołyńska, M.; Dehnen, S. *Z. Anorg. Allg. Chem.* **2010**, *636*, 1691–1693.

203. Eisenmann, B.; Klein, J. *Z. Kristallogr.* **1991**, *196*, 213–229.

204. Eisenmann, B.; Rössler, U. Kristallogr Z. – *New Cryst. Struct.* **2000**, *215*, 347–348.

205. Eisenmann, B.; Schäfer, H. *Z. Naturforsch., B* **1981**, *36*, 415–419.
206. Bryden, J. H. *Acta Crystallogr.* **1962**, *15*, 167–171.
207. Kim, S.-J. Hu, S.; Uher, C.; Kanatzidis, M. G. *Chem. Mater.* **1999**, *11*, 3154–3159.
208. Lam, R.; Mar, A. *Solid State Sci.* **2001**, *3*, 503–512.
209. Eisenmann, B.; Schäfer, H. *Z. Naturforsch.* **1981**, *36b*, 415–419.
210. Poth, L.; Weil, K. G. *Ber. Bunsenges. Phys. Chem.* **1992**, *96*, 1621–1626.
211. Stöhr, H.; Klemm, W. *Z. Anorg. Allg. Chem.* **1940**, *244*, 205–223.
212. Schubert, K.; Dörre, E.; Günzel, E. *Naturwissenschaften* **1954**, *41*, 448.
213. Hulliger, F.; Mooser, E. *J. Phys. Chem. Solids* **1963**, *24*, 283–295.
214. Bryden, J. H. *Acta Crystallogr.* **1962**, *15*, 167–171.
215. Wadsten, T. *Acta Chem. Scand.* **1967**, *21*, 593–594.
216. Rau, J. W.; Kannewurf, C. R. *Phys. Rev. B* **1971**, *3*, 2581–2587.
217. Mentzen, B. F.; Hillel, R.; Michaelides, A.; Tranquard, A.; Bouix, J. *C. R. Acad. Sci., Ser. II* **1981**, *293*, 965–967.
218. Mead, D. G. *Infrared Phys.* **1982**, *22*, 209–213.
219. Olesinski, R. W.; Abbaschian, G. J. *Bull. Alloy Phase Diagrams* **1985**, *6*, 250–254.
220. Gelato, L. M.; Parthé, E. *J. Appl. Crystallogr.* **1987**, *20*, 139–143.
221. Eisenmann, B.; Schäfer, H. *Z. Anorg. Allg. Chem.* **1982**, *484*, 142–152.
222. Khatun, M.; Stoyko, S. S.; Mar, A. *Inorg. Chem.* **2014**, *53*, 7756–7762.
223. Shreeve-Keyer, J. L.; Haushalter, R. C.; Lee, Y.-S.; Li, S.; O'Connor, C. J.; Seo, D.-K.; Whangbo, M.-H. *J. Solid State Chem.* **1997**, *130*, 234–249.
224. Paashaus, S.; Kniep, R. *Angew. Chem. Int. Ed. Engl.* **1986**, *25*, 752–753.
225. Yuan, H.; Wang, H.; Cui, Y. *Acc. Chem. Res.* **2015**, *48*, 81–90.
226. O'Keeffe, M.; Brese, N. E. *J. Am. Chem. Soc.* **1991**, *113*, 3226–3229.
227. Wadsten, T. *Acta Chem. Scand.* **1965**, *19*, 1232–1238.
228. Wadsten, T. *Acta Chem. Scand.* **1969**, *23*, 331–333.
229. Lee, K.; Synnestvedt, S.; Bellard, M.; Kovnir, K. *J. Solid State Chem.* **2015**, *224*, 62–70.
230. Blachnik, R.; Irle, E. *J. Less-Common Met.* **1985**, *113*, L1–L3.
231. Alemany, P.; Alvarez, S.; Hoffmann, R. *Inorg. Chem.* **1990**, *29*, 3070–3073.
232. Alemany, P.; Llunell, M.; Canadell, E. *Inorg. Chem.* **2006**, *45*, 7235–7241.
233. Hahn, H.; Frank, G. *Z. Anorg. Allg. Chem.* **1955**, *278*, 340–348.
234. Kuhn, A.; Chevalier, R.; Rimsky, A. *Acta Crystallogr.* **1975**, *B31*, 2841–2842.
235. Kuhn, A.; Chevy, A. *Acta Crystallogr.* **1976**, *B32*, 983–984.

236. d'Amour, H.; Holzapfel, W. B.; Polian, A.; Chevy, A. *Solid State Commun.* **1982**, *44*, 852–855.

237. Benazeth, S.; Dung, N.-H.; Guittard, M.; Laruelle, P. *Acta Crystallogr.* **1988**, *C44*, 234–236.

238. Villars, P.; Cenzual, K. *Pearson's Crystal Data – Crystal Structure Database for Inorganic Compounds*, release 2010/11; ASM International: Materials Park, OH, 2010.

239. Klüfers, P.; Mewis, A. *Z. Kristallogr.* **1984**, *169*, 135–147.

240. Zheng, C.; Hoffmann, R.; Nesper, R.; von Schnering, H.-G. *J. Am. Chem. Soc.* **1986**, *108*, 1876–1884.

241. Zheng, C.; Hoffmann, R. *J. Solid State Chem.* **1988**, *72*, 58–71.

242. Burdett, J. K.; Miller, G. J. *Chem. Mater.* **1990**, *2*, 12–26.

243. Kranenberg, C.; Johrendt, D.; Mewis, A. *Z. Anorg. Allg. Chem.* **1999**, *625*, 1787–1793.

244. Kranenberg, C.; Johrendt, D.; Mewis, A. *Solid State Sci.* **2002**, *4*, 261–265.

245. Wartenberg, F.; Kranenberg, C.; Pocha, R.; Johrendt, D.; Mewis, A.; Hoffmann, R.-D.; Mosel, B. D.; Pöttgen, R. *Z. Naturforsch. B: J. Chem. Sci.* **2002**, *57*, 1270–1276.

246. Alemany, P.; Llunell, M.; Canadell, E. *J. Comput. Chem.* **2008**, *29*, 2144–2153.

247. Gascoin, F.; Ottensmann, S.; Stark, D.; Haïle, S. M.; Snyder, G. J. *Adv. Funct. Mater.* **2005**, *15*, 1860–1864.

248. Wang, X.-J.; Tang, M.-B.; Chen, H.-H.; Yang, X.-X.; Zhao, J.-T.; Burkhardt, U.; Grin, Yu. *Appl. Phys. Lett.* **2009**, *94*, 092106-1–092106-3.

249. Flage-Larsen, E.; Diplas, S.; Prytz, Ø.; Toberer, E. S.; May, A. F. *Phys. Rev. B* **2010**, *81*, 205204-1–205204-7.

250. Guo, K.; Cao, Q.-G.; Feng, X.-J.; Tang, M.-B.; Chen, H.-H.; Guo, X.; Chen, L.; Grin, Yu.; Zhao, J.-T. *Eur. J. Inorg. Chem.* **2011**, 4043–4048.

251. May, A. F.; McGuire, M. A.; Singh, D. J.; Ma, J.; Delaire, O.; Huq, A.; Cai, W.; Wang, H. *Phys. Rev. B* **2012**, *85*, 035202-1–035202-10.

252. Blanchard, P. E. R.; Stoyko, S. S.; Cavell, R. G.; Mar, A. *J. Solid State Chem.* **2011**, *184*, 97–103.

253. Gladyshevskii, E. I.; Kripyakevich, P. I.; Bodak, O. I. *Ukr. Fiz. Zh.* **1967**, *12*, 447–452.

254. Ban, Z.; Sikirica, M. *Acta Crystallogr.* **1965**, *18*, 594–599.

255. Leciejewicz, J.; Siek, S.; Szytuła, A. *J. Less-Common Met.* **1988**, *144*, L9–L13.

256. Gaultois, M. W.; Grosvenor, A. P.; Blanchard, P. E. R.; Mar, A. *J. Alloys Compd.* **2010**, *492*, 19–25.

257. Blanchard, P. E. R.; Cavell, R. G.; Mar, A. *J. Alloys Compd.* **2010**, *505*, 17–22.

258. Gelato, L. M.; Parthé, E. *J. Appl. Crystallogr.* **1987**, *20*, 139–143.

259. Stoyko, S. S.; Mar, A. *Inorg. Chem.* **2011**, *50*, 11152–11161.

260. Eisenmann, B.; Klein, J.; Somer, M. *Z. Kristallogr.* **1991**, *197*, 267–268.

261. Slater, J. C. *J. Chem. Phys.* **1964**, *41*, 3199–3204.

262. Hoffmann, R.; Zheng, C. *J. Phys. Chem.* **1985**, *89*, 4175–4181.

263. Hoffmann, R. *Solids and Surfaces: A Chemist's View of Bonding in Extended Structures*; VCH Publishers: New York, 1998.

264. Huheey, J. E.; Keiter, E. A.; Keiter, R. L. *Inorganic Chemistry: Principles of Structure and Reactivity*, 4th ed.; Harper Collins: New York, 1993.

265. Johrendt, D.; Felser, C.; Jepsen, O.; Andersen, O. K.; Mewis, A.; Rouxel, J. *J. Solid State Chem.* **1997**, *130*, 254–265.

266. Gustenau, E.; Herzing, P.; Neckel, A. *J. Solid State Chem.* **1997**, *129*, 147–156.

267. Kang, D.-B. *Bull. Korean Chem. Soc.* **2003**, *24*, 1215–1218.

268. An, J.; Sefat, A. S.; Singh, D. J.; Du, M.-H. *Phys. Rev. B* **2009**, *79*, 075120-1–075120-6.

269. Singh, D. J. *Phys. Rev. B* **2009**, *79*, 153102-1–153102-4.

270. Chefki, M.; Abd-Elmeguid, M. M.; Micklitz, H.; Huhnt, C.; Schlabitz, W.; Reehuis, M.; Jeitschko, W. *Phys. Rev. Lett.* **1998**, *80*, 802–805.

271. Kovnir, K.; Thompson, C. M.; Zhou, H. D.; Wiebe, C. R.; Shatruk, M. *Chem. Mater.* **2010**, *22*, 1704–1713.

272. Brock, S. L.; Greedan, J. E.; Kauzlarich, S. M. *J. Solid State Chem.* **1994**, *109*, 416–418.

273. Shannon, R. D. *Acta Crystallogr., Sect. A* **1976**, *32*, 751–767.

274. Imai, M.; Abe, H.; Yamada, K. *Inorg. Chem.* **2004**, *43*, 5186–5188.

275. Schunemann, P. G.; Schepler, K. L.; Budni, P. A. *MRS Bull.* **1998**, *23*, *7*, 45–49.

276. Novotortsev, V. M.; Kalinnikov, V. T.; Koroleva, L. I.; Demin, R. V.; Marenkin, S. F.; Aminov, T. G.; Shabunina, G. G.; Boichuk, S. V.; Ivanov, V. A. *Zh. Neorg. Khim.* **2005**, *50*, 552–557.

277. Parker, D.; Singh, D. J. *Phys. Rev. B* **2012**, *85*, 125209-1–125209-7.

278. Wu, Y.; Bensch, W. *CrystEngComm* **2010**, *12*, 1003–1015.

279. Eller, P. G.; Bradley, D. C.; Hursthouse, M. B.; Meek, D. W. *Coord. Chem. Rev.* **1977**, *24*, 1–95.

280. Spek, A. L. *Acta Crystallogr., Sect. D: Biol. Crystallogr.* **2009**, *65*, 148–155.

281. Gelato, L. M.; Parthé, E. *J. Appl. Crystallogr.* **1987**, *20*, 139–143.

282. Nuss, J.; Kalpen, H.; Hönle, W.; Hartweg, M.; von Schnering, H. G. *Z. Anorg. Allg. Chem.* **1997**, *623*, 205–211.

283. Shreeve-Keyer, J. L.; Haushalter, R. C.; Lee, Y.-S.; Li, S.; O'Connor, C. J.; Seo, D.-K.; Whangbo, M.-H. *J. Solid State Chem.* **1997**, *130*, 234–249.

284. Kahlert, H.; Schuster, H. U. *Z. Naturforsch. B: Anorg. Chem., Org. Chem.* **1976**, *31*, 1538–1539.

285. Eisenmann, B.; Klein, J.; Somer, M. *Z. Kristallogr.* **1991**, *197*, 271–272.

286. He, H.; Stoyko, S. S.; Mar, A.; Bobev, S. *Acta Crystallogr., Sect. C: Cryst. Struct. Commun.* **2013**, *69*, 455–459.

287. Novotortsev, V. M.; Palkina, K. K.; Mikhailov, S. G.; Molchanov, A. V.; Ochertyanova, L. I.; Marenkin, S. F. *Inorg. Mater.* **2005**, *41*, 439–442.

288. Mikkelsen, Jr., J. C.; Hong, H. Y.-P. *Mater. Res. Bull.* **1974**, *9*, 1209–1218.

289. Mentzen, B. F.; Hillel, R.; Michaelides, A.; Tranquard, A.; Bouix, J. *C. R. Seances Acad. Sci., Ser. 2* **1981**, *293*, 965–967.

290. Bryden, J. H. *Acta Crystallogr.* **1962**, *15*, 167–171.

291. Ayouz, K.; Kars, M.; Rebbah, A.; Rebbah, H. *Acta Crystallogr., Sect. E* **2009**, *65*, i15.

292. Eisenmann, B.; Schäfer, H. *Z. Naturforsch. B: Anorg. Chem., Org. Chem.* **1981**, *36*, 415–419.

293. Eisenmann, B.; Jordan, H.; Schäfer, H. *Z. Naturforsch. B: Anorg. Chem., Org. Chem.* **1982**, *37*, 1564–1568.

294. Eisenmann, B.; Jordan, H.; Schäfer, H. *Z. Naturforsch. B: Anorg. Chem., Org. Chem.* **1983**, *38*, 404–406.

295. Cordier, G.; Ochmann, H.; Schäfer, H. *Mater. Res. Bull.* **1986**, *21*, 331–336.

296. Hurng, W.-M.; Corbett, J. D.; Wang, S.-L.; Jacobson, R. A. *Inorg. Chem.* **1987**, *26*, 2392–2395.

297. Kim, S.-J.; Kanatzidis, M. G. *Inorg. Chem.* **2001**, *40*, 3781–3785.

298. Park, S.-M.; Kim, S.-J.; Kanatzidis, M. G. *J. Solid State Chem.* **2003**, *175*, 310–315.

299. Dong, Y.; Ranjan, C.; DiSalvo, F. J. *J. Alloys Compd.* **2007**, *430*, 54–59.

300. Yang, G.; Yang, J.; Yan, Y.; Wang, Y. *Phys. Chem. Chem. Phys.* **2014**, *16*, 5661–5666.

Appendix 1

Supporting Information for Chapter 2

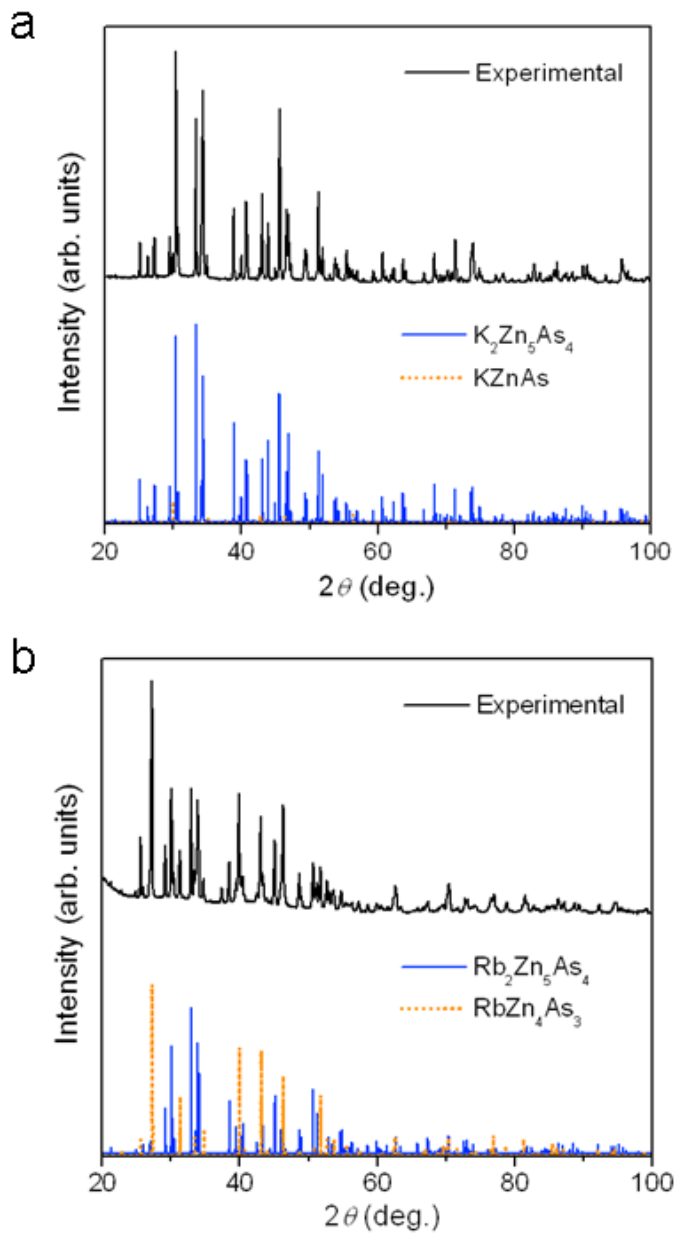

Figure A 1-1. Powder XRD patterns for $A_2Zn_5As_4$ (A = K, Rb) reactions.

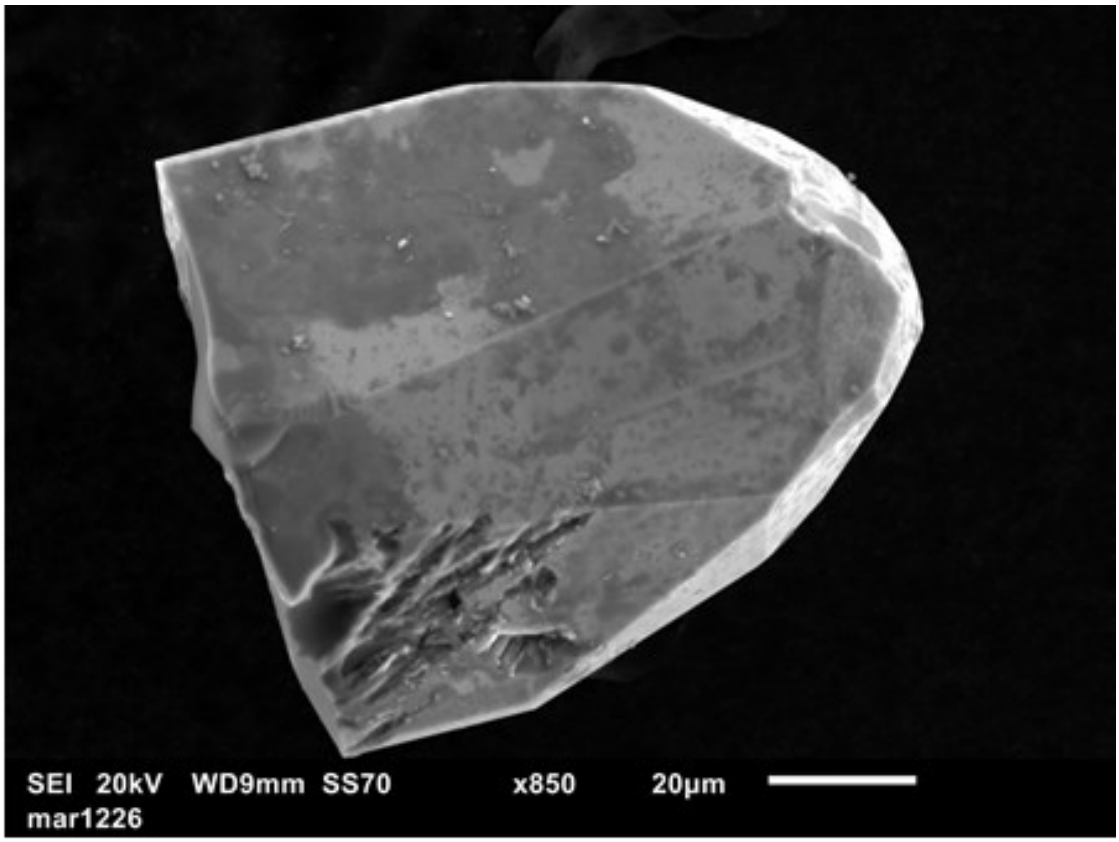

Figure A 1-2. SEM image of $Rb_2Zn_5As_4$.

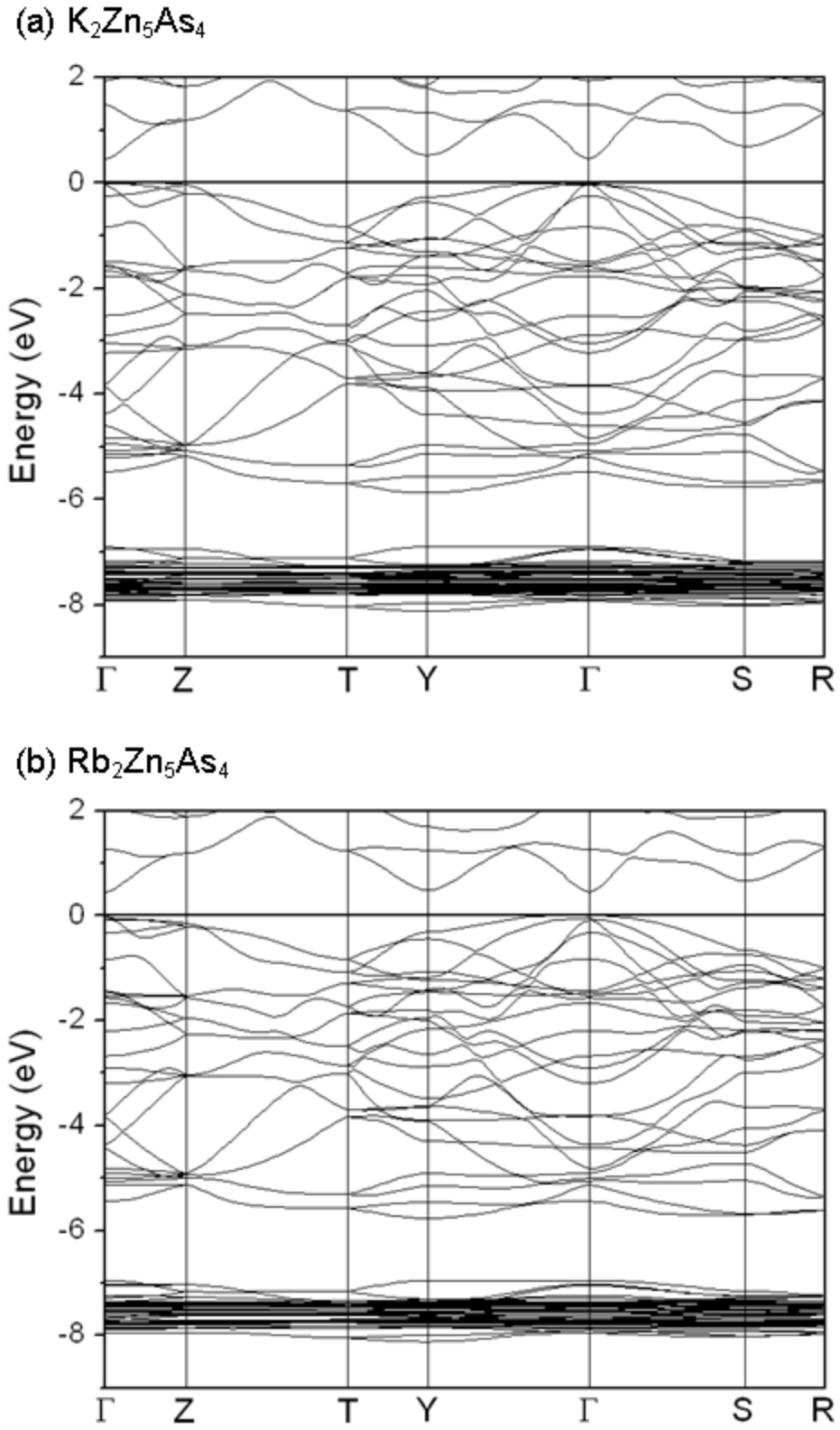

Figure A 1-3. Band dispersion diagrams for $A_2Zn_5As_4$ (A = K, Rb).

Appendix 2

Supporting Information for Chapter 3

Table A 2-1. EDX analyses (atomic %) of $Rb_4Zn_7As_7$, $Rb_4Mn_{3.5}Zn_{3.5}Sb_7$, $Rb_7Mn_{12}Sb_{12}$, and $Rb_7Mn_4Cd_8Sb_{12}$ crystals

	Observed	Calculated
$Rb_4Zn_7As_7$ (*n* = 5)		
Rb	26(1)	22.2
Zn	37(1)	38.9
As	36(1)	38.9
$Rb_4Mn_{3.5}Zn_{3.5}Sb_7$ (*n* = 7)		
Rb	21(1)	22.2
Mn	19(1)	19.4
Zn	19(1)	19.4
Sb	41(1)	38.9
$Rb_7Mn_{12}Sb_{12}$ (*n* = 3)		
Rb	22(2)	22.6
Mn	38(2)	38.7
Sb	40(2)	38.7
$Rb_7Mn_4Cd_8Sb_{12}$ (*n* = 7)		
Rb	24(1)	22.6
Mn	12(1)	12.9
Cd	27(1)	25.8
Sb	38(1)	38.7

[a] Number of point analyses (*n*) indicated for each compound.

Table A 2-2. Crystallographic data for $Rb_4Zn_7As_7$, $Rb_4Mn_{3.5}Zn_{3.5}Sb_7$, $Rb_7Mn_{12}Sb_{12}$, and $Rb_7Mn_4Cd_8Sb_{12}$

formula	$Rb_4Zn_7As_7$	$Rb_4Mn_{3.4(1)}Zn_{3.6(1)}Sb_7$	$Rb_7Mn_{12}Sb_{12}$	$Rb_7Mn_{4.2(1)}Cd_{7.8(1)}Sb_{12}$
formula mass (amu)	1323.91	1615.22	2718.57	3178.25
space group	*Cmcm* (No. 63)	*Cmcm* (No. 63)	*C*2/*m* (No. 12)	*C*2/*m* (No. 12)
a (Å)	4.1883(4)	4.3911(8)	26.544(12)	27.009(4)
b (Å)	24.844(2)	26.546(5)	4.448(2)	4.5752(7)
c (Å)	17.6056(17)	18.743(4)	16.676(8)	16.727(3)
β (°)	90	90	103.183(8)	103.221(2)
V (Å^3)	1831.9(3)	2184.7(7)	1917(2)	2012.2(5)
Z	4	4	2	2
ρ_{calcd} (g cm^{-3})	4.800	4.911	4.710	5.246
T (K)	173(2)	173(2)	173(2)	173(2)
crystal dimensions (mm)	0.17 × 0.04 × 0.02	0.20 × 0.02 × 0.02	0.16 × 0.03 × 0.02	0.19 × 0.03 × 0.02
radiation		graphite monochromated Mo $K\alpha$, λ = 0.71073 Å		
μ(Mo $K\alpha$) (mm^{-1})	32.09	23.04	20.91	21.63
transmission factors	0.118–0.559	0.177–0.722	0.265–0.754	0.264–0.734
2θ limits	3.28–66.42°	3.06–66.38°	2.50–66.08°	3.50–66.52°
data collected	$-6 \le h \le 6$, $-37 \le k \le 37$, $-26 \le l \le 26$	$-6 \le h \le 6$, $-40 \le k \le 39$, $-28 \le l \le 28$	$-39 \le h \le 39$, $-6 \le k \le 6$, $-25 \le l \le 25$	$-41 \le h \le 40$, $-6 \le k \le 6$, $-25 \le l \le 25$
no. of data collected	12886	15472	13834	14196

no. of unique data, including $F_o^2 < 0$	1988 (R_{int} = 0.133)	2358 (R_{int} = 0.092)	3978 (R_{int} = 0.203)	4119 (R_{int} = 0.062)
no. of unique data, with $F_o^2 > 2\sigma(F_o^2)$	1100	1606	1723	2933
no. of variables	60	63	96	101
$R(F)$ for $F_o^2 > 2\sigma(F_o^2)$ [a]	0.061	0.034	0.068	0.034
$R_w(F_o^2)$ [b]	0.161	0.068	0.130	0.065
goodness of fit	1.03	1.01	1.07	0.99
$(\Delta\rho)_{max}$, $(\Delta\rho)_{min}$ (e Å^{-3})	3.81, –6.08	2.40, –2.06	4.56, –2.82	1.80, –2.12

[a] $R(F) = \sum||F_o| - |F_c|| / \sum|F_o|$. [b] $R_w(F_o^2) = [\sum[w(F_o^2 - F_c^2)^2] / \sum wF_o^4]^{1/2}$; $w^{-1} = [\sigma^2(F_o^2) + (Ap)^2 + Bp]$, where $p = [\max(F_o^2,0) + 2F_c^2] / 3$.

Table A 2-3. Selected interatomic distances (Å) in $Rb_4Zn_7As_7$ and $Rb_4Mn_{3.5}Zn_{3.5}Sb_7$

	$Rb_4Zn_7As_7$	**$Rb_4Mn_{3.5}Zn_{3.5}Sb_7$**
Rb1–*Pn*1 (×2)	3.485(1)	3.633(1)
Rb1–*Pn*3 (×2)	3.512(2)	3.682(1)
Rb1–*Pn*2 (×2)	3.541(2)	3.748(1)
Rb2–*Pn*1 (×4)	3.405(1)	3.590(1)
Rb2–*Pn*4 (×2)	3.428(3)	3.591(1)
Rb3–*Pn*3 (×4)	3.528(1)	3.738(1)
Rb3–*Pn*2 (×4)	3.916(3)	4.010(1)
*M*1–*Pn*1	2.585(2)	2.722(1)
*M*1–*Pn*3 (×2)	2.549(1)	2.727(1)
*M*1–*Pn*4	2.772(4)	2.953(1)
*M*2–*Pn*1 (×2)	2.576(1)	2.766(1)
*M*2–*Pn*1	2.591(2)	2.758(1)
*M*2–*Pn*3	2.640(2)	2.806(1)
*M*3–*Pn*3	2.441(3)	2.660(1)
*M*3–*Pn*2	2.565(4)	2.730(1)
*M*3–*Pn*4 (×2)	2.729(2)	2.870(1)
*M*4–*Pn*4	2.574(4)	2.784(2)
*M*4–*Pn*2 (×4)	2.574(2)	2.804(1)
*M*1–*M*2 (×2)	2.944(2)	3.080(1)
*M*1–*M*3 (×2)	3.044(2)	3.281(1)
*M*2–*M*2 (×2)	2.940(2)	3.104(1)
*M*3–*M*3	2.950(5)	3.041(2)
*M*3–*M*4 (×2)	3.036(3)	3.184(1)
*Pn*2–*Pn*2	2.363(7)	2.864(1)

Table A 2-4. Selected interatomic distances (Å) in $Rb_7Mn_{12}Sb_{12}$, and $Rb_7Mn_4Cd_8Sb_{12}$

	$Rb_7Mn_{12}Sb_{12}$	**$Rb_7Mn_4Cd_8Sb_{12}$**
Rb1–Sb6 (×2)	3.611(2)	3.644(1)
Rb1–Sb4 (×2)	3.645(2)	3.668(1)
Rb1–Sb5 (×2)	3.680(2)	3.683(1)
Rb2–Sb6 (×2)	3.652(2)	3.650(1)
Rb2–Sb3 (×2)	3.661(2)	3.682(1)
Rb2–Sb1 (×2)	3.779(2)	3.751(1)
Rb3–Sb4 (×2)	3.653(3)	3.672(1)
Rb3–Sb2 (×2)	3.770(3)	3.752(1)
Rb3–Sb2 (×2)	3.799(3)	3.844(1)
Rb4–Sb3 (×4)	3.719(2)	3.720(1)
Rb4–Sb1 (×4)	4.051(2)	4.217(1)
*M*1–Sb3	2.692(4)	2.776(1)
*M*1–Sb1	2.777(4)	2.837(1)
*M*1–Sb5 (×2)	2.872(2)	3.035(1)
*M*2–Sb4	2.709(3)	2.800(1)
*M*2–Sb2	2.772(4)	2.836(1)
*M*2–Sb5 (×2)	2.858(2)	2.975(1)
*M*3–Sb6 (×2)	2.779(2)	2.884(1)
*M*3–Sb6	2.788(4)	2.877(1)
*M*3–Sb3	2.814(4)	2.964(1)
*M*4–Sb4 (×2)	2.759(2)	2.862(1)
*M*4–Sb4	2.784(4)	2.908(1)
*M*4–Sb5	2.880(3)	3.021(1)
*M*5–Sb5	2.808(4)	2.853(1)
*M*5–Sb1 (×2)	2.819(2)	2.872(1)
*M*5–Sb2 (×2)	2.832(2)	2.874(1)
*M*6–Sb3 (×2)	2.761(2)	2.865(1)
*M*6–Sb6	2.766(4)	2.870(1)
*M*6–Sb5	2.924(4)	3.089(1)
*M*1–*M*2	2.993(5)	3.333(1)

*M*1–*M*5 (×2)	3.224(3)	3.376(1)
*M*1–*M*6 (×2)	3.246(3)	3.412(1)
*M*2–*M*4 (×2)	3.212(3)	3.305(1)
*M*2–*M*5 (×2)	3.229(3)	3.380(1)
*M*3–*M*6 (×2)	3.153(3)	3.220(1)
*M*3–*M*3 (×2)	3.176(5)	3.188(1)
*M*4–*M*4 (×2)	3.144(4)	3.214(1)
Sb1–Sb2	2.883(2)	2.866(1)

Table A 2-5. Comparison of structural refinements for $Rb_4Zn_7As_7$

	Model 1 Full occupancies	**Model 1 Partial occupanices**
formula	$Rb_4Zn_7As_7$	$Rb_4Zn_{6.89(1)}As_{6.70(2)}$
Zn4 (4*c*; 0, *y*, ¼)		
occupancy	1	0.89(1)
y	0.00631(15)	0.00629(14)
U_{eq} (Å^2)	0.0509(11)	0.0432(14)
As2 (8*f*; 0, *y*, *z*)		
occupancy	1	0.85(1)
y	0.46937(10)	0.46935(9)
z	0.18290(19)	0.18301(17)
U_{eq} (Å^2)	0.0671(10)	0.0538(11)
no. of unique data, with $F_o^2 > 2\sigma(F_o^2)$	1100	1100
no. of variables	60	62
$R(F)$ for $F_o^2 > 2\sigma(F_o^2)$	0.0614	0.0565
$R_w(F_o^2)$	0.1606	0.1493
$(\Delta\rho)_{max}$, $(\Delta\rho)_{min}$ (e Å^{-3})	3.81, –6.08	4.47, –4.30

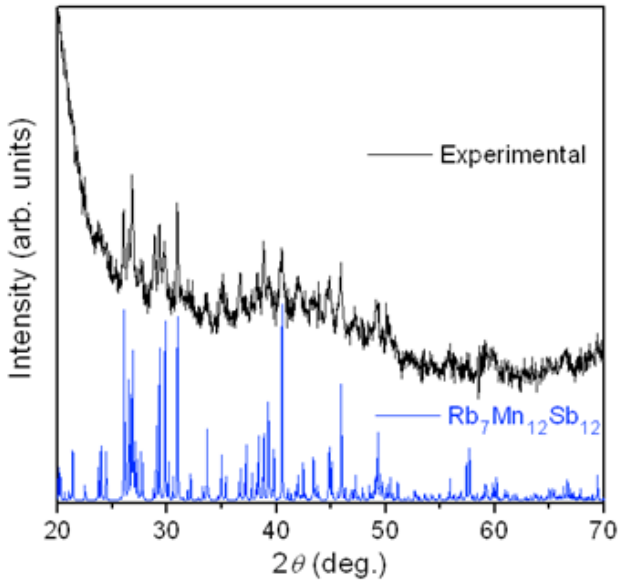

Figure A 2-1. Powder XRD pattern for $Rb_7Mn_{12}Sb_{12}$.

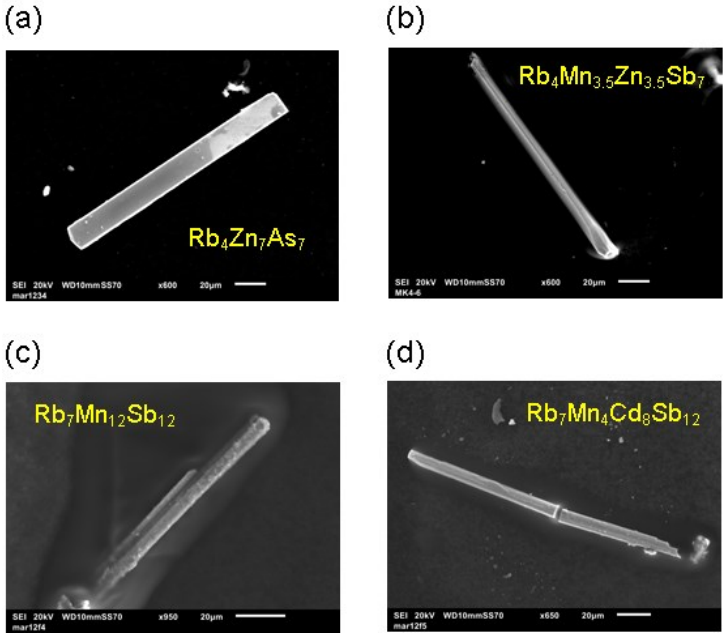

Figure A 2-2. SEM images of (a) $Rb_4Zn_7As_7$, (b) $Rb_4Mn_{3.5}Zn_{3.5}Sb_7$, (c) $Rb_7Mn_{12}Sb_{12}$, and (d) $Rb_7Mn_4Cd_8Sb_{12}$.

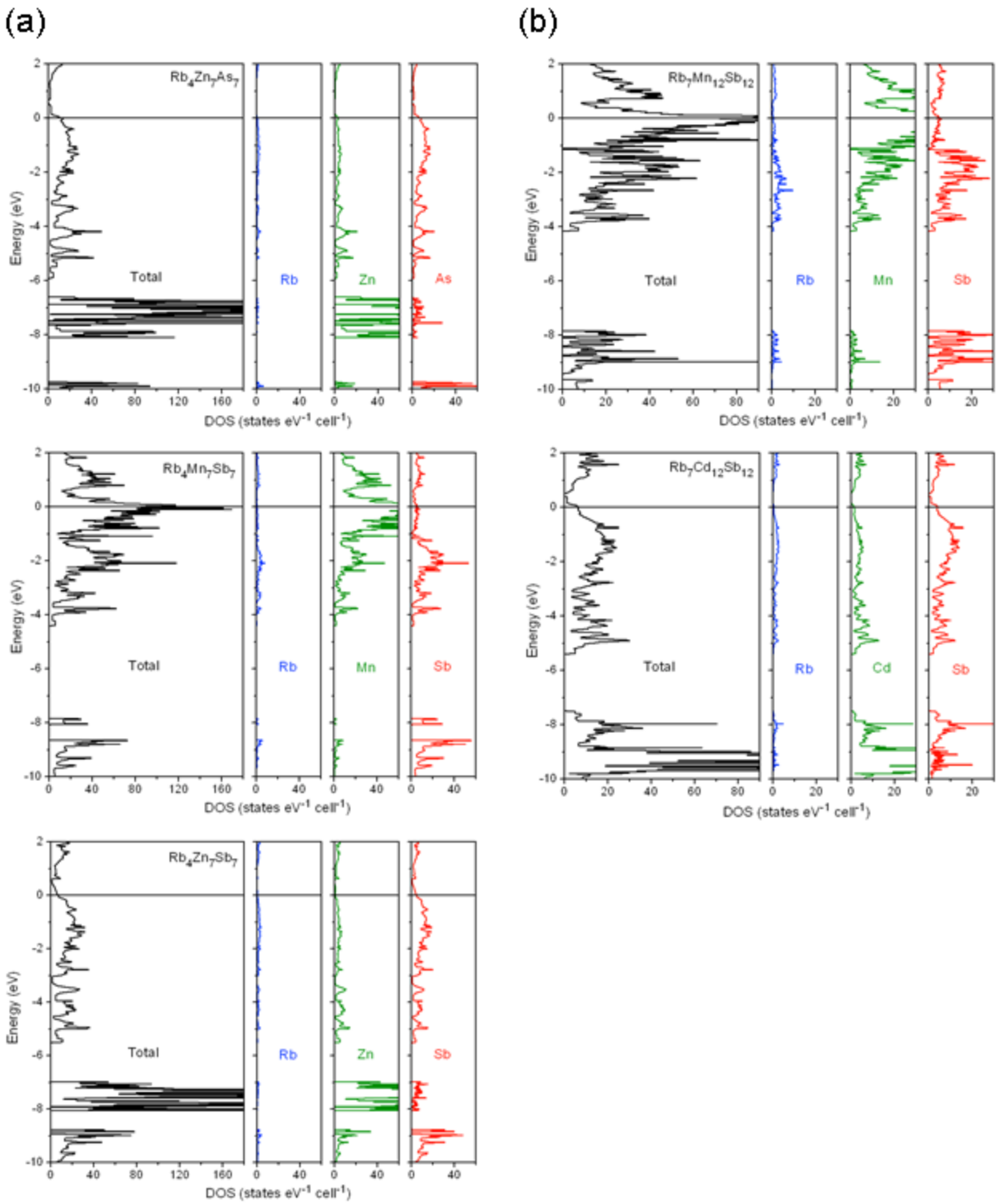

Figure A 2-3. Density of states (DOS) curves and their atomic projections for (a) $Rb_4Zn_7As_7$, $Rb_4Mn_7Sb_7$, and $Rb_4Zn_7Sb_7$, and (b) $Rb_7Mn_{12}Sb_{12}$ and $Rb_7Cd_{12}Sb_{12}$. The Fermi level is at 0 eV.

Appendix 3

Supporting Information for Chapter 4

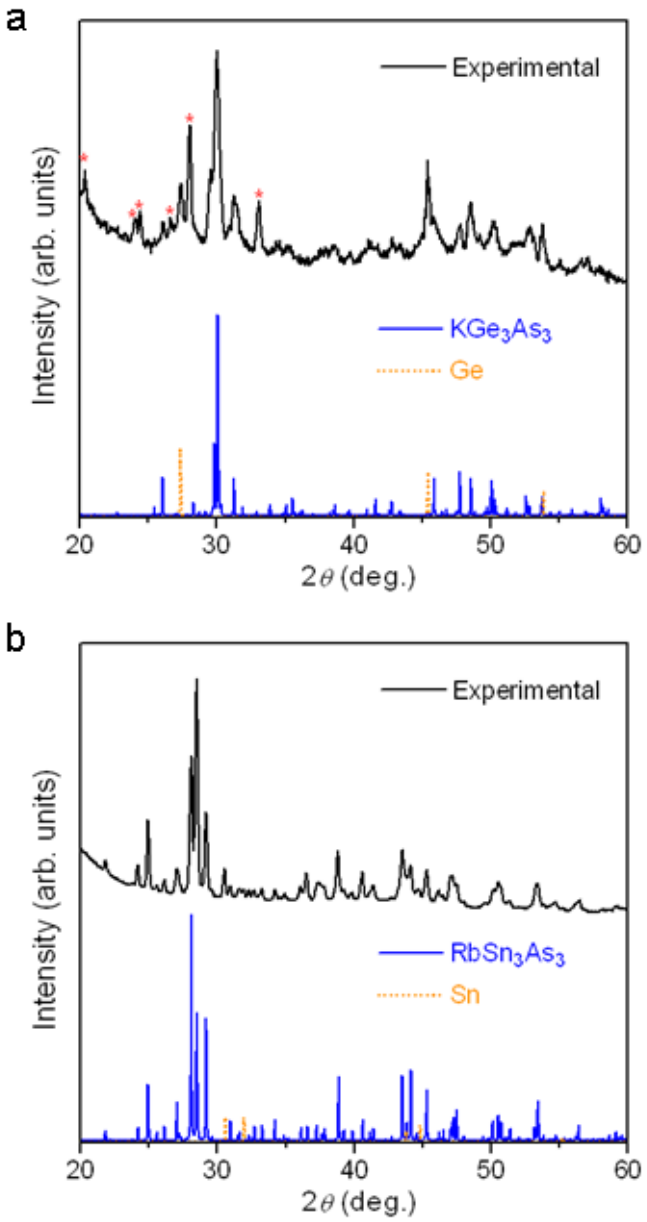

Figure A 3-1. Powder XRD patterns for (a) KGe_3As_3 and (b) $RbSn_3As_3$. Unidentified peaks in (a) are marked with asterisks.

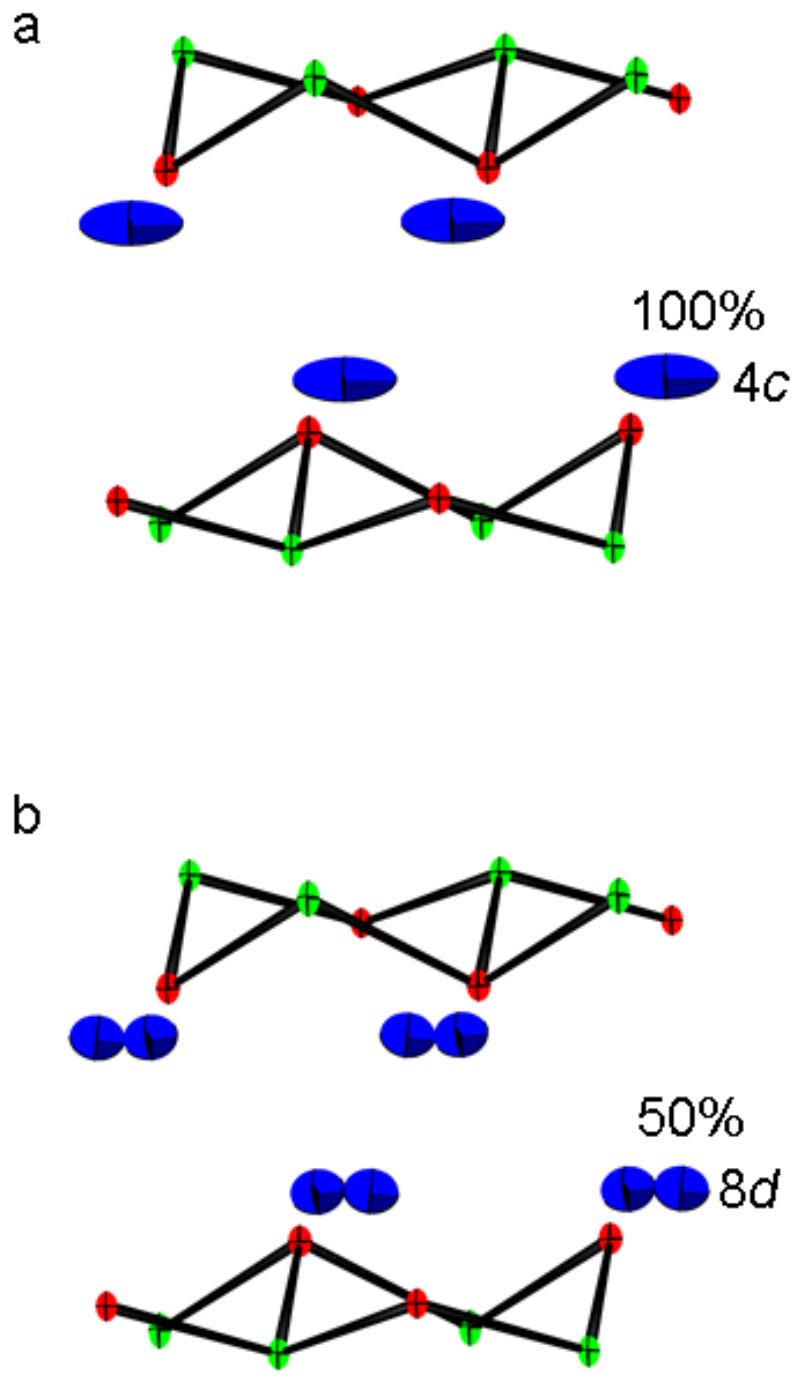

Figure A 3-2. Structure of $RbGe_3As_3$ modeled with (a) unsplit or (b) split Rb sites, with displacements elongated along the b-direction. Displacement ellipsoids are drawn at the 30% probability level.

Appendix 4

Supporting Information for Chapter 6

Table A 4-1. EDX analyses of $AM_{1.5}Tt_{0.5}As_2$ crystals

Compound	No. of spectra	Average composition (atomic %) [a]
$NaZn_{1.5}Si_{0.5}As_2$	4	89(1)% Na + Zn + As, 11(1)% Si
$NaZn_{1.5}Ge_{0.5}As_2$	4	88(1)% Na + Zn + As, 12(1)% Ge
$NaZn_{1.5}Sn_{0.5}As_2$	4	87(1)% Na + Zn + As, 13(1)% Sn
$NaCd_{1.5}Sn_{0.5}As_2$	6	30(1)% Na + Sn, 70(1)% Cd + As
$KZn_{1.5}Si_{0.5}As_2$	3	21(1)% K, 30(1)% Zn, 9(1)% Si, 40(1)% As
$KZn_{1.5}Ge_{0.5}As_2$	6	23(1)% K, 30(1)% Zn, 10(1)% Ge, 37(1)% As
$KZn_{1.5}Sn_{0.5}As_2$	5	30(1)% K + Sn, 70(1)% Zn + As
$KCd_{1.5}Sn_{0.5}As_2$	6	18(1)% K, 30(1)% Cd, 10(1)% Sn, 42(1)% As
$RbZn_{1.5}Ge_{0.5}As_2$	5	21(1)% Rb, 30(1)% Zn, 10(1)% Ge, 39(1)% As
$RbCd_{1.5}Sn_{0.5}As_2$	5	21(1)% Rb, 31(1)% Cd, 10(1)% Sn, 38(1)% As

[a] Expected composition for $AM_{1.5}Tt_{0.5}As_2$ is 20% *A*, 30% *M*, 10% *Tt*, and 40% As. When peaks from different elements overlap in the EDX spectra, the combined percentage is reported.

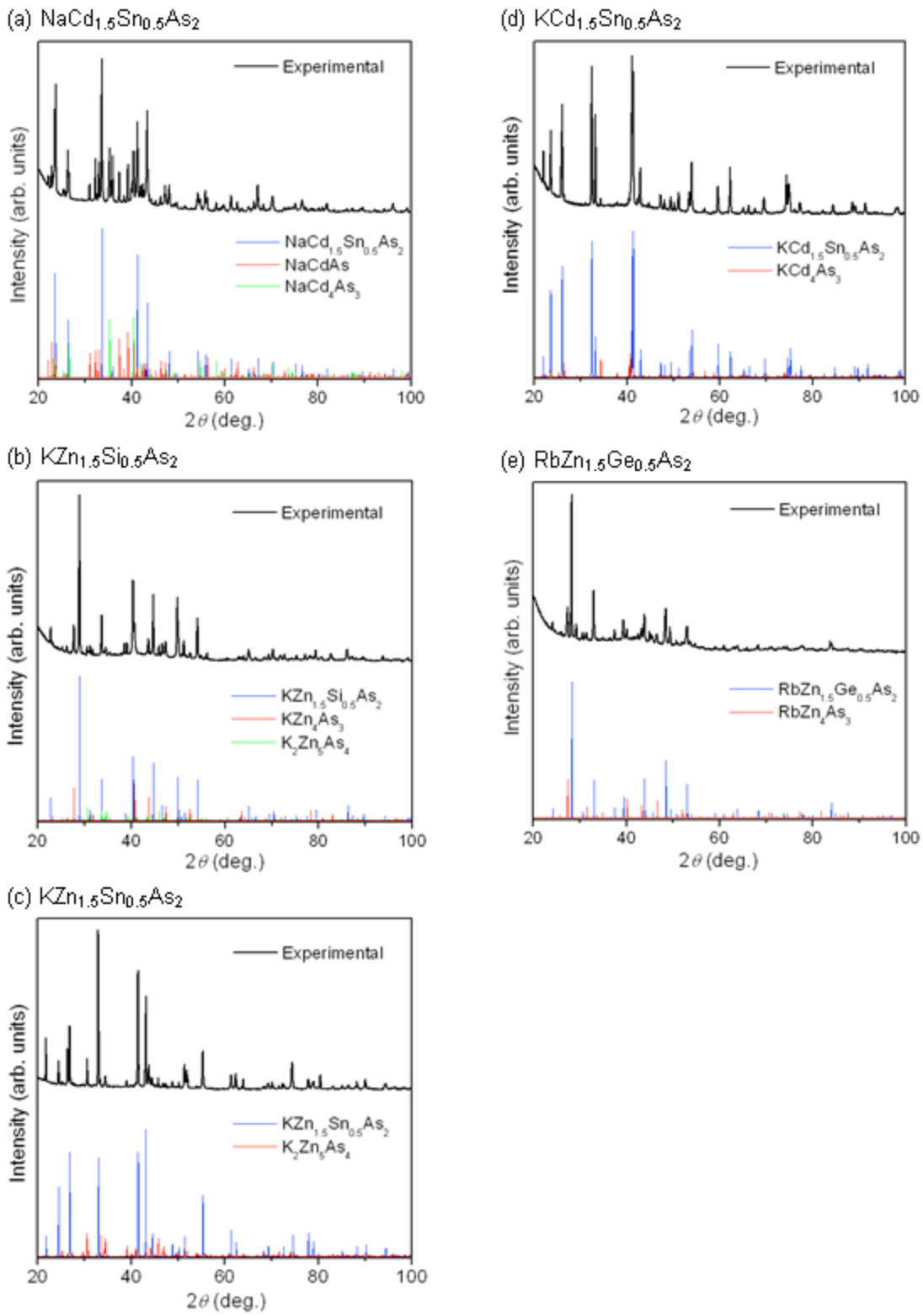

Figure A 4-1. Representative powder XRD patterns for $AM_{1.5}Tt_{0.5}As_2$ reactions.

(a) $NaZn_{1.5}Si_{0.5}As_2$

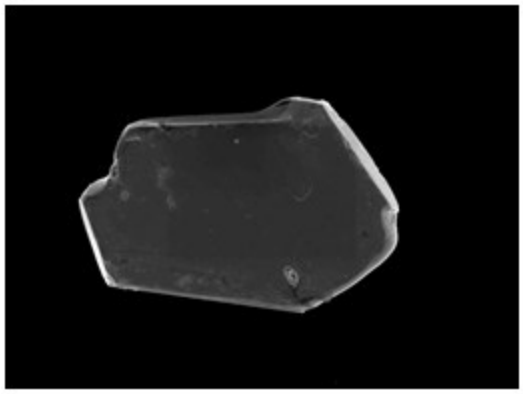

(b) $KZn_{1.5}Si_{0.5}As_2$

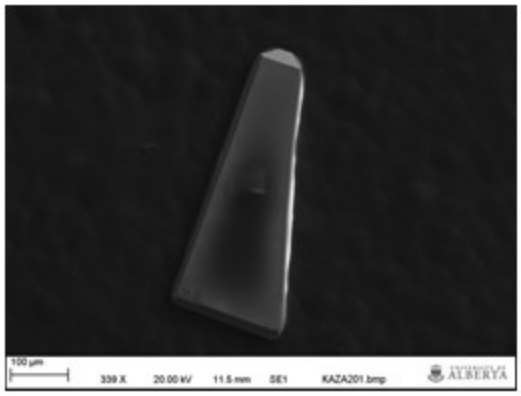

(c) $KZn_{1.5}Ge_{0.5}As_2$

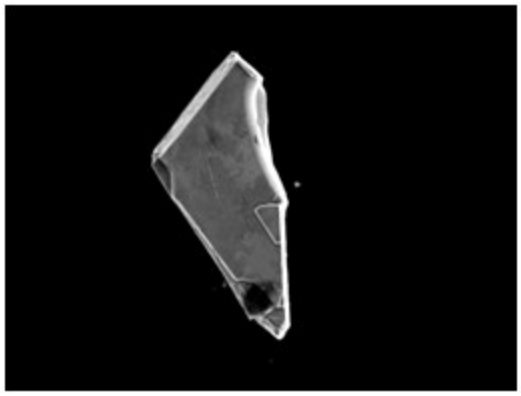

(d) $KZn_{1.5}Sn_{0.5}As_2$

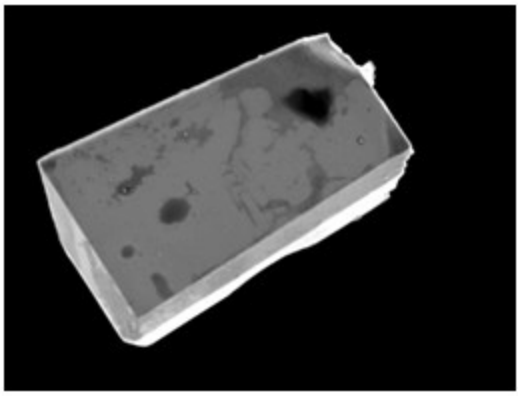

(e) $RbCd_{1.5}Sn_{0.5}As_2$

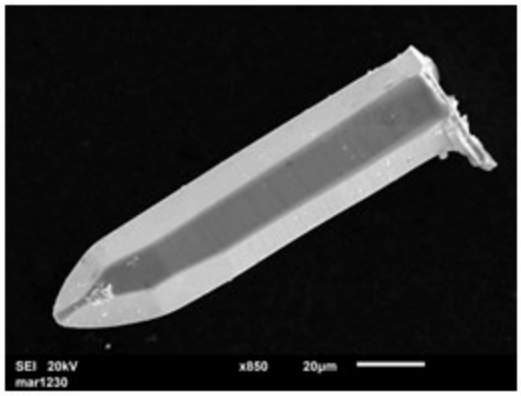

Figure A 4-2. Representative SEM images for $AM_{1.5}Tt_{0.5}As_2$ crystals.

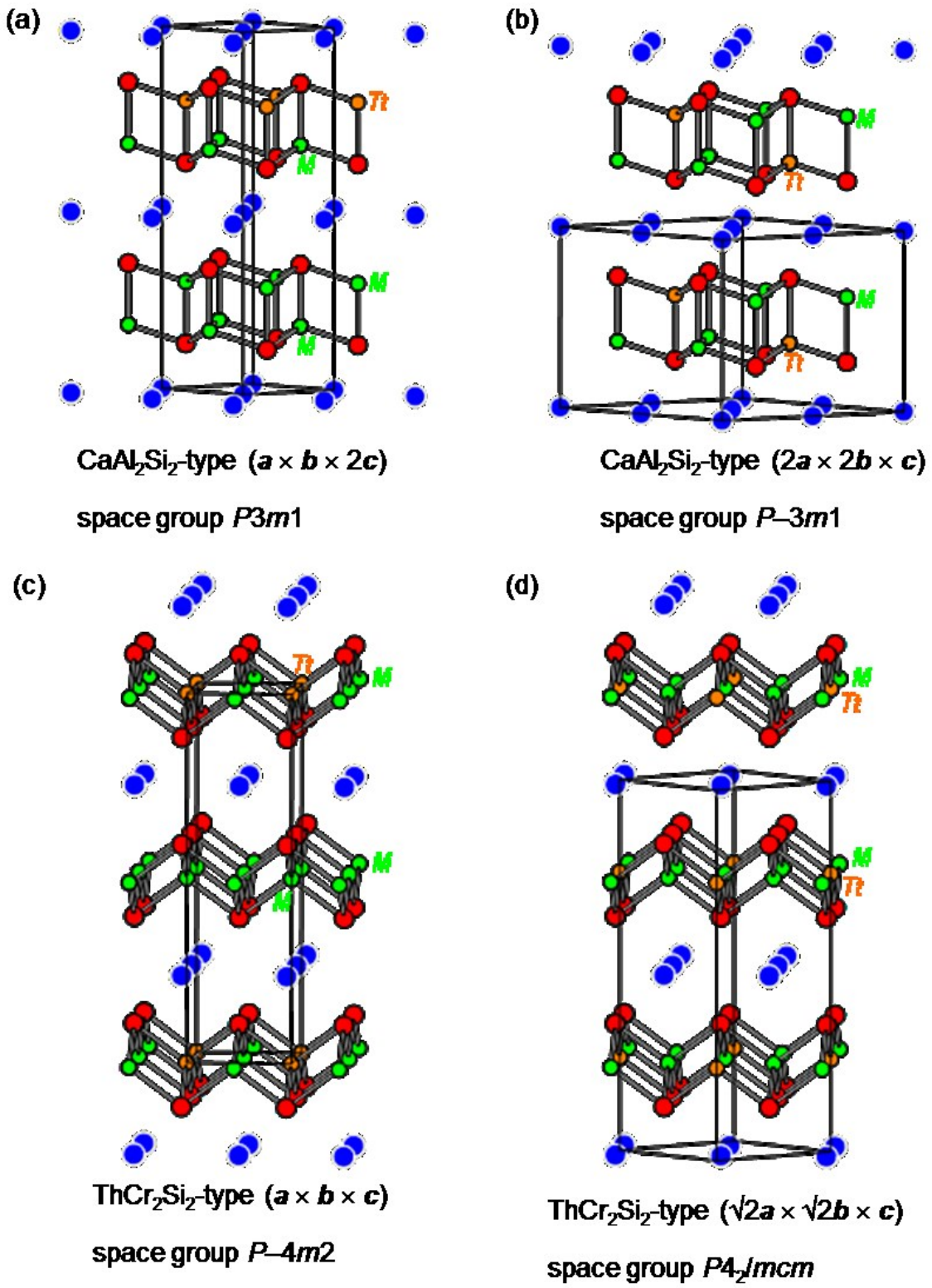

Figure A 4-3. Superstructure models for $AM_{1.5}Tt_{0.5}As_2$ considered in band structure calculations.

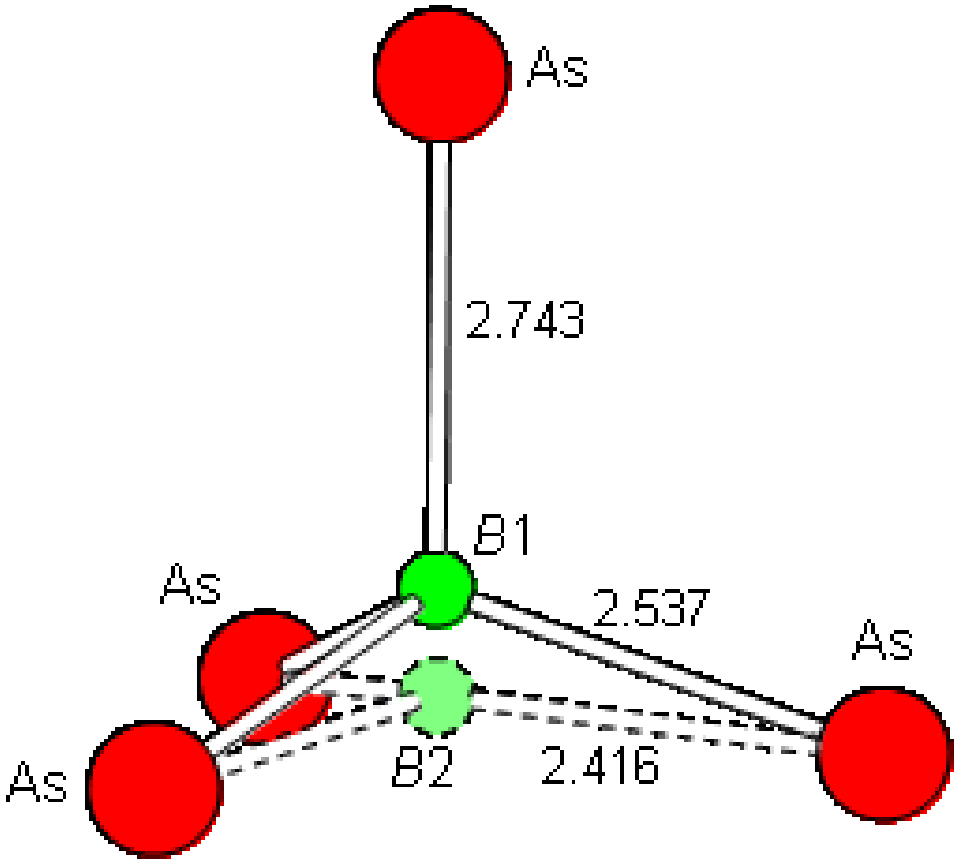

Figure A 4-4. Split sites for *B* atom in $NaZn_{1.5}Sn_{0.5}As_2$ and $NaCd_{1.5}Sn_{0.5}As_2$. The distances shown refer to $NaZn_{1.5}Sn_{0.5}As_2$.

Appendix 5

Supporting Information for Chapter 7

Table A 5-1. Bond valence sums (V_i) for ACdGeAs$_2$ (A = K, Rb)[a]

	KCdGeAs$_2$	**RbCdGeAs$_2$**
*A*1	1.19	1.01
*A*2	1.36	1.17
Cd1	1.74	1.73
Cd2	1.51	1.54
Ge1	3.68	3.68
Ge2	3.72	3.75
As1	2.64	2.56
As2	3.04	2.93
As3	2.63	2.57
As4	2.98	2.91

[a] The valence v_{ij} for a bond of length d_{ij} between atoms i and j was calculated through use of the equation $v_{ij} = \exp[(R_{ij} - d_{ij})/b]$, where the bond valence parameters R_{ij} were: K–As, 2.83 Å; Rb–As, 2.87 Å; Cd–As, 2.43 Å; Ge–As, 2.43 Å; Ge–Ge, 2.42 Å. An atom i then has a valence $V_i = \sum_j v_{ij}$.

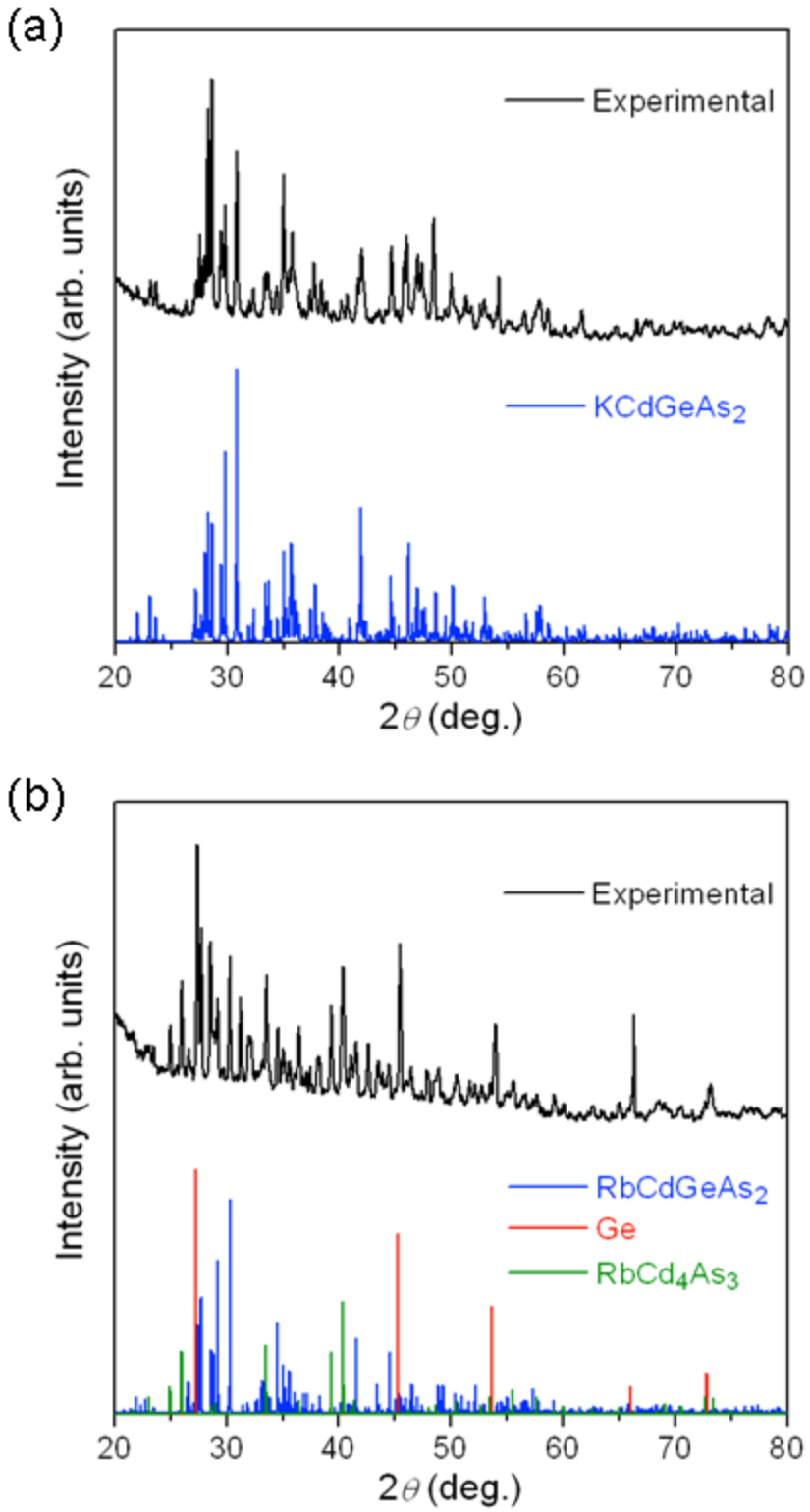

Figure A 5-1. Powder XRD patterns for (a) $KCdGeAs_2$ and (b) $RbCdGeAs_2$.

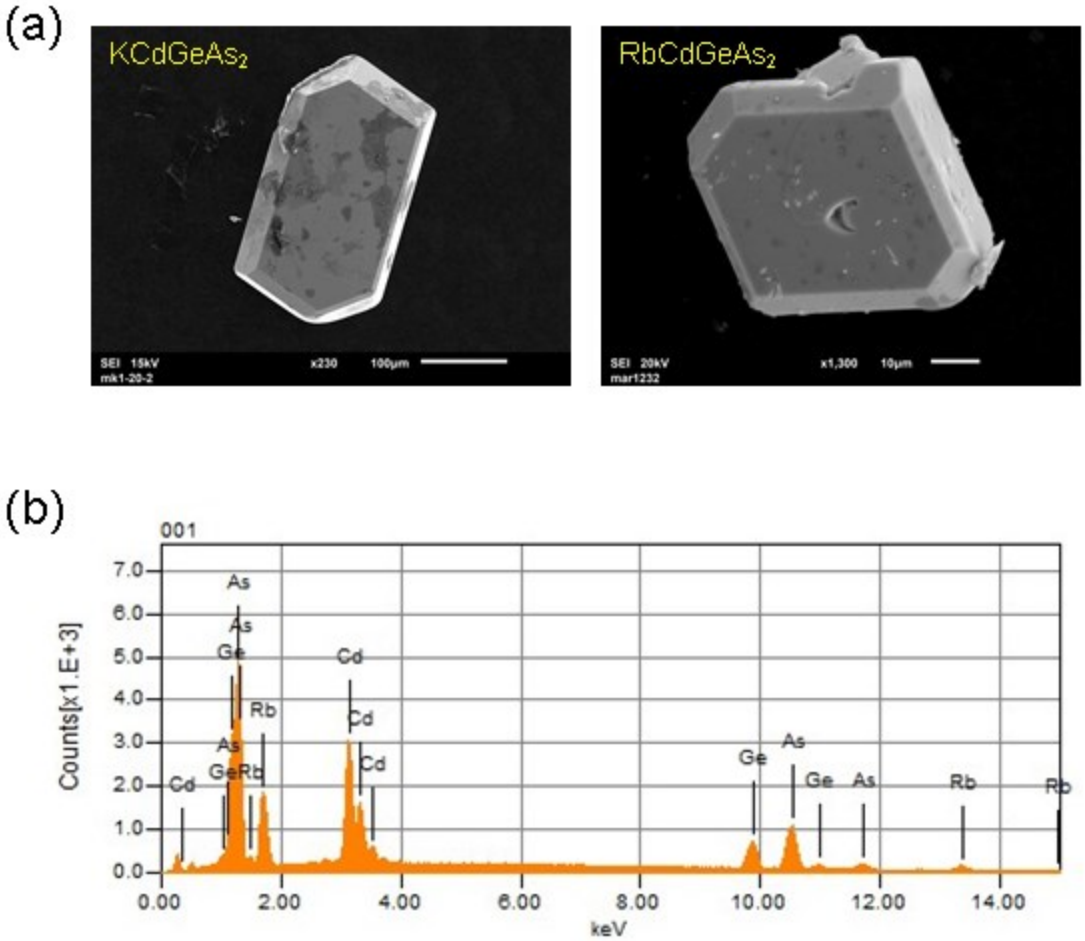

Figure A 5-2. (a) SEM micrographs for ACdGeAs$_2$ (A = K, Rb) and (b) EDX spectrum for RbCdGeAs$_2$.

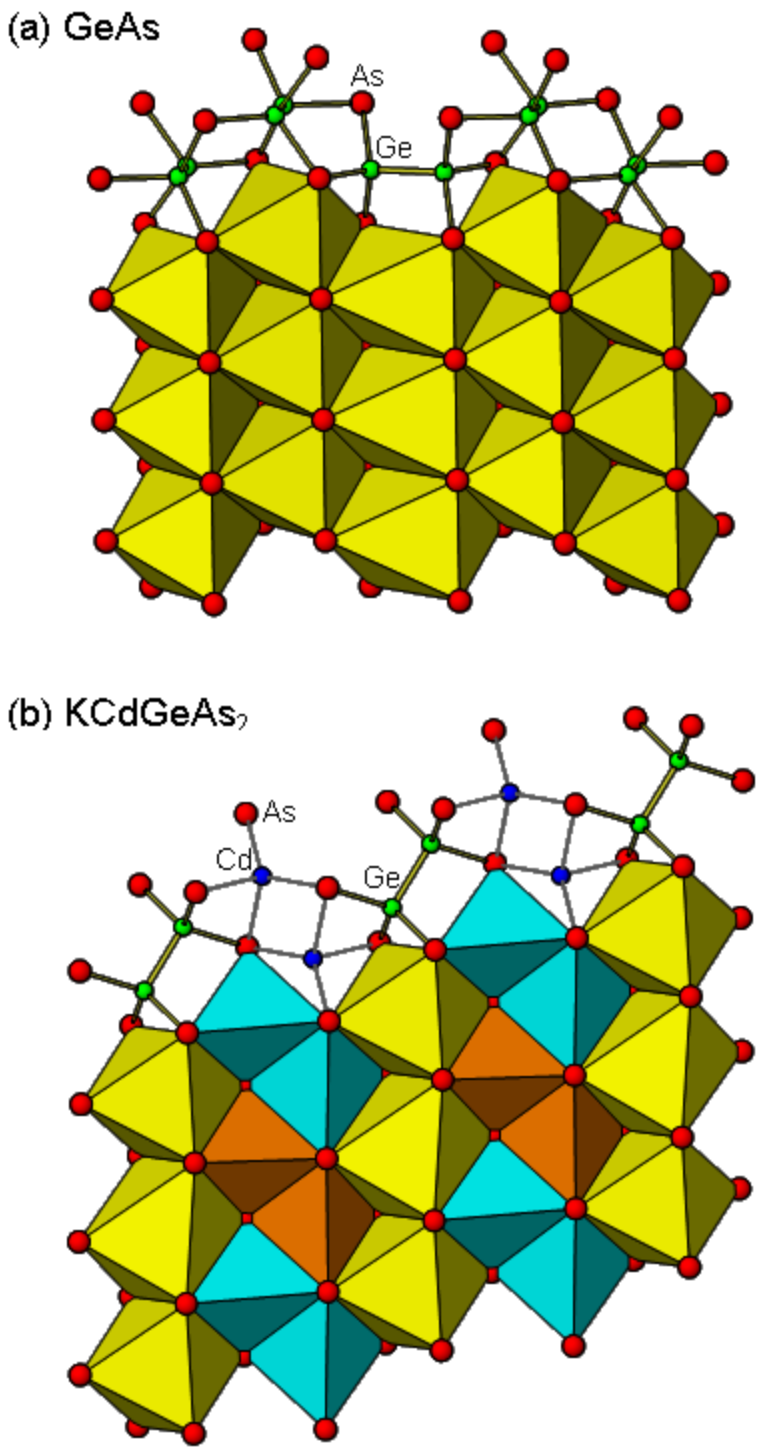

Figure A 5-3. Comparison of (a) layers in GeAs containing edge-sharing octahedra filled with Ge_2 dumbbells and (b) $[CdGeAs_2]$– layers in $KCdGeAs_2$ containing edge-sharing octahedra filled with Ge_2 dumbbells and edge-sharing tetrahedra filled with Cd atoms.

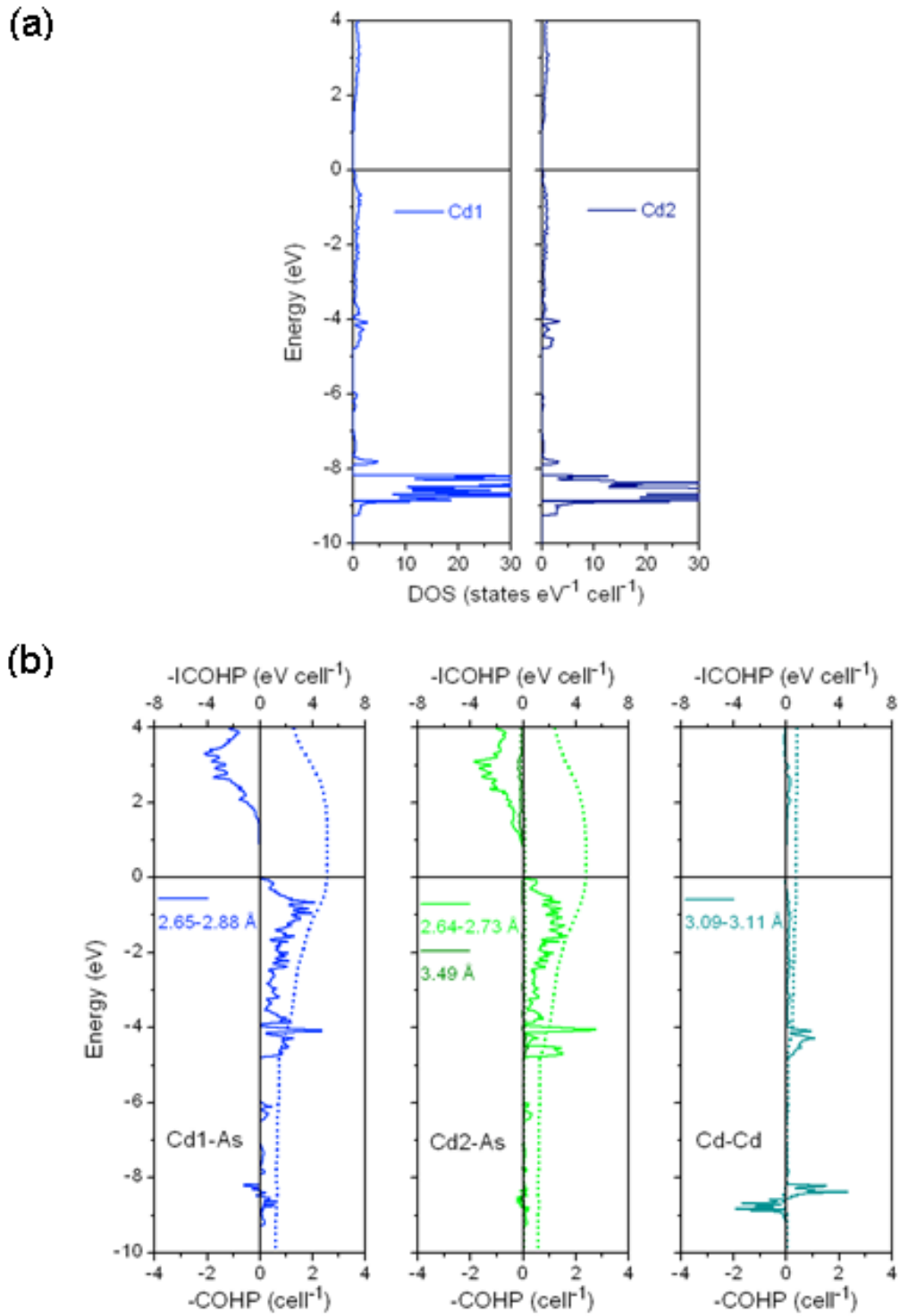

Figure A 5-4. (a) Atomic projections of density of states (DOS) for Cd1 (CN4) and Cd2 (CN3) in $KCdGeAs_2$. (b) Crystal orbital Hamilton population (COHP) curves for Cd1–As, Cd2–As, and Cd–Cd contacts in $KCdGeAs_2$. Note that the COHP scale here is different than in Figure 5 in the main text.

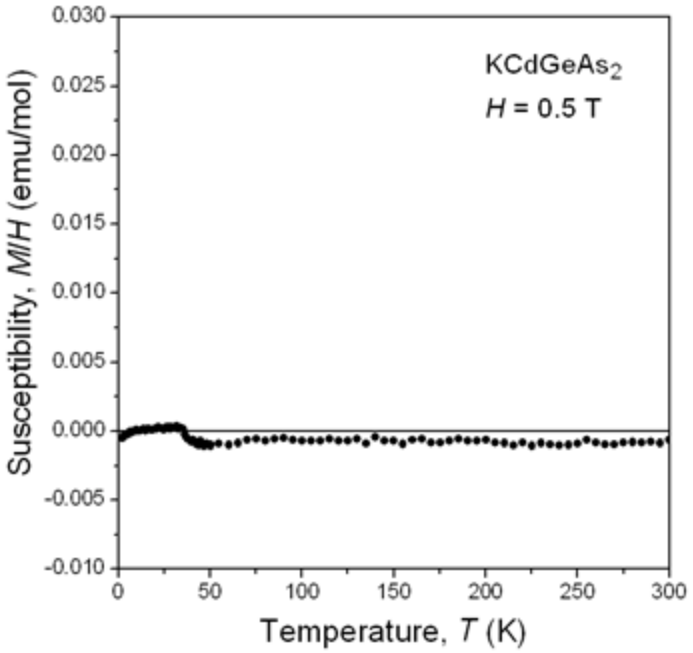

Figure A 5-5. Magnetic susceptibility of $KCdGeAs_2$.